Magnetic Properties of Self-assembled Manganese Oxide and Iron Oxide Nanoparticles

Spin Structure and Composition

Von der Fakultät für Mathematik, Informatik und Naturwissenschaften der RWTH Aachen University zur Erlangung des akademischen Grades einer Doktorin der Naturwissenschaften genehmigte Dissertation

vorgelegt von

Master of Science

Xiao Sun

aus
Qingdao, China

Berichter: Univ.-Prof. Dr. rer. nat. Thomas Brückel
Univ.-Prof. Dr. rer. nat. Joachim Mayer

Tag der mündlichen Prüfung: 04.06.2018

Diese Dissertation ist auf den Internetseiten der Universitätsbibliothek online verfügbar.

Abstract

Magnetic nanoparticles (NPs) have attracted much interest for decades due to their potential applications in high density data storage, spintronic devices and nanomedicine. In analogy to atoms, they can represent building blocks for NP superstructures. Below a critical size, NPs prefer to be in a magnetic single domain state. In this case, each NP can be considered as possessing one large magnetic moment called "superspin". The superspins in self-assembled NP superstructures interact with each other usually via dipolar interactions. With the interplay of individual and collective behaviour of the NPs, novel materials with appealing magnetic and electronic properties may be fabricated. In this thesis, the magnetic properties of two different transition metal oxide NP and bulk systems, manganese oxide and iron oxide, were studied.

For manganese oxides, the spin structure inside the NPs is of interest. Zero field cooled (ZFC) magnetization curves of MnO NPs usually show a low temperature peak at $\sim$25 K. No feature indicating the antiferromagnetic (AF)-to-paramagnetic (PM) phase transition of MnO was found near its bulk Néel temperature at 118 K. However, polarized neutron scattering shows the expected vanishing of the AF order parameter of MnO near 118 K. This contradiction between magnetometry and neutron scattering results can be explained assuming an AF-superparamagnetic (SPM) core with a ferrimagnetic (FiM) Mn_3O_4 shell. In order to study the magnetization dynamics of the AF-SPM core, AC-susceptibility measurements were performed. A low temperature peak is observed similar to that found in the ZFC curves. This peak shows a weak frequency dependence, which is expected for an AF system.

To further investigate the origin of the low temperature peak, bulk MnO was studied as a reference. Magnetometry and polarized neutron scattering experiments were performed on MnO powder and a single crystal to be compared with the results of NPs. The phase of manganese oxide was tuned by annealing the as-prepared samples in various environments. Their magnetic properties were compared to that of the as-prepared ones. Moreover, Monte Carlo simulations were performed for MnO NPs and "bulk".

In order to study the magnetic properties of self-organized NP superstructures, spherical iron oxide NPs were used. 2D ordered NP films were produced using various methods. The order of the NP superstructures was characterized using scanning electron microscopy (SEM) and grazing incidence small angle x-ray scattering (GISAXS). A weak feature near the Verwey transition of magnetite is found in ZFC/FC magnetization curves of NPs with 15 and 20 nm diameters. Above T_N of wüstite, the overall magnetic moment increases in the ZFC curves. This is due to the coupling between AF wüstite and FiM magnetite or maghemite. Moreover, a peak indicating the crossover between the blocked and the unblocked SPM or superspin glass (SSG) states of the NP superspins is observed in the ZFC curves. This peak temperature shows a strong field dependence as usually found for SPM and SSG systems. Moreover, the peak temperature shows a decrease as the NP size decreases due to the smaller energy barriers of smaller particles. In the hysteresis loops of 11 - 20 nm NPs, an Exchange Bias (EB) effect and a hardening effect are observed. The iron oxide phases of the NPs were also tuned using various annealing procedures. By annealing the particles in vacuum at 318°C for several hours, the ratio of wüstite and magnetite is increased. After the particles were annealed in air, they tend to be fully oxidized to maghemite.

Zusammenfassung

Magnetische Nanopartikel (NP) haben in den letzten Jahren aufgrund ihrer zahlreichen Anwendungsgebiete in verschiedenen Bereichen hohe Aufmerksamkeit erlangt. Zu den potentiellen Anwendungen zählen beispielsweise Datenspeicher mit hoher Integrationsdichte, Spintronik-basierte Bauelemente, sowie in der Nanomedizin. In Analogie zu Atomen können NP als Bauelemente für Überstrukturen aus NP dienen. Unterhalb einer kritischen Partikelgröße der NP wird ein eindomäniger magnetischer Zustand bevorzugt, der als ein einzelner großer Spin, dem sogenannten Superspin, angesehen werden kann. In selbstorganisierten Überstrukturen wechselwirken diese einzelnen Superspins via Dipolwechselwirkung. Durch das Wechselspiel von individuellem und kollektivem Verhalten der NP können neuartige Materialien mit vielseitigen magnetischen und elektronischen Eigenschaften entwickelt werden. Die vorliegende Arbeit beschäftigt sich mit der Untersuchung der magnetischen Eigenschaften zweier Übergangsmetalloxide, Manganoxid und Eisenoxid, die als NP sowie als Bulk vorliegen.

Im Fall von Manganoxid ist insbesondere die Spinstruktur innerhalb der NP von besonderen Interesse, da Magnetisierungsmessung nach Abkülen im Nullfeld (ZFC) einen Peak bei tiefen Temperaturen ($\sim 25\,\mathrm{K}$) zeigen. Im Gegensatz dazu kann kein Hinweis für den Phasenübergang Antiferromagnet (AF) zu Paramagnet gefunden werden, der im Bulk bei 118 K liegt. Allerdings konnte mit Hilfe von polarisierter Neutronenstreuung ein Verschwinden des AF Ordnungsparameters bei 118 K gefunden werden. Dieser scheinbare Widerspruch beider Messmethoden kann durch die Annahme erklärt werden, dass ein NP aus einem AF-superparamagnetischen (SPM) Kern und einer ferrimagnetischen (FiM) Mn_3O_4 Hülle besteht. Zur näheren Untersuchung dieses Effekts wurden AC-Suszeptibilitätsmessungen durchgeführt, wobei ein Peak bei niedrigen Temperaturen gefunden wurde. Dieses Ergebnis ist ähnlich zu dem in den ZFC gefundenen Verhalten. Der Peak zeigt eine schwache Frequenzabhängigkeit, die auf einen AF hinweist.

Um diesen Effekt zu untersuchen wurde MnO in Pulverform und als Einkristall als Referenz mittels Magnetometrie und polarisierter Neutronenstreuung untersucht. Anschließend wurden die Ergebnisse mit denen der NP verglichen. Die strukturelle Phase des Manganoxids wurde dabei mittels verschiedener Heizprozesse verändert. Monte-Carlo-Simulationen für MnO NP und Bulk ergänzen hier die experimentell ermittelten Daten.

Für die Untersuchung der magnetischen Eigenschaften von selbstorganisierten NP-Überstrukturen wurden sphärische Eisenoxidnanopartikel verwendet. Hierfür wurden NP Monolagen mit verschiedenen Methoden hergestellt. Die Anordnung der NP wurde anschließend mit Rasterelektronmikroskopie (SEM) und Kleinwinkelstreuung (GISAXS) detailliert untersucht. Darüber hinaus wurden die magnetischen Eigenschaften der Proben untersucht. ZFC/FC Magnetometriemessungen zeigten hier eine Besonderheit nahe des Verwey-Übergangs in NP mit einem Durchmesser von 15 bzw. 20 nm. Diese entsteht durch eine Kopplung des AF Wüstit und des FiM Magnetit oder Maghemit. Außerdem weist ein Peak auf den Übergang vom blockierten zum nicht blockierten SPM oder Superspinglas (SSG)-Zustand der NP-Superspins. Der Peak zeigt eine deutliche Feldabhängigkeit, die man so auch in SPM- oder SSG-Systemen erwartet. Zusätzlich verringert sich die Peaktemperatur für NP mit abnehmenden Durchmesser aufgrund der kleineren Energiebarriere für kleinere Partikelgrößen. In magnetischen Hysteresemessungen von NP mit einem Durchmesser von 11-20 nm konnte ein Exchange Bias und ein magnetischer "hardening" Effekt gefunden werden. Die Struktur der NP wurde hier ebenfalls durch verschiedene

Heizprozesse beeinflusst. Das Verhältnis zwischen Wüstit und Magnetit konnte durch Heizen im Vakuum für einige Stunden bei 318 °C verändert werden. Durch Heizen der Probe an Luft wurde die Struktur der NP zu reinem Maghemit.

Contents

1 Introduction

As potential candidates for novel materials with appealing properties, nanoparticles (NPs) have attracted interest for decades. Several materials show different optical properties as the size decreases [1]. For example, TiO_2 is an important white pigment. The commercial TiO_2 pigment has a typical size of $0.2 - 0.3\,\mu$m. As its size is reduced to the nanometer range, it becomes transparent. The colour of hermatite changes from dark violet to light red with a decreasing particle size. Moreover, NP clusters may order into different structures responding to an applied magnetic field, which will lead to different colours of the samples due to optical diffraction. Such size or structure dependent optical properties make nanomaterials attractive for applications such as pigments and optoelectronics. Furthermore, transition metal oxide NPs have attracted much interest because of potential applications, such as electrode materials for rechargeable solid-state batteries or efficient catalysts for fuel-cell reactions [2]. Using carbon nanotubes as anode and metal oxide NPs as cathode, the charge storage density of Li-ion batteries can be significantly improved [1]. Due to their small sizes, the diffusion pathway of Li ions is shorter and thus a higher current can be achieved. In addition, the interfacial contact areas of NPs with the electrolyte are larger, which may potentially increase the storage density.

Antiferromagnetic (AF) NPs, such as CoO and NiO NPs, have been previously studied [3–11]. Due to the finite size effect, the Néel temperature of Co_3O_4 is reported to be reduced in NP form [8]. Superparamagnetic behaviour has also been observed for AF NPs due to uncompensated surface spins [6,11,12]. Below the blocking temperature, large coercive fields were found [7]. The surface spins are reported to behave as a 2D DAFF (diluted AF in a field) using thermoremanent (TRM) and isothermoremanent (IRM) magnetization curves as a fingerprint [3,4]. Due to the coupling between the AF core and the surface spins, an exchange bias (EB) effect is often observed [6, 7, 11]. This coupling is reported to vanish below a critical size [9].

Nowadays nanomaterials with multifunctional properties are of particular interest. By combining two materials with different physical and/or chemical properties, novel materials with a broader spectrum of potential applications may be produced [12,13]. Core/shell, Janus, dumbbell or snowman nanostructures have been successfully synthesized recently. By covering superparamagnetic NPs with silica shells, they can be both physically and chemically protected from the surrounding environment [14]. Thus the stability is increased. The stability can be further increased by attaching poly(ethylene glycol) chains at the surface of the NPs. Due to the hydrophilicity of these chains, the particles become highly soluble in aqueous solutions, such as the human blood serum [14, 15]. This makes them suitable for biomedical applications, such as protein separation, targeted drug delivery, magnetic hyperhermia treatments, optical and magnetic resonance imaging [14–17]. Moreover, NPs can be filled into carbon nanotubes to reduce the toxicity [16].

Also, FePt NPs are known as ideal candidates for high density data storage devices due to their high anisotropy and high saturation magnetization. By attaching an AF MnO NP at the surface of a FePt NP, the magnetic moments of the FePt NP can be stabilized via exchange coupling [12]. Compared to single FePt or MnO NPs, the heterodimer NPs show higher characteristic temperatures as well as an enhanced coercive field and remanent magnetization [12, 18].

In order to fabricate nanostructures, there are two general approaches, i.e. top-down and bottom-up methods [19]. For top-down methods, one starts with larger structures.

The sizes of structures are then reduced using various processes, such as structuring or lithography [20]. One of the most often used processes is photolithography. With the help of a photoresist layer, desired patterns can be transferred from the masks to the substrate after exposure to UV light. However, this process is complex and expensive. In addition, the resolution of the structures is limited to ∼10 nm due to the diffraction limit of UV light. The resolution can be improved by replacing UV light by an electron beam or x-rays. However, electron beam lithography is very expensive and very slow and x-rays might destroy the masks. To reach even higher resolutions below ∼ 10 nm, NP self-assembly can be used, which is one of the bottom-up methods [20].

Opposite to the top-down methods, bottom-up methods start with smaller structures such as atoms or molecules. Using chemical methods, for example thermal decomposition, NPs with a controllable shape and size can be synthesized. Another method, which is often used to fabricate particles, is the NP condensation. By evaporating the material inside a vacuum chamber filled with an inert gas, the atoms or molecules are cooled after they collide with the inert gas. The vapor is then supersaturated, which may lead to the formation of particles with nanometer sizes. To produce patterned nanostructures with large sizes, self-assembly of small particles, such as molecules or NPs, can be used. Various self-assembly methods will be introduced later in section 6.2. Using these methods, nanostructures as 1D to 3D arrangements can be fabricated.

There are also approaches combining both top-down and bottom-up methods. For example, using self-assembled particle monolayers as masks, patterned structures, such as porous structures, can be fabricated. This approach is known as nanosphere lithography, which is an inexpensive and efficient method [21].

As nanostructures with the smallest dimension (i.e. 0D-structures), NPs have been experimentally studied intensely in the last decades using various methods, such as electron microscopy, magnetometry, x-ray and neutron scattering. The magnetic field distributions in 1D and 2D ordered NP structures have been studied using electron holography with a resolution below the particle size [22]. The magnetic order of the particles has been visualized in real space. In addition, modelling and simulations of the spin distribution have been performed to better understand the spin structure inside NPs as well as the dipolar interactions between them [7, 10, 19, 23, 24].

In this thesis, two transition metal oxide systems are in the focus. The current state of research will be reviewed in section 5.1 and 6.1.2, respectively.

The spin structure of MnO is still not fully understood, although it has been studied for decades. Moreover, MnO NPs usually show interesting magnetic behaviours, which are quite different from other AF NPs [11, 18, 25]. This might be due to intrinsic MnO. We focus on the spin structure inside the NPs. To have a better understanding of the nanosize effects, the results of bulk MnO are compared to that of the NPs in chapter 5. The experimental results are compared with that obtained from Monte Carlo simulations. To investigate the intrinsic magnetic behaviour of MnO as well as the influence of partially oxidized Mn_3O_4 or Mn_2O_3 onto the spin structure of MnO, the as-prepared samples were annealed. The results before and after annealing are compared.

Iron oxide NPs are of interest for biomedical applications due to their non-toxicity. Particles with relatively narrow size distribution can be fabricated. This makes the self-assembly of large areas of NP films possible. As magnetic particles, the magnetic correlations between the NPs within the film can be studied. In chapter 6, I will introduce several fabrication methods and the structural characterizations of 2D ordered NP films

using iron oxide NPs. A systematic study of the magnetic properties depending on the particle size will be shown. Moreover, both manganese oxide and iron oxide have various phases depending on their valences. This makes these two systems ideal candidates to study the magnetic properties with controlled variation of the oxygen content. We used various annealing procedures to vary the oxygen content within the NPs. The magnetic properties before and after the annealing procedures are compared.

2 Theoretical Background

2.1 Basics of Magnetism

Magnetism in condensed matter arises from the individual and collective behaviour of magnetic moments. Due to various interactions between magnetic moments as well as between magnetic moment, the lattice and an applied magnetic field, materials show individual magnetic properties. In this chapter, the magnetic moment is firstly introduced. After that the magnetic behaviours of isolated magnetic moments, as well as the influence of various interactions with regards to the arrangement of magnetic moments are discussed. Finally, some phenomena such as anisotropy, magnetic domains and the exchange bias effect are introduced.

2.1.1 Magnetic Moments

In classical electromagnetism, the magnetic moment results from circulating charges and can be expressed as:

$$d\vec{m} = I d\vec{A} \tag{1}$$

with $d\vec{m}$ the magnetic moment induced by a current I flowing around an area $d\vec{A}$ as shown in Fig. 1(a).

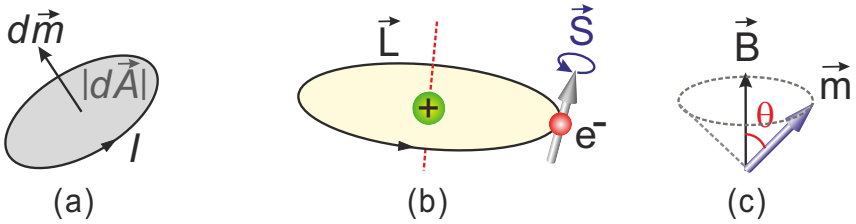

Figure 1: (a) Magnetic moment $d\vec{m}$ induced by a current I flowing around an area $d\vec{A}$. (b) Spin ($\vec{S}$) and orbital ($\vec{L}$) angular momentum of an electron moving around the nucleus. (c) A magnetic moment $\vec{m}$ precessing around a magnetic field $\vec{B}$. Adapted from [26].

Magnetic moments in condensed matter mainly originate from electrons, which have an intrinsic spin angular momentum $\vec{S}$. Moreover, electrons orbit around the nucleus and thus possess an additional orbital angular momentum $\vec{L}$ as illustrated in Fig. 1(b). The nucleus possesses a nuclear spin and thus has a nuclear magnetic moment. Nuclear magnetic moments are several orders of magnitude smaller (typically 10^{-3} - $10^{-4}\mu_B$) compared to the electron magnetic moments ($\sim \mu_B$), because their magnitudes are inversely proportional to the mass of the particles involved. Therefore, they are usually neglected for the discussion of solid state magnetism. Electron magnetic moments $\vec{m}_S$ and $\vec{m}_L$ coming from the spin and orbital angular momentum, respectively, and the total magnetic moment $\vec{m}_J$ can be written as:

$$\vec{m}_S = -g_S \mu_B \vec{S}$$
$$\vec{m}_L = -g_L \mu_B \vec{L}$$
$$\vec{m}_J = -g_J \mu_B \vec{J}$$

with $\mu_B = 9.274 \times 10^{-24}$ J/T the Bohr magneton, $g_S \approx 2$, $g_L = 1$ are the *g-factors* for spin and orbital parts, respectively, and g_J is known as *Landé g-factor*, which can be calculated from the spin and orbital angular momentum quantum numbers as follows:

$$g_J = \frac{3}{2} + \frac{S(S+1) - L(L+1)}{2J(J+1)} \tag{2}$$

The energy of a magnetic moment in a magnetic field $\vec{B}$, commonly named "Zeeman Energy", as shown in Fig. 1(c) can be calculated using:

$$E = -\vec{m} \cdot \vec{B} = -m\ B\ cos\theta \tag{3}$$

To minimize the energy, a torque $\vec{G} = \vec{\mu} \times \vec{B}$ tends to turn $\vec{m}$ to align parallel to $\vec{B}$. This will cause the precession of $\vec{m}$ around $\vec{B}$ as shown in Fig. 1(c), which is known as *Larmor precession*.

In magnetometry experiments, the overall magnetic moments of samples are usually measured. Therefore, *magnetization* is introduced, which is defined as the magnetic moment per volume, and represents the average magnetic moment density within the sample. The relationship between the magnetization and the magnetic field can be expressed using the *magnetic susceptibility*:

$$\chi = \frac{dM}{dH} \tag{4}$$

In simple cases, the induced magnetic moment $\vec{m}$ is linearly related to the magnetic field $\vec{H}$ as $\vec{m} = \chi\vec{H}$.

2.1.2 Isolated Magnetic Moments

For materials with fully filled electron shells, all electrons are paired and thus the magnetic moments due to single spin angular momentum are compensated. Therefore, only the orbital angular momentum plays a role in the magnetism of such materials. In the presence of a magnetic field, a magnetization opposite to the field direction is induced. This is known as *diamagnetism*, which exhibits a negative susceptibility. In classical electromagnetism, diamagnetism has been explained by the Lenz's law. However, it is a entirely quantum mechanical phenomenon [26]. Diamagnetism exists theoretically in all materials. However, it is usually very weak. Therefore, the magnetic behaviour of many materials is dominated by other magnetic mechanisms.

Materials with partially filled electron shells possess non-zero magnetic moments due to unpaired electrons. When the magnetic moments interact with each other very weakly, they can be considered as behaving independently. In the absence of a magnetic field, they are randomly oriented and show no net magnetization. However, applying a magnetic field to the material, the magnetic moments of single atoms tend to align parallel to the field in order to reduce the Zeeman energy, and thus the magnetization is increased. In this case, a positive susceptibility can be observed. This is known as *paramagnetism (PM)*. Compared to diamagnetism, PM is much stronger, and thus usually dominates the magnetic behaviour of materials containing non-interacting magnetic moments. The diamagnetism contributes only as a weak background.

2.1.3 Anisotropy

For some materials, it is easier to be magnetized in one or several directions than the others. These preferential magnetization directions or axes are known as *easy directions* or *easy axes*. In this case, magnetization is no longer isotropic in all directions as discussed above. For example, materials with a uniaxial anisotropy have the lowest energy when magnetized in directions along its easy axis. Energy minima of these two antiparallel orientations are separated by an energy barrier $\Delta E = KV$, where K is the anisotropy density and V the volume. Depending on the orientation of the magnetic moments, the anisotropy energy can be calculated as:

$$E_a = KVsin^2\theta \tag{5}$$

with θ the angle between the magnetization $\vec{M}$ and the easy-axis. The directions with the maximum energy cost are known as *hard-directions* or *hard-axes*.

Magnetic anisotropy may originate from various sources:

Shape anisotropy As the name expresses, shape anisotropy is related to the shape of the solid. Demagnetizing fields induced by the magnetic moments inside the solid can be described by $\vec{H}_d = -\underline{\underline{\mathcal{N}}} \cdot \vec{M}$ with $\underline{\underline{\mathcal{N}}}$ the demagnetizing tensor. For spheres, the demagnetizing field is isotropic in all directions, and the demagnetizing factor $\mathcal{N}_x = \mathcal{N}_y = \mathcal{N}_z = \frac{1}{3}$. However, the demagnetizing factor $\mathcal{N}_{ij}$ may vary along different directions due to the shape anisotropy. For a needle shaped structure, $\mathcal{N}$ is 0 parallel to the direction along the long direction of the needle and $\mathcal{N} = \frac{1}{2}$ along the two directions perpendicular to it. Within the plane of thin films $\mathcal{N} = 0$, while $\mathcal{N} = 1$ perpendicular to the plane. Therefore, the energy of the demagnetizing field can be non-uniform along different directions. The energy barrier between two energy minima caused by the shape anisotropy can be calculated by the difference between the easy- and hard-axes: $\Delta E = -\frac{1}{2}\mu_0 V M^2(\mathcal{N}_{easy} - \mathcal{N}_{hard})$ [27]. If the anisotropy energy cannot be overcome, magnetic moments will prefer to lie along the easy axis. Shape anisotropy is induced by the sample shape and is therefore not an intrinsic property of the material.

Magnetocrystalline anisotropy is an intrinsic property of the material. Due to the electrostatic interaction between the electron orbitals and its environment, energy splits into various levels for different orbitals. This is known as the *crystal-field effect*. According to the symmetry of the lattice, neighbouring orbitals overlap differently when the orbitals have different orientations, thus the energy cost varies along different crystallographic directions. Moreover, spin-orbit interaction stabilizes the spin moment lying parallel to the orbital moment. As a result, magnetic moments aligned along certain crystalline directions are favoured. Therefore, the magnetization becomes anisotropic when the sample is magnetized in different crystallographic directions. Easy- and hard-axes of the magnetocrystalline anisotropy are defined according to the crystal-field interaction and the spin-orbit interaction. For materials with single-ion uniaxial anisotropy like MnO, each magnetic ion is surrounded by an identical environment. Therefore, the overall anisotropy constant KV resulting from n ions in a volume V can be rewritten as $KV = nD\vec{S}^2$, where D is the anisotropy constant for one single spin $\vec{S}$.

Induced anisotropy Besides these two anisotropy types discussed above, originating from the sample itself, additional anisotropy axes can be "induced" by using alternative methods: certain alloys tend to align along a preferential direction when annealed in a magnetic field, thus an anisotropy is produced. Moreover, applying a uniaxial stress can also induce a magnetic anisotropy in some materials. Another way to induce an anisotropy is to introduce an exchange bias effect, which will be explained later in detail (section 2.1.7). Due to the coupling to an antiferromagnet at the interface, exchange biased ferromagnetic spins prefer to align along the magnetic field applied during the cooling procedure.

2.1.4 Interactions

Until now, interactions between magnetic moments were considered to be negligible. In this case, magnetic moments behave independently and show no order in the absence of a magnetic field. However, many materials show spontaneous magnetic order even without an applied magnetic field. This can be understood by introducing interactions between magnetic moments. As the strength of interactions increase, magnetic moments start to communicate with each other, and as a consequence, can show even collective behaviour.

Magnetic dipolar interaction Similar to electric dipoles, magnetic moments process a north pole and a south pole. A magnetic field produced by one magnetic dipole can interact with the neighbouring magnetic moments, and vice versa. This kind of interaction is known as *magnetic dipolar interaction*. Eq. 6 describes the energy of two magnetic moments $\vec{\mu_1}$ and $\vec{\mu_2}$ separated by a distance $\vec{r}$ with the magnetic permeability $\mu_0 = 4\pi \cdot 10^{-7} \frac{N}{A^2}$.

$$E = \frac{\mu_0}{4\pi r^3}[\vec{\mu_1} \cdot \vec{\mu_2} - \frac{3}{r^2}(\vec{\mu_1} \cdot \vec{r})(\vec{\mu_2} \cdot \vec{r})] \tag{6}$$

For atomic spins with $\mu \sim 1\,\mu_B$ separated by $|\vec{r}| = 1$ Å, the magnetic dipolar interaction between neighbouring moments can be estimated to be $\sim 10^{-23}$ J corresponding to ~ 1 K, which is quite weak compared to normal thermal energy. Therefore, the magnetic dipolar interaction cannot be the main reason for long-range magnetic order at high temperatures in solids, because it can easily be overcome by thermal fluctuations at a temperature of a few Kelvin. However, magnetic dipolar interaction can be a hundred orders of magnitude stronger for particles with large magnetic moments separated by a distance in the nm range. Therefore, it is an important interaction between nanoparticles. This will be discussed later in section 2.2.2.

Exchange interaction At the atomic scale, long range order such as ferromagnetic (FM) and antiferromagnetic (AF) order are governed by the *exchange interaction*, which is a result of both Coulomb interaction and Pauli principle. When bringing two electrons together, Coulomb repulsion tend to keep them apart, therefore one electron has to occupy a higher state thus increasing the kinetic energy. If the benefit of Coulomb energy cannot overcome the increase in the kinetic energy, two electrons stays in the same state. However, the Pauli principle forbids two electrons with the same quantum number to occupy the same orbital, therefore, they have to align antiparallel. The total spin state of two coupled electron spins can be 0 or 1, which is known as singlet and triplet states, respectively. A

singlet state is antisymmetric under the exchange of electrons, while the triplet state is symmetric. Electrons are Fermions, and the overall wave function, which is the product of the spatial and the spin wave functions, is antisymmetric. Therefore, the spatial part of the wave function for the singlet state is symmetric and for the triplet state, it is antisymmetric. The exchange constant J is defined by the energy difference of the singlet and triplet state as following:

$$J = \frac{E_S - E_T}{2} \tag{7}$$

with E_S and E_T being the energy of singlet and triplet states, respectively. When $J > 0$, the triplet state is favoured and two spins prefer to align parallel. However, the singlet state is preferred if $J < 0$, then the spins prefer to lie antiparallel. The Hamiltonian describing the exchange interaction between two neighbouring spins $\vec{S_1}$ and $\vec{S_2}$ can be expressed as:

$$\hat{\mathcal{H}} = -2J\vec{S_1} \cdot \vec{S_2} \tag{8}$$

Depending on the exchange constant J, $\vec{S_1}$ and $\vec{S_2}$ align parallel or antiparallel to minimize the energy. However, spins in solids usually experience exchange interaction with more than one neighbouring atom. Therefore, the Hamiltonian of the many-body exchange interaction is described by the *Heisenberg model*:

$$\hat{\mathcal{H}} = -2\sum_{i<j} J_{ij}\vec{S_i} \cdot \vec{S_j} \tag{9}$$

where J_{ij} is the exchange constant between $\vec{S_i}$ and $\vec{S_j}$, the summation $i < j$ is to ensure the interaction between $\vec{S_i}$ and $\vec{S_j}$ is only calculated once.

If two magnetic atoms are close enough so that their magnetic orbitals directly overlap, the electron of one atom can easily hop to its neighbouring atom. This kind of exchange interaction is known as ***direct exchange***. However, for localized electrons lying close to the nucleus such as 4f electrons in rare earth elements or 3d electrons in some transition metals, their orbitals in neighbouring magnetic atoms can rarely overlap. Thus the direct electron hopping between orbitals is not possible, and the direct exchange interaction cannot be achieved. However, ***indirect exchange interactions*** via various intermediaries are possible. Several types of indirect exchange interaction will be introduced in the following paragraphs.

For oxides like MnO, exchange interaction between two magnetic ions (Mn^{2+}) is mediated by a non-magnetic ion (O^{2-}). This kind of exchange interaction is longer ranged than the direct exchange interaction and is known as ***superexchange interaction***. Let us consider a simple case. There is only one single electron on the d-orbital of an ion M. As shown in Fig. 2(a) and (b), antiparallel spin alignment allows electrons to hop between the p-orbital in the non-magnetic ion and the d-orbitals in both magnetic ions. This delocalises electrons over the entire structure, thus reducing the kinetic energy. However, with parallel arrangement, electrons are only allowed to hop between the non-magnetic ion and one M ion, because two electrons with the same quantum state occupying the same orbital is forbidden. A parallel alignment costs more energy than an antiparallel alignment and hence a 180° superexchange interaction prefers antiparallel order between two half-filled orbitals or two empty orbitals. This kind of superexchange interaction is strong and known as the first *Goodenough-Kanamori-Anderson (GKA) rule*. However, superexchange interaction between one half-filled orbital and one empty orbital prefers

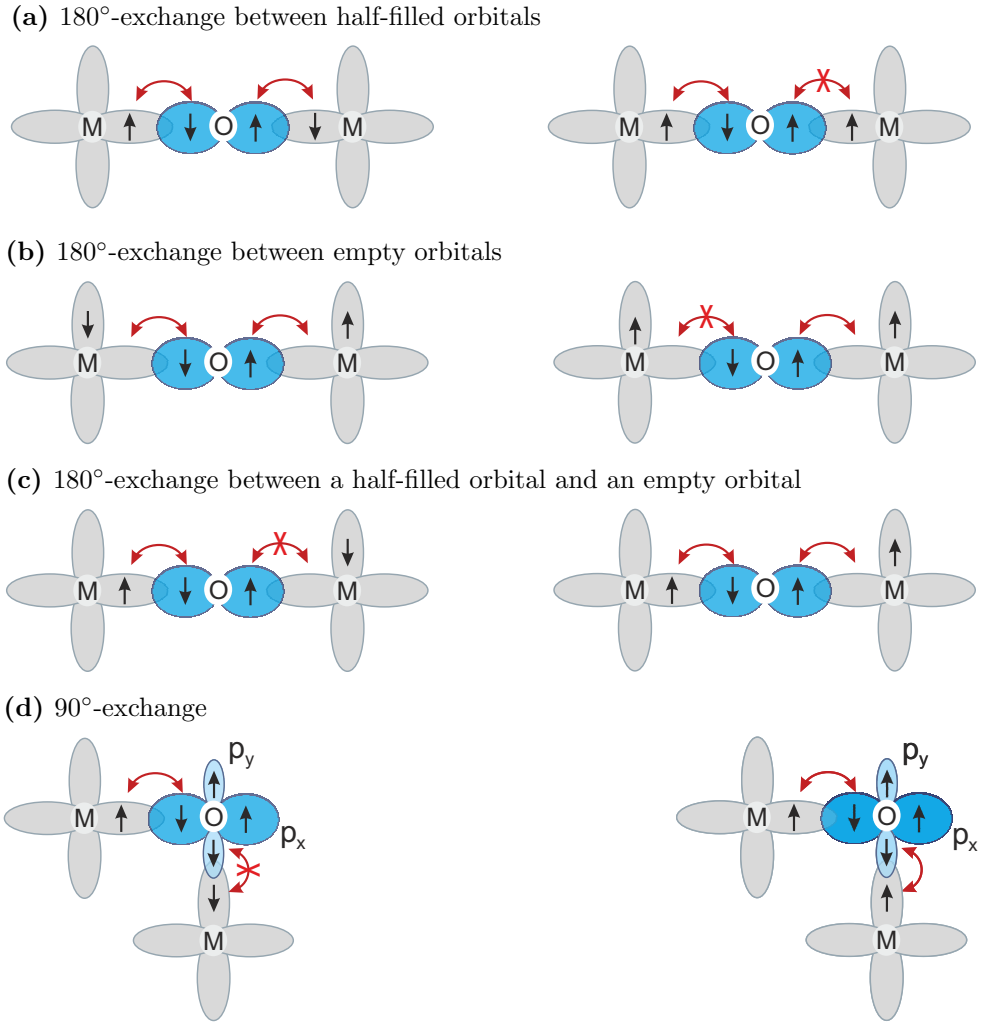

Figure 2: Superexchange interaction between two magnetic ions (M) mediated by a non-magnetic ion (O). (a) and (b) show the GKA-rule 1: antiparallel arrangement is favoured between two half-filled or two empty orbitals of magnetic ions with 180° arrangement, because it allows more hopping possibilities than the parallel arrangement. (c) GKA-rule 2: parallel arrangement is favoured between one half-filled orbital and one empty orbital with 180° exchange. (d) GKA-rule 3: 90° exchange interaction prefers parallel alignment of two spins in half-filled orbitals. M can be Mn^{2+} and O can be O^{2-} in the case of MnO.[28]

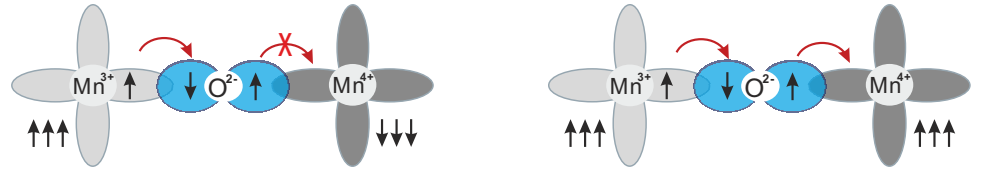

Figure 3: Charge transfer via double-exchange interaction between Mn^{3+} and Mn^{4+} mediated by an O^{2-} [28].

spins in neighbouring magnetic ions to arrange parallel (Fig. 2(c)), because the total spin angular momentum is maximized according to the first Hund's rule. This is known as

the second GKA-rule. Moreover, the third GKA-rule describes the case for 90° superexchange as shown in Fig. 2(d). For spins in two half-filled orbitals, arrangement shown in Fig. 2(d), parallel alignment is favoured.

For superexchange interactions, both magnetic ions have the same valence, therefore only virtual charge transfer is involved. However, if both magnetic ions are in different valence states, real charge transfer may take place during the exchange interaction. Thus the conductivity can be changed. This kind of interaction is known as ***double exchange***. As can be seen in Fig. 3, parallel alignment of spins in Mn^{3+} and Mn^{4+} allows the electron from Mn^{3+} to hop via the oxygen ion to Mn^{4+}. Therefore, $La_{1-x}Sr_xMnO_3$ may become FM when doping $LaMnO_3$ with Sr to a ratio of x=0.175 [26]. Moreover, below its Curie temperature $La_{0.825}Sr_{0.175}MnO_3$ becomes metallic. Another example in which double exchange is involved is Fe_3O_4. There are mixed valencies Fe^{2+} and Fe^{3+} in Fe_3O_4. Via double exchange Fe^{2+} and Fe^{3+} on the octahedral sites order parallel, and Fe^{3+} on tetrahedral sites align antiparallel to the Fe^{3+} on octahedral sites via superexchange interaction. This is the reason for the ferrimagnetic structure of Fe_3O_4, which will be discussed in section 2.1.5.

In certain materials, the exchange interaction between neighbouring atoms is mediated by conduction electrons. These electrons are polarized by a localized magnetic moment and then coupled to a neighbouring localized magnetic moment. This kind of indirect exchange interaction is called ***RKKY interaction*** named after: Ruderman, Kittel, Kasuya and Yosida.

Another type of exchange interaction is the ***anisotropic exchange interaction*** (also known as the ***Dzyaloshinsky-Moriya-interaction***). The Hamiltonian describing the interaction between two spins $\vec{S_1}$ and $\vec{S_2}$ is expressed as $\hat{\mathcal{H}} = -\vec{D}\cdot(\vec{S_1}\times\vec{S_2})$ with the vector $\vec{D}$ being related to the symmetry of the structure. If there is an inversion symmetry in the middle of the connecting line between $\vec{S_1}$ and $\vec{S_2}$, then $\vec{D} = 0$. Otherwise, the inverse symmetry is broken for example because of an oxygen ion as shown in Fig. 4, $\vec{D} \propto \overrightarrow{r_{1O}}\times\overrightarrow{r_{2O}}$ forces $\vec{S_1}$ and $\vec{S_2}$ to tilt in order to minimize the energy cost. This leads to a spin canting effect observed in some oxides. Therefore, a weak FM behaviour can be observed in some AF materials. Moreover, complex spin orders such as spiral or helical arrangement can also been formed due to this kind of exchange interaction [29].

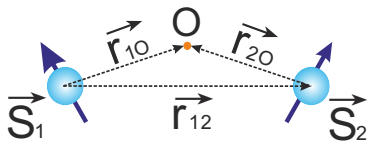

Figure 4: Illustration of two neighbouring spins influenced by the Dzyaloshinsky-Moriya-interaction due to a non-collinear oxygen ion.

2.1.5 Magnetic Order

As discussed above, exchange interaction is the most relevant for magnetic order in solids. With a positive J, spins prefer to arrange parallel, which results in a non-zero magnetization, even in the absence of an external magnetic field. This kind of magnetic order is known as ***ferromagnetic (FM)*** order as shown in Fig. 5(a). FM order is usually found in systems with itinerant electrons. When the electrons are localized, they will

interact with each other via superexchange. As a result, an ***antiferromagnetic (AF)*** order is preferred for magnetic moments between half-filled orbitals or empty orbitals. In this case, $J < 0$ and an antiparallel arrangement is favoured for neighbouring magnetic moments. A typical AF order is illustrated in Fig. 5(b), which can be considered as composed of two sublattices (blue and red). Magnetic moments of both sublattices have the same magnitude, but point into opposite directions. Therefore, no net magnetization is expected for perfect AF order, because magnetic moments from both sublattices compensate each other. However, when both sublattices have different magnitudes as shown in Fig. 5(c), a net magnetization can be found. This is known as ***ferrimagnetic (FiM)*** order, which is often observed in spinel structures such as Fe_3O_4. In a simple model of Fe_3O_4, an equal amount of Fe^{2+} and Fe^{3+} on octahedral sites are ordered FM via double exchange, and the same amount of Fe^{3+} on tetrahedral sites as on octahedral sites align AF via superexchange interaction. As there are twice as many Fe ions on octahedral site than on tetrahedral sites, magnetic moments pointing to both directions are different, and therefore, Fe_3O_4 shows FiM behaviour.

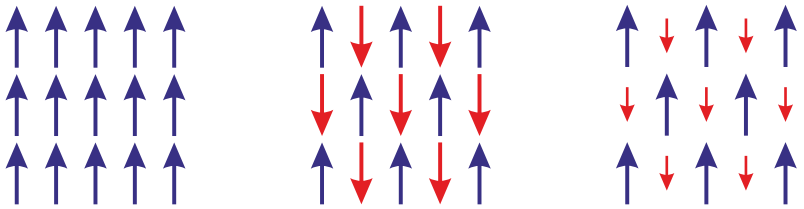

Figure 5: Magnetic spin ordering of (a) a ferromagnet, (b) an antiferromagnet and (c) a ferrimagnet.

Although exchange interaction is strong enough to produce spontaneous magnetic order in solids, thermal fluctuation at high temperatures may overcome it and thus destroy the magnetic order. Above a critical temperature, exchange interactions are too weak compared to thermal fluctuations, and therefore magnetic moments behaves quasi-independently and show PM behaviour. The critical temperature for FM/FiM and AF are known as *Curie temperature (T_C)* and *Néel temperature (T_N)*, respectively. The strength of the total interactions in materials can be estimated by fitting the susceptibility vs. temperature curve with the *Curie-Weiss law*:

$$\chi \propto \frac{1}{T - \theta} \tag{10}$$

with χ the magnetic susceptibility, T the temperature and θ the Weiss temperature. For PM systems, $\theta = 0$. For the simplest FM as shown in Fig. 5(a), $\theta = T_\mathrm{C}$. For AF, usually $\theta < 0$, however, $|\theta| \neq T_\mathrm{N}$. Therefore, PM, FM and AF can be distinguished from a magnetic susceptibility measurement. Experimentally, one can plot the inverse magnetic susceptibility vs. temperature and fit the data far above the critical temperature by the Curie-Weiss law. As shown in Fig. 6, a $1/\chi$ curve intersects with the x-axis at a positive value for FM and FiM systems (for the simplest FM order, $\theta = T_\mathrm{C}$), and at the origin for PM. For AF systems, the intersection is usually at a negative value, which is in many cases very different from the expected $-T_\mathrm{N}$ [26].

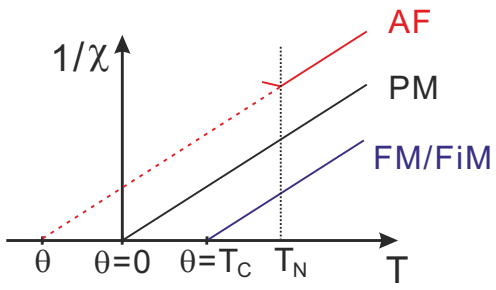

Figure 6: Inverse magnetic susceptibility vs. temperature for paramagnetic (black), ferro-/ferrimagnetic (blue) and antiferromagnetic (red) systems. Adapted from [26].

2.1.6 Magnetic Domains

For a single domain FM, the magnetization has a component normal to the surface, which induces a demagnetizing field inside and stray fields around it, respectively. To reduce the energy due to a demagnetizing field and stray fields, the FM prefers to break into domains. However, it costs energy to form domain walls. Therefore, the total energy of the system $\varepsilon_{total} = \varepsilon_{ex} + \varepsilon_a + \varepsilon_d + \varepsilon_Z + \varepsilon_{stress} + \varepsilon_{ms}$ [27], which includes the exchange energy ε_{ex}, anisotropy energy ε_a, demagnetizing energy ε_d, Zeeman energy ε_Z as well as the energy due to the applied stress ε_{stress} and magnetostriction ε_{ms}, has to be considered. By comparing the total energy for different number of domains, the most favourable state can be found.

The magnetization direction inside one domain is usually determined by the magnetocrystalline anisotropy. Different domains inside a crystal are separated by domain walls. Within domain walls, the spins rotate from one easy direction to another. The anisotropy tends to align the spins along one of the easy directions. However, the exchange interaction prefers the spins to stay parallel in FM materials and antiparallel for AF. The thickness of the domain wall is a result of the interplay between the exchange interaction and anisotropy.

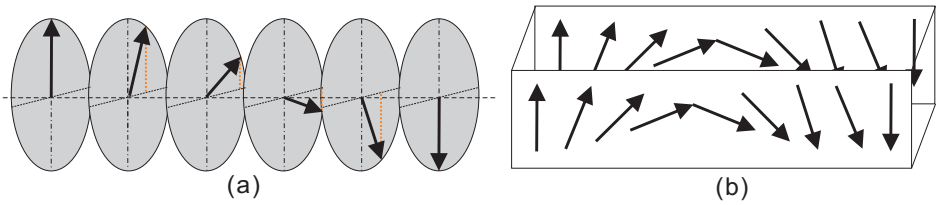

Figure 7: Illustration of the spin rotation inside (a) a Bloch wall and (b) a Néel wall. Adapted from [26].

Depending on the angle between the magnetic moments in two neighbouring domains, there are for example, 90° and 180° domain walls. It means that the magnetic moments are turned 90° and 180°, respectively, within the domain wall. In Fig. 7, two types of 180° domain walls (a) Bloch wall and (b) Néel wall are shown. For Bloch walls, the spins rotate within the plane of the domain wall, while the spins rotate within a plane perpendicular to the domain wall in a Néel wall.

Applying a magnetic field, the Zeeman energy has to be taken into account. This might cause the motion of the domain wall or the rotation of the magnetization direction

inside domains. As a result, magnetization reversal can be obtained.

2.1.7 Exchange Bias

The exchange bias (EB) effect was first reported in 1956 by Meiklejohn and Bean in the study of FM-AFM Co-CoO core-shell nanoparticles [30]. A unidirectional anisotropy is observed in torque measurements after the sample is cooled from above T_N of CoO to low temperature within a magnetic field. Moreover, a shift towards the opposite direction of the cooling field is found in the hysteresis loop. This phenomenon is explained due to the exchange coupling at the interface between an AF and a FM [30]. Due to potential applications in permanent magnets, high density data storage and as stabilizer in magnetic read heads [31–34], EB have been studied during the past years intensely.

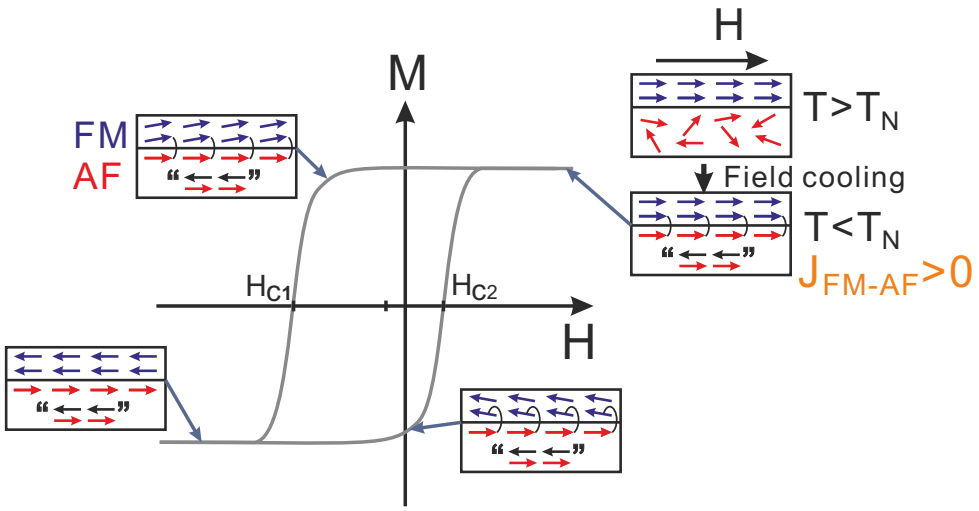

Figure 8: Illustration of the spin order influenced by the exchange bias effect during a hysteresis measurement. The spin structure in quotation marks means some AF order, where the exact type and direction is irrelevant for this illustration. Adapted from [31].

A typical model to understand the EB effect is shown in Fig. 8. We assume that the Curie temperature of the FM is much higher than the Néel temperature of the AF. At $T_C > T > T_N$, the magnetic moments in FM are aligned along the magnetic field, while the magnetic moments in AF are randomly ordered. As the system is cooled below T_N, the AF moments at the interface are coupled to the interfacial magnetic moments of the FM via exchange interaction. Depending on the exchange constant $J_{\text{FM-AF}}$, they align parallel or antiparallel. Then the remaining AF moments start to order and lock the interfacial AF moments in this direction. When the magnetic field decreases, the FM moments start to rotate. However, the exchange coupling between the AF and the FM interfacial moments stabilize the FM moments parallel to the direction of the cooling field. Therefore, a magnetic field H_{c1} larger than the coercive field H_c of the FM is needed to reverse the FM moments to the opposite direction. If the magnetic field further decreases (i.e. increase in the negative direction), it is at the point sufficient to align all FM moments in the opposite direction. We assume that the anisotropy of the AF is very large, therefore the AF order remains unchanged even when the magnetic field switches all FM moments. If we increase the magnetic field back, the interfacial FM and AF moments are satisfied to be aligned parallel (for $J_{\text{FM-AF}} > 0$) or antiparallel (for $J_{\text{FM-AF}} < 0$) again due to the

exchange interaction. Therefore, a smaller magnetic field H_{c2} than the H_c of the FM is sufficient to reverse the FM moments back along the positive field direction. As a result, the centre of the hysteresis is shifted towards the negative field direction, and the EB field can be calculated as $H_{ex} = \frac{1}{2}(H_{c1} + H_{c2})$.

In real systems, the magnetic moments in the FM may not order perfectly as shown in Fig. 8 due to, for example, interface roughness, thermal fluctuations, or different correlation lengths of FM and AF order. Moreover, if the AF layer has a relative small anisotropy, the interfacial AF moments can also be switched when all FM moments are aligned. In this case, an increase of H_{c2} is also expected as well as an increase in the coercive field. Other interesting effects such as vertical shifts in hysteresis loops, and training effects have also been found in some exchange bias systems [31, 33]. Therefore, the EB effect has to be explained using other models for special cases.

EB studies are often performed with thin film systems. This is not only due to their application in industrial devices, but also due to their controllable thickness of AF and FM layers as well as of the roughness at the AF-FM interface. An enhancement in the EB field H_{ex} is usually observed with an increasing thickness of the AF layer or a decreasing thickness of the FM layer [31–33]. Apart from AF-FM systems, EB has also been observed in FiM-FiM systems.

EB in nanostructured systems has also attracted much interest, because of its possibility to overcome the superparamagnetic limit due to the finite size effect, thus making the application of NPs in high density data storage feasible [34]. Close packed NPs are good candidates for high density data storage, because single domain FM NPs can be considered to possess a macro-moment composed of $\sim 10^4 - 10^6$ parallelly aligned atomic magnetic moments along its anisotropy axis. However, as the particle size reduces, its magnetic anisotropy energy decreases and may have the same order of magnitude as the thermal energy. Therefore, the magnetic order in NP systems becomes unstable even below their transition temperatures. This is known as superparamagnetism, which will be explained later in section 2.2.1. However, an additional exchange anisotropy induced at a FM-AF interface can potentially increase the stability of the magnetic order until the Néel temperature of the AF. Various EB nanostructured systems such as: patterned FM structures on a AF film, FMs embedded in an AF matrix and core-shell NPs, have been studied during the last years [34]. But the synthesis of NPs with controlled stoichiometry and thickness of a shell in core/shell systems is not trivial. This makes the systematic study of the EB effect in NP systems difficult. Moreover, the EB effect has also been observed in pure AF or FiM NPs. This can be explained by the coupling between the AF/FiM ordered core and disordered surface spins or a spin-glass shell.

2.2 Basics of Nanomagnetism

As the particle size decreases to the nanometer range, completely different magnetic behaviours can be observed compared to its bulk form. Due to the broken symmetry at the surface, spins at the first few atomic layers may behave differently than the other part. This phenomenon at the surface can be neglected in bulk material due to the small ratio of surface spins. However, for nano-sized materials, the surface to volume ratio becomes much larger, thus surface effects may sometimes dominate the magnetism in nano-materials. For example, disordered surface spins or a spin-glass like surface layer may play an important role on nanomagnetism. Moreover, below a critical size, the en-

ergy cost to form a domain wall, which is proportional to the interfacial area between the domains ($\sim r^2$), becomes larger compared to the benefit from the decrease of the demagnetizing energy, which is proportional to the volume ($\sim r^3$) in FM materials. Therefore, these particles prefer to stay *single-domain* (Fig. 9(a)).

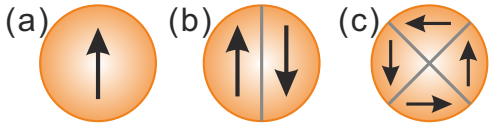

Figure 9: Cross section of a spherical or cylindrical FM particle with (a) one single domain, (b) two antiparallel domains, and (c) a closure domain structure.

The demagnetizing energy of a single domain FM can be calculated as:

$$E_d = -\frac{\mu_0}{2}\int \vec{M}\cdot\vec{H}_d\, dV \tag{11}$$

where μ_0 is the vacuum permeability, $\vec{M}$ the magnetization, $\vec{H}_d = -\underline{\underline{\mathcal{N}}}\cdot\vec{M}$ the demagnetizing field, and V the volume. For spherical particles, one has $\mathcal{N} = \frac{1}{3}$, and the demagnetizing energy can be rewritten as:

$$E_d = \frac{2}{9}\mu_0 M^2 \pi r^3 \tag{12}$$

with r the radius of the sphere. If this particle breaks into two domains separated by a 180° domain wall as shown in Fig. 9(b), the demagnetizing energy reduces to half as to its single domain state according to Eq. 12 assuming the domain wall width is negligible. However, the energy cost of forming the domain wall is:

$$E_{dw} = \pi r^2 \sigma_w^{180^\circ} \tag{13}$$

where σ_w is the energy cost of the domain wall per unit area, and the domain wall area for a 180° domain wall in spherical particles is πr^2. If the single domain state is favourable:

$$E^{(a)} < E^{(b)}$$
$$\frac{2}{9}\mu_0 M^2 \pi r^3 < \frac{1}{9}\mu_0 M^2 \pi r^3 + \pi r^2 \sigma_w^{180^\circ}$$

with $E^{(a)}$ and $E^{(b)}$ are the energy cost of domain states shown in Fig. 9(a) and (b). As a result, we obtain the following condition for the radius:

$$r < \frac{9\sigma_w^{180^\circ}}{\mu_0 M^2} \tag{14}$$

for particles to remain single domain.

A similar calculation can be performed for the closure domain structure in Fig. 9(c).

$$E^{(a)} < E^{(c)}$$
$$\frac{2}{9}\mu_0 M^2 \pi r^3 < 2\pi r^2 \sigma_w^{90^\circ}$$

In the case (c), the demagnetizing field is zero, because the demagnetizing fields from the domains are completely compensated. However, a larger area of the domain walls, $2\pi r^2$, is formed. The critical radius can be calculated as:

$$r < \frac{9\sigma_w^{90^\circ}}{\mu_0 M^2} \tag{15}$$

As discussed in section 2.1.6, σ_w results from the energy cost due to exchange interaction and anisotropy. In order to calculate $\sigma_w^{180^\circ}$, one can consider a chain of spins within the domain wall as shown in Fig. 7. The energy cost due to the exchange interaction and anisotropy can be calculated as:

$$E_{ex}^{180^\circ} = -2\sum_{i<j}^{N} J_{ij}\vec{S_i}\cdot\vec{S_j} \approx JN\theta^2S^2 = JN(\frac{\pi}{N})^2S^2 = J\frac{\pi^2S^2}{N} \tag{16}$$

$$E_a^{180^\circ} = \sum_{i}^{N} K\ sin^2\alpha_i \approx \frac{N}{\pi}\int_0^{\pi} K\ sin^2\alpha d\alpha = \frac{NK}{2} \tag{17}$$

where N is the number of spins within the domain wall, θ is the angle between two neighbouring spins within the domain wall, K is the anisotropy constant and α is the angle between spins within the domain wall and the anisotropy axis. In analogy, the energy cost for a closure domain structure as shown in Fig. 9(c) can be calculated. In this case, there are four times 90° rotations, and the anisotropy axes are 90° to each other. Therefore, the energy cost due to the exchange interaction and anisotropy can be calculated as

$$E_{ex}^{90^\circ} = -2\sum_{i<j}^{N} J_{ij}\vec{S_i}\cdot\vec{S_j} \approx 4JN\theta^2S^2 = 4JN(\frac{\pi}{2N})^2S^2 = J\frac{\pi^2S^2}{N} \tag{18}$$

$$E_a^{90^\circ} = \sum_{i}^{N} K\ sin^2(2\alpha_i) \approx \frac{N}{\pi/2}\int_0^{\pi/2} K\ sin^2(2\alpha)d\alpha = \frac{NK}{2} \tag{19}$$

One can see, that the energy cost to form a closure domain structure with 90° domain walls is the same as to build a 180° domain wall.

The energy cost per unit area σ_{ex}, σ_a due to the exchange interaction and anisotropy, respectively, and the total energy cost per unit area σ_w can be calculated as:

$$\sigma_{ex} = \frac{E_{ex}}{a^2} = J\frac{\pi^2S^2}{Na^2} \tag{20}$$

$$\sigma_a = E_a\frac{a^3}{a^2} = \frac{NKa}{2} \tag{21}$$

$$\sigma_w = \sigma_{ex} + \sigma_a = \frac{J\pi^2S^2}{Na^2} + \frac{NKa}{2} \tag{22}$$

with a the distance between two neighbouring spins inside the domain wall. Because the anisotropy constant K is per unit volume, a unit volume a^3 is multiplied to calculate the anisotropy energy density per unit area. $N = \pi S\sqrt{\frac{2J}{Ka^3}}$ can be found for the equilibrium

configuration $\frac{dE_{dw}}{dN} = 0$. By introducing the exchange stiffness $A = \frac{2JS^2Z}{a}$ with Z the number of atoms in unit cell, σ_w can be rewritten as:

$$\sigma_w = \sqrt{AK} \cdot \pi \tag{23}$$

Then the critical radius for spherical particles can be estimated as [26]:

$$r_c \approx 9\pi \frac{\sqrt{AK}}{\mu_0 M_s^2} \tag{24}$$

where M_s is the saturation magnetization. A typical radius for a single-domain usually ranges from 10 to 100 nm depending on the material [35].

A single-domain FM can be considered as possessing a "macro-spin" or "superspin", which has a magnitude of the sum of all atomic spins. For an ideal single-domain FM, the magnetic moment of the superspin can be estimated as $\vec{m}_{NP} = M_s V = \sum_i \vec{m}_i$ with V the volume of the particle, $\vec{m}_i$ the magnetic moment of a single atom. However, the magnetic moment in real NPs can be reduced due to disordered surface spins. Usually a single-domain FM has a magnetic moment of about 10^3 - $10^5\,\mu_B$ depending on the material [26].

The magnetization of a single-domain FM as function of an applied magnetic field can be calculated using the Stoner-Wohlfarth model [26,35]. The energy can be described as:

$$E = KV \sin^2\phi - \mu_0 M_s V H \cos(\theta - \phi) \tag{25}$$

with ϕ the angle between the magnetic moment and the anisotropy axis, θ the angle between the anisotropy axis and the applied field, and H is the amplitude of the applied field. By calculating the energy minimum, the favourable configuration can be found.

2.2.1 Superparamagnetism

For a strongly diluted NP ensemble, interparticle interactions can be neglected. In this case, the directions of the superspins are only a result of the competition between anisotropy and thermal fluctuations in the absence of a magnetic field. For large particles, the energy barrier $\Delta E = KV$ between two antiparallel configurations along the easy axis is large, and cannot be overcome by the thermal energy. Therefore, the superspins stay along their easy axis below the critical temperature of the material. However, as the size of NPs reduces, ΔE decreases. When the NP volume V becomes so small that the thermal energy $k_B T \gtrsim KV$, the NP superspin directions fluctuate in analogy to the spins in a paramagnet even below its critical temperature. Due to the huge magnetic moments of superspins, this mechanism is termed *super-paramagnetism* (SPM).

The mean time between two switching processes of superspins is known as *Néel-Brown relaxation time* and is given by the Arrhenius equation [26,35,36]:

$$\tau = \tau_0 \, \exp\left(\frac{KV}{k_B T}\right) \tag{26}$$

with τ_0 a pre-factor, which is usually $\sim 10^{-9} s$ for SPM systems [35–37]. If the measurement time $t \gg \tau$, the system fluctuates within t, thus an average magnetization of zero can be measured. However, as the temperature decreases, the relaxation time τ increases

due to the decreasing of the thermal energy. Below a characteristic temperature T_{B}, τ becomes comparable to t. In this case, the superspins seem to be blocked in one of the energy minima during the measurement. Therefore, T_{B} in SPMs is known as the *blocking temperature*. In the presence of a magnetic field, the superspins may tend to align along the field direction, thus showing a non-zero magnetization. However, the blocked state can only be observed when $\tau \geq t$. Therefore, T_{B} also depends on the measurement time t which corresponds to τ at T_{B} [26, 35]:

$$t = \tau(T_B) = \tau_0 \ \exp\left(\frac{KV}{k_B T_B}\right) \rightarrow T_B = \frac{KV}{k_B \ln(t/\tau_0)} \tag{27}$$

Below T_{B}, the superspins are in blocked states, while for $T > T_{\mathrm{B}}$, the superspins can easily be switched by thermal fluctuations.

2.2.2 Interacting Nanoparticles

In analogy to atoms, NPs can be building blocks for novel types of materials, which have potential applications in functional materials, high density data storage, spintronic devices, and biomedicine [35]. Depending on the spatial order of nanoparticles, artificial superlattices or supercrystals can be fabricated. Therefore, NP self-assembly has been of interest for decades. An important interaction which makes NPs self-organize is known as the *van der Waals interaction* [38, 39], which is an attractive force. However, to retain their nanosize properties, NPs are usually covered by organic shells such as oleic acid to avoid agglomeration.

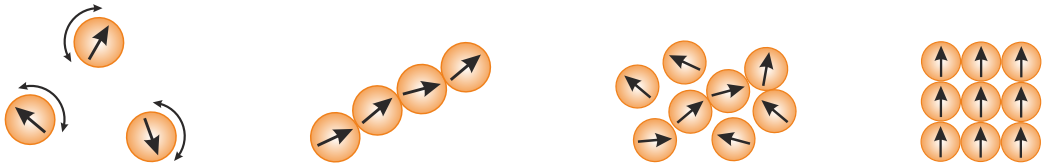

Figure 10: Influence of the magnetic dipolar interaction onto the magnetic order of superspins in single domain NPs: (a) SPM behaviour for isolated NPs, (b) chain structure in 1D order, (c) Superspin glass behaviour in a not perfectly ordered 2D structure, (d) superferromagnetism due to high magnetic dipolar interactions. Adapted from [40].

As discussed above, single domain FM NPs possesses a superspin. By ordering these NPs in superstructures, interesting magnetic order can be achieved. As can be seen in Fig. 10(a), isolated NPs behave independently and show SPM behaviour. As the interparticle distance decreases, magnetic interactions between NPs are no longer negligible. The most important interaction for magnetic order in NP superstructures is the *magnetic dipole-dipole interaction* discussed in section 2.1.4. For atomic spins, magnetic dipole-dipole interactions are usually too weak to produce magnetic order above a few K. However, for superspins in single domain NPs containing $\sim 10^4$ atomic spins, dipolar interactions can be several orders of magnitude stronger, and therefore play an important role in nanomagnetism. Let us consider two spherical magnetite NPs covered by a 2 nm thick oleic acid shell in close contact as an example. The magnetic dipolar interaction between two NPs with 5, 10 and 15 nm sizes can be estimated to be $\sim$5, 120 and 300 K,

respectively. Therefore, for agglomerated NPs with larger sizes, the magnetic dipolar interaction may dominate the magnetic properties of the sample. With the increase in interparticle interaction, NPs start to "talk" to each other and show eventually a collective behaviour [35, 38–41]. If several NPs are close to each other by chance, a 1D chain structure can usually be formed as shown in Fig. 10(b) to minimize the dipolar energy. If we increase the NP concentration, 2D or 3D structures start to form. Similar like a spin glass system, a collective behaviour can also be observed in disordered superspins, which is known as *superspin-glass (SSG)* (Fig. 10(c)). In imperfectly ordered 2D and 3D superstructures, SSG behaviour can be observed. As the NP concentration further increases, interactions between NPs increases. At one stage ferromagnetically ordered superspins are possible. This is known as *superferromagnetism (SFM)* (Fig. 10(d)).

Depending on the interaction strength, various models describing the relaxation time of NP ensembles can occur [35, 37, 41]:

$$\text{(i) SPM :} \qquad \tau = \tau_0 \ \exp\left(\frac{KV}{k_B T}\right) \tag{28}$$

$$\text{(ii) Modified SPM :} \qquad \tau = \tau_0 \ \exp\left(\frac{\Delta E^*}{k_B T}\right) \tag{29}$$

$$\text{(iii) Glass-like freezing :} \qquad \tau = \tau_0 \ \exp\left(\frac{\Delta E^*}{k_B (T - T_0)}\right) \tag{30}$$

$$\text{(iv) SSG :} \qquad \tau = \tau_0^* \left(\frac{T - T_g}{T_g}\right)^{-z\nu} \tag{31}$$

$$\text{(v) SFM :} \qquad \tau = \tau_0^* \left(\frac{T - T_c}{T_c}\right)^{-z\nu} \tag{32}$$

For non-interacting NPs, τ is described by the Arrhenius equation introduced in section 2.2.1. When NPs start to interact with each other weakly, a modified energy barrier ΔE^* according to an effective contribution of the interparticle interactions has to be introduced as in model (ii). As the interaction strength further increases, they start to behave glass-like and can be described by model (iii) with T_0 the glass temperature. With stronger interactions, SSG behaviour is achieved. τ can be described by model (iv) with T_g the critical temperature, below which the system transforms to a SSG state. τ_0^* is the relaxation time for individual particle moment, ν is the critical exponent of the correlation length ξ with $\xi \sim \frac{T-T_g}{Tg}^{-\nu}$, and z relates to τ and ξ as $\tau \sim \xi^z$. When the NPs interact with each other so strongly that a SFM state is obtained, then the relaxation time τ can be described by model (v) with T_C, the Curie temperature.

Experimentally, AC-susceptibility results on NP ensembles are usually fitted by one of these models to describe their magnetic behaviour [36, 42–44]. The maximum in the AC-susceptibility curve depending on temperature usually corresponds to the characteristic temperature between the "blocked" or "frozen" state and the "unblocked" or "unfrozen" states. At this point, τ equals to the inverse of the frequency of the AC field. By comparing the frequency dependence of the peak temperature in AC-susceptibility curves with the equations discussed above, a model can be found to describe the system.

2.3 Self-assembly

As discussed above, materials may show novel properties at the nanometer scale, which is very different from that of their bulk form. The NP superspins interact with each other via interparticle interactions and thus show a collective behaviour. Using NPs as building blocks, novel types of materials can be fabricated. By tuning the interactions between the particles, they may self-organize into different superstructures. In the following paragraphs, several important interactions will be introduced.

Magnetic dipolar interaction As introduced in section 2.1.4 and 2.2.2, magnetic dipolar interactions play an important role in the magnetic order of NP superspins.

For two fixed magnetic dipoles (i.e. when the superspins are in a "blocked" state), the static dipolar interaction can be calculated using Eq. 6. However, below the characteristic temperature, the superspins start to fluctuate, thus a dynamic dipolar interaction has to be taken into account:

$$E_{fluc} = -\frac{1}{3k_BT}\left(\frac{\mu_1\mu_2}{4\pi\mu_0 r^3}\right)^2 \tag{33}$$

where μ_1 and μ_2 are two fluctuating dipoles separated by a distance r, k_B is the Boltzmann constant, T is the temperature, μ_0 is the vacuum permeability. As can be seen, the dynamic dipolar interaction is proportional to $\sim 1/r^6$, which is much weaker compared to the static interaction ($\sim 1/r^3$).

If the NPs are diluted, for example, dispersed in solution, the average distance between them is very large, thus the magnetic dipolar interaction is much weaker compared to that between agglomerated samples. Compared to the interaction strength estimated for NPs in close contact in section 2.2.2, it may become several orders of magnitude weaker. If we separate two magnetite NPs with 5, 10 and 15 nm to a distance of 100 nm, the interaction strength can be reduced to ~ 0.005, 0.3 and 2.4 K, respectively.

Van der Waals interactions It is an intermolecular interaction, which is much weaker compared to the chemical bondings such as covalent, ionic and metallic bondings. It includes the interactions between two permanent dipoles, between a permanent dipole and an induced dipole, and between two induced dipoles. It can be attractive or repulsive depending on the distance between the molecules. In NP dispersions, the van der Waals interactions are usually attractive.

Steric repulsion When a NP approaches another due to attractive interactions, they tend to agglomerate to minimize the surface energy. To avoid this effect, repulsive interactions need to be introduced to study the nanosize effect. This can be achieved by coating the particles by long chained molecules. Usually these molecules are attached to the NPs on one end and the other ends are free. When the NPs are close to each other, the free ends of the molecules repel each other due to steric repulsion, and thus the particles are kept separate.

Capillary force The capillary effect is due to the interplay of adhesion and surface tension. The liquid between two walls close to each other tend to adhere to the wall, while surface tension tries to minimize the liquid surface. As a result, the liquid is dragged

upwards. In analogy, the solvent between two freely moving NPs separated by a small gap tend to adhere to the particles. To reduce the surface tension, the particles are brought closer together.

2.4 Scattering Theory

Scattering is a unique method to study the arrangement of atoms or particles in reciprocal space. For a theoretical description, first we consider a simple case: a plane wave is scattered by an object with a similar size as its wavelength. This will result in a spherically scattered wave. Now we change the object to an ensemble of identical particles arranged periodically with a spacing in the same order of magnitude as the wavelength of the plane wave. The scattered spherical waves from each particle interfere with each other and produce an interference pattern at the detector. This phenomenon is known as the *Huygens-Fresnel principle*. With a wise choice of the wave type, the structure of the material can be studied accurately.

In condensed matter physics, x-ray and neutron scattering are widely used. This is because the wavelengths of x-rays and neutrons from typical sources have the same order of magnitude as the atomic spacing in materials. Compared to x-ray scattering, neutron scattering has several advantages. Neutrons are neutral particles with spin $\frac{1}{2}$. Due to their large penetration depth, neutron scattering is an ideal method to measure bulk properties of large samples. Besides, the magnetic moments of neutrons can interact with the magnetic moments in the material, thus providing information about the magnetic order inside the material. In this section, the basics of scattering as well as several scattering methods will be introduced according to Ref. 45–48.

2.4.1 Basics of Scattering

In a scattering event, incident and scattered waves are described by wave vectors $\vec{k_i}$ and $\vec{k_f}$, respectively. The scattering vector $\vec{Q}$ is defined by $\vec{Q} = \vec{k_f} - \vec{k_i}$. During a scattering process, the momentum transfer is $\vec{p} = \hbar(\vec{k_f} - \vec{k_i}) = \hbar\vec{Q}$ as illustrated in Fig. 11. For elastic scattering, there is no energy change between incident and scattered waves:

$$\Delta E = \frac{(\hbar\vec{k_i})^2}{2m_\mathrm{n}} - \frac{(\hbar\vec{k_f})^2}{2m_\mathrm{n}} = 0 \Leftrightarrow |\vec{k_i}| = |\vec{k_f}| = k = \frac{2\pi}{\lambda} \tag{34}$$

with m_n the mass of the neutron, $\hbar$ is the reduced Planck constant. Therefore, the length of the scattering vector can be calculated as:

$$\begin{aligned} Q = |\vec{Q}| &= \sqrt{(\vec{k_f} - \vec{k_i})^2} = \sqrt{2k^2(1 - cos(2\theta))} \\ \Longrightarrow Q &= \frac{4\pi}{\lambda} sin(\theta) \end{aligned} \tag{35}$$

In a scattering experiment, the measured intensity is proportional to the so called *cross section*, which indicates the probability of the scattering event detected within a defined solid angle. As introduced by the Huygens principle, the scattered wave propagates isotropically in all directions, i.e. a solid angle of $\Omega = 4\pi$. However, a detector in a real experiment can only cover a small solid angle. Therefore, the *differential cross section* is introduced as:

$$\frac{d\sigma}{d\Omega} = \frac{n}{\Phi d\Omega} \tag{36}$$

with n the number of scattered particles per second into the solid angle $d\Omega$, and Φ the incident flux. Then the *total scattering cross section*, which gives the total scattering probability of the sample, can be calculated by integrating the differential cross section over the entire solid angle:

$$\sigma = \int_0^{4\pi} \frac{d\sigma}{d\Omega} d\Omega \tag{37}$$

If we describe the incident wave using a wave function $\psi_i = \psi_0 \, e^{i\vec{k_i}\cdot\vec{R}}$, with ψ_0 the amplitude of the incident wave, and $\vec{R}$ the position of the scatterer, then the scattered wave $\vec{k_f}$ shown in Fig. 12 can be described as:

$$\psi_f = \psi_0 \, e^{i\vec{k_i}\cdot\vec{R}} \, f(\lambda,\theta) \, \frac{e^{i\vec{k_f}\cdot(\vec{r}-\vec{R})}}{|\vec{r}-\vec{R}|} \tag{38}$$

with $f(\lambda,\theta)$ known as the *form factor*, which will be introduced later in detail. For $\vec{R} \ll \vec{r}$, a *Fraunhofer* or *far-field approximation* can be applied, and thus $|\vec{r}-\vec{R}| \approx |\vec{r}| = r$.

The amplitude of the scattered wave of an ensemble of scatters at position $\vec{r}$ is given by the superposition of the scattered waves from all scatters:

$$\begin{aligned} \psi_f(\vec{r}) &= \frac{\psi_0}{r} \sum_{j=1}^{N} f_j(\lambda,\theta) \, e^{i(\vec{k_i}-\vec{k_f})\cdot\vec{R_j}} \, e^{i\vec{k_f}\cdot\vec{r}} \\ &= \frac{\psi_0}{r} \, e^{i\vec{k_f}\cdot\vec{r}} \sum_{j=1}^{N} f_j(\lambda,\theta) \, e^{-i\vec{Q}\cdot\vec{R_j}} \end{aligned} \tag{39}$$

However, in a real experiment, ψ_f is not measurable. Instead, the scattered intensity I proportional to the square of the scattering amplitude is measured:

$$I(\vec{Q}) \propto |\psi(\vec{Q})|^2 = \frac{\Phi}{r^2} \, |\sum_j f_j \, e^{-i\vec{Q}\cdot\vec{R_j}}|^2 \tag{40}$$

with $\Phi = \psi_0^2$ the incident flux. Therefore, the phase information is lost in the measurement, which makes the reconstruction of the structure difficult. This is known as the phase problem of scattering.

The *form factor* $f(\lambda,\theta)$ is a function describing the interaction potential depending on the size and shape of the scatter. For point-like scatterers, the form factor is approximately constant with $f(\lambda,\theta) = -b$. b is a complex number known as *scattering length*. In SI, the unit is m. For different isotopes, b can be very different. However, the imaginary part of

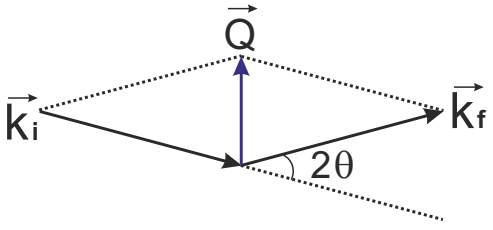

Figure 11: A sketch of the scattering process and the definition of $\vec{Q}$.

b is generally very small, thus b is usually considered as a real number. For non point-like scatterers, the form factor is given as:

$$f(\vec{Q}) = \int_V \rho(\vec{r})\ e^{i\vec{Q}\cdot\vec{r}} d^3\vec{r} \tag{41}$$

where $\rho(\vec{r})$ is the *scattering length density* proportional to the interaction potential at position $\vec{r}$.

Until now the scatterers have been considered to be disordered. However, due to various interactions between scatterers, periodically ordered structures, such as crystallites or self-assembled NP supercrystals may form. In this case, a *structure factor* has to be introduced. The measured intensity dependent on the structure factor can be estimated as:

$$I(\vec{Q}) - B = A \cdot |F(\vec{Q})|^2 \otimes R(\vec{Q}) \tag{42}$$

with $I(\vec{Q})$ the measured intensity, B is the background, A is a scale factor including all instrumental parameters, such as incident flux, detector efficiency, the absorption correction, the extinction coefficient etc. $F(\vec{Q})$ is the structure factor describing the atomic coordinates, site occupations and the thermal vibrations of the structure:

$$F(\vec{Q}) = \sum_j f_j(\vec{Q}) e^{i(\vec{Q}\cdot\vec{r_j})} \cdot T_j(\vec{Q}) \tag{43}$$

with T_j the Debye-Waller factor referring to the the dynamical and static displacement of a particle j from its equilibrium position. Moreover, the resolution of diffractometers is angle dependent, and therefore described by a resolution function $R(\vec{Q})$ in Eq. 42. The measured intensity is the convolution of the square of the modulus of the structure factor and the resolution function.

2.4.2 Diffraction

In a diffraction experiment, the interference pattern of elastically reflected waves from a set of crystal planes are measured. For elastic scattering $|\vec{k_i}| = |\vec{k_f}| = k$. There are many scattering vectors satisfying the Laue condition $\vec{Q} = n\vec{G}$. n is an integer. $\vec{G}$ is the reciprocal lattice vector with $\vec{G} = h\vec{b_1} + k\vec{b_2} + l\vec{b_3}$ and $|\vec{G}| = \frac{2\pi}{d_{hkl}}$. With $k = 2\pi/\lambda$, the square of the modulus of the scattering vector can be calculated as:

$$|\vec{Q}|^2 = 2k^2(1 - cos(2\theta))$$
$$(n\frac{2\pi}{d_{hkl}})^2 = 4(\frac{2\pi}{\lambda})^2 sin(\theta)$$

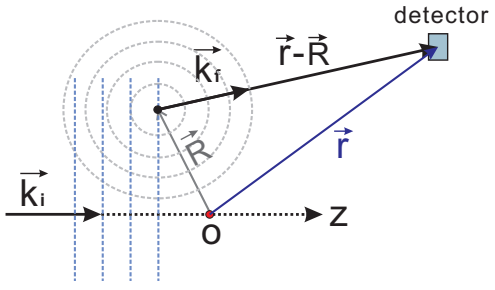

Figure 12: Illustration of a plane wave scattered by an object at position $\vec{R}$.

which can be simplified as $n\lambda = 2d_{hkl}sin\theta$ known as Bragg's law. In real space, the position of an atom j inside the unit cell of a single crystal can be given by:

$$\vec{r_j} = x_j\vec{a_1} + y_j\vec{a_2} + z_j\vec{a_3} \tag{44}$$

with x_j, y_j, z_j the fractional atomic coordinates, and $\vec{a_1}$, $\vec{a_2}$, $\vec{a_3}$ the basis vectors of the unit cell. The corresponding reciprocal basis vectors $\vec{b_1}$, $\vec{b_2}$, $\vec{b_3}$ are defined as

$$\vec{b_i} = \frac{2\pi(\vec{a_j} \times \vec{a_k})}{\vec{a_1} \cdot (\vec{a_2} \times \vec{a_3})} \tag{45}$$

with $i \neq j \neq k \in \{1, 2, 3\}$. Then the structure factor in Eq. 43 can be rewritten as:

$$F(\vec{Q}) = \sum_j b_j e^{2\pi ni(hx_j+ky_j+lz_j)} \tag{46}$$

assuming that the Debye-Waller factor is unity. For a face centered cubic (fcc) lattice as for MnO, there are four atoms at positions (0,0,0), (0,$\frac{1}{2}$,$\frac{1}{2}$), ($\frac{1}{2}$,0,$\frac{1}{2}$), ($\frac{1}{2}$,$\frac{1}{2}$,0) in the unit cell. Thus the structure factor for fcc lattice can be written as:

$$\begin{aligned} F(\vec{Q}) &= b\left(e^{2\pi ni(h\cdot 0+k\cdot 0+l\cdot 0)} + e^{2\pi ni(h\cdot 0+k\cdot \frac{1}{2}+l\cdot \frac{1}{2})} + e^{2\pi ni(h\cdot \frac{1}{2}+k\cdot 0+l\cdot \frac{1}{2})} + e^{2\pi ni(h\cdot \frac{1}{2}+k\cdot \frac{1}{2}+l\cdot 0)}\right) \\ &= b\left(1 + cos(\pi n(k+l)) + cos(\pi n(h+l)) + cos(\pi n(h+k))\right) \end{aligned} \tag{47}$$

Therefore, $F(\vec{Q})$ is non-zero only when h, k, l are all even or all odd. Otherwise, $F(\vec{Q})$ is zero, thus the measured intensity zero. This is known as the extinction principle. Different structures have different extinction rules. By fitting the diffraction pattern with the calculated intensity using the structure form factor from a known structure, the crystal structure can be determined.

2.4.3 Polarization Analysis

As discussed in section 2.4.1, the scattering cross-section can be calculated with the scattering amplitude as following:

$$\frac{d\sigma}{d\Omega}(\vec{Q}) \propto |\psi(\vec{Q})|^2 \propto \left\langle \sum_i b_i\, e^{-i\vec{Q}\cdot\vec{R}_i} \cdot \sum_j b_j^*\, e^{i\vec{Q}\cdot\vec{R}_j} \right\rangle \tag{48}$$

Since b is usually a real number, $b^* = b$. Let $< b >$ be the average scattering length of the sample and $\delta b_i = b_i - < b >$. The scattering cross-section can be rewritten as:

$$\begin{aligned} \frac{d\sigma}{d\Omega}(\vec{Q}) &\propto \left\langle \sum_{i,j} ((< b > +\delta b_i)\ (< b > +\delta b_j)\ e^{-i\vec{Q}\cdot(\vec{R}_i-\vec{R}_j)} \right\rangle \\ &= < b >^2 \sum_{i,j} < e^{-i\vec{Q}\cdot(\vec{R}_i-\vec{R}_j)} > + 2 < b > \sum_{i,j} \delta b_i\ < e^{-i\vec{Q}\cdot(\vec{R}_i-\vec{R}_j)} > \\ &\quad + \sum_{i,j} \delta b_i\ \delta b_j\ < e^{-i\vec{Q}\cdot(\vec{R}_i-\vec{R}_j)} > \end{aligned} \tag{49}$$

with $\sum_i \delta b_i = 0$. Therefore, the second term in Eq. 49 vanishes. Moreover, for $i \neq j$, the third term also equals zero. Thus the cross-section can be simplified as:

$$\frac{d\sigma}{d\Omega}(\vec{Q}) \propto < b >^2 \sum_{i,j} < e^{-i\vec{Q}\cdot(\vec{R}_i - \vec{R}_j)} > \qquad \text{coherent scattering} \tag{50}$$

$$+ \sum_i \delta b_i^2 \qquad \text{incoherent scattering} \tag{51}$$

The first term is known as *coherent scattering*, coming from the interfering scattered waves. The second term describes the *incoherent scattering* due to deviation from the average scattering length. This part of the scattered wave cannot interfere with each other, thus produces only a flat background. For $i = j$, $e^{-i\vec{Q}\cdot(\vec{R}_i - \vec{R}_j)} = 1$. For $i \neq j$, $\vec{Q} \cdot (\vec{R}_i - \vec{R}_j)$ is very small, thus $e^{-i\vec{Q}\cdot(\vec{R}_i - \vec{R}_j)} \approx 1$. Therefore, a total coherent scattering cross-section for one element with various isotopes can be calculated as $\sigma_{coh} = 4\pi < b >^2$ in units of $barn = 10^{-28} m^2$. Moreover, the isotope incoherent scattering cross-section due to various scattering lengths of different isotopes can be calculated as $\sigma_{incoh}^{isotope} = 4\pi \sum_i (b_i - < b >)^2$.

For isotopes possessing a non-zero nuclear spin $I \neq 0$, the neutron spin and the nuclear spin may align parallel or antiparallel during the scattering process, which will result in a total spin state of $J_+ = I + \frac{1}{2}$ or $J_- = I - \frac{1}{2}$, respectively. Therefore, there will be $2I + 2$ and $2I$ multiplicities for J_+ and J_- states, and thus the probabilities for the compound occupying state J_+ and J_- are $p_+ = \frac{I+1}{2I+1}$ and $p_- = \frac{I}{2I+1}$, respectively. Since scattering lengths are different for spin state J_+ and J_-, another type of incoherent scattering is produced, which is known as *nuclear spin incoherent scattering*. It can be calculated using the same formula as for the isotope incoherent scattering.

A neutron has a spin $\frac{1}{2}$, and thus possesses a magnetic dipolar spin moment. The magnetic moment operator for neutrons is given as:

$$\hat{\mu}_n = g_n \hat{S} \mu_N = \gamma_n \mu_N \hat{\sigma} = -1.913 \mu_N \hat{\sigma} \tag{52}$$

with g_n the g-factor, γ_n the gyromagnetic factor for neutron, $\hat{S} = \frac{\hat{\sigma}}{2}$ is the spin operator, μ_N is the nuclear magneton, $\hat{\sigma}$ is the Pauli-spin matrix. During the scattering process, the interaction between a neutron and the magnetic field in the material caused by the spin and orbital moment of electrons can be described with a potential $V_M = -\hat{\mu}_n \cdot \vec{B}$ with $\vec{B} = \vec{B_S} + \vec{B_L}$, which is the sum of the magnetic field due to spin and orbital moments. Following several lengthy calculations described in Ref. 48, the magnetic cross-section can be calculated as [45, 48]:

$$\frac{d\sigma}{d\Omega}_{mag} = (\gamma_n r_0)^2 \left| \frac{1}{2\mu_B} \left\langle S_f | \hat{\sigma} \cdot \vec{M}(\vec{Q}) | S_i \right\rangle \right|^2 \tag{53}$$

with r_0 the classical electron radius, S_i, S_f the incident and scattered neutron spin state, respectively, and $\vec{M}(\vec{Q})$ the Fourier transform of the magnetization, which is given by the magnetic moments per unit volume. Therefore, the magnetic scattering amplitude can be written as:

$$\psi(\vec{Q}) = \frac{\gamma_n r_0}{2\mu_B} \sum_\alpha \langle S_f | \hat{\sigma}_\alpha | S_i \rangle \, M_\alpha(\vec{Q}) \tag{54}$$

S_i, S_f can be $|+\rangle = \binom{1}{0}$ or $|-\rangle = \binom{0}{1}$ for spin-up and spin-down states, respectively. Summarizing all possibilities for S_i and S_f, the amplitude of magnetic scattering can be given by:

$$\psi(\vec{Q}) = -\frac{\gamma_n r_0}{2\mu_B} \cdot \begin{cases} M_z & \text{for ++ non spin-flip (NSF),} \\ -M_z & \text{for -- NSF,} \\ M_x - iM_y & \text{for +- spin-flip (SF),} \\ M_x + iM_y & \text{for -+ SF.} \end{cases} \tag{55}$$

However, a magnetization component parallel to $\vec{Q}$ is not measurable as illustrated in Fig. 13.

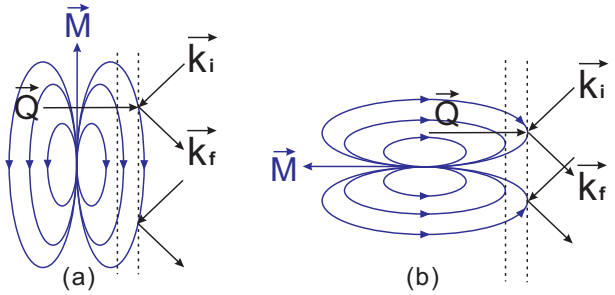

Figure 13: Configurations of magnetization $\vec{M}$ (a) perpendicular and (b) parallel to the scattering vector $\vec{Q}$ resulting in constructive and destructive interference, respectively. This figure is adapted from [45].

Neutron spins produced by e.g. a fission source are randomly distributed. This means, its polarization $P = \frac{n_\uparrow - n_\downarrow}{n_\uparrow + n_\downarrow}$ is zero, with $n_\uparrow$ and $n_\downarrow$ the number of neutrons with spin-up and spin-down states, respectively. However, by applying a polarizing devices such as polarized ^{3}He cell, a super mirror or Heusler alloys, neutrons with either spin-up or spin-down state can be selected. Combining this with a guide field, neutron beams with one defined polarization direction can be achieved. This makes polarization analysis possible. For polarization analysis, we need a polarized incident beam. After the scattering process, the flipped and not flipped spins are measured separately using an analyser. Different scattering component measured in spin-flip (SF) and non spin-flip (NSF) channels are listed in table below [45, 49–51]:

Polarization	SF	NSF
$\vec{P} \parallel x \parallel \vec{Q}$	$\frac{2}{3}\frac{d\sigma}{d\Omega}^{spin}_{inc} + \frac{d\sigma}{d\Omega}^{y}_{mag} + \frac{d\sigma}{d\Omega}^{z}_{mag} + bg$	$\frac{1}{3}\frac{d\sigma}{d\Omega}^{spin}_{inc} + \frac{d\sigma}{d\Omega}_{coh} + \frac{d\sigma}{d\Omega}^{iso}_{inc} + bg$
$\vec{P} \parallel y \perp \vec{Q}$	$\frac{2}{3}\frac{d\sigma}{d\Omega}^{spin}_{inc} + \frac{d\sigma}{d\Omega}^{z}_{mag} + bg$	$\frac{1}{3}\frac{d\sigma}{d\Omega}^{spin}_{inc} + \frac{d\sigma}{d\Omega}_{coh} + \frac{d\sigma}{d\Omega}^{y}_{mag} + \frac{d\sigma}{d\Omega}^{iso}_{inc} + bg$
$\vec{P} \parallel z \perp \vec{Q}$	$\frac{2}{3}\frac{d\sigma}{d\Omega}^{spin}_{inc} + \frac{d\sigma}{d\Omega}^{y}_{mag} + bg$	$\frac{1}{3}\frac{d\sigma}{d\Omega}^{spin}_{inc} + \frac{d\sigma}{d\Omega}_{coh} + \frac{d\sigma}{d\Omega}^{z}_{mag} + \frac{d\sigma}{d\Omega}^{iso}_{inc} + bg$

The scattering geometry is illustrated in Fig. 14. $\frac{d\sigma}{d\Omega}_{coh}$ is the coherent cross-section, bg is the background, $\frac{d\sigma}{d\Omega}^{spin}_{inc}$ and $\frac{d\sigma}{d\Omega}^{iso}_{inc}$ are the nuclear spin and isotope incoherent cross-section, respectively. $\frac{d\sigma}{d\Omega}^{y,z}_{mag}$ stands for the y, z-component of the magnetic cross-section, respectively. However, the x-component of the magnetic cross-section cannot be measured

since the x-axis is parallel to $\vec{Q}$. Combining the equations listed above, different scattering components can be separated:

$$\frac{d\sigma}{d\Omega}_{mag} = 2\left(\frac{d\sigma}{d\Omega}_x^{SF} + \frac{d\sigma}{d\Omega}_y^{SF} - 2\frac{d\sigma}{d\Omega}_z^{SF}\right) \tag{56}$$

$$= -2\left(\frac{d\sigma}{d\Omega}_x^{NSF} + \frac{d\sigma}{d\Omega}_y^{NSF} - 2\frac{d\sigma}{d\Omega}_z^{NSF}\right) \tag{57}$$

$$\frac{d\sigma}{d\Omega}_{inc} = \frac{3}{2}\left(-\frac{d\sigma}{d\Omega}_x^{SF} - \frac{d\sigma}{d\Omega}_y^{SF} + 3\frac{d\sigma}{d\Omega}_z^{SF}\right) \tag{58}$$

$$\frac{d\sigma}{d\Omega}_{coh} = \frac{d\sigma}{d\Omega}_z^{SF} - \frac{1}{2}\frac{d\sigma}{d\Omega}_{mag} - \frac{1}{3}\frac{d\sigma}{d\Omega}_{inc} \tag{59}$$

For powder samples, $|\vec{M}_x| = |\vec{M}_y| = |\vec{M}_z| = \frac{1}{3}|\vec{M}|$, therefore the total magnetic cross-section measured is $\sigma_{mag} = \sigma^y_{mag} + \sigma^z_{mag} = 2\sigma^y_{mag}$.

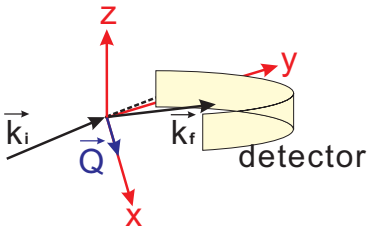

Figure 14: The geometry of an xyz-polarization analysis experiment. $\vec{Q}$ is parallel to the x-axis and the yz-plane is perpendicular to $\vec{Q}$. Adapted from [51].

2.4.4 Small Angle Scattering

Scattering methods are widely used, not only to determine atomic structures but also microstructures in the ∼nm range. As introduced in previous sections, the scattering vector obeys, $\vec{Q} = 4\pi sin\theta/\lambda \sim 1/d_{hkl}$, in case of Bragg scattering. With the same λ, structures with large d_{hkl} can be observed in a small $\vec{Q}$ range. In order to study microstructures like polymers and self-assembled NPs, scattering pattern at small Q range has to be focused on. Therefore, a small incident angle θ has to be applied. This method is known as *small angle scattering (SAS)*. With x-ray or neutron as radiation, it is termed small angle x-ray scattering (SAXS) or small angle neutron scattering (SANS), respectively. Due to the small scattering angle, the sample-to-detector distance needs to be large in order to observe the scattering pattern with reasonable resolution.

Particles measured with SAS are often dispersed in solvents with random orientations. The scattered intensity is measured in transmission geometry. As discussed in section 2.4.1, size and shape of structures can be described by the form factor (Eq. 41). For homogeneous spherical particles, the scattering length density $\rho(\vec{r})$ can be expressed as:

$$\rho(\vec{r}) = \begin{cases} \rho, & \text{for } |\vec{r}| < \mathrm{R} \\ 0, & \text{for } |\vec{r}| > \mathrm{R} \end{cases} \tag{60}$$

with R the radius of the sphere. Then the form factor can be rewritten in spherical coordinates as:

$$\begin{aligned} f(\vec{Q}) &= \int_r \int_\theta \int_\phi \rho(\vec{r}) \cdot e^{i\vec{Q}\cdot\vec{r}} \cdot r^2 sin\theta \; dr \; d\theta \; d\phi \\ &= 4\pi \int_{r=0}^{R} \rho(\vec{r}) \; \frac{sin(Qr)}{Q} r \; dr \\ &= \frac{4}{3}\pi R^3 \; \rho \; \frac{3[sin(QR) - QR \; cos(QR)]}{(QR)^3} \end{aligned} \tag{61}$$

In a SAS measurement, the scattering amplitude of a sample containing N isolated monodispersed particles is considered to be $|\psi| = N \cdot f(\vec{Q})$. Fitting the measured intensity with the calculated intensity, the size and shape of the structure can be estimated. However, real samples are usually not perfectly monodisperse. Therefore, an additional function $d(R, R_0, \sigma)$ describing the size distribution of the particles need to be introduced. In this thesis, size distributions of the NPs are described by a log-normal function:

$$d(R, R_0, \sigma) = \frac{1}{\sqrt{2\pi}\sigma R} \; exp\left(-\frac{[ln(\frac{R}{R_0})]^2}{2\sigma^2}\right) \tag{62}$$

with R the radius of NPs, R_0 the mean value of the radius, and σ the standard deviation. The scattering cross-section considering a log-normal size distribution of NPs can be calculated as:

$$\frac{d\sigma}{d\Omega}(Q) = N\rho^2 \int_R (f(Q,R))^2 \cdot d(R, R_0, \sigma) dr \tag{63}$$

The influence of the polydispersity on the scattering intensity is shown in Fig. 15.

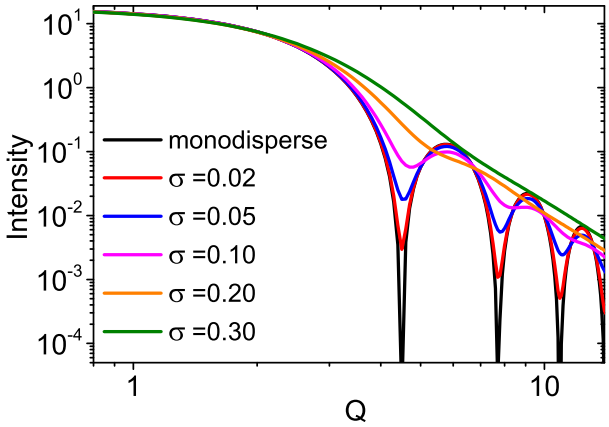

Figure 15: Influence of the particle size distribution on the scattering intensity for SAS measurements. Adapted from [52].

Grazing Incidence Small Angle Scattering Slightly different from SAS, *Grazing Incidence Small Angle Scattering (GISAS)* is measured in a different geometry as shown

in Fig. 16. The incident beam reaches the sample with a grazing incidence angle, which results in a large footprint on the sample. As shown in Fig. 16, the reflected beam can be observed above the horizon, and the transmitted beam found below the horizon. At a in-plane angle $\theta = 0$ and a out-of-plane angle $\alpha_f = \alpha_i$, *specular reflectivity* of the sample can be obtained. By measuring the specular reflectivity, which depends on α_i, information such as layer thickness, surface roughness can be obtained. Intensities measured at $\theta = 0$ and $\alpha_f \neq \alpha_i$ are known as the *off-specular reflectivity*, which provides information about the arrangement perpendicular to the substrate. At $\theta \neq 0$ and $\alpha_f \neq \alpha_i$, a scattering pattern containing the information about the lateral structure of the sample can be observed. For 2D ordering, vertical lines can be found. If the particles order in 3D, Bragg peaks can be observed in the scattering pattern. Below the horizon, the transmitted beam can be detected.

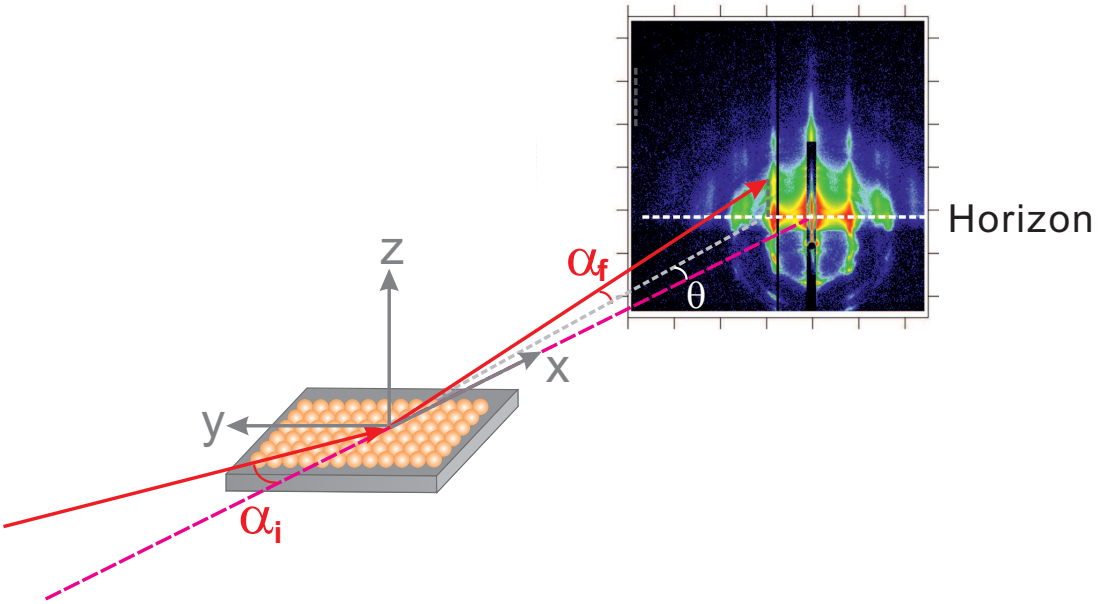

Figure 16: Geometry of a GISAS experiment.

3 Monte Carlo Simulations

Together with theoretical calculations and real experiments, simulations provide a way to better understand nature [53]. In physics, Monte Carlo (MC) methods are widely used to verify theoretical hypotheses. Through calculations with a large amount of sampling statistics and based on physical models, experimental results can be predicted. Therefore, MC simulations are often used to predict the feasibility of experiments, which require much effort, for example, nuclear reactions, neutron transport. In this way, experimental results can be simulated without the concern of safety. Moreover, results from MC simulations can be compared with real experiments, thus confirming the theoretical model described in the simulation. In this thesis, the MC method is used to simulate the spin structure inside MnO NPs and bulk systems under various conditions.

3.1 Basics of Monte Carlo Simulations

An important step of MC simulations is to generate random numbers, which are usually produced by software based on different algorithms [53,54]. These algorithms are actually deterministic, which means, the random numbers are only pseudo-random. The reliability of simulated results depends strongly on the quality of the random numbers. A bad quality of random numbers can lead to large systematic errors within the simulations. Therefore, a wise choice of the random number generator is the first important step of MC simulation. In this thesis, a commonly used method R250 of the shift register algorithm is used to produce pseudo-random numbers [53].

The next step is the sampling of spin configurations of the system. Using the Marsaglia method [55], spins with completely random orientations in 3D are produced. With defined positions, an initial spin structure is produced. The energy of the initial configuration is calculated according to the Hamiltonian of the system. After that, the system is evolved to a new state following a **Markov process**. According to this process, the generated new state only depends on the previous one. The possibility to evolve from a state α to a new state α' is $P(\alpha \to \alpha')$, which obeys the sum rule:

$$\sum_{\alpha'} P(\alpha \to \alpha') = 1 \tag{64}$$

A series of states generated by the Markov process is known as a **Markov chain** [53,54]. The occurrence frequency of state α found in the chain is proportional to its probability p_α. Therefore, two conditions have to be fulfilled to produce a Markov chain [54]:

(1) Accessibility assumption: all possible configurations can be produced with a sufficient number of generations.

(2) Microreversibility: $p_\alpha P(\alpha \to \alpha') = p_{\alpha'} P(\alpha' \to \alpha)$.

One of the algorithms obeying these conditions is the **Metropolis algorithm**, which is often used in MC simulations. By comparing the energy $E_{\alpha'}$ of the new state with the initial one E_α, a new configuration is accepted or rejected under following conditions [54]:

$$E_{\alpha'} - E_\alpha \begin{cases} \leq 0, & \alpha' \text{ is accepted.} \\ > 0, & \alpha' \text{ can be accepted with a probability } e^{-\beta(E_{\alpha'} - E_\alpha)} \end{cases}$$

In other words, if the new state has lower energy, the new configuration is accepted, otherwise if the initial state is energetically favourable, the new configuration can be

accepted with a probability of $P = e^{-\beta(E_{\alpha'}-E_{\alpha})}$ by comparing P to a random number $r \in [0,1]$: if $r < P$, α' is accepted, otherwise rejected. For an ensemble of spins, one random spin is first chosen and evolved to a new state through a test rotation. This test rotation is achieved by adding a random vector in 3D generated using the Marsaglia method to the original spin unit vector, and then the new vector is normalized by its modulus. The new state is either accepted or rejected according to the Metropolis algorithm. After repeating this for N times, with N being the number of spins, one so-called MC step is finished. This procedure is repeated a number of times until an energetically favourable configuration for all spins is found. In this thesis, 10000 MC steps are chosen to simulate NP systems. The simulations converges already by much less MC steps (Appendix B).

3.2 Physical Models

In this thesis, the spin structure of MnO NPs with sizes from 3^3 to 20^3 Mn atoms is the primary focus. Moreover, a reference bulk MnO system is also simulated by applying periodic boundary conditions. For AF MnO, the configuration of atomic spins is governed by the exchange interaction with their neighbours, anisotropy, as well as the interaction with an external magnetic field. The magnetic dipolar interaction for atomic spins is too weak compared to other interactions, and is therefore neglected in the simulations. The Hamiltonian for MnO used in this thesis is the following:

$$H = J_{1m}\sum_{nn}^{p}\vec{S}_i\cdot\vec{S}_j + J_{1p}\sum_{nn}^{a}\vec{S}_i\cdot\vec{S}_j + J_2\sum_{nnn}\vec{S}_i\cdot\vec{S}_j + D\sum_{nn}\vec{S}_{ix}^2 + g\mu_B\sum\vec{S}_i\cdot\vec{B} \quad (65)$$

where J_{1m}, J_{1p} are the exchange constants for nearest neighbours in the same plane and in neighbouring planes of one Mn ion, respectively, J_2 is the exchange constant for next nearest neighbours, $\vec{S}_i$ is the spin at position i. D is the anisotropy constant, $\vec{S}_{ix}$ is the magnetic spin component along the easy-axis of MnO, which corresponds to the crystallographic $\langle 111\rangle$ or $\langle 11\bar{2}\rangle$ direction depending on two different spin configuration models of MnO as shown in Fig. 17, respectively. In the textbook spin model (a), the

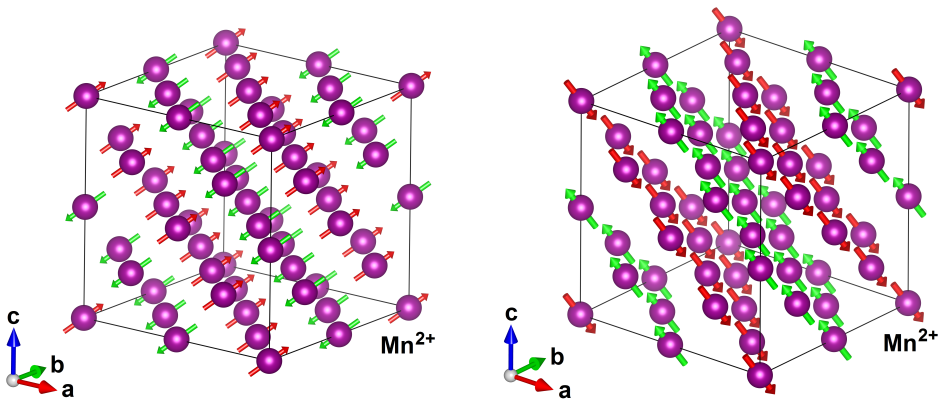

(a) (b)

Figure 17: Two models of spin structure of MnO: (a) spins align parallel/antiparallel to the crystallographic $\langle 111\rangle$ direction [26] or lie within the (111) plane [56–58], for example (b) parallel/antiparallel to the crystallographic $\langle 11\bar{2}\rangle$ direction [57].

spins align parallel or antiparallel to the ⟨111⟩ direction [26]. However, recent studies show that spins in MnO prefer to lie within the (111) plane [56–58], for example along $\langle 11\bar{2}\rangle$ [57] (Fig. 17(b)). g is the *g-factor*, μ_B is the Bohr magneton, $\vec{B}$ is the magnetic field, which is usually chosen to point along the crystallographic ⟨111⟩ direction of MnO as also in this thesis unless otherwise defined. The locations of Mn^{2+} ions are defined using a trigonal coordinate system as shown in Fig. 18. Nearest and next-nearest neighbours interacting with single Mn^{2+} are described in the simulations as illustrated in Fig. 18.

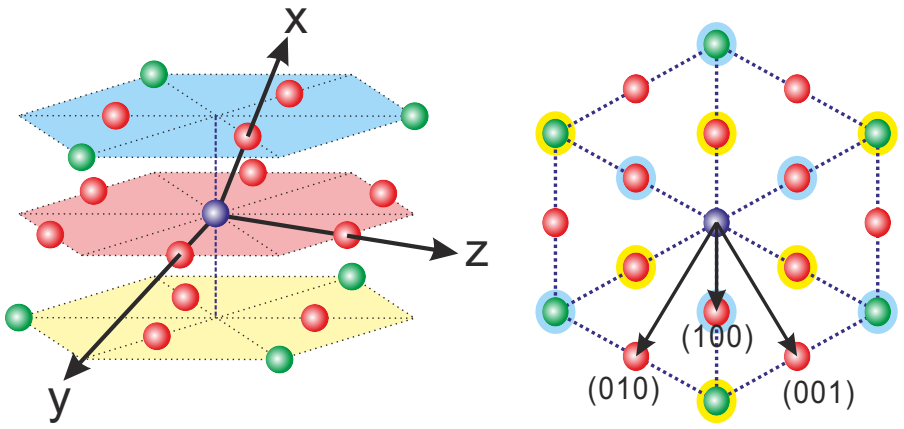

(a) (b)

Figure 18: Illustration of 12 nearest neighbours (red) and 6 next-nearest neighbours (green) defined for one Mn^{2+} (purple) in the MC simulations. (b) shows the top view of (a). In (b), the yellow and blue shells surrounding the nearest (red) and next-nearest neighbours (green) correspond to the yellow and blue background in (a), i.e. the neighbours in two neighbouring (111) planes, respectively. The neighbours without a shell lie within the same plane as the purple Mn^{2+}.

For NP systems, the number of atoms along x-, y-, and z-directions are finite. Spins at the surface of the NPs interact with an asymmetric environment due to the missing neighbours. However, for bulk systems periodic boundary conditions have to be applied. By continuously translating the entire lattice along the x-, y-, and z-directions, virtual neighbours for the surface spins can be generated.

3.3 Simulation Procedures

Depending on the size of NPs, a lattice with randomly oriented unit spins is generated using the Marsaglia method as described in section 3.1. With this, an initial spin configuration is set. All simulations in this thesis start from 300 K and in zero magnetic field. Then the first MC step starts by choosing one random spin in the lattice. The energy of the initial configuration is calculated using the Hamiltonian introduced in section 3.2, with the parameters listed in appendix A. After that, a test rotation using the Marsaglia method is performed. The new configuration is accepted or rejected according to the Metropolis algorithm by comparing the energy of the new configuration with the initial one. After this the MC step is repeated 10000 times, known as relaxation loop. Subsequently, the real "measurement" can start. During the following 10000 MC steps, the x-, y- and z-components of the magnetization resulting from each MC step are recorded,

averaged separately and normalized to the theoretical saturation magnetization of the system. The results are stored as the x-, y- and z-components of the net magnetization of the system, respectively. Furthermore, even and odd (111) layers corresponding to two AF sublattices are recorded separately. The square of the difference between the magnetization component along the field direction (x-direction) resulting from each loop and the average magnetization is considered as the magnetic susceptibility according to the fluctuation-dissipation theorem. For the entire system, the magnetic susceptibility is averaged over 10000 MC steps and normalized to the saturation magnetization. Moreover, a spin table containing the information about the positions, and x-, y-, and z-components of each spins are saved. The procedure is repeated for 1 - 50 times corresponding to complete different configurations. The final results are obtained by averaging all simulated configurations.

In this thesis, I focus on temperature and magnetic field dependent magnetization curves. Firstly, the temperature is reduced from 300 to 2 K with 1 K steps. At each temperature, the magnetic moment and the magnetic susceptibility are recorded (as described above). After the 2 K simulation is finished, a magnetic field is applied. Upon increasing the temperature from 2 K to 300 K, the so-called zero-field cooling (ZFC) magnetization curve is recorded. After that, a field cooling (FC) curve while cooling the system again to 2 K in the presence of the same magnetic field is recorded.

4 Experimental Methods and Instruments

4.1 Magnetometry

The macroscopic magnetization of MnO and FeO_x systems have been studied using a SQUID (superconducting quantum interference device) magnetometer (MPMS XL, Quantum Design) and a VSM (vibrating sample magnetometer) (PPMS or Dynacool, Quantum Design). The basic setup of all three systems (MPMS/PPMS/Dynacool) comprises a sample chamber, which may connect to various additional options, and a control system connecting to a computer.

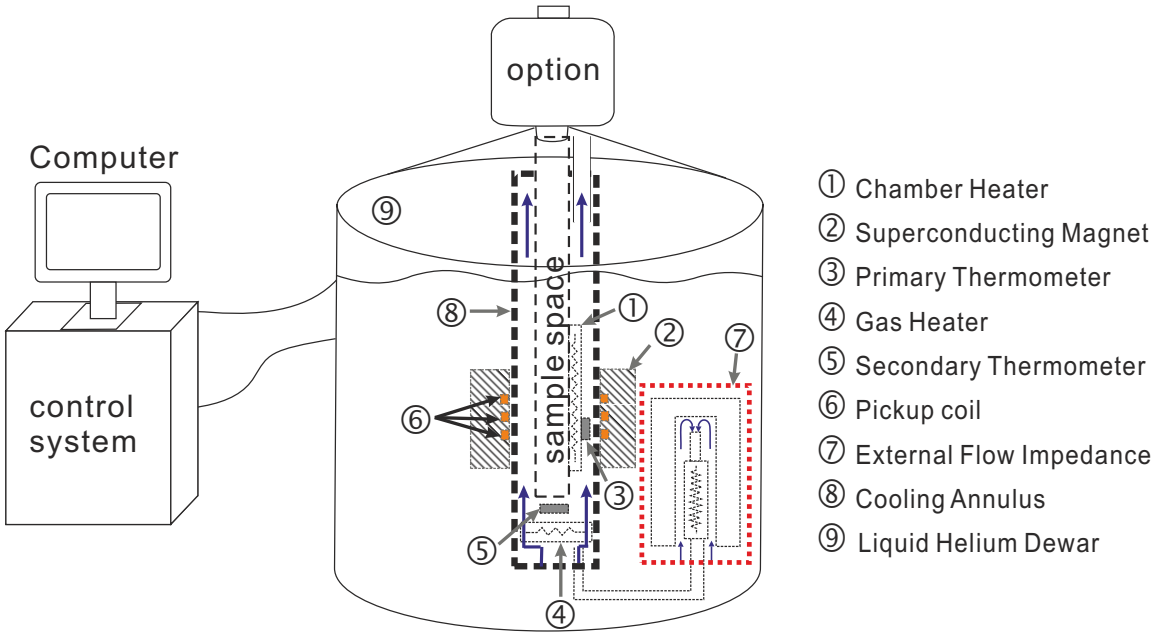

Figure 19: Setup of the SQUID magnetometer. Adapted from [59].

Fig. 19 illustrates the setup of the SQUID magnetometer. The left part is the control console composed of a control system combined with a computer, which provides automatic control of the electronic systems and data collection. In the right part, liquid helium is filled in the dewar. The sample space within the dewar is isolated from the liquid helium by a vacuum sleeve. The sample is fixed on the sample holder and attached to the end of a sample rod. The sample rod is then inserted into the sample space. In order to cool the sample, a controlled amount of liquid helium is allowed to flow into the bottom of the cooling annulus, evaporates and flows as a gas stream through the cooling annulus. The He gas stream cools the sample space. Temperature is controlled by counter-heating with an electrical heater.

Inside the sample space a static He exchange gas atmosphere is maintained for heat exchange to the sample. To heat the sample, both a chamber heater and a gas heater are used. The gas heater preheats the helium gas flow and transfers heat to the sample tube. The chamber heater surrounding the sample tube heats the sample space in addition.

For all three systems, the magnetic field is produced by a superconducting magnet. For the SQUID magnetometer, a vertical magnetic field from -7 to 7 T is available. For the PPMS and the Dynacool, samples can be measured within an applied magnetic field of -9 – 9 T in the vertical direction. When a magnetized sample passes through the pickup coil, a

current is induced. For a SQUID magnetometor, the current is coupled to a SQUID-ring, which is composed of a superconducting loop with a weak link. The pickup coil used in our SQUID magnetometer is a second-order gradiometer as shown in Fig. 20 to avoid any background signal from homogeneous fields. The SQUID-ring acts as a LC circuit and is coupled to an external RF oscillating circuit. The LC circuit has a resonant frequency $f_{res} = \sqrt{1/LC}$. The inductance L and the capacity C result from the superconducting loop and the Josephson junction of the SQUID ring, respectively. Moreover, the SQUID-ring is also coupled to the signal transferred from the pickup coil. The current transferred from the pickup coil produces an additional magnetic flux penetrating the SQUID-ring and thus induces a current inside the superconducting ring to reduce the total flux inside the ring. As a result, a change in the resonant frequency can be observed. Since the magnetic flux Φ penetrating the SQUID-ring is quantized $\Phi = n\Phi_0$ with $\Phi_0 = h/2e$ being the magnetic flux quantum and n an integer, the total flux through the SQUID-ring is given by [60, 61]:

$$\Phi = \Phi_{ext} - LI_c sin(2\pi \frac{\Phi}{\Phi_0}) \tag{66}$$

with Φ_{ext} the external flux due to the RF oscillating circuit, L and I_c the inductance and the critical current of the SQUID-ring, respectively.

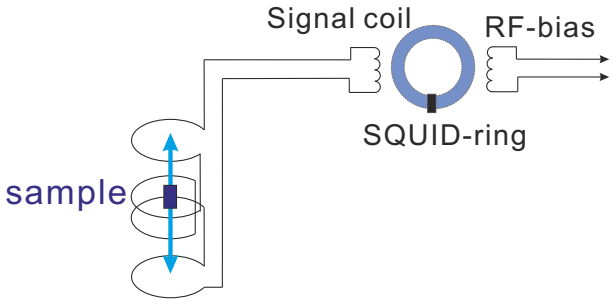

Figure 20: Detection system of a RF-SQUID. Adapted from [59].

In order to measure the magnetic moment of the sample using the SQUID magnetometer, the sample is moved up and down through the pick-up coils, and thus a current is induced in the coils. The response of the magnetic moment of the sample is measured using the software "MPMS MultiVu". After the response curve is fitted to an ideal dipole response using a non-linear, least-squared fitting routine, the sample position can be determined. Then the MPMS MultiVu calculates the magnetic moment of the sample using a measurement algorithm. This method works for both the DC and RSO (Reciprocating Sample Option) options of the SQUID magnetometer. Using a RSO option, an oscillation of the sample around the measurement position is performed.

For the VSM option of the PPMS, another technique is used. Fig. 21 shows a sketch of the VSM system. VSM uses a linear motor, which can rapidly slew the sample over a few cm range. The sample is sinusoidally vibrated at the center of the pick-up coil. The position and the oscillation amplitude is controlled using a motor module connected to the linear motor. The voltage induced in the pick-up coil is detected by the VSM module. Using the signal from the motor module as a reference, the detected signal is send to the computer.

The voltage induced in the pick-up coil due to a sinusoidally vibrating magnetic mo-

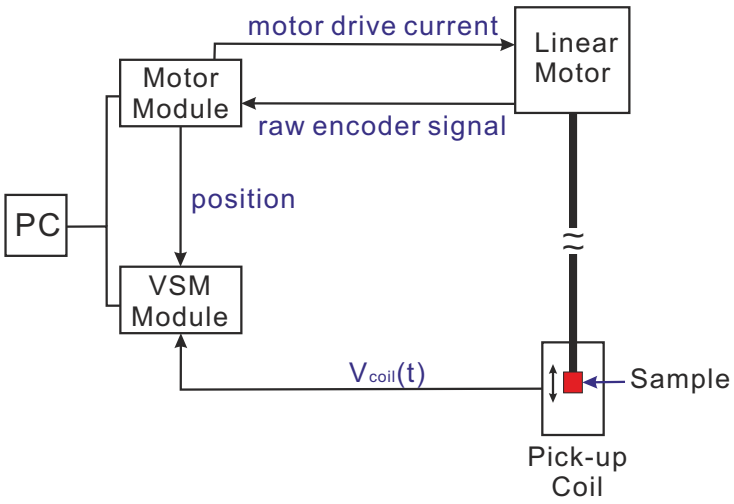

Figure 21: Operating principle for the VSM option of the PPMS. Adapted from [62].

ment can be calculated as:

$$V_{coil} = \frac{d\Phi}{dt} = \left(\frac{d\Phi}{dz}\right)\left(\frac{dz}{dt}\right) = 2\pi f C m A \sin(2\pi f t) \tag{67}$$

with Φ the magnetic flux within the pick-up coil, z the vertical position of the sample with respect to the coil, t the time, C a coupling constant, m the DC magnetic moment of the sample, A and f the amplitude and the frequency of oscillation, respectively. Therefore, by measuring the time dependent value of V_{coil}, the magnetic moment of the sample can be obtained.

In this thesis, the temperature dependent magnetization has been measured via different procedures. *Zero field cooled* (ZFC) magnetization curves are measured after the sample is cooled from high temperatures (above the phase transition) to a low temperature in the absence of a magnetic field. After that a magnetic field is switched on and the magnetization of the sample is measured during warming up. For a *field cooled* (FC) magnetization curve, the magnetization of the sample is measured during cooling the sample in the presence of a magnetic field. Field dependent magnetization curves, $M(H)$, were measured via changing the magnetic field at a constant temperature. By comparing the temperature and field dependent magnetization curves with different models, information about the magnetic ordering can be achieved.

For spin glass (SG) and superspin glass (SSG) systems, the so-called *memory effect* is important. To observe the memory effect, a regular ZFC curve is first measured. Then a similar procedure as the ZFC measurement is performed. The only difference is that during the zero field cooling procedure a stop at a temperature below the transition temperature of the SG or SSG system is made. After that, the sample is further cooled down to low temperatures and the magnetization is measured while warming up with the same magnetic field as done for the regular ZFC measurement. By subtracting the regular ZFC curve from the ZFC curve with the stop, a peak near the stopping temperature is expected for SG or SSG systems. This is known as the memory effect, i.e. the system remembers the previous stop during the zero field cooling procedure.

Another method to characterize magnetic properties is the thermal/isothermal remanent magnetization (TRM/IRM). Similar to the FC measurements, the sample is cooled

in a magnetic field for TRM measurements. At low temperatures, the magnetic field is switched off and the remanent magnetization is measured. For an IRM measurement, the sample is cooled in the absence of a magnetic field. At low temperatures, the magnetic field is switched on for a short time and then switched off. After that, the magnetization is measured. These procedures are repeated at different magnetic fields. The field dependent TRM/IRM curves show different behaviours for different systems as fingerprint, and thus additional information about the sample can be obtained.

4.2 AC-Susceptibility

The ACMS option of the PPMS and Dynacool is a useful tool to perform AC-susceptibility measurements. There, an AC magnetic field is applied and the dynamics of the sample magnetization can be studied. For very low driving frequencies, the magnetic moments in the sample has enough time to follow the driving field. Therefore, the AC susceptibility χ_{AC} can approximately be considered as the DC susceptibility. Therefore, the magnetization of the sample can follow the $M(H)$ curve as measured in a DC measurement at low frequencies and small AC fields:

$$M(t) = (dM/dH) \cdot H_{AC} \sin(\omega t) \tag{68}$$

with dM/dH the susceptibility χ, H_{AC} the amplitude of the AC driving field, ω the driving frequency. However, as ω increases, the magnetic moments cannot follow. Therefore, a phase shift ϕ between the AC susceptibility and the driving field occurs. In this case, the AC-susceptibility of the sample can be expressed by a complex quantity:

$$\widetilde{\chi} = \chi_0 \ \exp|i\phi| = \chi_0 \ \cos\phi + i\chi_0 \sin\phi = \chi' + \chi'' \tag{69}$$

with a modulus of $\chi_0 = \sqrt{\chi'^2 + \chi''^2}$. The real part or "in-phase" component χ' describes the magnetic component following the driving field and the imaginary part or "out-of-phase" component χ'' indicates the energy loss.

For SPM and SG (SSG) systems, the AC-susceptibility is often measured to study the relaxation time. Temperature dependent susceptibility curves usually show peaks indicating the blocking or freezing temperature of SPM or SG systems, respectively. By comparing the frequency dependence of the peak temperature with theoretical models as described in section 2.2.2, the magnetic behaviour of the samples can be characterized.

4.3 Heat Capacity

Heat capacity (HC) measurements have been performed using the heat capacity option of the PPMS and Dynacool. There, HC of samples is measured at a constant pressure:

$$C_p = \frac{dQ}{dT} \tag{70}$$

with dQ the thermal energy applied to or removed from the sample and dT the temperature change of the sample. The schematic illustration of the sample platform is shown in Fig. 22. The sample is attached to the platform via a thin layer of apiezon grease. After applying a heat pulse by the heater attached to the bottom of the platform, the temperature response of the sample is measured by the thermometer. The sample platform is fixed

in the middle of the puck frame via small wires, which provides also electrical connection to the heater and thermometer. Moreover, these wires provides thermal conduction between the heater/thermometer and the thermal bath, thus lead to a better thermal equilibrium of the sample and the platform during the measurements. HC measurements are performed in a high vacuum environment to isolate the platform thermally. Since the platform and the grease produce an additional heat capacity, a so-called addenda measurement with only the platform and the grease is performed before the sample is mounted. The result is considered as background. The HC of the sample is obtained after the result from the sample measurement is subtracted from the background. Temperature dependent HC measurements are sensitive for both structural and magnetic phase transitions. Usually a peak or a similar feature can be observed at the phase transition temperature in a temperature dependent curve. A λ-shaped peak usually indicates a first order phase transition.

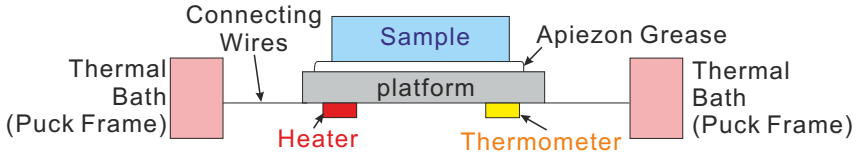

Figure 22: Basic setup of the platform for a heat capacity measurement in a PPMS. Adapted from [59].

4.4 Torque Magnetometry

To measure the angular dependent magnetization, a torque magnetometer option has been used. The magnetic torque $\vec{\tau} = \vec{m} \times \vec{B}$ produced by a magnetic moment $\vec{m}$ in a magnetic field $\vec{B}$ is measured using a piezoresistive technique. As shown in Fig. 23, the sample is mounted on a torque-lever chip. Due to a torque τ, the two torque levers on the chip are twisted and thus the resistances R_1 and R_2 become different. Then a torque $\tau \sim \Delta\left(\frac{R_1-R_2}{R_{bridge}}\right)$ can be calculated. Torque magnetometry detects a twist instead of a bending of the levers to avoid a gravity effect of the sample. This torque-lever chip is mounted on a PPMS sample rotator. By varying the angle between the magnetic moment of the sample and the magnetic field by rotating the sample platform controlled by the software "MultiVu" as shown in Fig. 23, the magnetic anisotropy of the sample can be studied.

4.5 X-ray Diffraction

The crystal structure of MnO powder and single crystal samples were characterized using x-ray diffraction. For powder samples, a Huber Guinier G670 camera is used. The powder diffraction is performed in transmission geometry using a CuKα radiation with $\lambda = 1.5418$ Å. The positions of the observed Bragg reflections are compared with those of various manganese oxides phases, so that the composition of the powder can be determined. Moreover, the diffraction pattern is refined with the program "Fullprof", which is based on the Rietveld method. By refining the parameters published in the Inorganic Crystal Structure Database (ICSD) for MnO, a proper model describing the structure of

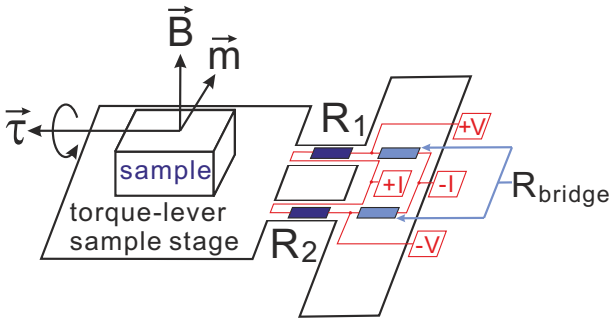

Figure 23: Schematic illustration of a torque-lever chip. Two piezoresistor grids with a resistance of R_1 and R_2, respectively, are located on the legs of the torque-lever. A Wheatstone bridge circuit measures the change in the resistance, $\Delta(R_1 - R_2)$, when the legs are twisted due to the torque. R_{bridge} marks the two known resistances in the Wheatstone bridge circuit. Between "+I" and "-I", a voltage is applied and the voltage between "+V" and "-V" is measured. Adapted from [59].

the sample can be found. Diffraction patterns have been measured at various temperatures ($15\,\text{K} - 300\,\text{K}$) to observe the structural phase transition of MnO at low temperatures.

Single crystal x-ray diffraction was performed using a Supernova diffractometer. A small piece (about a few hundred μm^3) of MnO single crystal is stuck on the sample holder, which has two rotational degrees of freedom. X-ray radiation from a molybdenum source ($\lambda_{\text{Mo}} = 0.709\,\text{Å}$) has been used. The diffraction patterns have been measured at room temperature (300 K) and at 90 K. The sample is cooled by a nitrogen gas flow. The software "CrysAlisPro" is used to control the experiment as well as for data analysis.

4.6 Neutron Diffraction

Neutron diffraction experiments performed in this thesis have been done at the DNS (Diffuse Neutron Scattering) instrument of the Jülich Centre for Neutron Science at the Heinz Maier-Leibnitz Zentrum in Garching, Germany [63, 64]. The DNS instrument is a high-flux time-of-flight spectrometer with xyz-polarization analysis. Polarization analysis has been introduced in section 2.4.3, which is a useful method to separate small magnetic moments from the background. This is especially relevant for NPs covered by oleic acid shells. The hydrogen contained in the shells produce a huge spin-incoherent background, which will dominate the entire diffraction pattern. Only by using xyz-polarization analysis, the magnetic and nuclear scattering components of the NPs can be separated. At the sample position, DNS has a neutron flux of $\sim 10^8\,\text{n}\,\text{cm}^{-2}\,\text{s}^{-1}$ for non-polarized neutrons and $\sim 5 \cdot 10^6$ - $10^7\,\text{n}\,\text{cm}^{-2}\,\text{s}^{-1}$ for polarized neutrons.

The schematic illustration of DNS is shown in Fig. 24. Neutrons produced by the reactor are guided to the instrument through the neutron guide ①. Using a monochromator ②, neutrons with a wavelength in the range from 2.4 to 6.0 Å can be selected. Through a velocity selector ③, the focused neutron beam is guided to the sample position ⑥. For time-of-flight experiments, a chopper can be used to define the start time of the neutrons. By comparing the time neutrons arriving the detector and the calculated time using the velocity of neutrons, the energy transfer can be determined. Using a polarizer ④ in combination with xyz-coils around the sample position, neutrons with polarization along x-, y- or z-directions can be realized. Combining a flipper before the sample space and

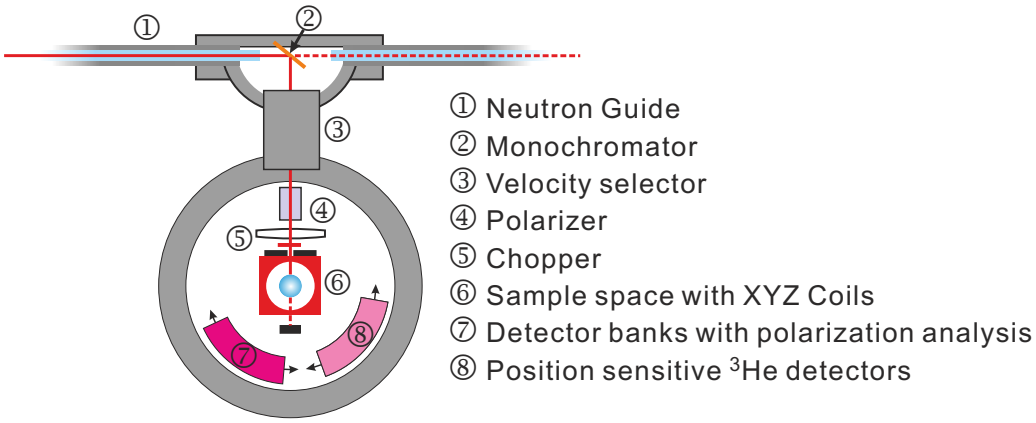

Figure 24: Instrumental setup of the DNS instrument. Reproduced from [63].

24 detector banks with polarization analysis ⑦, spin-flip (SF) and non-spin flip (NSF) intensities can be measured separately. For non-polarized neutron scattering, 128 position sensitive ^{3}He tubes are used. DNS provides a low temperature sample environment down to ~ 20 mK by using a cryostat around the sample position. Moreover, a vertical magnetic field up to 5 T can be provided using a cryomagnet.

In this thesis, polarized neutron scattering has been performed on MnO powder and MnO single crystal to be compared with the results of MnO NPs [18, 65]. For the NP studies, 12 nm diameter MnO NPs were chosen. 50 mg of dried MnO NP powder are wrapped in aluminium foil and placed in a cylindrical aluminium sample holder. Polarized neutron diffraction has been performed using a wavelength of $\lambda = 4.2$ Å. Two different MnO powder samples have been measured at the DNS instrument. Firstly, commercially available MnO powder (Alfa Aesar GmbH, 99.99%) was measured. The results are compared with that of MnO powder after an annealing procedure, which will be discussed later in section 5. The wavelength for both measurements was $\lambda = 3.3$ Å. The MnO single crystal (Surface Net GmbH) with dimensions $5 \times 5 \times 2\,\text{mm}^3$ is pre-characterized using a Laue diffraction camera and fixed onto the sample holder so that the $(1\bar{1}0)$ axis is perpendicular to the scattering plane. Single crystal neutron diffraction was performed with $\lambda = 4.2$ Å .

4.7 (Grazing Incidence) Small Angle X-ray Scattering

SAXS and GISAXS measurements are performed using a high brilliance laboratory small angle X-ray scattering instrument GALAXI (Gallium Anode Low-Angle X-ray Instrument) at JCNS, Forschungszentrum Jülich [66]. Fig. 25 shows the main components of GALAXI [66]. To produce x-ray radiation, a Metaljet source is used. An electron beam hits the liquid metal jet, which is composed of a GaInSn alloy, and x-rays are produced. Using parabolic Montel-type optics, monochromatic GaK_α radiation with an energy of E = 9243 eV is achieved. Using two slits S1 and S2 separated by 4 m distance, the x-ray beam can be collimated with an inclination of 0.4°. After that, a third slit S3 is used to reduce background. At the sample position, the x-ray beam with a flux of 10^9 photons/mm^2·s hits the sample and the scattered photons are detected by a Pilatus 1M 2D position sensitive detector. Different Q-ranges can be detected by changing the detector distance between 0.8 to 3.5 m in 5 steps, and thus structures between 2 and 100 nm

sizes can be studied.

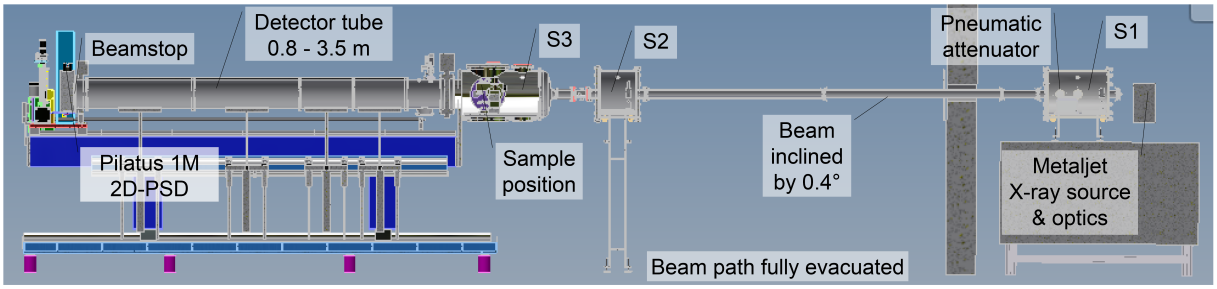

Figure 25: Instrumental setups of GALAXI [66].

For SAXS measurements, the NPs are diluted in a solvent and sealed in a capillary. Background measurements with empty capillaries as well as capillaries filled with solvent were performed. SAXS measurements were performed in transmission geometry. The Q dependent intensity curves were fitted by Eq. 63 as described in section 2.4.4 using the software "SasView". From SAXS measurements, information about the shape, mean size and the size distribution of NPs can be obtained.

The GISAXS geometry of GALAXI is very useful to characterize the structrual order of self-assembled NP films. As introduced in section 2.4.4, GISAXS is perfomed in reflection geometry. Self-assembled NPs on Si substrates were placed onto the sample platform of GALAXI, which has two rotational (α and β) and two translational (along y- and z-axes) degrees of freedom as shown in Fig. 26. Scattering patterns at various incident angles have been measured and compared with a scattering simulation using "BornAgain" [67], which is a software to simulate and fit grazing incidence small-angle scattering results. By comparing the experimental results with the simulated patterns, information about shape, size and the lateral order of the particles can be found.

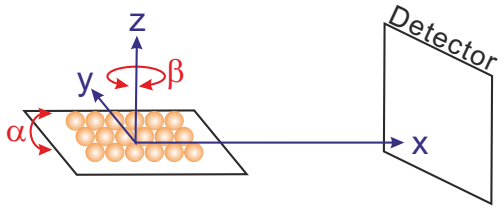

Figure 26: Geometry of a GISAXS measurement with GALAXI.

5 Investigation of the Spin Structure of Manganese Oxide

As one of the first studied materials using neutron scattering [68], MnO has been investigated for decades. However, this system is still not well understood despite numerous studies. In this thesis, we focus on spherical MnO NPs with 12 nm diameter. The spin structure of the NP samples has been studied and compared with bulk systems. In section 5.1, the current state of research on manganese oxides will be introduced. After that, the synthesis of MnO NPs as well as the annealing procedures to vary the phase of manganese oxide will be described. The structural characterizations can be found in section 5.3. The experimental results will be discussed in section 5.4. Monte Carlo simulations have been performed to be compared with the experimental results (section 5.5). Moreover, the spin structure of MnO obtained from the simulations are visualized.

5.1 Introduction to Manganese Oxide

MnO is a text-book AF with a rocksalt crystal structure at room temperature. At the Néel temperature of 118 K, a PM-to-AF phase transition is usually observed [68, 69]. In Ref. 70–72, this transition was reported to be of first-order. However, a continuous phase transition was observed in Ref. 73. Magnetic moments of Mn^{2+} were reported to align parallel within the (111) planes below T_N, while magnetic moments between neighbouring planes arrange antiparallel [57,68]. Recent studies reported that the magnetic moments of MnO prefer to lie within the (111) planes [56–58, 74] in contrast to the common textbook knowledge (parallel or antiparallel to the [111] direction) [26]. Both spin models of MnO with an anisotropy axis within the (111) plane or perpendicular to the (111) plane were shown in Fig. 17 in section 3.2.

The exchange constants for the nearest neighbours and the next nearest-neighbours as well as the anisotropy constant of MnO have been obtained using inelastic neutron scattering [75–77]. Accompanying its magnetic phase transition, a structural distortion was also found at its Néel temperature of 118 K [57,58,75]. Below T_N, the crystal structure of MnO was refined using a rhombohedral or a monoclinic model [57, 58]. Beside the well-known phase transition at 118 K, a spin-glass transition in the temperature range of 25 - 50 K was reported for MnO powder [78]. This was explained by a slight off-stoichiometry of MnO_{1+x} with x≤0.01. Moreover, an anomaly at about 50 K was found in the specific heat measurements in Ref. 73.

MnO can easily be oxidized in air at room temperature. Therefore, the commercially available MnO is often not single phase. A significant amount of Mn_3O_4 was found in the magnetic susceptibility and the magnetization measurements of four commercial samples in Ref. 79. In this work, a feature at 43 K was found, which matches the T_C of Mn_3O_4 [71, 80, 81]. Moreover, an EB effect at 4.2 K was measured, which suggests the exchange coupling between the FiM Mn_3O_4 and AF MnO. To obtain single phase MnO, various methods can be used as reported in Ref. 79, 82, 83. By annealing the as-prepared samples using an evacuated sealed quartz tube with the presence of Mn at another position in the tube at 1293 K for about 200 h, the Mn_3O_4 part can be converted into MnO. Ref. 82 reported that the MnO phase can be stabilized by heating at 1000°C for several hours in an inert or a hydrogen atmosphere. By doing this, MnO can be prevented from reoxidation

at room temperature. This can also be achieved below 800°C by adding other oxides in the quartz tube, for example ZnO, without contaminating MnO. Ref. 83 reported that the phase of manganese oxides can be varied with methane. At a temperature higher than 723 K, manganese oxides with higher oxidation states can be reduced to MnO by oxidizing methane into water and carbon dioxide. In an oxygen atmosphere, the reduced MnO can be reoxidized to Mn_2O_3 and Mn_3O_4 at 823 K and 1073 K, respectively.

Hausmannite Mn_3O_4 has a tetragonally distorted spinel crystal structure below 1443 K [80, 81, 84]. Below ∼43 K, Mn_3O_4 is a FiM [71, 80, 81]. The magnetic unit cell is doubled compared to its crystal unit cell [80, 81]. All oxides and hydroxides of manganese form Mn_3O_4 if heated in air to about 1000°C [84].

Manganese sesquioxide (Mn_2O_3) exists in two forms: α-Mn_2O_3 and γ-Mn_2O_3. α-Mn_2O_3 can be produced through oxidation of a lower oxidation state of manganese oxide, or through reduction of a higher state. γ-Mn_2O_3 has not been reported to exist in nature [84]. Above 302 K, α-Mn_2O_3 has a crystal structure of an undistorted cubic bixbyite. Below 302 K, it has an orthorhombically distorted bixbyite structure [85]. It is reported to be AF below $T_N \approx 80$ - 90 K with a magnetic unit cell equal to the crystal unit cell. In Ref. 85, the intensity of different magnetic peaks shows different temperature dependencies. This suggests that the magnetic ordering in α-Mn_2O_3 cannot be described by a single order parameter.

Not only their bulk form, but also manganese oxide NPs have been intensely studied using magnetometry and neutron scattering [18, 86–89]. ZFC curves of MnO NPs often show a low temperature peak at ∼25 K instead of a feature near the bulk Néel temperature of 118 K as reported in our previous work [18] as well as other studies [86, 88, 90, 91]. However, neutron scattering shows the expected vanishing of the AF order parameter of MnO near the bulk Néel temperature [18, 86–89]. This contradiction between the magnetometry and neutron scattering results was explained by SPM, SSG behaviour, diluted AF states, finite size or surface effects in Ref. 3, 19, 41, 92–94. However, none of these models can fully describe the magnetic behaviour of MnO NPs. We suggested an antiferro-superparamagnetic (AF-SPM) core + Mn_3O_4 shell model in Ref. 18. Due to the different probing times of neutron scattering and magnetometry measurements, the different results can be understood. Moreover, a reduced Néel temperature was observed in neutron diffraction experiments on 8 nm MnO NPs [86]. In Ref. 87 and 91, a continuous magnetic phase transition is reported for MnO NPs. The AF correlation length of MnO NPs is found to be much smaller compared to their particle sizes. This was explained by surface spins or a Mn_3O_4 shell [18, 87, 88]. As the size of NPs decreases, an increase in the peak temperature was observed [11, 18, 25]. This is different from the size dependence of the characteristic temperatures found for other AF NPs. In Ref. 95, the structural distortion of MnO below T_N=118 K was reported to disappear at low temperatures in nanostructured MnO confined in matrices.

Due to their novel properties, core/shell NPs with an AF MnO core and a Mn_2O_3 or Mn_3O_4 shell have been studied in previous works [91,96–98]. The phase of the mangnanese oxide shell is reported to be dependent on the size of NPs [91]. At the interface between AF core and FiM shell, an EB effect was usually observed [96, 97]. Due to the strain of the oxidized shell, the cell parameter of the MnO core is reported to be reduced [98]. This may also lead to an increase in the T_N of MnO. Due to the interplay of the strain caused by the shell and the finite size effect, the AF-to-PM transition may take place at various temperatures [98]. This may explain the dispersion of T_N reported in previous

works. Moreover, Mn_3O_4/MnO core/shell NPs were studied in Ref. 99. For these NPs, an EB effect was also observed. Due to the EB between AF MnO and FiM Mn_3O_4, a much larger coercive field was often measured in NPs compared to that of bulk Mn_3O_4 [97, 99].

Single phase Mn_3O_4 NPs were studied in Ref. 25, 100, 101. A relatively sharp peak was usually found at ∼42 K. This temperature agrees with the T_C of bulk Mn_3O_4. This peak temperature decreases with a decrease in the NP size [25]. Moreover, the dynamics of these NPs has been measured using AC-susceptometry. The frequency dependence of the peak temperature observed in the AC susceptibility can be well described by the Vogel-Fulcher law [100]. This suggests a glassy behaviour of the Mn_3O_4 NPs.

Even though γ-Mn_2O_3 is thermally less stable than the α-phase, its NP form was successfully studied in Ref. 102. Below its T_C of 39 K, γ-Mn_2O_3 NPs show a FiM behaviour. Moreover, a large coercive field was also observed below its T_C.

5.2 Sample Preparation

Spherical MnO NPs with 12 nm diameter were synthesized by Heiko Bauer, Anna Schilmann and Oskar Köhler from the collaboration group of Professor Dr. Wolfgang Tremel at the Institut für Anorganische Chemie und Analytische Chemie of the Johannes-Gutenberg-Universität Mainz. The synthesis of the NPs will be introduced in section 5.2.1. The bulk MnO samples used in this thesis are commercially available MnO powder (Alfa Aesar GmbH, 99.99%), single crystals (Surface Net GmbH) and MnO powder grown on a Mn target of an Oxide Molecular Beam Epitaxy (OMBE) system at our institute. In order to obtain single phase MnO bulk as well as to study the magnetic properties of manganese oxide NPs with various phases, the as-prepared samples were annealed. The annealing procedures for bulk and NP samples will be described in sections 5.2.2 and 5.2.3, respectively.

5.2.1 Synthesis of MnO Nanoparticles

MnO NPs were synthesized by thermal decomposition of a manganese oleate precursor as described in Ref. 18. 1.24 g of manganese oxide precursor were dissolved in 10 mL of 1-octadecene and degassed three times at 80°C under a reduced pressure of 1×10^{-2} mbar. After refilling with argon, the reaction mixture was heated up to 180°C. Then the temperature was slowly increased up to 320°C with 2°C/min. The mixture was refluxed at 320°C for 30 min. After that, it was cooled down to room temperature. The NPs were precipitated with ethanol or acetone and collected by centrifugation. After they were washed three times in a non-polar solvent, such as hexane, and reprecipitated again with ethanol, the NPs were stored in hexane at 4°C. By controlling the solvent, reaction time, temperature, and heating rate, 12 nm spherical MnO NPs were synthesized. In order to avoid agglomeration, the as-prepared particles are covered with an oleic acid shell. The size distribution of these NPs is about 20%.

5.2.2 Annealing of Powder and Single crystal

Both commercially available MnO powder and single crystal show an anomaly at low temperatures in the ZFC magnetization curves suggesting a possible existence of nano-sized MnO or a higher oxidation state Mn_3O_4 or Mn_2O_3. Results of the as-prepared MnO

powder and single crystal will be discussed later in section 5.4.2. In order to study MnO bulk systems, the as-prepared MnO powder and single crystal were annealed following various procedures. Firstly, MnO powder or the single crystal were placed into a crucible. After that the crucible was sealed in a quartz tube at 10^{-6} mbar vacuum. For several samples, the evacuated tube was again filled with 20 mbar Ar or N_2 gas. The quartz tube was then heated in an oven at 920°C for 150 h. After that the temperature was increased to 1000°C and held at 1000°C for several hours to avoid re-oxidation. Finally, the quartz tube was either naturally cooled or quenched in water. The MnO samples focused on in this work are listed in Tab. 1.

5.2.3 Annealing of Nanoparticles

In order to study the magnetic behaviour of pure MnO NPs as well as the influence of partial oxidation to higher oxidation states (Mn_3O_4 or Mn_2O_3) onto the magnetic properties, the as-prepared NPs were annealed under various conditions (Tab. 1). The annealing procedures were performed using a heatable chamber, which can be evacuated and a vacuum of $\sim 10^{-6}$ mbar can be reached. To anneal the as-prepared samples, the NP dispersion was drop-casted on a piece of Si(100) substrate ($5 \times 5\,mm^2$). After the dispersion was completely dried, the sample was placed into the chamber. To achieve fully oxidized Mn_3O_4 NPs, the as-prepared NPs were heated at 100 °C in air for 15 h.

However, to reduce the oxygen content, the chamber was continuously pumped during the annealing procedure, so that a high vacuum condition was applied. After 10^{-6} mbar pressure was reached, the chamber was heated at 310°C for 3.5 h. Then the chamber was naturally cooled. The sample was taken out of the chamber and the magnetic properties were measured using a magnetometer.

sample name	form	annealing environment	T [°C]	t [h]
MnO_np	NP	-	-	-
MnO_np^{ann}	NP	vacuum	310	3.5
MnO_np^{oxi}	NP	air	100	15
MnO_p	powder	-	-	-
MnO_p^{ann}	powder	vacuum	920	150
MnO_sc	single crystal	-	-	-
MnO_sc^{ann}	single crystal	vacuum	920	150

Table 1: List of manganese oxide samples studied in this thesis. The “oxi” and “ann” in the superscript indicate that the samples were oxidized in air or annealed in vacuum, respectively.

5.3 Structural Characterization

The crystal structures of MnO powder and of the single crystal were characterized by x-ray diffraction (XRD) using an in-house x-ray powder diffractometer and a single-crystal diffractometer described in section 4.5. The XRD patterns were measured above and below the well-known structural distortion of MnO at 118 K. The results are compared with those from previous works. Both, the powder and the single crystal sample, were measured at room temperature. At this temperature, MnO is reported to have a cubic structure. For MnO powder and the milled single crystal samples, powder diffraction was measured at various temperatures from 15 to 300 K. Above 118 K, no obvious difference in the diffraction patterns can be found compared to the 300 K data (data not shown). Similarly, there is also no difference observed in the diffraction patterns below 118 K. In this thesis, only the 15 K data is shown. For the single crystal diffraction, the sample was cooled by liquid nitrogen, which has a boiling point at 77 K. However, it was transformed into gas form before reaching the sample position. Therefore, the lowest temperature, which this instrument can reach, is about 90 K. To study the crystal structure of the single crystal below T_N, single crystal x-ray diffraction was performed at 90 K. XRD was also performed for MnO NPs. However, the reflections from the NPs could not be separated from the background. This is due to the small amount of sample. Moreover, the Bragg reflections on NPs become very broad due to their nanometer size, which makes the separation even more difficult.

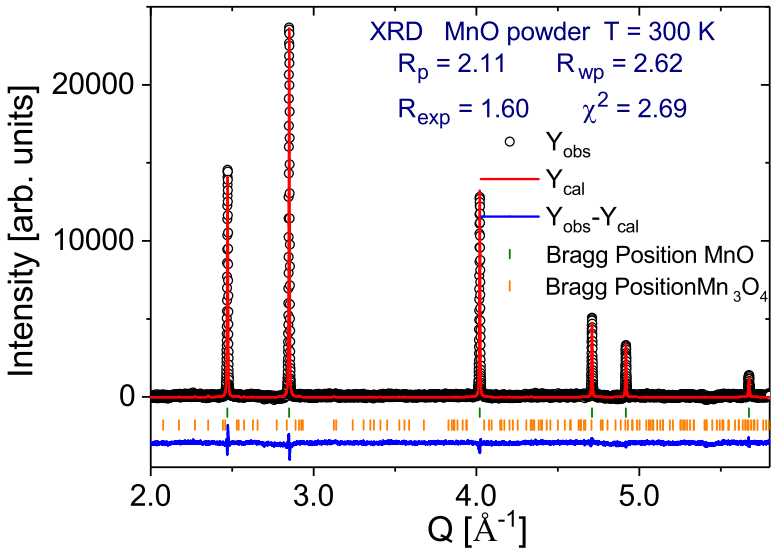

Figure 27: X-ray powder diffraction of the as-prepared MnO powder measured at room temperature. Y_{obs} is the observed pattern, Y_{cal} is the calculated pattern assuming the sample contains mainly MnO with 1 % Mn_3O_4 using the Rietveld method. The green and red bars mark the Bragg positions of MnO and Mn_3O_4, respectively.

The diffraction patterns of the as-prepared MnO powder and the single crystal (after milled into powder form) measured at room temperature are shown in Fig. 27 and 28, respectively. As can be seen, both patterns can be refined using the Rietveld method

with a space group $Fm\bar{3}m$ and a lattice parameter of $a = 4.44281(12)$ Å for the as-prepared MnO powder and $a = 4.44205(11)$ Å for the milled single crystal. In Fig. 27, the intensity is calculated considering 1% Mn_3O_4 is contained in the sample. No additional peak resulting from Mn_3O_4 can be obviously seen within the noise of background for both observed and calculated pattern. Therefore, no other phase with a ratio of more than 1% was detected in the sample.

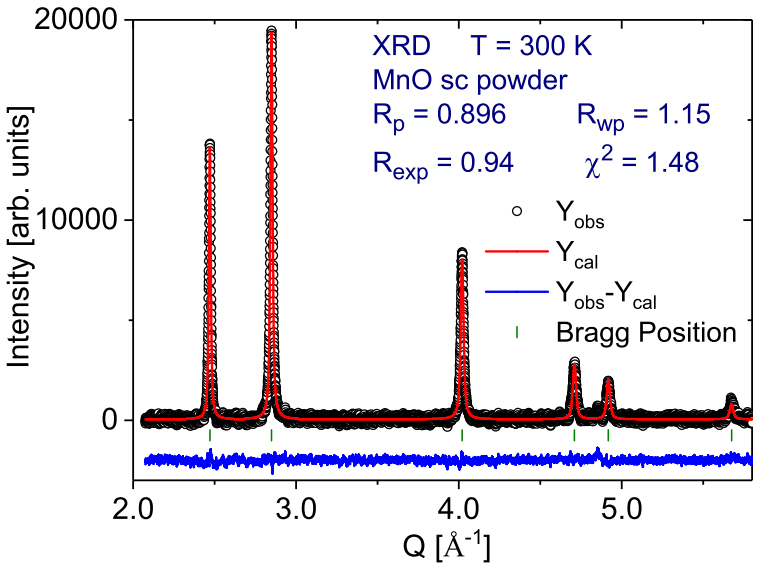

Figure 28: X-ray powder diffraction of the as-prepared MnO single crystal after milled into powder form measured at room temperature. Y_{obs} is the observed pattern, Y_{cal} is the calculated pattern using the Rietveld method.

As introduced in section 5.1, a cubic-to-rhombohedral distortion has been reported for MnO at the Néel temperature of 118 K. Due to the reduction of symmetry, some of the Bragg peaks may split below $T_N = 118$ K. This can be observed in the XRD patterns measured at 15 K as shown in Fig. 29 and 30 for MnO powder and the milled single crystal sample, respectively. Using the space groups reported in Ref. 57,58, the diffraction patterns could not be successfully refined.

Single crystal x-ray diffraction patterns performed for the as-prepared MnO single crystal are shown in Fig. 31. At room temperature, the Bragg reflections can be indexed by a fcc cubic lattice with a lattice constant of $a = 4.4386(2)$ Å. However, these reflections are relatively broad. Moreover, mosaic broadening can also be observed near the Bragg reflections. This might be due to different crystallites. At different positions of the single crystal, 2 - 3 crystallites have been observed using a Laue camera. Below T_N of MnO, additional peaks along the $\left[\frac{1}{2}\frac{1}{2}l\right]$, $\left[\frac{3}{2}\frac{3}{2}l\right]$, $\left[\frac{\bar{1}}{2}\frac{\bar{1}}{2}l\right]$, and $\left[\frac{\bar{3}}{2}\frac{\bar{3}}{2}l\right]$ directions can be observed at 90 K. Fig. 32 shows the line cuts along various directions. As can be seen, additional reflections can be observed with $l \approx \pm\frac{1}{2}, \pm\frac{3}{2}, \pm\frac{5}{2}$. This suggests a doubling of the unit cell along the [111] direction. However, the values for l are not exactly half-integer but slightly larger. Even though a structural distortion at the Néel temperature of MnO has been observed, a doubling of the unit cell has not been reported. These additional reflections

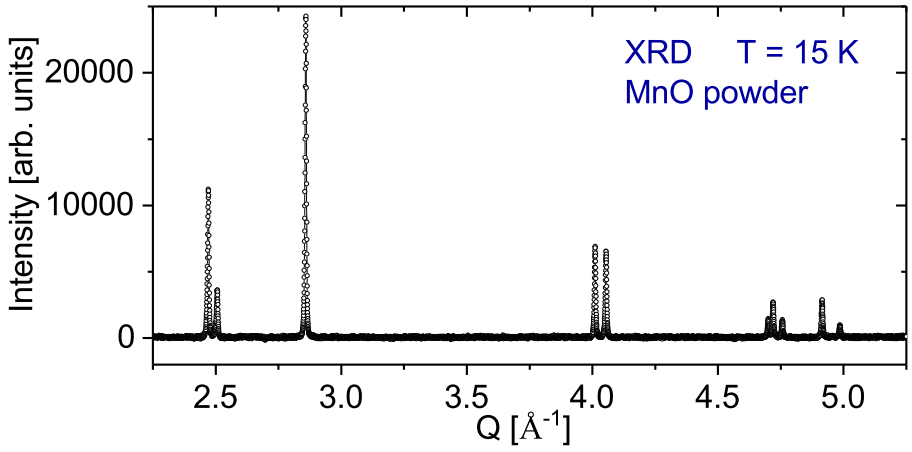

Figure 29: X-ray powder diffraction of the as-prepared MnO powder measured at 15 K.

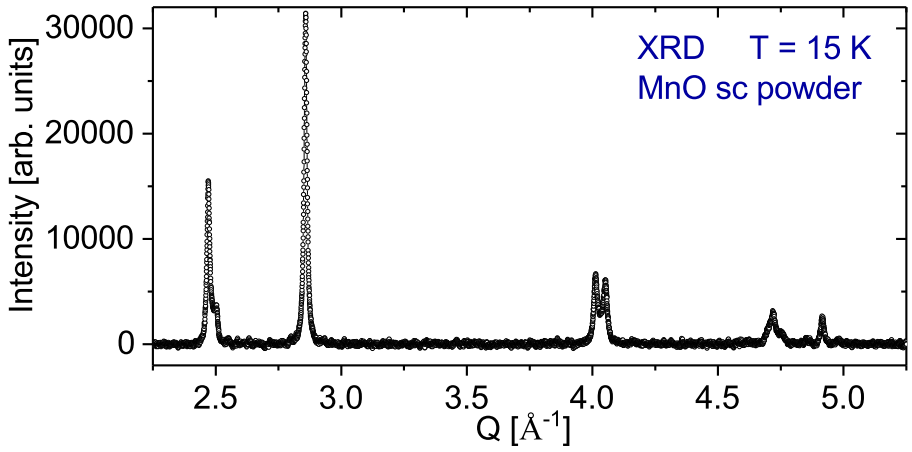

Figure 30: X-ray powder diffraction of the MnO single crystal after milled in powder form measured at 15 K.

observed at 90 K are possibly due to charge order of nonstoichiometric MnO.

In order to obtain single phase MnO bulk, the as-prepared samples were annealed. Due to a slight structural distortion because of the reduction of the oxygen content, the annealed samples show different degrees of splitting of the Bragg reflections. However, this is not the focus of this thesis. Therefore, XRD patterns of these samples are shown in appendix C.

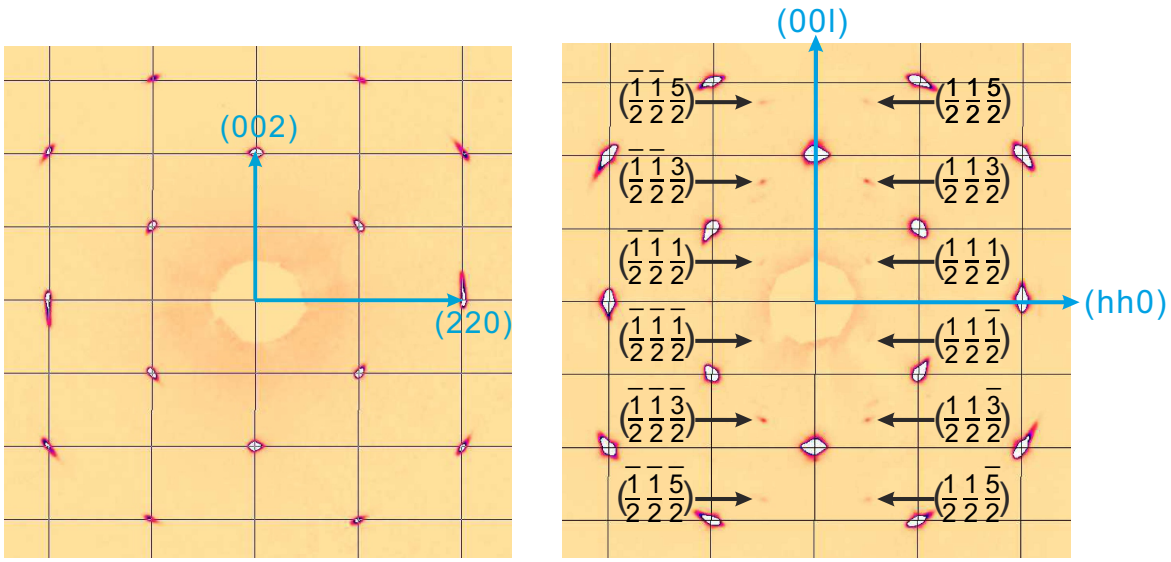

Figure 31: Single crystal diffraction pattern of the as-prepared MnO single crystal measured at (a) 300 K and (b) 90 K.

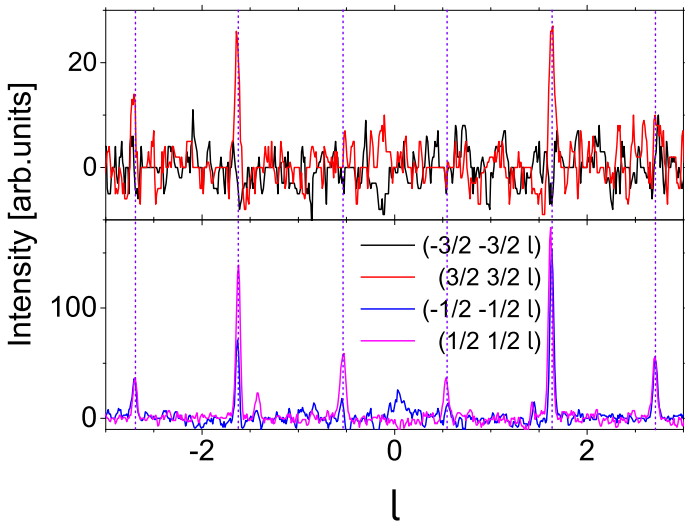

Figure 32: Intensity of the single crystal diffraction pattern measured along the $\left[\frac{1}{2}\frac{1}{2}l\right]$, $\left[\frac{3}{2}\frac{3}{2}l\right]$, $\left[\bar{\frac{1}{2}}\bar{\frac{1}{2}}l\right]$, and $\left[\bar{\frac{3}{2}}\bar{\frac{3}{2}}l\right]$ directions for the as-prepared MnO single crystal.

5.4 Experimental Results

5.4.1 As-prepared MnO Nanoparticles

The as-prepared MnO NPs with 12 nm diameter have already been studied in my master thesis using magnetometry and neutron scattering. The results have been published in Ref. 18. ZFC magnetization curves of the as prepared MnO NPs with 12 nm diameter show a low temperature peak at about 25 K. A feature indicating the Néel temperature of MnO (∼118 K) is missing. However, polarized neutron diffraction shows the vanishing of the AF order parameter of MnO at ∼120 K. Around the peak temperature of 25 K found in the ZFC curves, no obvious feature can be seen in the temperature dependence of the AF order parameter within error bars. This contradiction between the magnetometry and neutron scattering results can be explained using an antiferro-superparamagnetic (AF-SPM) model.

Similar to a SPM system, the Néel vector of MnO is "blocked" below the peak temperature T_p. Therefore, the AF order can be measured using neutron scattering. Magnetometry results show also signatures of the AF order. Above T_p, the Néel vector starts to fluctuate. For neutron scattering, a neutron probes a NP on a time scale of ∼ps. During the measurement time, the AF order of MnO still appears to be "blocked", and thus the AF order parameter does not vanish until its T_N. However, magnetometry probes the macroscopic magnetization within ∼s. During this time, the AF Néel vector of MnO fluctuates. As a result, the net magnetization decreases rapidly above T_p.

In addition, an EB effect and a reduction in the AF correlation length have also been observed, which can be explained by the existence of disordered surface spins or a FiM Mn_3O_4 shell.

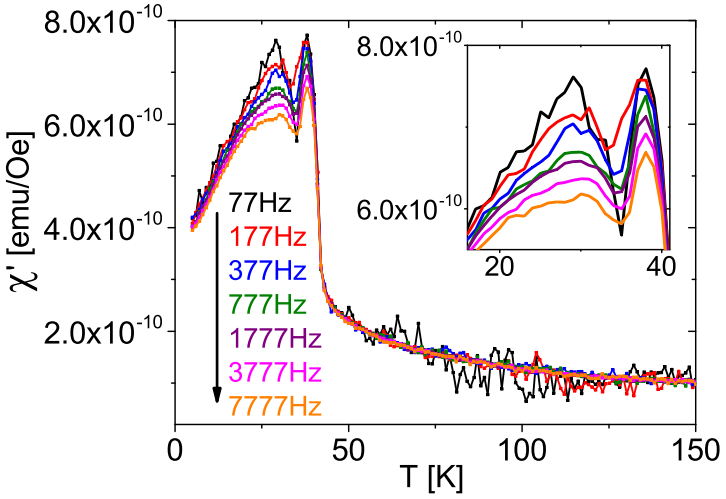

Figure 33: Ac-susceptibility vs temperature of MnO NPs with 12 nm diameter measured at various frequencies. The inset shows an enlarged view near the peaks. The ac excitation amplitude was 0.08 mT and H_{dc}=0.

In order to gain a better understanding of the dynamics of the AF-SPM behaviour of MnO NPs, ac-susceptibility measurements have been performed. Fig. 33 shows the temperature dependent ac-susceptibility of the as-prepared MnO NPs with 12 nm diameter measured at various frequencies. At about 28 and 37 K, two peaks can be observed. In

the enlarged view around these peaks (Fig. 33 inset), a weak frequency dependence can be seen for the first peak at ∼28 K. However, the second peak at ∼37 K shows no obvious frequency dependence. These two peaks have also been observed in the ZFC/FC magnetization curves at 5 mT [18]. The first peak at ∼28 K is relatively broad, and thus is explained to be originating from the AF-SPM MnO core. The second peak shows a steep drop above ∼38 K, which is often observed near a FM-to-PM phase transition. Moreover, the peak temperature (∼38 K) locates near the Curie temperature of Mn_3O_4 (43 K) or Mn_2O_3 (39 K). Hence the second peak is possibly coming from an oxidized Mn_3O_4 or Mn_2O_3 shell. The NP dispersion we used has a concentration of about 25mg/mL. We estimate that 1 μL NP dispersion is drop-casted on the substrate, i.e. 0.025 mg NPs is measured. Assuming the second peak results from bulk Mn_3O_4, its mass can be roughly estimated to be 0.002 mg. It means, that about 8% of Mn_3O_4 may show comparable magnetization as 92% of AF-SPM MnO.

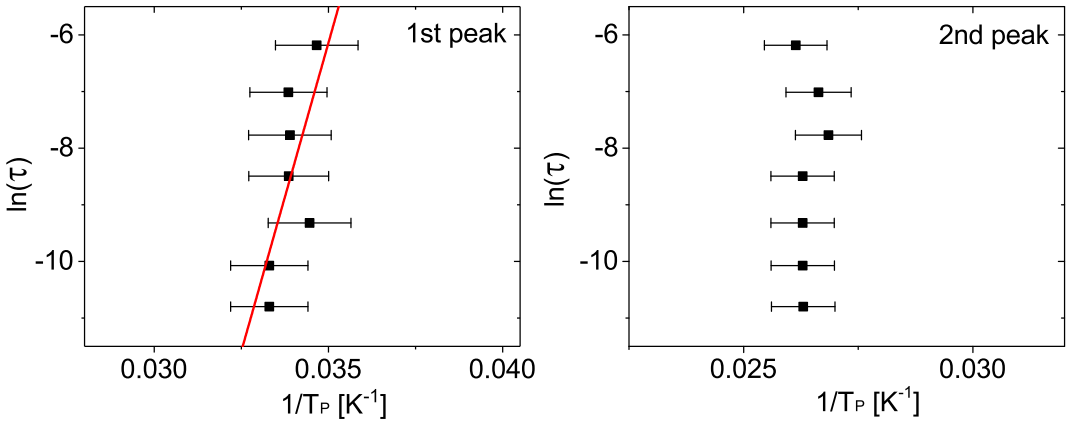

Figure 34: Relaxation time vs inverse peak temperature in a log-lin plot for (a) the first peak at ∼28 K and (b) the second peak at ∼38 K in the ac-susceptibility measurements. Black squares with error bars indicating the inverse peak temperature obtained from Fig. 33 at various frequencies. The red line is a linear fit.

As introduced in section 2.2.2, relaxation time is differently related to the blocking temperature or the freezing temperature of a SPM or SG/SSG system, respectively. The maximum in the ac-susceptibility vs temperature curves indicates the temperature, at which the relaxation time corresponds to the ac frequency. By fitting the frequency dependence of the peak temperature with various models discussed in section 2.2.2, a proper model to describe the magnetic behaviour of the system may be found. Fig. 34 shows the relaxation time versus the inverse peak temperature for the first (a) and the second (b) peak obtained from Fig. 33. The peak temperatures were determined from smoothed curves. As can be seen in Fig. 34(a), the first peak at ∼28 K shows a weak frequency dependence. From the fit (red line) of the data using the Arrhenius equation, $\tau_0 = 10^{-34} \pm 10^{15}$ s and $\frac{KV}{k_B} = 2205 \pm 1042$ K can be obtained. Neither of these constants can be realistic for a SPM system. For SPM systems, τ_0 usually ranges from 10^{-9}-10^{-12} s [103], and the energy barrier is at a much lower temperature $\frac{KV}{k_B}$. A fit using realistic values of τ_0 and $\frac{KV}{k_B}$ has been performed (Appendix D). However, the fit does not quite

match the experimental results even though the error bars are very large. Moreover, fits using other models described in section 2.2.2 have also been performed. However, no realistic values can be obtained from any of these models (data not shown). Therefore, the peak at ∼28 K cannot be explained by any model known for NP systems so far. This indirectly confirms that the low temperature peak at ∼28 K may be coming from an AF-SPM system. The second peak, in contrast, shows no obvious frequency dependence as expected for a FiM-PM transition in Mn_3O_4 or Mn_2O_3.

5.4.2 As-prepared MnO Bulk

The particular low temperature peak often observed at about 25 K in MnO NPs has usually been explained by either AF-SPM, SPM, SSG, diluted AF states, finite size or surface effects [3, 18, 19, 41, 92, 93]. However, this low temperature feature may also originate from intrinsic frustrated superexchange interactions in MnO, because a similar low temperature anomaly has also been reported for polycrystalline [73] and powder [78] MnO. Moreover, the spin structure of MnO is still not fully understood despite numerous investigations [56–58, 68, 73, 74, 104]. Therefore, MnO powder and a single crystal have been studied in this thesis to have a better understanding of the origin of the low temperature feature. In contrast to NPs, bulk MnO is ideal to study intrinsic magnetic properties of MnO. The effect of surface spins, which are only a very small fraction of all spins in bulk MnO, can be neglected.

MnO Powder

As-prepared MnO powder from Alfa Aesar GmbH has been studied in this thesis using magnetometry, susceptometry and neutron scattering. The results are compared with those of MnO NPs. Fig. 35 shows the (a) temperature and (b) field dependent magnetization curves of the as-prepared MnO powder. ZFC/FC magnetization curves measured at various magnetic fields show the expected feature at the Néel temperature of MnO (∼118 K). Interestingly, a broad peak at about 30 K is also found. This low temperature peak observed in MnO powder has a similar shape as the peak often found in MnO NPs at ∼25 K, which is much different from the sharp peak usually observed at the Curie temperature of FM/FiM systems, such as the second peak shown in Fig. 33 at ∼40 K due to oxidized FiM Mn_3O_4 or Mn_2O_3. Therefore, this low temperature peak in the ZFC curves of MnO powder is possibly coming from either particles with grain sizes in nanometer range or is intrinsic MnO. Moreover, this peak temperature shows a weak field dependence until 1 T, which is similar to that found in MnO NPs [18]. Above 7 T, this peak disappears. This can be expected for an AF-SPM system as described above. ZFC and FC curves measured at 50 mT coincide at 300 K, which is the highest temperature recorded for the ZFC curve (data not shown). Before the FC curve is measured, an equilibrium state is possibly not reached. The magnetization continues relaxing while cooling down within a magnetic field, thus a higher magnetization is measured at the beginning of the FC curve compared to that measured at the same temperature in the ZFC curve. Therefore, the ZFC and FC curves split already at 300 K.

Field dependent magnetization curves of MnO powder have been studied at 5 K after field cooling at various magnetic fields (Fig. 35(b)). The centers of the hysteresis loops are slightly shifted towards negative field direction. This phenomenon indicates an EB effect, which is usually found on the interface between an AF and a FM. Exchange coupling

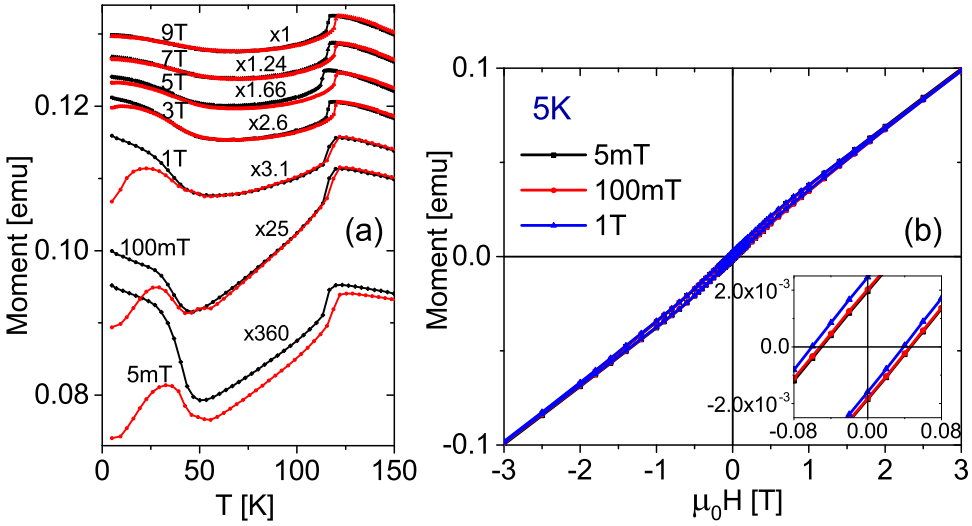

Figure 35: (a) ZFC/FC magnetization curves measured at various magnetic fields. (b) Hysteresis loops of the as-prepared MnO powder measured at 5 K after cooled at various magnetic fields. Inset in (b) shows an enlarged view around the origin.

between AF MnO and FiM Mn_3O_4 / Mn_2O_3 or disordered surface spins in nano-sized MnO particles can lead to an EB effect. This may explain the EB effect found in MnO powder in analogy to MnO NPs. As shown in section 5.3, no obvious reflections indicating other phases of manganese oxide were found in the XRD pattern of this sample. However, the existence of Mn_3O_4 cannot be excluded, because less than 1% of other phases of manganese oxide cannot be detected within the sensitivity of the instrument. Moreover, the EB field H_{ex} found in the powder sample at 5 K increases slightly with an increase in the cooling field as expected for most EB systems [31–33].

To further study the feature found at low temperature in the MnO powder, memory effect measurements have been performed. After subtracting a ZFC curve with a pause of 10000 s at 24 K (marked as ZFC') by a regular ZFC curve, a peak can be seen at ∼24 K in the difference (Fig. 36), even though the error bar is relatively large. This indicates a memory effect, which is usually found in SG or SSG systems. However, a memory effect has also been observed in MnO NPs. This confirms the hypothesis that the low temperature feature observed in the as-prepared MnO powder originates from nano-sized MnO particles.

An accurate study on the AF order parameter near the low temperature feature was not possible for MnO NPs due to the extremely small amount of sample [18]. However, this study can be achieved by performing polarized neutron powder diffraction with the as-prepared MnO powder assuming the low temperature peak found in the ZFC curves comes from nano-sized MnO particles. Fig. 37(a) shows the separated contributions of the as-prepared MnO powder measured at the DNS-instrument at 4 K. The expected magnetic $\left(\frac{1}{2}\frac{1}{2}\frac{1}{2}\right)$ and nuclear (111) Bragg peaks can be observed at Q = 1.2 and 2.4 Å, respectively. The AF order parameter of this sample has been studied by measuring the temperature dependence of the magnetic $\left(\frac{1}{2}\frac{1}{2}\frac{1}{2}\right)$ Bragg peak. Fig. 37(b) shows the integrated intensity of this Bragg peak vs temperature. As expected, the AF order parameter of MnO powder vanishes at the Néel temperature of 118 K. However, near the peak temperature observed in the ZFC curves (∼30 K), no feature is found within error bars. This observation

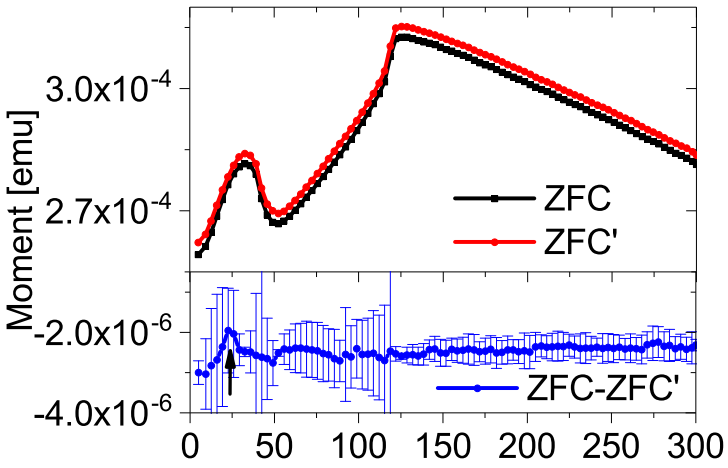

Figure 36: Memory effect of the as-prepared MnO powder. The black curve is a regular ZFC curve measured at 5 mT, the red curve is measured during warming up in a magnetic field of 5 mT after cooling in zero magnetic field with a pause of 10000 s at 24 K arrow (ZFC'). The blue curve shows the difference between the black and the red curve. A peak near the stopping temperature in the blue curve indicates a memory effect, which is the case here.

confirms our conclusion for MnO NPs, i.e. that the neutron scattering experiment does not show a feature at low temperature because of the different probing time scales. Moreover, the AF-order parameter depending on the temperature is fitted with a mean field model with J=5/2 (Appendix. E). A "virtual" $T_N = 170$ K is obtained, which is much higher than the real $T_N = 170$ K. Such phenomenon might be observed for a first order phase transition, where a jump at T_N is expected.

Moreover, the intensity at the Q-value of the magnetic $\left(\frac{1}{2}\frac{1}{2}\frac{1}{2}\right)$ peak was measured during warming up within a magnetic guide field of about 0.7 mT after a zero field cooling procedure (ZFC). The result is then compared with the curves measured during a field cooling (FC) or field warming (FW) procedure at 3 mT. As can be seen in Fig. 37(c), again no feature can be observed at low temperature ($\sim$30 K) in any of these curves. Moreover, no obvious difference can be seen in the AF order parameter during ZFC, FC and FW procedures.

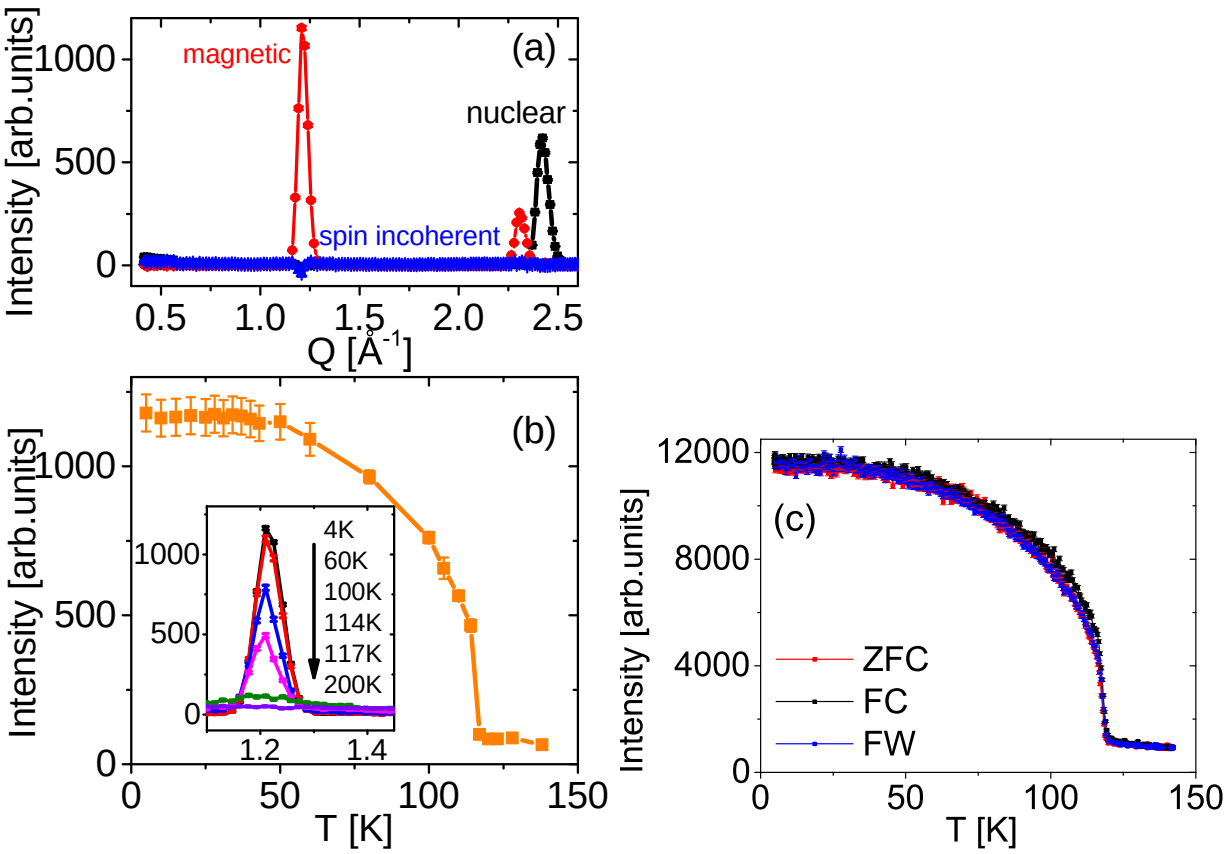

Figure 37: (a) Nuclear coherent (black), nuclear spin-incoherent (blue) and magnetic (red) components of the as-prepared MnO powder from polarized neutron scattering measured at 4 K. (b) Temperature dependence of the integrated intensity of the AF $\left(\frac{1}{2}\frac{1}{2}\frac{1}{2}\right)$ Bragg peak. The orange squares with error bars represent the integrated intensity of the AF $\left(\frac{1}{2}\frac{1}{2}\frac{1}{2}\right)$ Bragg peak. The inset in (b) shows the magnetic $\left(\frac{1}{2}\frac{1}{2}\frac{1}{2}\right)$ Bragg peaks at different temperatures. (c) Temperature dependence of the intensity at the Q-value of the AF $\left(\frac{1}{2}\frac{1}{2}\frac{1}{2}\right)$ Bragg peak measured after a zero field cooling procedure, or during a FC / FW procedure at a magnetic field of 3 mT.

For the comparison with MnO NPs, the ac-susceptibility of the as-prepared MnO powder was measured (Fig. 38). At the bulk Néel temperature of MnO, a kink showing no obvious frequency dependence can be observed. This is expected for an AF system. Moreover, a low temperature peak as found in the ZFC curves can also be observed. This peak shows a very weak frequency dependence, which is similar to that measured for MnO NPs. Due to their much larger sizes ($\sim$ a few hundred nm) compared to the NP sample (12 nm), the frequency dependence of this low temperature peak looks more bulk-like, which shows no obvious frequency dependence. This further confirms that the low temperature peak may originate from nano-sized MnO.

Heat capacity measurement is sensitive to both magnetic and structural phase transitions. In order to investigate whether the low temperature peak observed in the as-prepared MnO powder results from a phase transition or from just a crossover between the blocked and fluctuated AF-SPM states, heat capacity measurements have been performed. As can be seen in Fig. 39(a), only a peak at the bulk Néel temperature of MnO

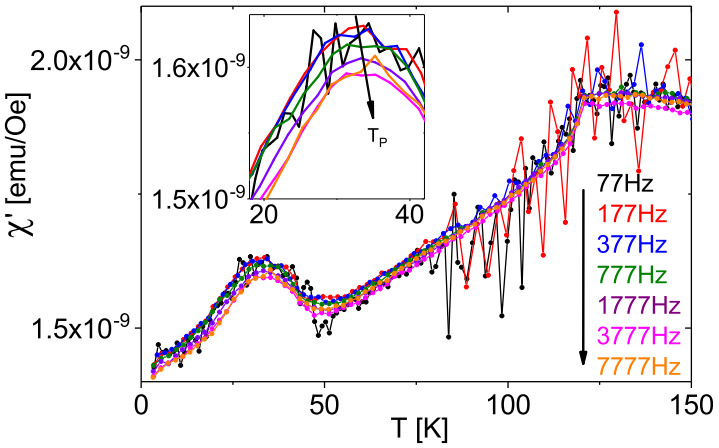

Figure 38: Ac-susceptibility vs temperature of the as-prepared MnO powder measured at various frequencies. The ac excitation amplitude is 0.08 mT and H_{dc}=0.

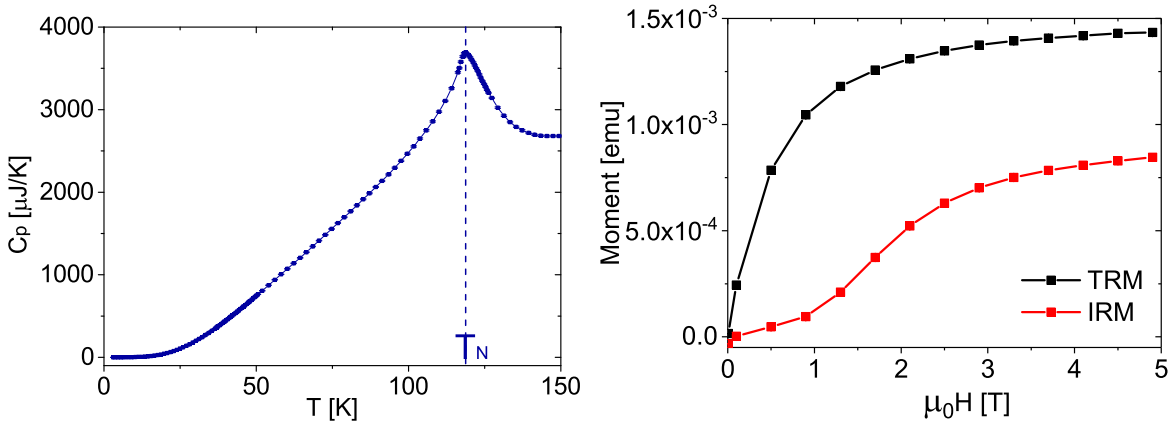

Figure 39: (a) Heat capacity, and (b) TRM/IRM measurements of the as-prepared MnO powder.

is found. At low temperatures, no feature can be observed. This suggests that the low temperature peak observed in the ZFC curves does not likely indicate a phase transition.

To have a better understanding of the AF-SPM behaviour in both MnO NPs and powder, TRM/IRM measurements have been performed (Fig. 39(b)). For a perfect AF, both TRM and IRM curves remain zero. However, both TRM and IRM curves increase with an increase in the magnetic field. Moreover, the magnetic moments in both TRM and IRM magnetization curves are not saturated even at a magnetic field of 5 T. This is similar as observed in MnO NPs. Similar behaviour has already been reported for Co_3O_4 nanowires [3], which is explained by a 2D DAFF (two-dimensional diluted antiferromagnet in a field) system.

MnO Single Crystal

As discussed above, the magnetic behaviour of the as-prepared MnO powder is likely to be influenced by nano-sized particles. The results shown above are useful to understand the nano-size effect on MnO. However, single phase MnO is interesting for the study of magnetic properties of bulk MnO and its intrinsic properties. In order to discriminate between intrinsic and nanosize properties, a piece of MnO single crystal (Surface Net GmbH) was investigated as reference. The results are compared with those on MnO NPs and powder.

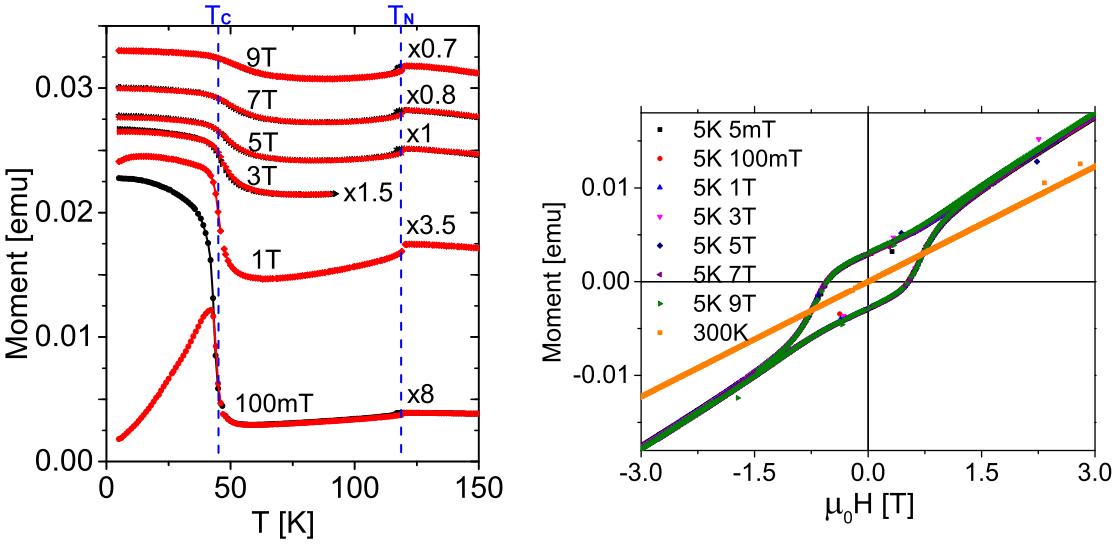

(a) (b)

Figure 40: (a) ZFC/FC magnetization curves measured at various magnetic fields. (b) Hysteresis loops after cooling at various magnetic fields measured at 5 K and 300 K for the as-prepared MnO single crystal.

Fig. 40(a) shows the ZFC/FC magnetization curves of the as-prepared MnO single crystal measured at various magnetic fields. Surprisingly, a low temperature peak at ∼40 K is also found in additional to the expected feature at 118 K indicating the AF-to-PM phase transition of bulk MnO. The peak at ∼40 K is relatively sharp compared to that observed in MnO NPs and powder. The steep slope above the peak temperature is more likely due to a FM/FiM-to-PM phase transition. Moreover, the peak temperature of 40 K is close by the Curie temperature of Mn_3O_4 (43 K) or Mn_2O_3 (39 K). Therefore, the as-prepared MnO single crystal is possibly not single phase MnO, but partially oxidized to Mn_3O_4 or Mn_2O_3. However, in both x-ray diffraction and x-ray fluorescence analysis on this single crystal, no impurities were found. At higher magnetic fields, the sharp phase transition is smeared out. This phenomenon can be found in FM/FiM systems. This can be confirmed by the hysteresis loops shown in Fig. 40(b). As can be seen, the single crystal shows hysteresis loops at 5 K with a coercive field H_c of ∼1 T. This is possibly coming from regions, which are partially oxidized to Mn_3O_4 or Mn_2O_3. At 300 K, only a linear increase is observed. Above the Curie temperature, Mn_3O_4 or Mn_2O_3 show PM behaviour. For AF MnO, a monotonic increase up to 3 T is expected, because a much higher magnetic field is required to saturate the magnetization of bulk MnO. However, in contrast to the results observed on MnO powder and NPs, no EB effect is found in the

hysteresis loops of MnO single crystal. This indicates, that AF MnO and the oxidized Mn_3O_4 or Mn_2O_3 are not strongly coupled. Moreover, hysteresis loops of MnO single crystal show no difference after a FC procedure within various magnetic fields.

In order to further study the low temperature peak at ∼40 K found in the ZFC curves of the single crystal, polarized neutron single crystal diffraction has been performed. After characterizing the orientation of the crystal using a Laue camera, it was fixed on the sample holder so that the $(1\bar{1}0)$ axis is perpendicular to the scattering plane. As discussed in section 2.4.3, both y- and z-components of the magnetic contribution are measured in the spin-flip (SF) channel and the full nuclear coherent contribution is measured in the non-spin-flip (NSF) channel, when the polarization of the neutrons is parallel to the scattering vector. The magnetic contribution along the x-direction, which is parallel to the scattering vector, cannot be measured.

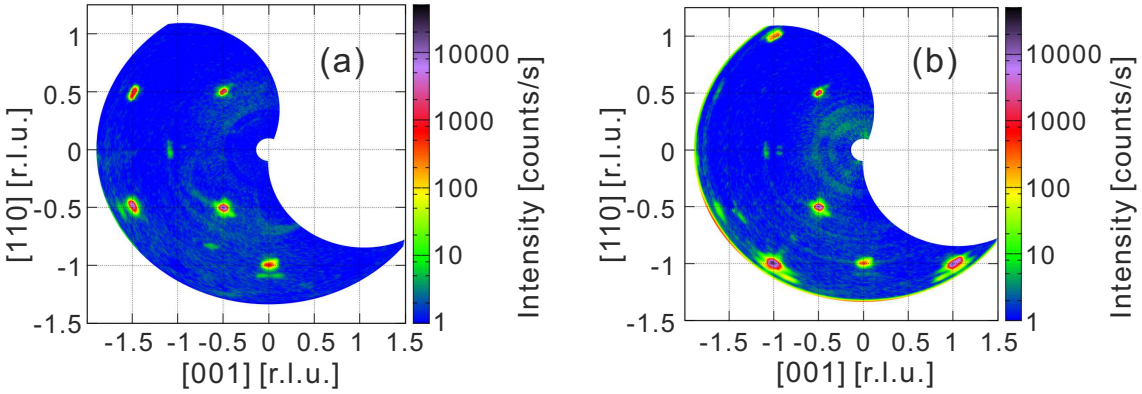

Figure 41: (a) SF and (b) NSF channels of the polarized neutron diffraction pattern of the as-prepared MnO single crystal measured at 4 K.

After the background, flipping ratio and detector efficiency corrections, the magnetic contribution of the single crystal with 2/3 of the nuclear spin incoherent background is shown in the SF channel (Fig. 41(a)) and the nuclear contribution with 1/3 of the nuclear spin incoherent background is shown in the NSF channel (Fig. 41(b)). These results were measured at 4 K, which is below the AF-to-PM phase transition of MnO. AF $\left\{\frac{1}{2}\frac{1}{2}\frac{1}{2}\right\}$ as well as the $\left\{\frac{1}{2}\frac{1}{2}\frac{3}{2}\right\}$ Bragg peaks can be observed in the SF channel. The nuclear $\{111\}$ peaks are found in the NSF channel. Moreover, a cubic-to-rhombohedral structural transition is reported accompanying the magnetic phase transition at the Néel temperature of MnO. Therefore, additional peaks such as $\{00\overline{1.1}\}$ and $\{\bar{1}\bar{1}0\}$ can also been found.

Interestingly, nuclear $\left\{\frac{1}{2}\frac{1}{2}\frac{1}{2}\right\}$ peaks have also been found in the NSF channel, which indicates a doubling of the lattice parameter along the [111] direction. This effect has also been observed in the x-ray single crystal diffraction. However, x-ray powder diffraction of the milled MnO single crystal shows no peak at the expected Q-value for the $\left(\frac{1}{2}\frac{1}{2}\frac{1}{2}\right)$ peak. These $\left\{\frac{1}{2}\frac{1}{2}\frac{1}{2}\right\}$ nuclear peaks might be originating from the arrangement of Mn_3O_4 layers between different MnO twins. Below T_N of MnO, the fcc structure of MnO is distorted. A doubling of the unit cell along the crystallographic [111] direction may occur randomly in combination with the Mn_3O_4 layers. Moreover, these half-integer peaks have much lower intensity in the XRD pattern than that in neutron diffraction. They are possibly because of the charge order due to the non-stoichiometric MnO.

The temperature dependence of the intensity detected in the SF and NSF channels at

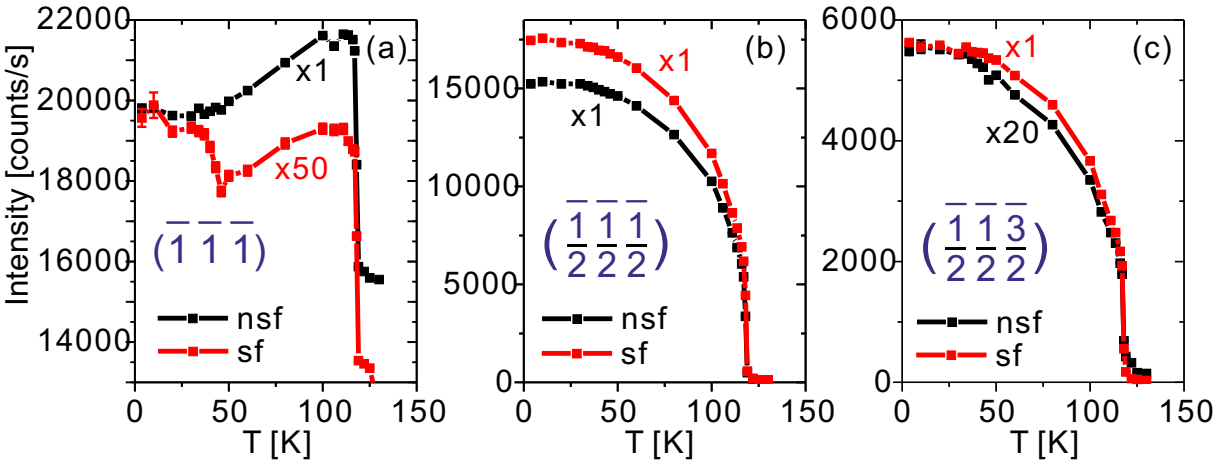

Figure 42: Temperature dependence of the intensities in the SF and NSF channel at the position of (a) $(\bar{1}\bar{1}\bar{1})$, (b) $\left(\frac{\bar{1}}{2}\frac{\bar{1}}{2}\frac{\bar{1}}{2}\right)$, and (c) $\left(\frac{\bar{1}}{2}\frac{\bar{1}}{2}\frac{\bar{3}}{2}\right)$ Bragg peaks of the as-prepared MnO single crystal.

the position of the $(\bar{1}\bar{1}\bar{1})$, $\left(\frac{\bar{1}}{2}\frac{\bar{1}}{2}\frac{\bar{1}}{2}\right)$, and $\left(\frac{\bar{1}}{2}\frac{\bar{1}}{2}\frac{\bar{3}}{2}\right)$ Bragg peaks of MnO single crystal are shown in Fig. 42. The SF channels at both positions of the $\left(\frac{\bar{1}}{2}\frac{\bar{1}}{2}\frac{\bar{1}}{2}\right)$, and the $\left(\frac{\bar{1}}{2}\frac{\bar{1}}{2}\frac{\bar{3}}{2}\right)$ Bragg peaks show the expected vanishing of the AF order parameter of MnO at ∼118 K. By fitting the temperature dependent curves of these Bragg peaks using a mean field model with $J = 5/2$, a virtual higher "T_N" is found (Appendix E). This indicates a first order phase transition. Similar behaviour has also been found in the NSF channels at the positions of the $\left(\frac{\bar{1}}{2}\frac{\bar{1}}{2}\frac{\bar{1}}{2}\right)$, and the $\left(\frac{\bar{1}}{2}\frac{\bar{1}}{2}\frac{\bar{3}}{2}\right)$ Bragg peaks.

At the positions of the $\left(\frac{\bar{1}}{2}\frac{\bar{1}}{2}\frac{\bar{3}}{2}\right)$ Bragg peak, the intensity is very low in the NSF compared to the the intensity measured in the SF channel, which is possibly due to an imperfect flipping ratio correction or multiple scattering. Compared to this peak, the intensity of the $\left(\frac{\bar{1}}{2}\frac{\bar{1}}{2}\frac{\bar{1}}{2}\right)$ Bragg peak much stronger, which is opposite to the results measured by x-ray, where the $\left(\frac{\bar{1}}{2}\frac{\bar{1}}{2}\frac{\bar{3}}{2}\right)$ peak is stronger. However, the intensity measured in the NSF channel at the position of the $\left(\frac{\bar{1}}{2}\frac{\bar{1}}{2}\frac{\bar{1}}{2}\right)$ Bragg peak has almost the same intensity as in the SF channel. This suggest a doubling of the lattice constant along the crystallographic [111] direction associated with the AF-to-PM phase transition. At the position of the $(\bar{1}\bar{1}\bar{1})$ peak of MnO, the NSF channel shows a steep drop above ∼118 K. Below 118 K, the intensity also decreases. This can be explained by the extinction effect due to the structural distortion of MnO below its Néel temperature. Similar behaviour has also been observed in the SF channel above 50 K at the position of the $(\bar{1}\bar{1}\bar{1})$ peak of MnO. However, the intensity is much lower, which is again possibly due to an imperfect flipping ration correction or multiple scattering.

Moreover, a small feature at about 40 K can be observed in the SF channel before background, flipping ratio and detector efficiency corrections (Fig. 42(a)). The intensity drops above ∼40 K, which matches the peak temperature found in the ZFC magnetization curves. Moreover, this feature has an overall shape of a typical FM order parameter. The $(\bar{1}\bar{1}\bar{1})$ Bragg peak of MnO is located near the expected Q-value of the (2 0 2) and (2 1 1)

Bragg peaks of FiM Mn_3O_4. Taking the broadening of the Bragg peaks into account, this feature found at the position of the $(\bar{1}\bar{1}\bar{1})$ Bragg peak of MnO might be due to the FiM transition of Mn_3O_4, which is oxidized from MnO at twin boundaries.

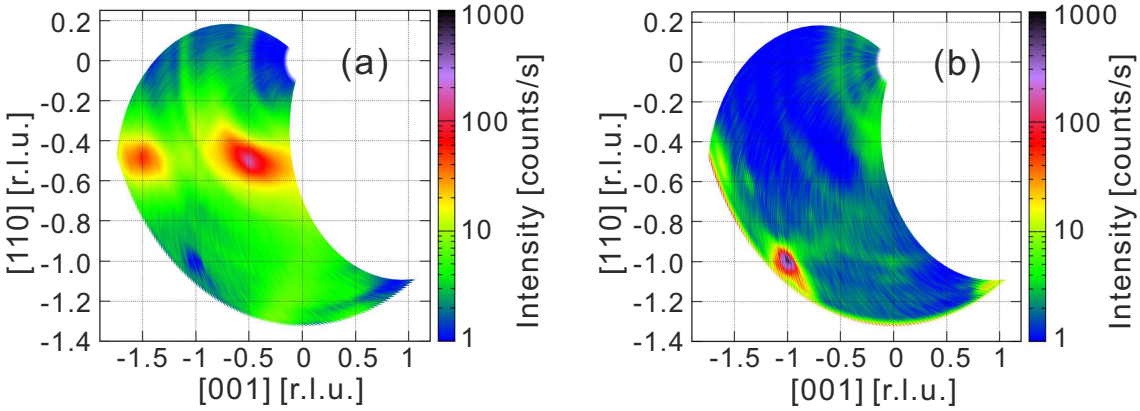

Figure 43: (a) SF and (b) NSF channels of the polarized neutron diffraction pattern of the as-prepared MnO single crystal measured at 121 K.

For comparison, polarized neutron diffraction has been performed above the Néel temperature of MnO (Fig. 43). At 121 K, diffuse scattering can be observed at the position of the magnetic $\left(\frac{1}{2}\frac{1}{2}\frac{1}{2}\right)$, and $\left(\frac{1}{2}\frac{1}{2}\frac{3}{2}\right)$ Bragg peaks in the SF channel. In the NSF channel only the expected (111) nuclear peak is found. Other reflections have been extinct due to the symmetry of the cubic structure.

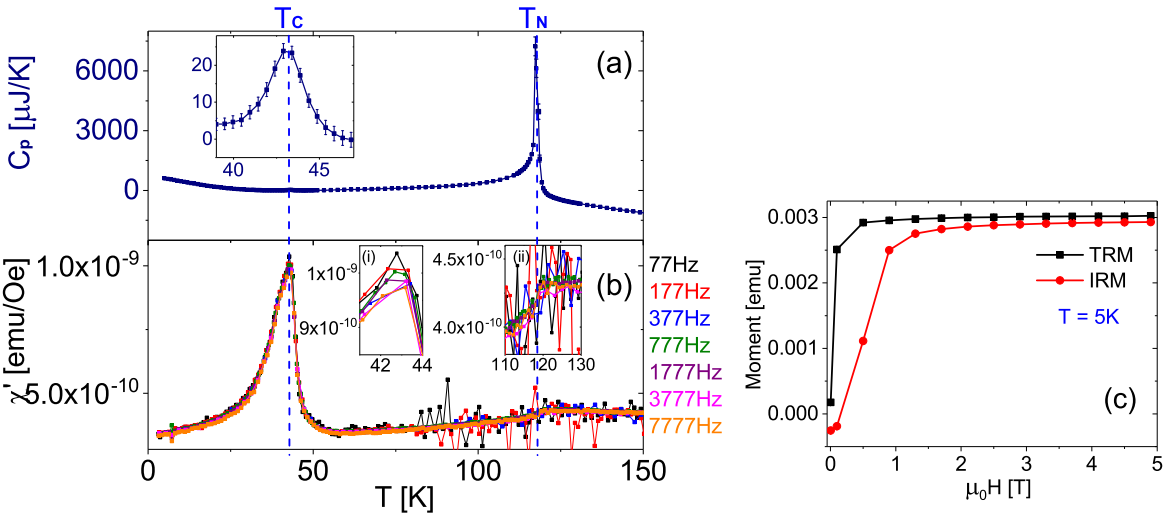

Figure 44: (a) Heat capacity, (b) ac-susceptibility and (c) TRM/IRM measurements of the as-prepared MnO single crystal.

Further studies have been performed to gain a better understanding of the low temperature feature observed in the single crystal. Temperature dependent heat capacity curve has been measured for the single crystal. As can be seen in Fig. 44(a), features at both the peak temperature of ∼40 K and the Néel temperature of MnO can be observed. This suggest that the low temperature peak in the MnO single crystal marks a real phase transition rather than a crossover from a blocked to a fluctuated AF-SPM state as in MnO

powder and NPs. The matching of the peak temperature with the Curie temperature of Mn_3O_4 further confirms the existence of oxidized Mn_3O_4 inside the MnO single crystal. The peak at T_N of MnO shows an asymmetric form, which is due to a latent heat released above the phase transition. Therefore, the AF-to-PM transition of MnO is likely to be first order.The shape of the peak at T_C of Mn_3O_4 is relatively symmetric, which marks a continuous second order phase transition.

Moreover, ac-susceptibility measurements have been performed at various frequencies. Similar to features observed in the ZFC curves, two peaks can be found in the ac-susceptibility measurements. Both peaks mark the Curie temperature of Mn_3O_4 ($\sim$40 K) and the Néel temperature of MnO ($\sim$118 K) and show no frequency dependence as expected. TRM/IRM curves have also been measured at 5 K. Both curves show an increase with the increasing magnetic field. Different from that observed in MnO powder and NPs, both TRM and IRM curves of MnO single crystal reach the saturation at about 2 T. This behaviour is possibly due to partially oxidized FiM Mn_3O_4 in additional to the vanishing magnetization of AF MnO.

5.4.3 Annealed MnO

As discussed above, all the as-prepared MnO NPs, powder, and the single crystal show particular features at low temperature either due to nano-size effect or possible higher oxidation states. In order to study the magnetic properties from MnO intrinsic to be compared with the results of NPs as well as the magnetic behaviours of manganese oxide NPs with different phases, various annealing procedures have been performed (Tab. 1).

MnO Powder

Literature shows success in removing higher oxidation states to obtain single phase MnO by annealing the sample in various environments [79, 82]. Various parameters, such as temperature, heating time as well as gas environment (vacuum, Ar and nitrogen) have been varied in this thesis to find the best condition to obtain single phase MnO. The following procedure shows the best results in obtaining pure MnO. By heating the as-prepared MnO powder at 920°C in vacuum for 150 h, Mn_3O_4 can be removed. Then the temperature is increased to 1000°C and held constant for several hours to avoid the re-oxidation after cooling down to room temperature.

Fig. 45 shows the magnetization and ac-susceptibility results of the annealed MnO powder. As can be seen in both ZFC/FC curves (a) and ac-susceptibility (b), no feature can be observed at low temperature. This also confirms that the low temperature feature found in the as-prepared MnO powder is not likely to originate from MnO as intrinsic feature. Moreover, the field dependent magnetization curve of the annealed powder measured at 10 K shows the expected behaviour for an AF. No opening is found near the origin (Fig. 45(c)).

The disappearance of the low temperature peak in the annealed powder is possibly due to the sintering of MnO during the annealing procedure. As can be seen in Fig. 46(a), the powder has an average size of $\sim 3\mu$m. However, particles with a few hundred nanometer size can also be observed. After annealing (Fig. 46(b)), particles with almost uniform structure and similar sizes ($\sim 3\mu$m) can be found.

For comparison with the as-prepared MnO powder, polarized neutron diffraction has been performed for the powder after the annealing procedure. Fig. 47(a) shows the mag-

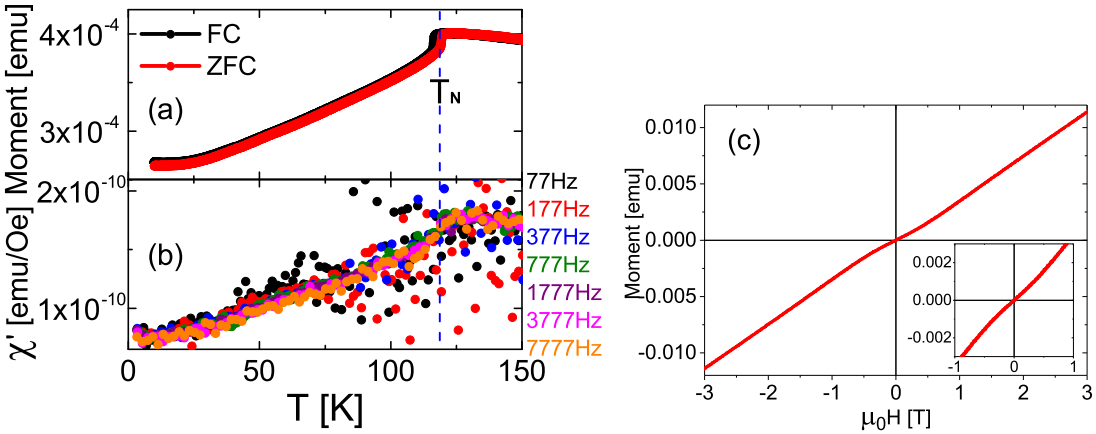

Figure 45: Magnetometry measurements performed with the MnO powder annealed at 920°C for 150 h to be compared with Fig. 35 and 38 for the as-prepared powder. (a) ZFC/FC magnetization curves measured at 100 mT[65], (b) ac-susceptibility with an excitation amplitude of 0.08 mT, and (c) hysteresis loops measured at 10 K after cooling in a magnetic field of 100 mT. Inset in (b) shows an enlarged view near the origin.

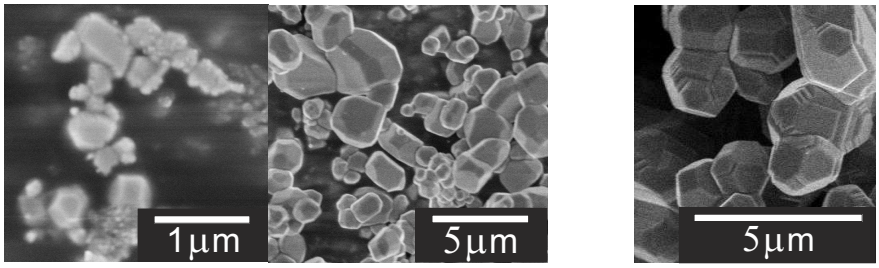

(a) (b)

Figure 46: SEM images of (a) the as-prepared MnO powder and (b) MnO powder after annealing at 920°C for 150 h.

netic (red), nuclear (black) and nuclear spin incoherent (blue) contributions. As observed for the as-prepared powder, magnetic $\left(\frac{1}{2}\frac{1}{2}\frac{1}{2}\right)$ and $\left(\frac{1}{2}\frac{1}{2}\frac{3}{2}\right)$ Bragg peaks as well as the nuclear (111) Bragg peak can be found at Q = 1.25, 2.3, and 2.5 Å, respectively. The temperature dependence of the magnetic $\left(\frac{1}{2}\frac{1}{2}\frac{1}{2}\right)$ Bragg peak is shown in Fig. 47(b). Similar to the as-prepared powder, the annealed powder shows only the vanishing of the AF order parameter at ∼120 K. The AF order parameter depending on the temperature is fitted using a mean field model with J=5/2 (Appendix E). A "virtual" T_N, which is much higher than 118 K, is obtained. This indicates a first order phase transition.

MnO Single Crystal

The same annealing procedure has also been applied to the as-prepared MnO single crystal. However, single phase MnO in the "single crystal" has not been achieved. After annealing, the crystal shows either metallic colour or cannot be found any more in the crucible. It might be chemically reacted with the crucible.

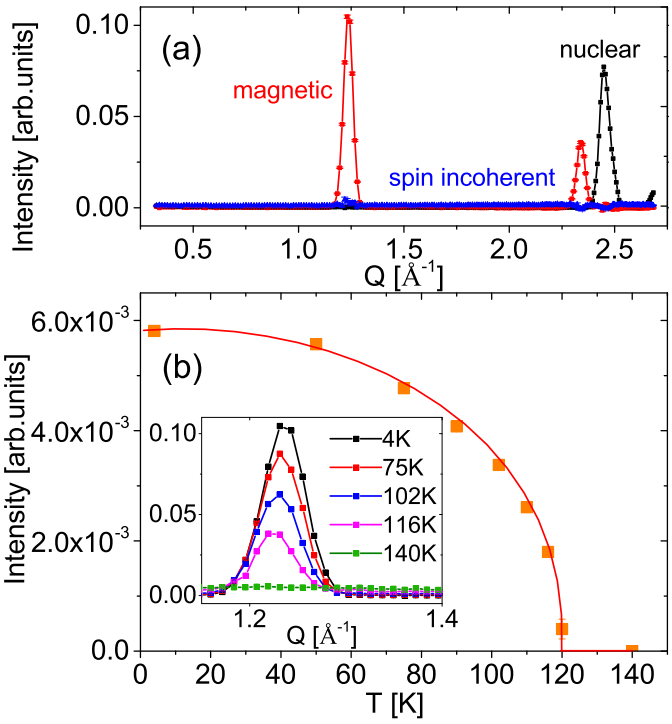

Figure 47: (a) Nuclear coherent (black), nuclear spin-incoherent (blue) and magnetic (red) components of the polarized neutron diffraction of MnO powder after annealing at 920°C for 150 h measured at 4 K. (b) Temperature dependence of the integrated intensity of the AF $\left(\frac{1}{2}\frac{1}{2}\frac{1}{2}\right)$ Bragg peak. The orange squares represent the intensity of the AF $\left(\frac{1}{2}\frac{1}{2}\frac{1}{2}\right)$ Bragg peak with error bars and the red line is a guide to the eye. Inset in (b) shows the magnetic $\left(\frac{1}{2}\frac{1}{2}\frac{1}{2}\right)$ Bragg peak at different temperatures.[65]

MnO Nanoparticles

After the success in obtaining pure MnO powder, the annealing procedure has also been applied to MnO NPs. Considering the small size of NPs, as well as the stability of the oleic acid shell surrounding the NPs, the NPs were only heated up to a maximum temperature of 330°C. The NPs with 12 nm diameter were chosen, so that the results can be compared with previous studies.

As introduced before, MnO can be easily oxidized to higher oxidation states. Therefore, a Mn_2O_3 or Mn_3O_4 shell is often found at the surface of MnO NPs. After the sample is stored in air for 4 years, the 12 nm NPs were remeasured using magnetometry to be compared with that of the as-prepared sample. Fig. 48 shows the comparison of the ZFC/FC curves measured at a magnetic field of 5 mT. Instead of the broad peak observed at ∼25 K in ZFC curves of the as-prepared NPs [18], a relatively sharp peak at ∼40 K can be seen. This can be explained by a higher fraction of the oxidized Mn_3O_4 in the NPs, which dominates the magnetic behaviour at small magnetic fields.

In order to vary the phase of manganese oxide, these aged NPs were annealed in vacuum or in air to achieve lower or higher oxygen contents, respectively. After the as-prepared NPs were heated at 310°C in vacuum for 3.5 h, the peak temperature decreases to ∼25 K as can be seen in Fig. 49(a). This peak becomes relatively broad compared to that before annealing and shows a similar behaviour as found in the ZFC curves of the as-prepared NPs [18]. This indicates a tendency towards almost pure MnO NPs.

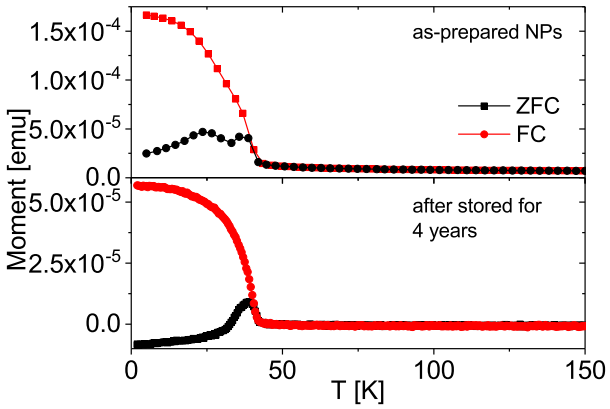

Figure 48: Comparison of the ZFC and FC magnetization curves measured at 5 mT for MnO NPs with 12 nm diameter. (a) As-prepared sample, (b) after being stored in air for 4 years.

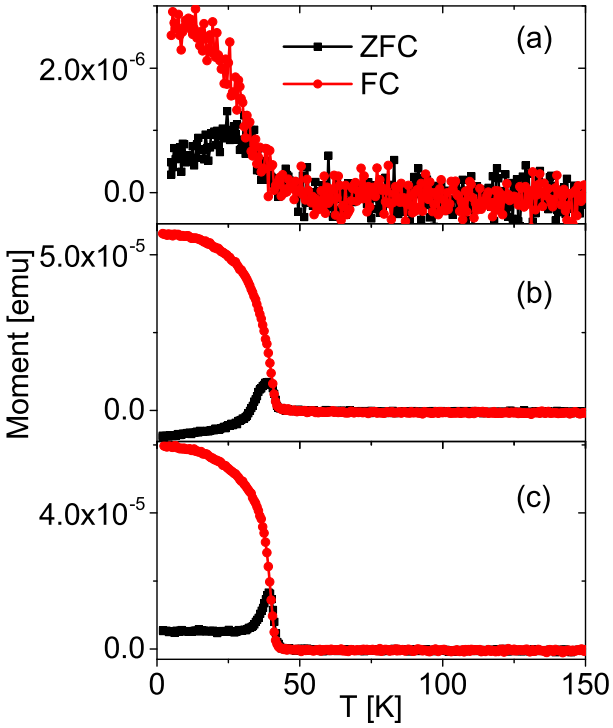

Figure 49: ZFC and FC magnetization curves measured at 5 mT for MnO NPs with 12 nm diameter (a) after heated in vacuum at 310°C for 3.5 h (MnO), (b) stored in air for 4 years (mixture of MnO and Mn_3O_4), and (c) after heated in air at 100°C for 15 h (Mn_3O_4).

In contrast, the low temperature peak becomes sharper and over one order of magnitude higher compared to the sample annealed in vacuum after the NPs were heated in air at 100°C for 15 h. A steep drop above ∼40 K and the overall shape of the ZFC/FC curves show a typical FM-like behaviour. In this case, the NPs are possibly fully oxidized to Mn_3O_4. However, in all MnO NPs, no feature at the Néel temperature of MnO can be found.

In order to further investigate the influence of the amount of Mn_3O_4 onto the magnetic

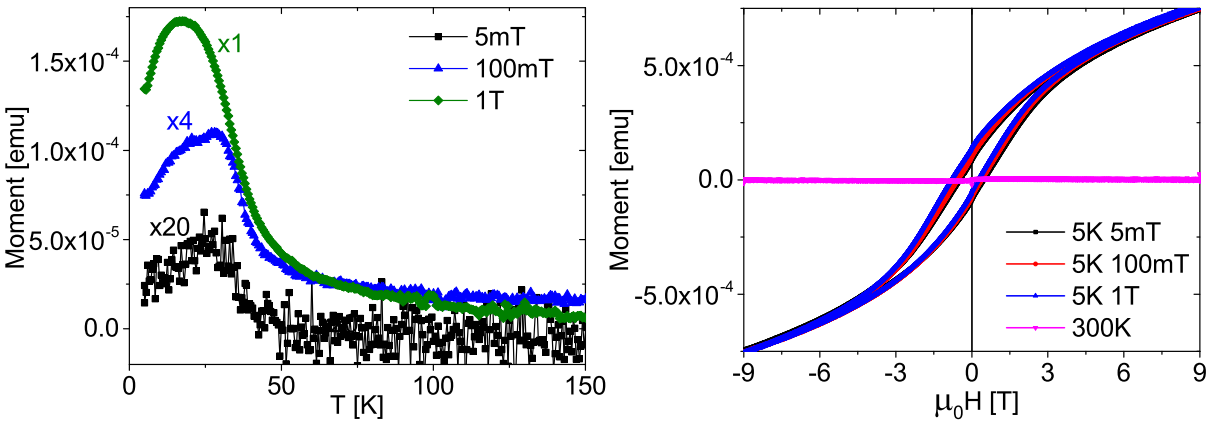

Figure 50: Magnetometry results on MnO NPs with 12 nm diameter after heated in vacuum at 310°C for 3.5 h. (a) ZFC magnetization curves measured at various magnetic fields. (b) Hysteresis loops measured at 300 K and 5 K after cooled at various magnetic fields.

properties of MnO NPs, three samples with different oxygen content discussed above in Fig. 49 have been further studied. Fig. 50(a) shows the ZFC curves of the NPs after heating at 310°C for 3.5 h measured at various magnetic fields. In this sample, almost pure MnO NPs are expected. As can be seen, the peak temperature shows no obvious field dependence until 1 T similar to that found in the as-prepared MnO NPs (see our previous results in Ref. 18). In the ZFC curve measured at 100 mT, two separated features ∼23 K and ∼28 K can be observed. The feature at the lower temperature is possibly from the AF-SPM MnO, and the second feature at a higher temperature results from not fully reduced Mn_3O_4. At 5 mT, the small fraction of FM component dominates the magnetic behaviour of the sample. As the magnetic field increases, the AF moments start to align along the field direction, thus the peak indicating the crossover between the blocked and unblocked AF-SPM states of MnO becomes much stronger. Moreover, hysteresis loops of this sample have been measured at 5 K after cooled at various magnetic fields (Fig. 50(b)). A small shift of the center of the hysteresis loops has been found, which indicates an EB effect. With an increasing cooling field, the shift toward the negative field direction becomes more obvious. This indicates an increase in the EB field H_{ex}. The EB effect in this sample is either due to the exchange coupling between the AF MnO core and disordered surface spins or not completely reduced Mn_3O_4. At 300 K, only PM behaviour is found in the hysteresis loop.

After the as-prepared MnO NPs were stored for 4 years, a mixture of MnO and Mn_3O_4 can be expected in the sample. The ZFC curve measured at 5 mT is dominated by the FiM behaviour of Mn_3O_4, since AF MnO show very weak signal at low magnetic field compared to FiM Mn_3O_4 (Fig. 51). Compared to the as-prepared sample, the ratio of Mn_3O_4 in this sample seems to be much higher than that in the as-prepared NPs. As the magnetic field increases, a hump at about 20 K can be observed in the ZFC curves measured at 100 mT and 1 T. This broad feature is likely to be due to the AF-SPM MnO as found in the ac-susceptibility curves of the as-prepared MnO NPs. Hysteresis loops measured at 5 K show much larger coercive fields compared to the almost single phase

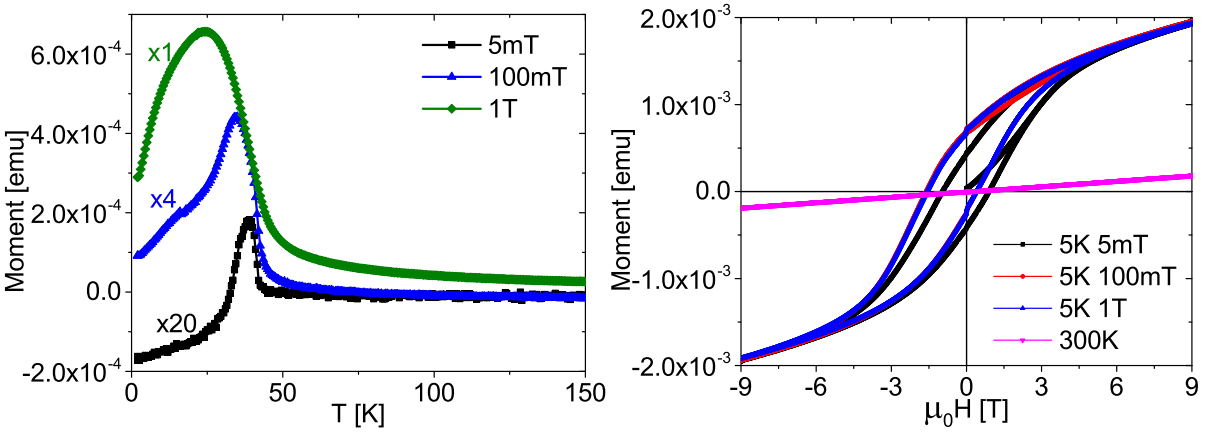

Figure 51: Magnetometry results of MnO NPs with 12 nm diameter after they were stored in air for 4 years. (a) ZFC magnetization curves measured at various magnetic fields. (b) Hysteresis loops measured at 300 K and 5 K after cooled at various magnetic fields.

MnO NPs (Fig. 51(b)). Moreover, a more obvious shift of the center of the hysteresis loops can be observed with an increasing cooling field. This marks an increasing EB field H_{ex} in this sample. From 5 mT to 100 mT, $|H_{ex}|$ increases from 0.025(20) to 0.595(20) T. As $|H_{FC}|$ further increases to 1 T, no obvious increase in $|H_{ex}|$ can be found within the error bars.

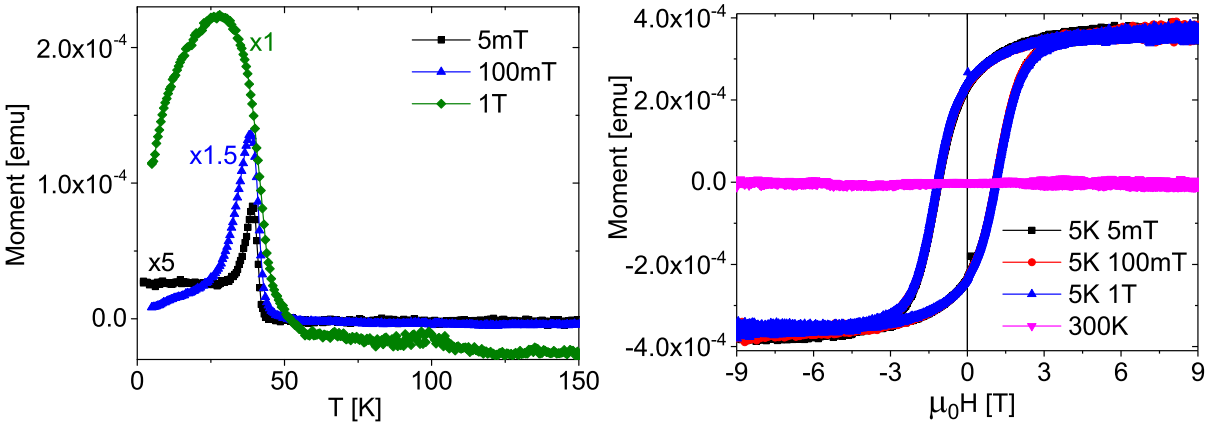

Figure 52: Magnetometry results of the manganese oxide NPs with 12 nm diameter after heated in air at 100°C for 15 h. (a) ZFC magnetization curves measured at various magnetic fields. (b) Hysteresis loops measured at 300 K and 5 K after cooled at various magnetic fields.

The aged NPs were further oxidized by heating the sample at 100°C in air for 15 h. As can be seen in Fig. 52(a), ZFC curves until 100 mT show only a sharp peak at ∼40 K which matches the Curie temperature of FiM Mn_3O_4. However, the peak becomes broader at 1 T. This might be because of the nano-size effect of FiM Mn_3O_4. At a magnetic field of 1 T magnetic moments of Mn_3O_4 may start to align along the field direction already

at a much lower temperature. Hysteresis loops of this sample measured at 5 K show no obvious difference after cooled at various magnetic fields. Moreover, no obvious shift of the center of the hysteresis loops can be observed. This indicates that no EB effect is observed, which is expected for pure FiM Mn_3O_4.

5.5 Monte Carlo Simulations

In order to have a better understanding of the spin structure inside bulk MnO as well as the influence of the finite-size effect onto the spin structure of MnO, MC simulations have been performed for "bulk" and NPs with various sizes. Moreover, MC simulations may also shed light on the contradiction between the magnetometry and neutron scattering results observed in the NPs in experiments.

The convergence of the simulations was firstly tested by simulating the sum of the x-, y- and z-components of 10×10×10 unit vectors after different Monte Carlo (MC) steps. At the beginning, all the vectors were set as (100), which means aligning along the x-direction. After that, a random vector was chosen and rotated to a random direction in 3D. This procedure was repeated for 1000 times assuming all vectors are rotated once. This is known as one MC step. After each MC step, the sum of the x-, y- and z-components of all vectors were recorded. As can be seen in Appendix B, the vectors can reach an equilibrium after several MC steps with a larger rotation angle. For a smaller rotation angle, more than 1000 MC steps are needed.

For the simulations, the sizes of MnO NPs are defined as $a \times b \times c$ with a, b, and c the number of Mn atoms along x-, y-, and z-directions of a triclinic coordinate system, respectively. The triclinic coordinate system used in this thesis to describe the position of Mn atoms has been introduced in section 3. Results for "bulk" MnO have been achieved by applying periodic boundary conditions to the system. In this case, surface spins of NPs can interact with virtual neighbours, which do not exist for NPs. The virtual spins are copies of real spins with translations along x-, y- and z-directions. They are updated after each MC step. Therefore, the system will behave in analogy to a bulk system, which has a negligible fraction of surface spins.

For all simulations performed in this thesis, magnetization components in x-, y-, and z-directions start to be recorded already during a cooling procedure at H=0 for "bulk" and NPs. In experiments, the magnetization during this procedure is not of interest. In the absence of a magnetic field, magnetic moments are randomly frozen during the cooling procedure. Therefore, no net magnetization is expected. However, this curve can be useful in simulations to check the quality of statistics. With good random numbers and good statistics, the magnetization of MnO should stay zero as expected in experiments during cooling at H=0. With poor statistics, magnetic moments may be frozen in a preferential direction at low temperature, and thus a non-zero magnetization can be found. After 2 K is reached, ZFC and FC magnetization curves for x-, y-, and z-components are recorded as measured in experiments. Simulated magnetization curves shown in this thesis are all normalized to the saturation magnetization of the real spins.

As discussed before, MnO shows a cubic-to-rhombohedral structural distortion at the Néel temperature ∼118 K. However, a simulation of a simultaneous magnetic and structural phase transition is not trivial. Therefore, the structural distortion is firstly neglected in the simulations to obtain an idea about the Néel temperature of MnO. In this case, the exchange constants $J_{1\mathrm{m}}$ and $J_{1\mathrm{p}}$ for nearest neighbours in the same plane and in neighbouring planes of the chosen Mn ion, respectively, are assumed to be the same. An averaged J_1 shown in appendix A is used for all nearest neighbours.

Fig. 53 shows the temperature dependence of the x-component of the magnetization of "bulk" MnO simulated at various magnetic fields. During cooling at H=0, a straight line with noise around zero can be seen for all three curves. This indicates a good statistics

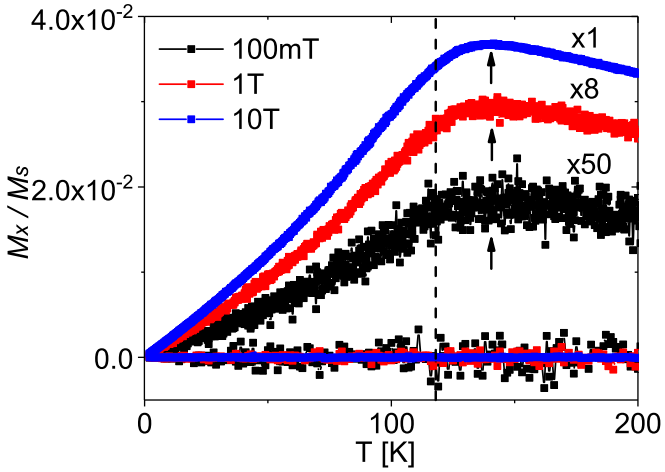

Figure 53: Temperature dependent magnetization curves simulated for "bulk" MnO at various magnetic fields. The magnetic field is applied along the x-direction, and the x-component of the magnetization is shown. The arrows indicate the peak temperatures in the ZFC/FC curves, which correspond to the critical temperature $T_c(H)$ of MnO. The dashed line indicates the experimental bulk Néel temperature $T_N = T_c(H{=}0)$. Exchange constants are $J_{1m}{=}J_{1p}{=}J_1{=}$constant.

of the simulations. The ZFC and FC curves overlap for simulations at all three magnetic fields. Until an applied field of 10 T, a peak at about 140 K can be observed in both ZFC and FC curves. This peak temperature indicates the critical temperature, which corresponds to the experimental Néel temperature of MnO at 118 K (dashed line). The difference between the Néel temperature obtained from the simulation and the experiment might be due to the simplified model applied in spin wave analysis of MnO, when the J-value were experimentally obtained [75–77].

Moreover, the stability of this peak temperature until 10 T is also expected for an AF. Usually a very high magnetic field (∼1000 T) is needed to align all magnetic moments in an AF along the field direction. The magnetization components in y- and z-directions show only noise around zero (data shown in appendix F). One should note that these results do not completely model MnO, because the structural distortion at T_N is neglected.

In Fig. 54, the simulation results is compared to the experimental data. As can be seen, no splitting can be observed for both simulated and measured curves. Moreover, the overall behaviour of both curves look similar except that the shape of the kink at T_N is different. This might be because that the structural distortion, which is accompanying the magnetic phase transition, is neglected in these simulations.

In order to simulate the influence of the structural distortion onto the magnetic structure of MnO, exchange constants J_1 splits into J_{1m} and J_{1p} for nearest neighbours in the same plane and in neighbouring planes of each Mn ion, respectively. In this case, the crystal structure of MnO is assumed to be distorted already at 300 K. Values for J_{1p} and J_{1m} used here are listed in appendix A as reported in [75–77]. Fig. 55 shows the temperature dependent magnetization curves. At a magnetic field of 100 mT, ZFC/FC curves show similar behaviour as in Fig. 53. A peak near the experimental Néel temperature of MnO can be found. Moreover, the peak temperatures obtained from the 1 T and 10 T magnetization curves are about 160 K, which is much higher than the expected Néel tem-

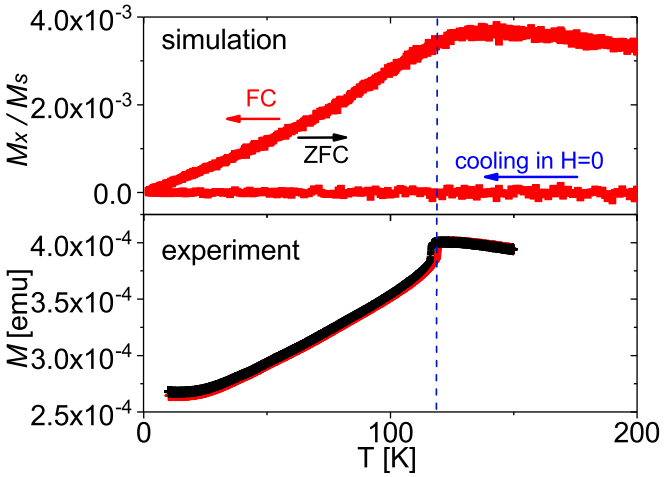

Figure 54: Temperature dependent magnetization curves simulated for "bulk" MnO at various magnetic fields. Magnetic field is applied along the x-direction, and the x-component of the magnetization is shown. The arrows indicate the peak temperatures in the ZFC/FC curves, which correspond to the critical temperature $T_c(H)$ of MnO. The dashed line indicates the experimental bulk Néel temperature $T_N = T_c(H{=}0)$. Exchange constants are $J_{1m}{=}J_{1p}{=}J_1$=constant. H=100mT

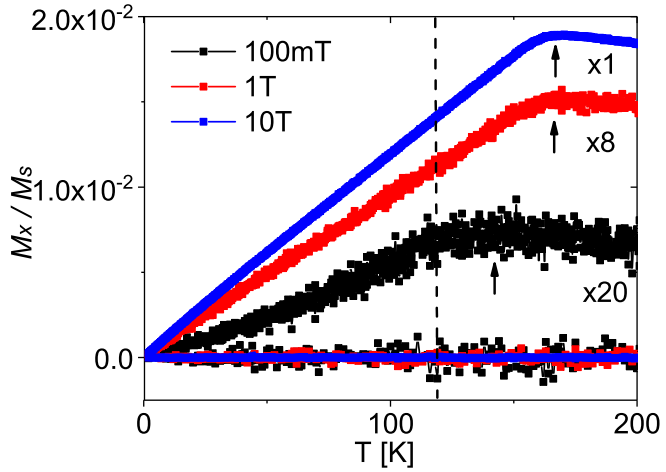

Figure 55: Temperature dependent magnetization curves simulated for "bulk" MnO with $J_{1p} \neq J_{1m}$ at various magnetic fields. The magnetic field is applied along the x-direction, and the x-component of the magnetization is shown. The arrows indicate the peak temperatures in the ZFC/FC curves, which correspond to the critical temperature $T_c(H)$ of MnO. The dashed line indicates the experimental bulk Néel temperature $T_N = T_c(H{=}0)$.

perature of MnO. The contradiction between the peak temperatures obtained from Fig. 53 and Fig. 55 is due to the not correctly defined Néel temperature, at which a structural distortion takes place.

To obtain more information about the magnetic phase transition of MnO, magnetization curves for both sublattices a and b simulated at 100 mT are plotted separately in Fig. 56. An accurate determination of the critical temperature T_c is not possible, because of the identity problem, which causes the large noise near T_c. This is due to the fluctuation near the phase transition, which makes it impossible to define the sublattices a

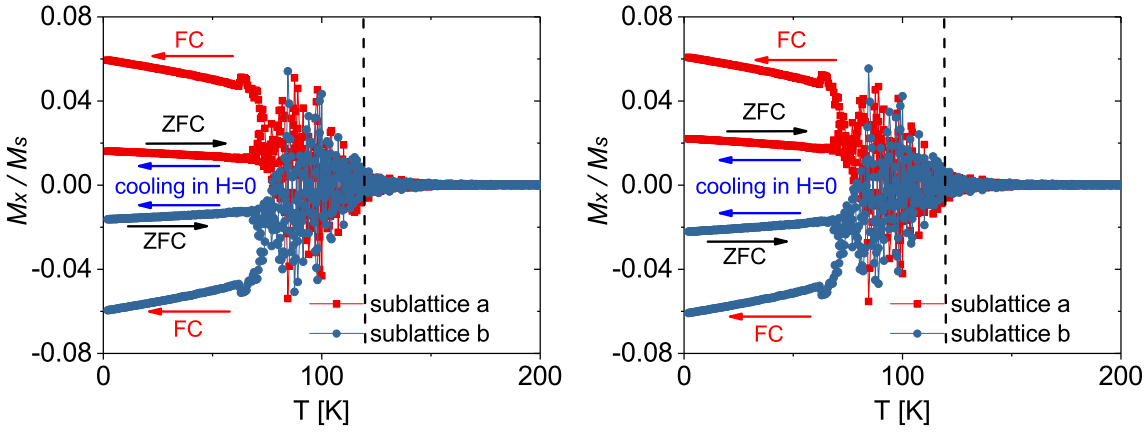

Figure 56: Magnetization curves for a and b sublattices of AF MnO dependent on temperature simulated for "bulk" MnO at a magnetic field of 100 mT. The magnetic field is applied along the x-direction, and the x-component of the magnetization is shown. The exchange constants are (a) J_{1m}=J_{1p}=J_1=constant and (b) $J_{1m} \neq J_{1p}$.

and b. For both cases (a), where the structural distortion is neglected, and (b), where an structural distortion is considered, the magnetization of separated sublattices vanishes at a similar temperature slightly above the experimentally obtained T_N = 118 K. This results matches the observations in Fig 53 and 55.

Another method to simulate the magnetic behaviour of MnO is to manually define a temperature, at which the structural distortion occurs. However, the simulation results will not be correct, because the Néel temperature is correlated to the structural phase transition temperature, which is already defined. Therefore, only MnO with cubic and distorted structures in the full temperature range are simulated and compared in this thesis.

As NPs are in the focus of this thesis, MnO NPs with various sizes have been simulated to be compared with the experimental results, and thus to have a better understanding of the nano-size effect onto the spin structure of MnO NPs. At first, a MnO NP with 10×10×10 Mn ions was investigated. MnO with 10×10×10 Mn corresponds to a NP size of ∼4-5 nm, which is similar to the magnetic correlation length (6-7 nm at 4 K) of the as-prepared MnO NPs with 12 nm diameter obtained from neutron scattering.

Fig. 57 shows a comparison of the simulated and experimentally measured ZFC/FC magnetization curves for NPs with a correlation length of about 5 - 6 nm. In the simulations, no splitting between the ZFC and FC curves can be observed. The overall behaviour of the curves looks similar tof a "bulk" MnO with a reduced critical temperature due to the finite size effect. However, the experimental results show a SPM-like behaviour. The peak temperature is found at a much lower temperature compared to the simulations. This might be because that the real NPs may consist of various sizes of magnetic domains. The magnetization in both sublattices might not be compensated as good as in the simulations, where the number of spins in each sublattice and the number of layers is well defined. The magnetic behaviour of a real sample will be a superposition of different sizes of particles.

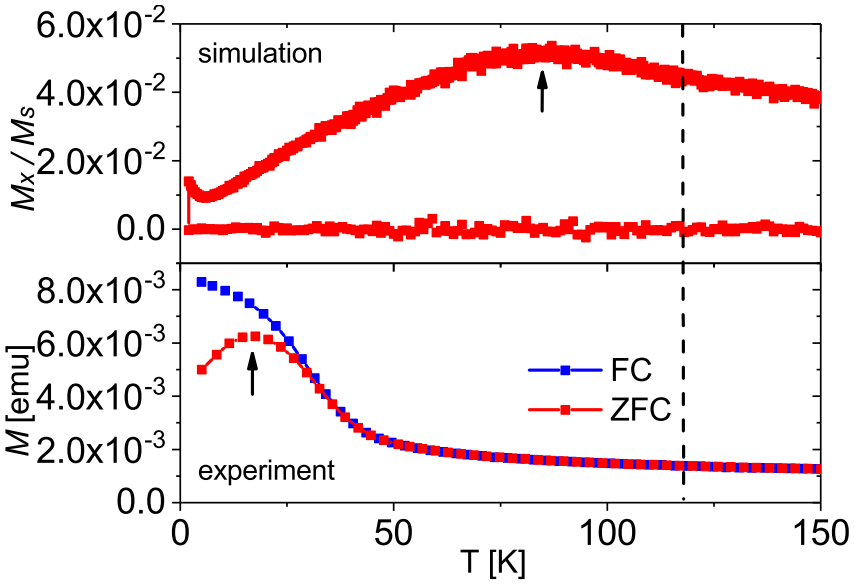

Figure 57: Comparison of simulated and experimentally measured ZFC/FC magnetization curves at a magnetic field of 1 T. For the simulations a 10×10×10 NP is used, which corresponds to $d_{\mathrm{NP}} \approx 5\,\mathrm{nm}$. The experimental results are recorded using 12 nm diameter NPs with a correlation length of 6-7 nm at 4 K. The magnetic field is applied along the x-direction for the simulations, and the x-component of the magnetization is shown. The arrows indicate the peak temperatures in the ZFC/FC curves, which correspond to the critical temperature $T_{\mathrm{c}}(H)$. The dashed line indicates the experimental bulk Néel temperature $T_{\mathrm{N}} = T_{\mathrm{c}}(H{=}0)$. Here I used J_1=constant.

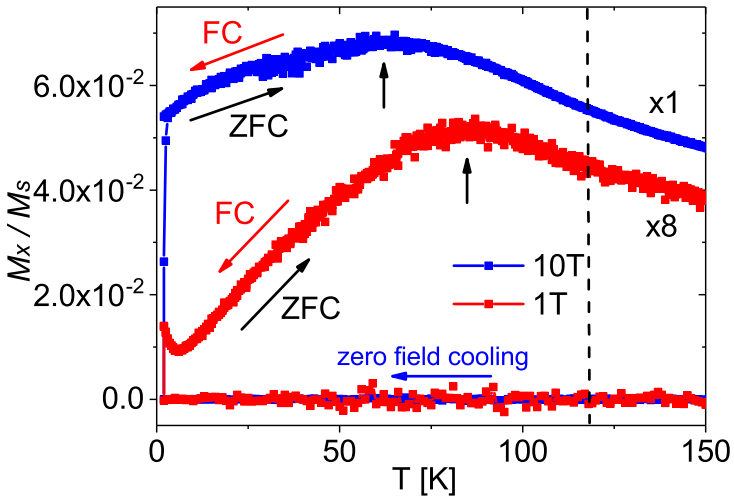

Figure 58: ZFC/FC magnetization curves at various magnetic fields simulated for a 10×10×10 NP, which corresponds to $d_{\mathrm{NP}} \approx 5\,\mathrm{nm}$. The magnetic field is applied along the x-direction, and the x-component of the magnetization is shown. The arrows indicate the peak temperatures in the ZFC/FC curves, which correspond to the critical temperature $T_{\mathrm{c}}(H)$. The dashed line indicates the experimental bulk Néel temperature $T_{\mathrm{N}} = T_{\mathrm{c}}(H{=}0)$. Here I used J_1=constant.

Fig. 58 shows the ZFC/FC magnetization curves simulated for a 10×10×10 MnO NP at 1 T and 10 T. An averaged exchange constant J_1 is used for all nearest neighbours in these simulations. After the NP is cooled in the absence of a magnetic field, a magnetic field is applied, and the ZFC curve is recorded during warming up. The FC curve is simulated after the particle is cooled within the magnetic field. As can be seen in Fig. 58, ZFC and FC curves show no splitting as observed for "bulk" MnO. ZFC/FC curves at a smaller magnetic field (100 mT) have also been simulated (Fig. 131 in appendix F). However, the magnetization increases as the system is cooled in the absence of a magnetic field, which indicates a bad statistics. Therefore, the curves are not representative. At 1 T, ZFC/FC curves show similar behaviour as for "bulk" MnO. However, a reduced Néel temperature can be found at ∼ 80 K. This can be explained by the finite-size effect. The slight increase in the magnetization below 10 K is probably due to the PM behaviour of the disordered surface spins. At 10 T, not only the surface spins but also part of the AF ordered magnetic moments tend to be aligned along the magnetic field. Therefore, a higher magnetization is found in the ZFC/FC curves at 10 T compared to that at 1 T. Moreover, the simulated Néel temperature is further decreased to ∼50 K at 10 T. The sharp increase at very low temperature in the ZFC curve at 10 T possibly indicates a blocking temperature of SPM behaviour of the surface spins.

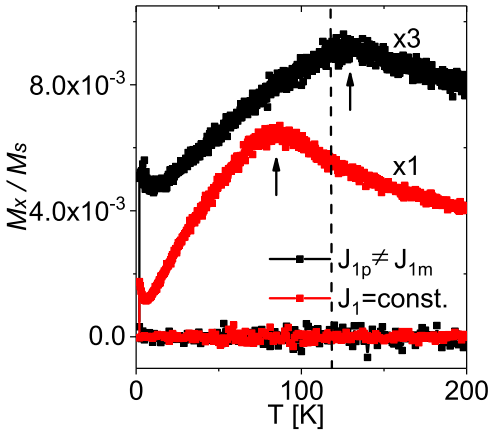

Figure 59: Comparison of ZFC/FC curves simulated for a 10×10×10 NP at a magnetic field of 1 T with and without a splitting of the exchange constants J_{1m} and J_{1p} for nearest neighbours in the same plane and in neighbouring planes of one Mn ion. The magnetic field is applied along the x-direction, and the x-component of the magnetization is shown. The arrows indicate the peak temperatures in the ZFC/FC curves, which correspond to the critical temperature $T_c(H)$. The dashed line indicates the experimental bulk Néel temperature $T_N = T_c(H{=}0)$.

In order to study the influence of the structural distortion onto the peak temperature of MnO NPs, ZFC/FC curves of a 10×10×10 MnO NP have been simulated using splitted exchange constants J_{1m} and J_{1p} for nearest neighbours in the same plane and in neighbouring planes of one Mn ion. Fig. 59 shows the comparison of ZFC/FC curves simulated with J_1=const. and $J_{1p} \neq J_{1m}$. As can be seen, a higher Néel temperature is observed, when the exchange constant J_1 is splitted. However, this temperature is also reduced compared to the bulk Néel temperature using the same parameters. Moreover, no splitting between the ZFC and FC curves can be observed. This indicates a bulk AF-like

behaviours.

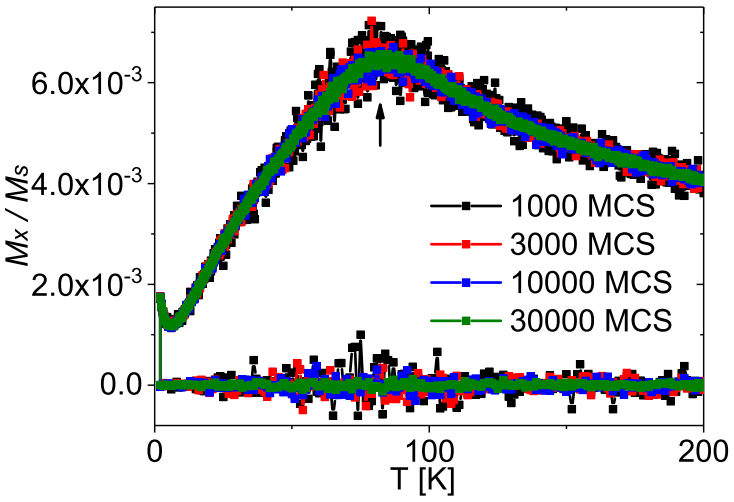

Figure 60: ZFC/FC curves simulated for a 10×10×10 MnO at a magnetic field of 1 T with various MCS. Magnetic field is applied along the x-direction, and the x-component of the magnetization is shown. The arrows indicate the peak temperatures in the ZFC/FC curves, which correspond to the critical temperature $T_c(H)$ of MnO. The dashed line indicates the experimental bulk Néel temperature $T_N = T_c(H{=}0)$. J_1=constant.

In order to investigate whether the peak temperature observed in the 10×10×10 NP is the reduced Néel temperature due to finite size effect or a blocking temperature marking a SPM system, ZFC/FC curves of a 10×10×10 NP have been simulated with various Monte Carlos step numbers (MCS), which corresponds to different measurement times in real experiments. As can be seen in Fig. 60, the peak temperature shows no obvious time dependence. This indicates, that the peak observed in the 10×10×10 NP is more likely to be a reduced Néel temperature. This is possibly because of equal number of both sublattices. The magnetization of both sublattices can be almost perfectly compensated. Moreover, the surface spins might still be strongly coupled to the AF core, so that no obvious SPM behaviour can be observed.

To further study the nano-size effect on the spin structure of AF MnO, the size of MnO NP is further reduced. Fig. 61 shows the ZFC/FC curves simulated for MnO NPs with sizes from 3×3×3 to 9×9×9 Mn ions and compared with the results of a 10×10×10 MnO NP. Interestingly, NPs with even and odd number of Mn ions show different behaviours. NPs with an odd number of Mn behave like a SPM system, and show a much higher magnetization than that of NPs with even number of Mn. Above the blocking temperature, NPs behave SPM. Below the blocking temperature, ZFC and FC curves split. After a ZFC procedure, the superspins in a SPM system are frozen in random orientation, thus show zero magnetization. When a magnetic field is applied, superspins start to align along the field direction as the temperature increases. However, above the blocking temperature, the magnetic order is again destroyed by thermal fluctuations. During a FC procedure, the superspins tend to be frozen along the field direction as thermal fluctuations decrease, and thus the magnetization increases. SPM behaviour observed for NPs with odd number of Mn is possibly due to an uncompensated layer in one of the AF sublattices of MnO, which dominates the magnetic behaviour of the entire NP. As the size of NP decreases,

the blocking temperature decreases due to a smaller energy barrier as expected for SPM systems.

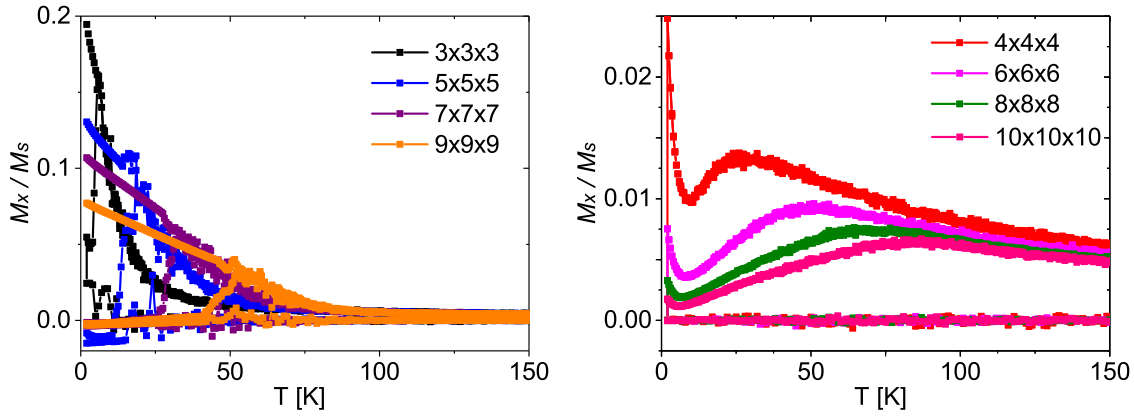

(a) (b)

Figure 61: ZFC/FC magnetization curves of MnO NPs with various sizes from 3×3×3 to 10×10×10 Mn ions simulated at a magnetic field of 1 T. The magnetic field is along the x-direction (crystallographic [111] direction of MnO). (a) shows the ZFC/FC curves with odd number of Mn ions, (b) shows the ZFC/FC curves with even number of Mn ions.

ZFC/FC magnetization curves of MnO NPs with even number of Mn behave more like an AF system with a reduced Néel temperature. The increase below ∼10 K is possibly due to the PM behaviour of disordered surface spins, which have a larger influence on the magnetic behaviour for smaller NPs than larger NPs. Moreover, the magnetization of NPs with even number of Mn is about one order of magnitude smaller than the SPM behaviour observed for NPs with an odd number of Mn. This is also understandable, because the magnetization from both sublattices can be almost compensated for NPs with even number of layers. The decreasing of the Néel temperature with decreasing the NP size can be explained by the decrease of the energy barrier.

Fig. 62 shows the T_p depending on the size of NPs obtained from the simulations and experiments. As can be seen, for the simulations with both odd and even numbers of Mn atoms, T_p shows a linear increase with an increase of the particle size as expected. However, the experimental results show an opposite behaviour. This might be because of smaller domain sizes in larger NPs.

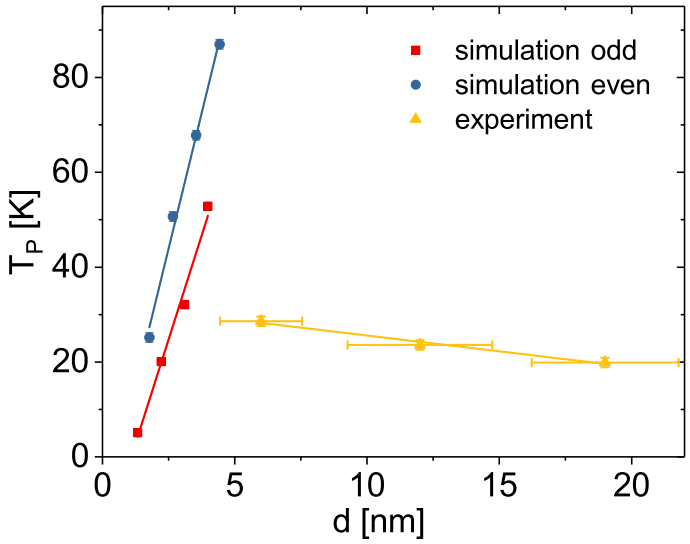

Figure 62: Size dependent peak temperature T_p obtained from the simulations with even and odd numbers of layers and from the experiments.

Fig. 63 shows the ZFC/FC curves simulated at various magnetic fields for NP with sizes between 9×9×9 and 3×3×3 Mn ions. For both NPs with odd and even number of Mn, the peak temperature shows a decrease with an increase in the magnetic field. However, this decrease is faster for NPs with odd number of Mn than that with even number of Mn. This phenomenon is expected when comparing a SPM with a fluctuating AF system. Moreover, the blocking temperature of a SPM system depends also on the measurement time, which has been introduced in section 2.2.1. Fig. 64 shows the ZFC/FC curves for a 3×3×3 MnO NP simulated with various number of MCS, i.e. different measurement times. As can be seen in Fig. 64, a decrease in the blocking temperature is observed with increasing number of MCS (i.e. increasing measurement time), which is expected for a SPM system.

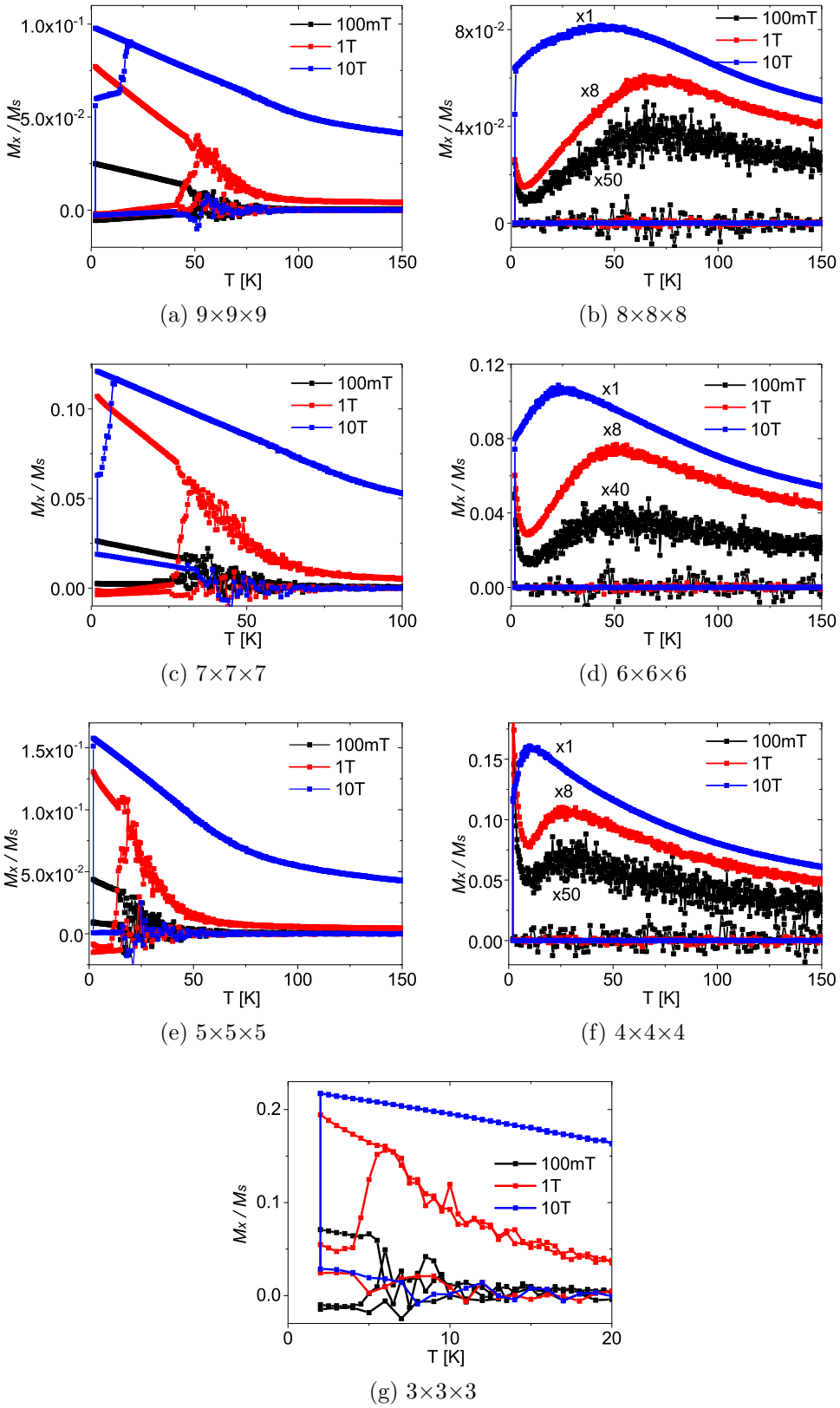

(a) 9×9×9 (b) 8×8×8

(c) 7×7×7 (d) 6×6×6

(e) 5×5×5 (f) 4×4×4

(g) 3×3×3

Figure 63: Comparison of ZFC/FC magnetization curves simulated at various magnetic fields for MnO NP with size of (a) 9×9×9, (b) 8×8×8, (c) 7×7×7, (d) 6×6×6, (e) 5×5×5, (f) 4×4×4, and (g) 3×3×3 Mn ions. Both the anisotropy axis and the magnetic field are parallel to the x-direction (crystallographic [111] direction of MnO). Hereby, J_1=const.

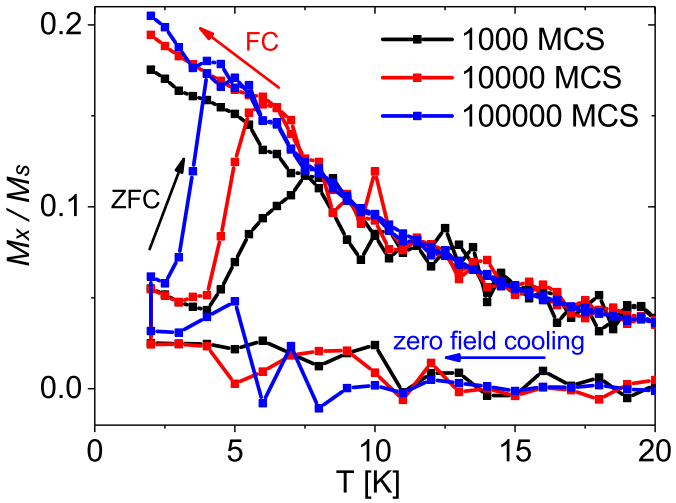

Figure 64: Comparison of ZFC/FC curves for a 3×3×3 NP simulated at a magnetic field of 1 T with various number of MCS (i.e. different measurement time). The magnetic field is applied along the x-direction, and the x-component of the magnetization is shown. Hereby, J_1=constant.

Until now, only the x-component of the magnetization was shown for both bulk and NPs, because the y- and z-components show only noise around zero. The y-, and z-components of the magnetization of a 3×3×3 MnO NP as well as "bulk" during ZFC/FC procedures can be found in appendix F. For all simulation results shown above, both the anisotropy axis and the magnetic fields are defined to be along the x-direction, which corresponds to the crystallographic [111] direction of MnO assuming a textbook spin structure of MnO as described in [26]. However, MnO power and NPs measured in real experiments are randomly ordered. Therefore, the magnetic field can be along different crystallographic directions for different grains with a statistically equal distribution over all orientations. Fig. 65 shows the y-component of the magnetization vs temperature for a 20×20×20 NP and "bulk", respectively, with a magnetic field along the y-direction (within the (111) plane). The magnetization components along the hard axis (x-, and z-directions) shows only noise around zero (data shown in appendix F).

As can be seen in Fig. 65(a), the y-component of the magnetization for a 20×20×20 NP show a monotonic increase with decreasing temperature in the ZFC/FC curves. However, ZFC/FC curves for "bulk" show a peak at ∼125 K matching the Néel temperature of MnO (Fig. 65(b)).

For AFs, a very high magnetic field (∼hundreds or thousands of Tesla) is usually needed to align all magnetic moments along the field direction. Such high magnetic field cannot be achieved in real experiments. However, this can be realized in simulation. Fig. 66 shows the ZFC/FC magnetization curves of "bulk" simulated at a magnetic field of 10000 T. As can be seen, all magnetic moments are aligned along the field direction (x-direction) even at 300 K. Y-, and z-components of the magnetization show only noise around zero (Fig. 66(b) and (c)).

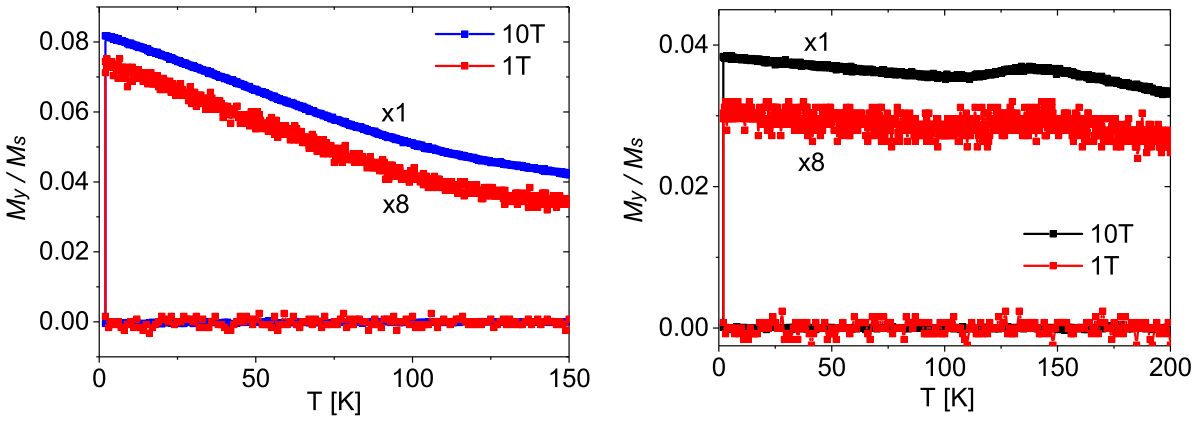

Figure 65: ZFC/FC magnetization curves of (a) a 20×20×20 MnO NP, and (b) "bulk" MnO simulated along the y-directions at various magnetic fields. The anisotropy axis is along the crystallographic [111] direction of MnO and the magnetic field is perpendicular to the [111] direction (within the (111) plane).

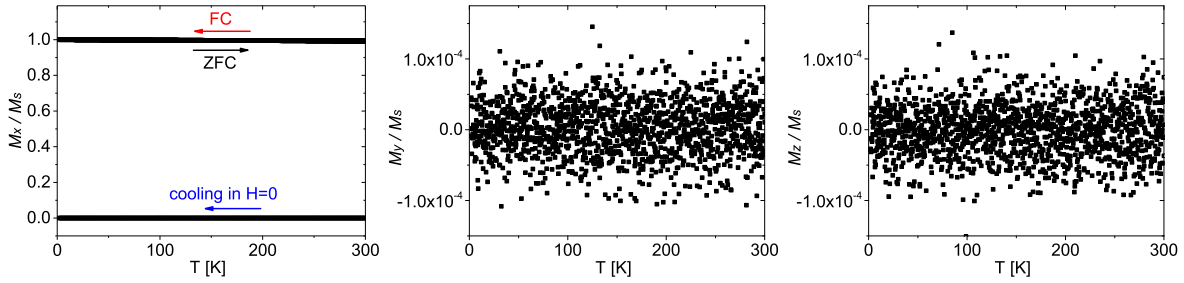

Figure 66: ZFC/FC magnetization curves of "bulk" MnO simulated along (a) x-, (b) y-, and (c) z-directions at 10000 T. Both the anisotropy axis and the magnetic field are parallel to the x-direction (crystallographic [111] direction of MnO). Hereby, J_1=const.

Moreover, hysteresis loops of "bulk" and NPs have also been simulated at 2 K. As can be seen in Fig. 67, the magnetization of both NPs and "bulk" can be saturated at a magnetic field of ∼250 T. A more accurate determination of the saturation magnetic field is not achieved due to the extremely long computing time. For "bulk", the magnetization stays almost zero when the magnetic field is smaller than ∼20 T. This is often observed for AF, because the Zeeman energy is too small for a small magnetic field to overcome the AF exchange interaction of MnO. Thus the magnetic moments in the sublattice, which shows a magnetization against the field direction, cannot be flipped. However, for NPs, a steeper increase is observed near the origin. This behaviour might be due to the surface spins in the NPs, which can be easier saturated compared to the AF aligned magnetic moments. At 2 K, the total magnetization of the inner part of the NP is about 0.7 % as much as that of the surface spins at a magnetic field of 1 T. Therefore, the surface spins may show a much stronger effect compared to the AF behaviour of MnO, thus dominates the behaviour of the field dependent magnetization of MnO NPs at small magnetic fields.

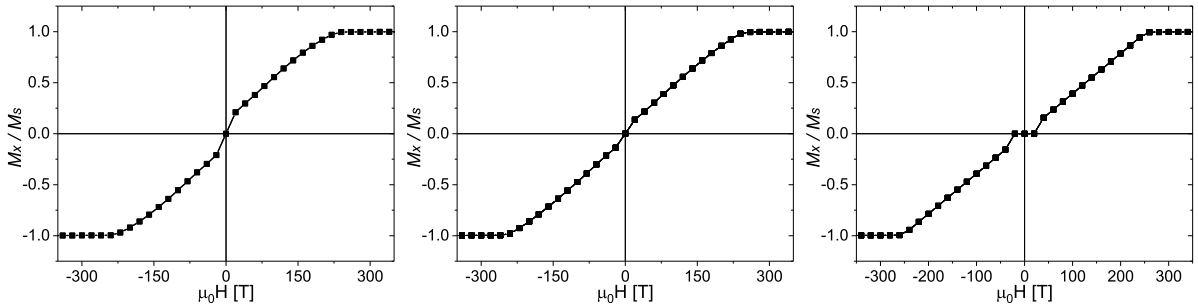

Figure 67: Field dependent magnetization curves of (a) a 10×10×10 NP, (b) a 20×20×20 NP, and (c) "bulk" MnO simulated at 2 K. Both the anisotropy axis and the magnetic field are parallel to the x-direction (crystallographic [111] direction of MnO). Hereby, J_1=const.

5.5.1 Spin Structure Visualization

During MC simulations, tables containing information about the position and the x-, y-, z-components of each magnetic moment have been recorded from the first and the tenth configuration after 10000 relaxation and 10000 average loops, respectively. Spin structures of "bulk" and NPs are visualized by plotting the spin table using the program "AViz" [105].

Fig. 68 shows the spin structures simulated for "bulk" MnO by applying periodic boundary conditions to a 10×10×10 system. The surface spins interact with virtual spins using periodic boundary conditions. For this simulation, exchange constants $J_{1\mathrm{m}}$ and $J_{1\mathrm{p}}$ for nearest neighbours in the same plane and in neighbouring planes are the same. A constant J_1 is used, which is an average of $J_{1\mathrm{m}}$ and $J_{1\mathrm{p}}$ as reported in Ref. 75–77. The anisotropy axis is defined to be along the crystallographic [111] direction of MnO as described in [26]. Results in Fig. 68 are obtained from the first configuration after 10000 average loops. Reference results obtained from the tenth configuration after the average loops as well as results after 10000 relaxation loops can be found in appendix G. Magnetization results shown in section 5.5 have been averaged over different configurations. The spin visualization provides us a direct view of the various spin orders of the system.

Fig. 68 shows the snapshots of the spin structure of the "bulk" system at 2 K and 200 K. During simulations of the ZFC/FC magnetization curves at a magnetic field of 1 T (Fig. 53), the spin structure at 2 K at the beginning of a ZFC curve and after a FC procedure as well as at 200 K were recorded. Red and blue colours in Fig. 68 indicate the maximum and minimum values of the spin component in the [111] direction, respectively, i.e. parallel and antiparallel to the [111] direction in this case. The MnO atoms are located at the centre of the bottom of the cones. As can be seen in Fig. 68(a), an AF ordered structure can be observed at 2 K, when a magnetic field of 1 T is applied after a ZFC procedure. However, a different type of AF order can be found at the same temperature (2 K) after a FC procedure (Fig. 68(b)). Spin order in separated (111) layers are shown in Fig. 69 to have a better view. Both AF orders have the same probability to be found at 2 K in various configurations (appendix G). This indicates, that both AF orders correspond to local energy minima at 2 K. Above the Néel temperature of MnO, spins are randomly

oriented at 200 K as expected.

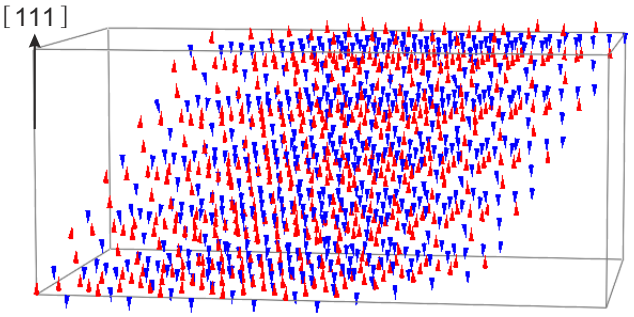

(a) 2 K at the beginning of a ZFC curve

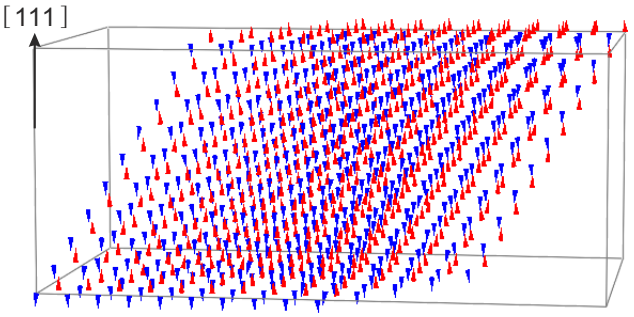

(b) 2 K after a FC procedure

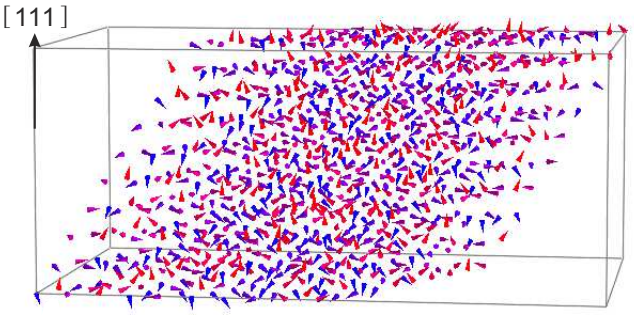

(c) 200 K

Figure 68: Illustration of the spin structure of "bulk" MnO simulated with a magnetic field of 1 T (a) at 2 K at the beginning of a ZFC curve, (b) at 2 K after a FC procedure, and (c) at 200 K resulting from the first configuration after 10000 average loops. Red and blue cones mark the maximum and minimum values of the spin component in the [111] direction, respectively (here parallel and antiparallel to the [111] direction). The MnO atoms are located at the centre of the bottom of the cones. Both the anisotropy axis and the magnetic field are parallel to the x-direction (crystallographic [111] direction of MnO). Hereby, J_1=constant.

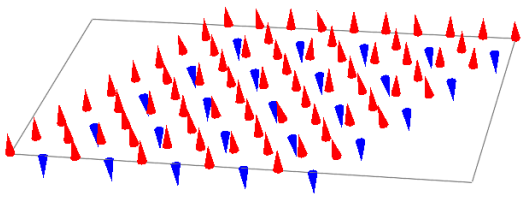

(a) First layer at 2 K at the beginning of a ZFC curve

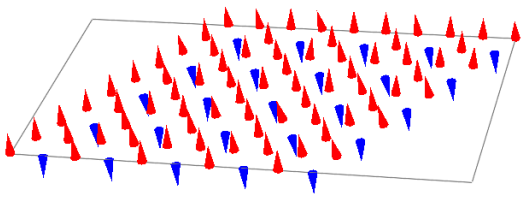

(b) Second layer at 2 K at the beginning of a ZFC curve

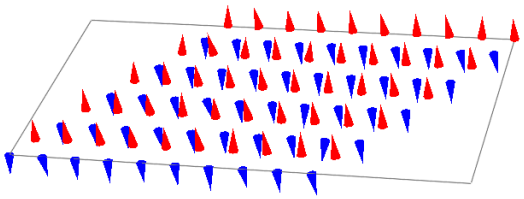

(c) First layer at 2 K after a FC procedure

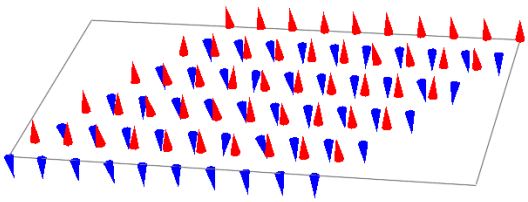

(d) Second layer at 2 K after a FC procedure

Figure 69: Illustration of (a) the first and (b) the second layers counting from the bottom of the spin structure of "bulk" MnO simulated with a magnetic field of 1 T at 2 K at the beginning of a ZFC curve (Fig. 68(a)), and (c) the first and (d) the second layers of the spin structure at 2 K after a FC procedure (Fig. 68(b)). The crystallographic [111] direction is perpendicular to these layers. For MnO, the magnetic moments are reported to order AF along the [111] direction. Therefore, the spin order in neighbouring (111) layers are expected to be representative for two sublattices. Red and blue cones mark the maximum and minimum values of the spin component in the [111] direction, respectively (here parallel and antiparallel to the [111] direction). The MnO atoms are located at the centre of the bottom of the cones. Both the anisotropy axis and the magnetic field are parallel to the x-direction (crystallographic [111] direction of MnO). Hereby, J_1=constant.

In order to have a better impression about the AF spin structures at 2 K, the spin order in the first and the second (111) layers counting from bottom of spin structures shown in Fig. 68(a) and (b) are shown in Fig. 69. As reported in previous studies, an AF order along the [111] direction is expected for MnO bulk. Therefore, the spin order in the first and the second (111) layers should be representative for all odd and even layers, respectively. As can be seen in Fig. 69, the first and second layers show similar spin order along the triclinic z-direction in both spin structures at 2 K instead of the expected AF ordering. Moreover, neither of these layers shows a perfect FM order within the (111) plane along the crystallographic [111] direction as reported. The contradiction between the spin structure obtained from the simulations and the experiment is possibly due to the neglected structural distortion below $T_N \approx 118$ K.

To investigate the influence of the structural distortion at the Néel temperature, the spin structure of "bulk" obtained from the simulations with $J_{1m} \neq J_{1p}$ for nearest neighbours in the same plane and in neighbouring planes are visualized (Fig. 70). Red and blue

cones indicate the maximum and minimum values of the spin component along the [111] direction in each layer, respectively. In this case, the red cones in Fig. 70(a) mark the spins, which show the largest deviation from the [111] direction, and the blue cones in Fig. 70(b) mark the spins, which have the largest deviation from the $[\bar{1}\bar{1}\bar{1}]$ direction. The MnO atoms are located at the centre of the bottom of the cones. Results in Fig. 70 are obtained from the first configuration after the average loops. Reference results from the tenth configuration after the average loops can be found in appendix G. As can be seen, the textbook AF order of MnO along the crystallographic [111] direction can be found during both ZFC and FC procedures. To have a better view of the spin order within odd and even layers, spin structures within the representative first and second (111) layers are visualized in Fig. 71. As can be seen, within the same layer, magnetic moments align parallel, and magnetic moments within neighbouring (111) planes lie antiparallel. This confirms the experimental studies of the magnetic structure of MnO [75–77], and vice versa proves the reliability of our simulation results. Moreover, above the experimental $T_{\mathrm{N}} \approx 118\,\mathrm{K}$, magnetic moments are randomly distributed as expected. This indicates that the AF order observed in MnO below $\mathrm{T}_N \sim 118\,\mathrm{K}$ is strongly correlated to the structural distortion.

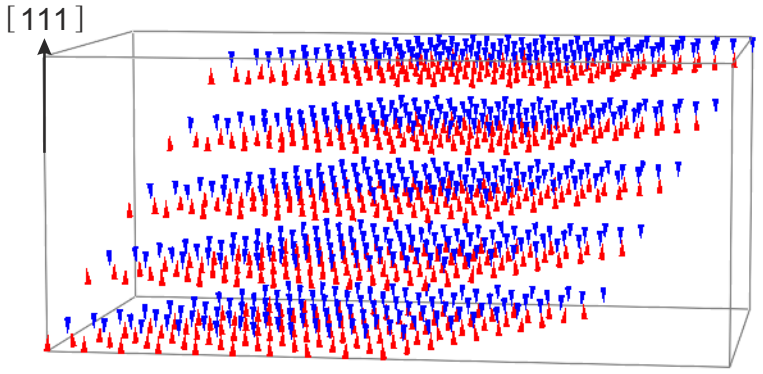

(a) 2 K at the beginning of a ZFC curve

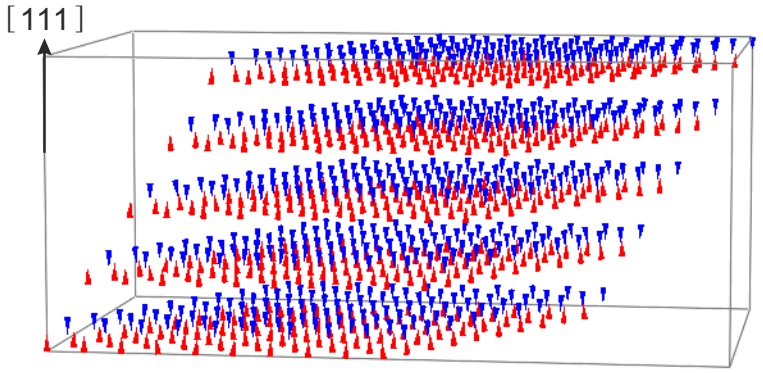

(b) 2 K after a FC procedure

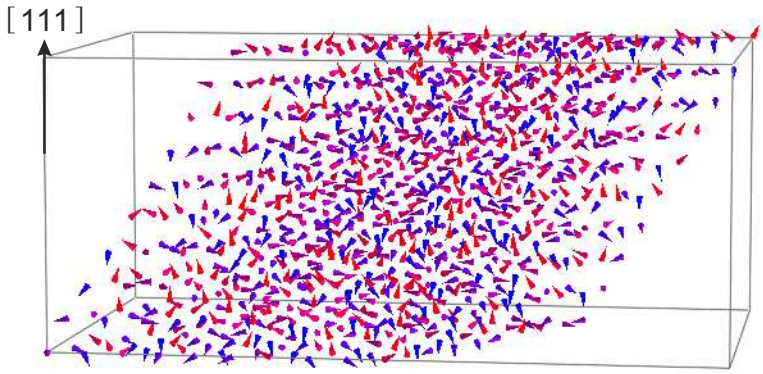

(c) 300 K

Figure 70: Illustration of the spin structure of bulk MnO simulated with a magnetic field of 1 T (a) at 2 K at the beginning of a ZFC curve, (b) at 2 K after a FC procedure, and (c) at 300 K resulting from the first configuration after 10000 average loops with $J_{1m} \neq J_{1p}$ for nearest neighbours in the same plane and in neighbouring planes. Red and blue cones indicate the maximum and minimum values of the spin component in the [111] direction, respectively (here parallel and antiparallel to the [111] direction). The MnO atoms are located at the centre of the bottom of the cones. Both the anisotropy axis and the magnetic field are parallel to the x-direction ([111] crystallographic direction of MnO).

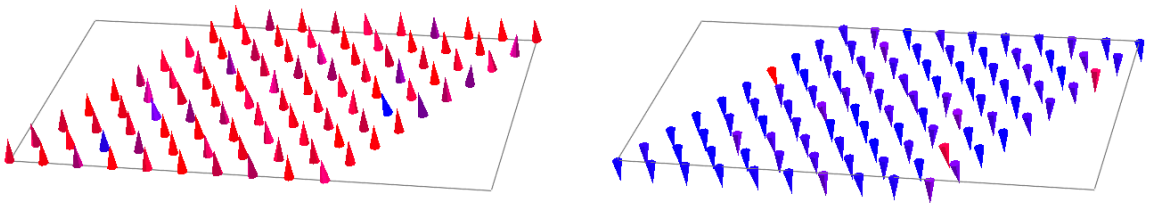

(a) First layer at 2 K at the beginning of a ZFC curve

(b) Second layer at 2 K at the beginning of a ZFC curve

Figure 71: Illustration of (a) the first and (b) the second layer counting from bottom of the spin structure of "bulk" MnO simulated with a magnetic field of 1 T at 2 K at the beginning of a ZFC curve. Red and blue cones indicate the maximum and minimum values of the spin component in the [111] direction for each layer, respectively. The MnO atoms are located at the centre of the bottom of the cones. Both the anisotropy axis and the magnetic field are parallel to the x-direction ([111] crystallographic direction of MnO).

After the AF order is obtained in the visualization of the spin structure of MnO "bulk", it is interesting to compare the results with that of NP systems to shed light onto the influence of the nano-size effect to the spin structure of MnO. Here we focused on the spin structure of a 10×10×10 NP corresponding to a NP with 5 nm size, which has similar correlation length as the as-prepared MnO NPs with 12 nm diameter ($\sim$ 6-7 nm) measured at 4 K. The influence of the structural distortion onto the spin structure of MnO NPs has been studied by comparing the results using the same exchange constant J_1 with that using different exchange constants $J_{1\mathrm{m}}$ and $J_{1\mathrm{p}}$ for nearest neighbours in the same plane and in neighbouring planes. The finite-size and surface effect can be observed by comparing the spin structure of NPs with that of "bulk".

As can be seen in Fig. 72 and 74, spin structures of NPs show similar results as that of "bulk" system. With J_1=constant, the NP show various types of AF orders at 2 K (Fig. 72 and 143 in appendix G). A better impression about the AF spin structure of NPs at 2 K can be obtained by visualizing the spin order in the first and the second (111) layers of the spin structure during various magnetization procedures from the first configuration after the average loops. As can be seen in Fig. 73, most of the magnetic moments arrange parallel within the same (111) layer. Several magnetic moments align antiparallel to its in-plane neighbours. Moreover, most of the magnetic moments in neighbouring (111) planes align antiparallel. This matches relatively good to the experimental results. However, no AF ordering along the [111] direction can be found in NPs at 2 K (appendix G).

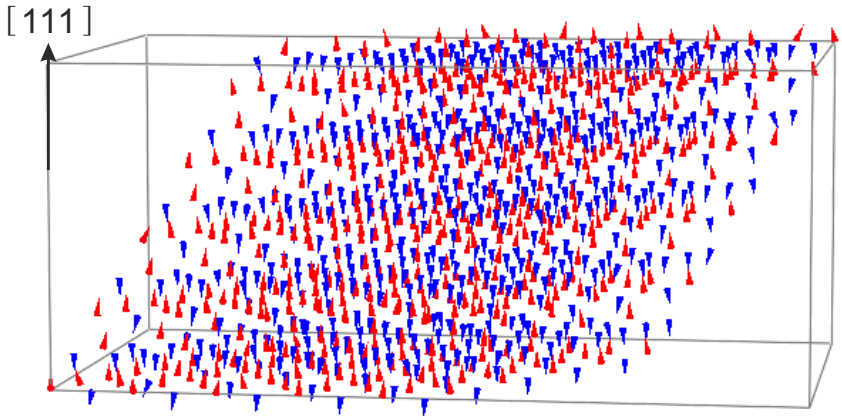

(a) 2 K at the beginning of a ZFC curve

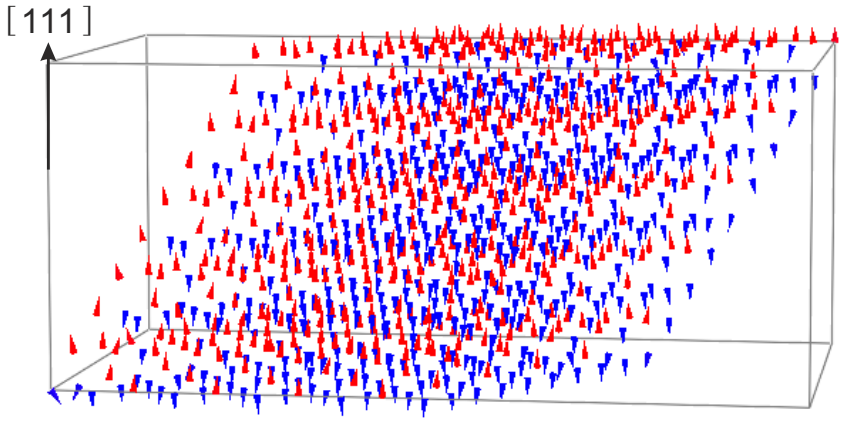

(b) 2 K after a FC procedure

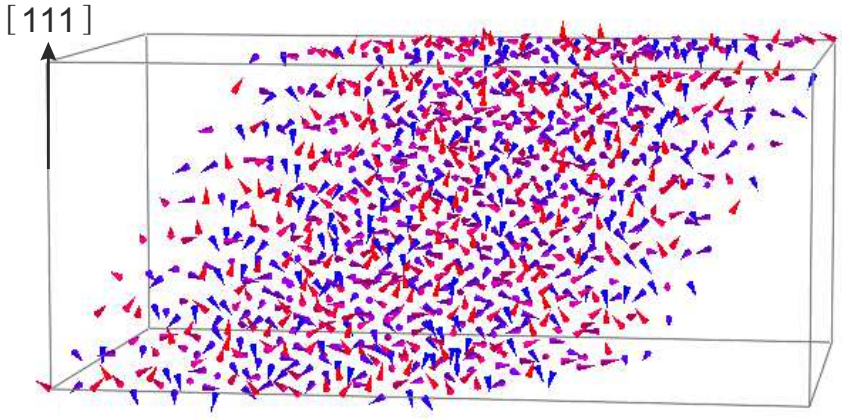

(c) 200 K

Figure 72: Illustration of the spin structure of a 10×10×10 MnO NP simulated with a magnetic field of 1 T (a) at 2 K at the beginning of a ZFC curve, (b) at 2 K after a FC procedure, and (c) at 200 K resulting from the first configuration after 10000 average loops. Both the anisotropy axis and the magnetic field are parallel to the x-direction (crystallographic [111] direction of MnO). Hereby, J_1=constant.

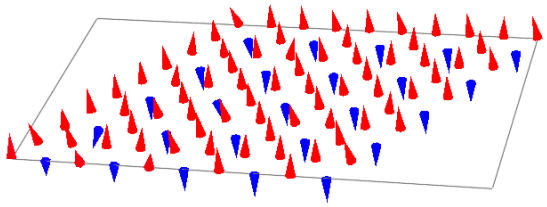

(a) First layer at 2 K at the beginning of a ZFC curve

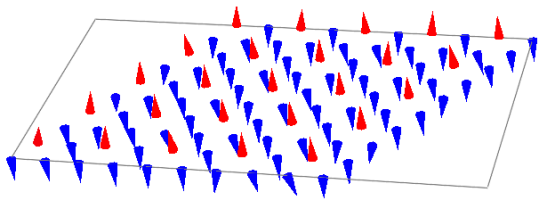

(b) Second layer at 2 K at the beginning of a ZFC curve

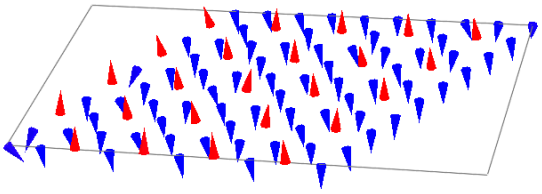

(c) First layer at 2 K after a FC procedure

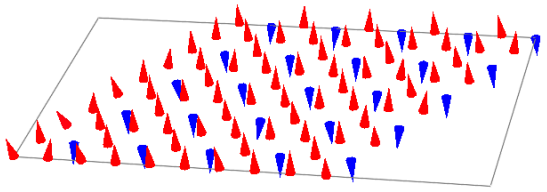

(d) Second layer at 2 K after a FC procedure

Figure 73: Illustration of (a) the first and (b) the second layers counting from the bottom of the spin structure of a 10×10×10 MnO NP simulated with a magnetic field of 1 T at 2 K at the beginning of a ZFC curve (Fig. 72(a)), and (c) the first and (d) the second layers of the spin structure at 2 K after a FC procedure (Fig. 72(b)). Both the anisotropy axis and the magnetic field are parallel to the x-direction (crystallographic [111] direction of MnO). Hereby, J_1=constant.

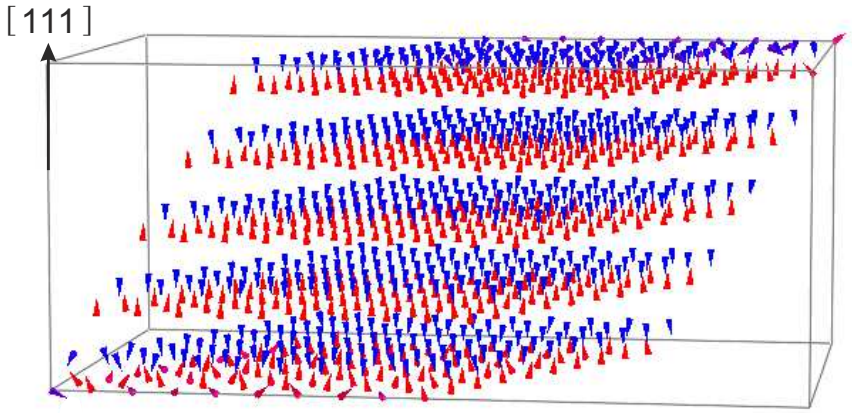

(a) 2 K at the beginning of a ZFC curve

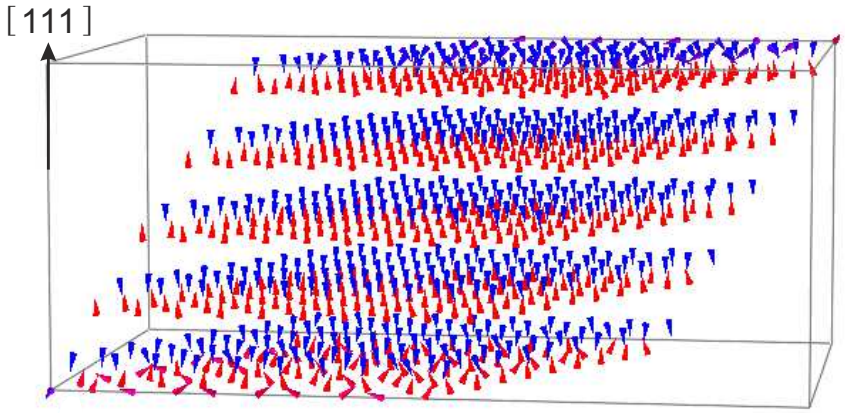

(b) 2 K after a FC procedure

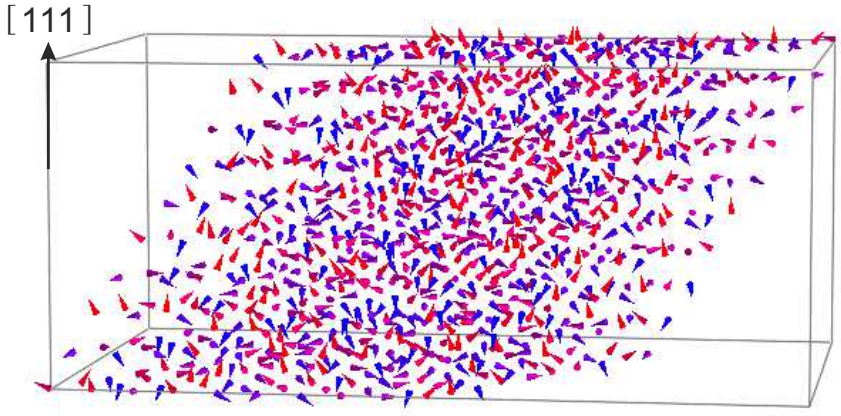

(c) 300 K

Figure 74: Illustration of the spin structure of a 10×10×10 NP simulated with a magnetic field of 1 T (a) at 2 K at the beginning of a ZFC curve, (b) at 2 K after a FC procedure, and (c) at 300 K resulting from the first configuration after 10000 average loops with $J_{1m} \neq J_{1p}$ for nearest neighbours in the same plane and in neighbouring planes. Both the anisotropy axis and the magnetic field are parallel to the x-direction (crystallographic [111] direction of MnO).

Taking the structural distortion into account (i.e. $J_{1m} \neq J_{1p}$ for nearest neighbours in the same plane and in neighbouring planes), a stable AF order along the crystallographic [111] direction as described in [26] can be found (Fig. 74). Only spins in the outermost layers show slight deviations from the [111] direction, which does not have an obvious influence onto the spin structure of the AF core. This indicates that the exchange interaction is still the dominant interaction to keep perfect AF order with a correlation length of about 5 nm at a magnetic field of 1 T. The average magnetization and the standard deviation in x-, y- and z-directions for different (111) layers of a 10×10×10 NP and a MnO "bulk" are listed in Tab. 2 and 3, respectively. The magnetic moments have been normalized to a unit spin. As can be seen, the average magnetization in the surface layers is obviously reduced in the x-direction for the NP compared to "bulk". Moreover, the standard deviation is much larger for the surface layers. Compared to "bulk" MnO, the average magnetization in the inner (111) layers are also slightly reduced. This is due to the surface spins in each layer. Moreover, above the experimental T_N at 118 K, NPs show a random order as expected in both Fig. 72 and 74.

Layer	$\langle M_x \rangle$	$\langle(\langle M_x\rangle\text{-}M_x)^2\rangle$	$\langle M_y \rangle$	$\langle(\langle M_y\rangle\text{-}M_y)^2\rangle$	$\langle M_z \rangle$	$\langle(\langle M_z\rangle\text{-}M_z)^2\rangle$
1	0.824	0.055	0	0.078	0.033	0.187
2	-0.974	0.001	0.014	0.016	-0.032	0.033
3	0.992	0	-0.012	0.005	0.018	0.011
4	-0.994	0	0.011	0.004	-0.021	0.007
5	0.995	0	-0.009	0.004	0.021	0.005
6	-0.994	0	0.007	0.005	-0.022	0.006
7	0.993	0	-0.019	0.006	0.024	0.007
8	-0.991	0	0.017	0.006	-0.023	0.010
9	0.973	0.001	-0.019	0.017	0.024	0.034
10	-0.797	0.059	0.009	0.099	-0.010	0.207

Table 2: List of the normalized average magnetization $\langle M_i \rangle$ and the standard deviation $\langle(\langle M_i\rangle - M_i)^2\rangle$ for different (111) layers of a 10×10×10 NP in x-, y- and z-directions, respectively.

Layer	$\langle M_x \rangle$	$\langle(\langle M_x \rangle\text{-}M_x)^2\rangle$	$\langle M_y \rangle$	$\langle(\langle M_y \rangle\text{-}M_y)^2\rangle$	$\langle M_z \rangle$	$\langle(\langle M_z \rangle\text{-}M_z)^2\rangle$
1	0.9964	0	0.003	0.003	-0.014	0.004
2	-0.996	0	-0.004	0.003	0.003	0.005
3	0.997	0	-0.003	0.003	-0.005	0.004
4	-0.996	0	0.005	0.004	0.007	0.004
5	0.996	0	-0.004	0.003	-0.004	0.004
6	-0.997	0	0.002	0.004	0.011	0.005
7	0.995	0	0.008	0.005	-0.014	0.005
8	-0.995	0	-0.002	0.004	0.014	0.004
9	0.996	0	-0.002	0.005	-0.011	0.004
10	-0.996	0	0.003	0.004	0.001	0.004

Table 3: List of the normalized average magnetization $\langle M_i \rangle$ and the standard deviation $\langle(\langle M_i \rangle - M_i)^2\rangle$ for different (111) layers of a MnO "bulk" in x-, y- and z-directions, respectively.

As discussed in Fig. 66 in section 5.5, the magnetic moments in MnO "bulk" show a complete alignment along the field direction in the ZFC/FC magnetization curves at a magnetic field of 10000 T even up to 300 K. In this case, the AF order is destroyed. To confirm this result, spin structure of bulk MnO simulated at 10000 T is visualized in Fig. 75. As can be seen, all magnetic moments in "bulk" MnO are pointing towards the [111] direction at both 2 K and 300 K, which is parallel to the field direction. Only a few magnetic moments show small deviations from the [111] direction. Blue and red colour indicates the minimum and the maximum value of the x-component of the magnetic moments. At 2 K, magnetic moments with relatively small value in x-direction are still pointing to the [111] direction with a small deviation, which can hardly be observed by naked eyes. However, several magnetic moments show obviously a deviation from the [111] direction at 300 K. This is due to thermal fluctuations at high temperatures, which allows magnetic moments to turn towards the AF order. This result shows a perfect agreement with the magnetization curves (Fig. 66) shown in section 5.5.

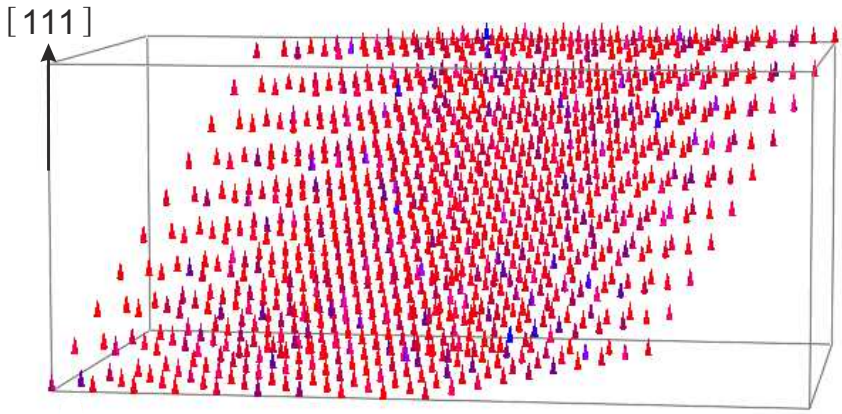

(a) 2 K at the beginning of a ZFC curve

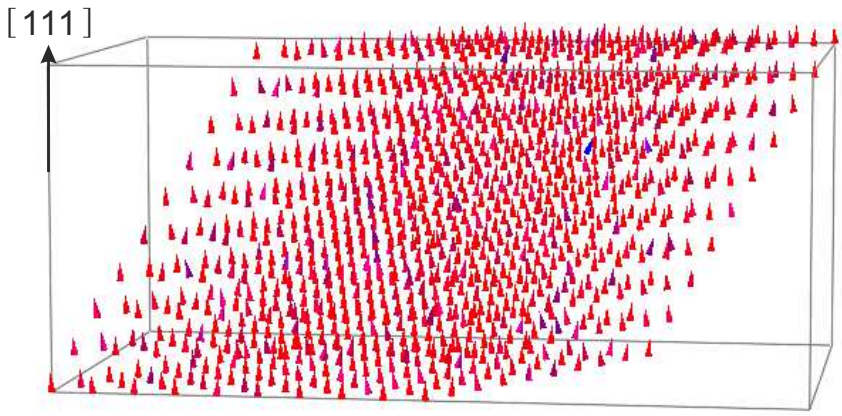

(b) 300 K

Figure 75: Illustration of the spin structure of bulk MnO simulated with a magnetic field of 10000 T (a) at 2 K at the beginning of a ZFC curve, (b) at 300 K resulting from the tenth configuration after 10000 average loops. Both the anisotropy axis and the magnetic field are parallel to the x-direction (crystallographic [111] direction of MnO).

5.6 Summary

In this chapter, the spin structure of MnO NPs, powder and single crystal has been studied using magetometry and neutron scattering. The influence of the existence of a FiM Mn_3O_4 component onto the magnetic behaviour of MnO has been investigated by varying the oxygen content inside the sample following various annealing procedures. Monte Carlo simulations have been performed for various sizes of MnO NPs as well as "bulk" MnO. The simulated results have been compared with the experimental results.

As-prepared MnO nanoparticles

ZFC curves of MnO NPs often show a low temperature peak at ∼25 K instead of a feature indicating the Néel temperature of MnO at T_N≈118 K. However, neutron scattering results of MnO NPs show the expected vanishing of the AF order parameter of MnO near its bulk Néel temperature. This contradiction between the magnetometry and neutron scattering results can be explained using an AF-SPM model as we show in Ref. 18. A model to explain the magnetic behaviour of MnO NPs is shown in Fig. 76. Similar to a SPM system, the Néel vector of the AF MnO fluctuates above the peak temperature as measured in the ZFC magnetization curves. However, below the peak temperature, the AF order is blocked in one of its states during the probing time. By measuring the ac-susceptibility of NPs with 12 nm diameter, the dynamics of the system have been studied. The peak temperature of NPs shows a weak frequency dependence in the ac-susceptibility. However, no reasonable values can be obtained from the fitting of the frequency dependence of the relaxation time with the models described in section 2.2.2. For an AF, no frequency dependence is expected for the feature marking the AF-to-PM phase transition. For a fluctuating system such as a SPM, a much stronger frequency dependence is expected. However, no formula describing the frequency dependence of the relaxation time for an AF-SPM has been reported. Therefore, we speculate that the low temperature peak found at ∼25 K in both the ZFC magnetization curves and ac-susceptibility is likely due to the AF-SPM core in MnO NPs. Moreover, a ferrimagnetic (FiM) Mn_2O_3 or Mn_3O_4 shell is possibly coupled to the core, which may explain the exchange bias (EB) effect found in MnO NPs.

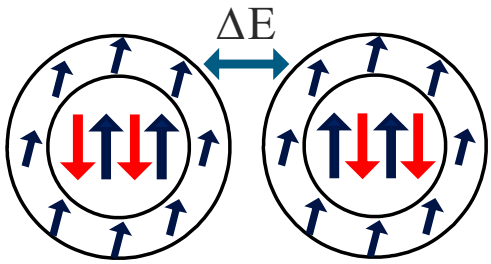

Figure 76: Model to explain the magnetism of MnO NPs. The MnO core shows an AF-SPM behavior which is exchange coupled to a FiM Mn_2O_3 or Mn_3O_4 shell.

As-prepared MnO powder

Commercially available MnO powder and a single crystal show also a low temperature feature in the magnetometry curves in addition to the expected feature at the Néel

temperature of MnO. The low temperature peak observed in the powder sample has a relatively broad shape, which is similar to that usually found in MnO NPs. However, this peak shows no obvious frequency dependence in the ac-susceptibility measurements, which might be due to higher energy barrier for larger NP sizes. Hysteresis loops have been observed at 5 K for the as-prepared MnO powder. The center of the hysteresis loops shifts slightly towards the negative direction, which indicates an EB effect. One should note that an EB effect has also been found in NPs, which might be due to disordered surface spins or an oxidized Mn_3O_4 shell. Moreover, heat capacity measurements show no feature near the low temperature peak. This suggests that the low temperature peak is possibly a crossover from a blocked to a fluctuating AF state rather than a real phase transition. Therefore, we speculate that the low temperature peak observed in the as-prepared powder is likely due to nano-sized MnO particles.

Figure 77: As-prepared MnO powder sample composed of particles with a large size distribution. Large particles with a size of $\sim \mu$m show AF behaviour and small particles ($\sim$ several hundred nm size) show AF-SPM behaviour. After annealing, particles with similar sizes ($\sim \mu$m) can be fabricated.

Moreover, TRM/IRM curves of the as-prepared powder show a similar behaviour as for NPs. To confirm our assumption, the as-prepared MnO powder has been studied using a SEM. In the SEM images, particles with $\sim$hundreds nm size can be found. This further shows that the low temperature peak in the powder sample is likely due to particles with a few hundred nm size. The AF order parameter near the low temperature peak of MnO NPs was not studied using polarized neutron scattering due to the extremely small amount of sample. However, this is achieved by studying the as-prepared MnO powder assuming the low temperature peak comes from the nano-sized particles. The AF order parameter curve of the as-prepared MnO powder shows no obvious feature near the peak temperature at $\sim$30 K observed in the ZFC curves. Using the AF-SPM model, this contradiction between the magnetometry and neutron scattering results can be understood.

As-prepared MnO single crystal

The low temperature peak found in the ZFC magnetization curves of a MnO single crystal has a different shape compared to that found in powder and NPs. The steep drop above the peak temperature and the overall shape of the peak shows a typical FM behaviour. Moreover, the peak temperature matches the Curie temperature of Mn_3O_4 and Mn_2O_3. At 5 K, hysteresis loops were also measured. Therefore, the MnO single crystal seems not to be a pure MnO, but partially oxidized to Mn_3O_4 and Mn_2O_3. Moreover, a weak feature near $\sim$40 K is observed at the Q-value of the (111) Bragg peak of MnO in

the magnetic component of the polarized neutron scattering. Considering the broadening of the peak, this magnetic phase transition might be from the (202) or (211) Bragg peak of FiM Mn_3O_4. Moreover, a nuclear $(\frac{1}{2}\frac{1}{2}\frac{1}{2})$ peak has also been measured in both neutron scattering and x-ray single crystal diffraction. This is possibly due to the Mn_3O_4 grown on the interface between different twins of the crystal, which occasionally results in a doubling of the unit cell along the (111) direction, or due to charge order because of oxygen nonstoichiometry.

Above the Néel temperature of MnO, the diffraction pattern of both polarized neutron scattering and x-ray diffraction can be indexed by a fcc structure. In polarized neutron scattering, magnetic diffuse scattering has been observed at 121 K. Further experiments, such as heat capacity and ac-susceptibility measurements have been performed to confirm the existence of Mn_3O_4 within the MnO single crystal. In both temperature dependent curves of heat capacity and ac-susceptibility, a low temperature peak at ∼40 K can be observed. This peak in the χ' vs. T curves shows no frequency dependence, which is expected for a FM/FiM-to-PM transition. These results further confirm that the low temperature peak found in MnO single crystal is more likely due to oxidized Mn_3O_4. Moreover, TRM/IRM curves have also been measured for the single crystal. Both the TRM and IRM curves show different behaviour from that found in powder and NPs. This can be explained by a superposition of the magnetization of AF MnO and FiM Mn_3O_4.

Annealed MnO

In order to study the intrinsic magnetic properties of single phase bulk MnO, the as-prepared MnO powder was annealed. After being heated at 920°C in vacuum for 150 h, the low temperature peak (∼30 K) disappears in both magnetometry and ac-susceptibility. Moreover, an AF behaviour is found in the field dependent magnetization curve measured at 10 K. Polarized neutron diffraction of the annealed MnO powder shows only the vanishing of the AF order parameter of MnO at 120 K, as expected.

After studying the influence of the nano-size effect as well as the oxidized Mn_3O_4 or Mn_2O_3 onto the magnetic properties of MnO bulk, manganese oxide NPs with various oxygen contents have been studied. As-prepared MnO NPs with 12 nm diameter show strong tendency to be oxidized to higher oxidation state after being stored in air for four years. In this case, a mixture of MnO and Mn_3O_4 is measured. A sharp peak at ∼40 K has been found in the ZFC magnetization curves at a small magnetic field. Above the peak temperature, a steep drop can be observed indicating the Curie temperature of Mn_3O_4 or Mn_2O_3. At high magnetic fields, AF-SPM MnO dominates the magnetic behaviour of the entire system.

Moreover, hysteresis loops with an extremely large coercive field (∼1.5 T) have been measured at 5 K. The center of the hysteresis shifts towards negative direction after cooled within a magnetic field. This indicates an EB effect at the interface between the AF MnO and FiM Mn_3O_4 or Mn_2O_3. The EB field increases with an increase in the cooling field.

To investigate the magnetic properties of pure MnO NPs, the oxygen content within the NPs were reduced by annealing the sample in a vacuum chamber at 310°C for 3.5 h. In this case, almost pure MnO NPs are expected. ZFC/FC curves of the annealed MnO NPs show similar behaviour as that for the as-prepared MnO NPs. A broad peak at about 25 K is found. Moreover, no feature indicating the bulk Néel temperature of MnO can be seen within noise. However, hysteresis loops with a weak EB effect were measured

at 5 K. This might be due to disordered surface spins or not completely reduced Mn_3O_4. Compared to the sample before annealing, the amount of Mn_3O_4 is successfully reduced. The annealed NPs are likely to be single phase MnO with disordered spins or covered by an reoxidized Mn_3O_4 shell.

Moreover, fully oxidized Mn_3O_4 NPs are also of interest to be compared with the results of MnO NPs. Therefore, NPs containing a mixture of MnO and Mn_3O_4 were further oxidized by heating in air at 100° for 15 h. The peak in the ZFC curves at ∼40 K is much sharper than that for the mixture of MnO and Mn_3O_4. Moreover, no EB bias effect is found in the hysteresis loops. These results suggest the success of achieving single phase Mn_3O_4.

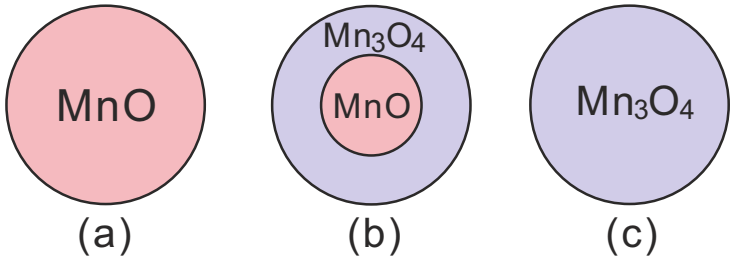

Figure 78: (a) Almost pure MnO NPs can be obtained after the as-prepared sample was annealed in vacuum at 310°C for 3.5 h. (b) MnO/Mn_3O_4 core/shell NPs can be found after the as-prepared particles were stored in air for 4 years. (c) Pure Mn_3O_4 NPs can be fabricated after the NPs were heated in air at 100° for 15 h.

Fig. 78 shows the possible models of the NPs produced after various procedures. However, it is also possible that the oxygen content and thus the crystal structure in the NPs varies continuously from surface to the center. In this case, no clear boundary between the MnO core and Mn_3O_4 shell is expected. Moreover, the core and shell might be so strongly coupled so that no separated feature resulting from MnO and Mn_3O_4 can be observed.

Monte Carlo Simulations

In order to have a better understanding of the spin structure in MnO bulk and NPs, Monte Carlo (MC) simulations have been performed. By using a Hamiltonian with constants obtained from previous studies, ground state spin structures of NPs and "bulk" can be simulated. Firstly, the textbook spin model of MnO is used, where the anisotropy axis is parallel to the crystallographic [111] direction. During ZFC and FC procedures, magnetization curves of NPs with various sizes as well as "bulk" were simulated and compared with the experimental results. Also, simulations have also been performed using splitted exchange constants J_{1m} and J_{1p} for nearest neighbours within the same plane and in neighbouring planes, respectively. This splitting due to a cubic-to-rhombohedral structural distortion below the Néel temperature has been reported in previous studies. The results are compared with that using a non-split J_1. However, a simultaneous simulation of both magnetic and structural phase transitions is not trivial and has therefore not been performed. The magnetization curves with and without considering a structural distortion were simulated separately, and the results were compared.

"Bulk" MnO without a splitting of J_1 shows a similar behaviour in the ZFC/FC curves

as measured in experiments. A peak at ∼140 K indicating the AF-to-PM phase transition of MnO is found. However, a higher Néel temperature is obtained, when $J_{1m} \neq J_{1m}$ is used.

Moreover, MC simulations have also been performed for NPs with various sizes. Interestingly, NPs with even and odd number of Mn show different behaviour. For NPs with an even number of Mn, a reduced Néel temperature is found. In contrast to "bulk" MnO, which shows no obvious field dependence at its critical temperature, the critical temperature of NPs is reduced as the magnetic field increases.

Moreover, the peak temperature of a 10×10×10 MnO NP shows no difference with different MC steps indicating different measurement time. This is expected for an AF. However, NPs with an odd number of Mn show SPM behaviour. This is due to an uncompensated layer in one of its AF sublattices. For NPs with an even number of layers, the magnetization from both AF sublattices can be almost fully compensated. Therefore, only AF behaviour is found. Both the blocking temperature and the reduced Néel temperature decrease with a decrease of the NP size. This can be explained by a nano-size effect.

To get a direct view of the spin structure of MnO, snapshots of the spin structure below and above the Néel temperature are visualized. Without considering a structural distortion, MnO "bulk" and NPs show various AF ordering at 2 K. However, none of these AF orders show a perfect parallel alignment of magnetic moments within (111) planes as well as an AF ordering in neighbouring plane as obtained from experiments. When a splitting of the exchange constant $J_{1m} \neq J_{1m}$ is used, the textbook AF order can be seen at 2 K. In addition, above the T_N of MnO, magnetic moments are randomly ordered as expected. Compared to "bulk", the NPs show a slight disorder of the surface spins.

In real experiments, not only NPs with one defined size n×n×n is measured. The real samples are usually a mixture of various sizes of particles, such as (n+1)×(n+1)×(n+1), n×n×(n+1) or n×n×(n+2). Therefore, we cannot directly compare the simulations with the experimental results, which is the superposition of the magnetic behaviour of individual NPs.

6 Magnetism of Iron Oxide Nanoparticle Superstructures

As introduced in section 2.2, superspins in single domain FM or FiM NPs may interact with each other and thus show collective behaviour. In this thesis, the magnetic properties of self-organized iron oxide NP structures have been investigated. Various sizes of iron oxide NPs (5 - 20 nm) were used. The NPs with 5, 15 and 20 nm sizes are from Ocean NanoTech and the 11 - 13 nm NPs are from the collaboration group of Dr. Aladin Ullrich from the University of Augsburg . Sizes and shapes of the NPs were characterized using scanning electron microscopy (SEM), transmission electron microscopy (TEM) as well as small angle x-ray scattering (SAXS).

Depending on the concentration of NPs in the dispersions as well as depending on the self-assembly methods, various structures from quasi-0D to 3D were achieved. Structural characterization of self-organized iron oxide NPs was performed using SEM and grazing incidence small angle x-ray scattering (GISAXS). Phases of iron oxides in the NPs were determined by x-ray powder diffraction (XRD) in combination with magnetometry measurements. The magnetic properties of self-assembled NP structures were measured. The influence of the dipolar interactions between NP superspins were studied by comparing the results of samples with various NP concentrations. Moreover, a hardening effect was found in the hysteresis loops after the sample is cooled at various magnetic fields. Also, the oxygen content within iron oxide NPs was varied and the influence onto the magnetic properties were studied.

In this chapter, iron oxide as well as the current state of research on iron oxide NP will be introduced at first in section 6.1. Then the methods of NP self-assembly as well as the annealing procedures to vary the crystalline phases of iron oxide NPs will be introduced in section 6.2 and 6.3. After that, the structural characterization and magnetometry results of self-assembled NP will be discussed in section 6.4 and 6.5, respectively.

6.1 Introduction to Iron Oxides

Iron oxides have been widely used since centuries due to their ubiquitous existence in nature. Various phases of iron oxides have different colours. For example, hematite and magnetite have bright red and black colours, respectively [106, 107], goethite is yellow [108]. Therefore, they have been found in rock paintings as well as famous ancient vases as pigments. This is also due to their extremely stable structure. Moreover, iron oxides can be produced at low cost, which makes the application of iron oxides more popular. Iron oxides are also well-known as catalysts for both organic and inorganic reactions. In biomedicine, iron oxide NPs are of huge interest due to their non-toxicity.

6.1.1 Phases of Iron Oxide

Iron is a transition metal with an electron configuration $[Ar]3d^6 4s^2$. For iron oxides, it is the 3d electrons in Fe ions that determine the electronic and magnetic properties of the compounds. Despite a wide range of possible oxidation states of iron, Fe^{2+} and Fe^{3+} are the most commonly found. Combining divalent and trivalent irons with various ratios, different phases of iron oxide can be formed. In this section, four naturally existing iron oxides will be introduced based on Ref. 109.

Wüstite Wüstite (FeO) is a black material with a rocksalt crystal structure as shown in Fig. 79(a). It contains only divalent irons. However, stoichiometric FeO does not exist at atmospheric pressure. Only non-stoichiometric $Fe_{1-x}O$ with 1-x ranging from 0.83 to 0.95 is stable above 567°C at atmospheric pressure. When it is slowly cooled down to room temperature, $Fe_{1-x}O$ disproportionates to Fe and Fe_3O_4. However, this non-stoichiometric structure can remain as a metastable phase at room temperature if it is quenched from above 567°C [109, 110]. Moreover, wüstite is an important intermediate in the reduction of iron ores.

Wüstite is an AF with a Néel temperature of 198 K in bulk [111–113]. Neighbouring Fe^{2+} ions interact with each other via superexchange mediated by an oxygen ion. Within its (111) planes, magnetic moments align parallel. However, magnetic moments in neighbouring (111) planes arrange antiparallel [109].

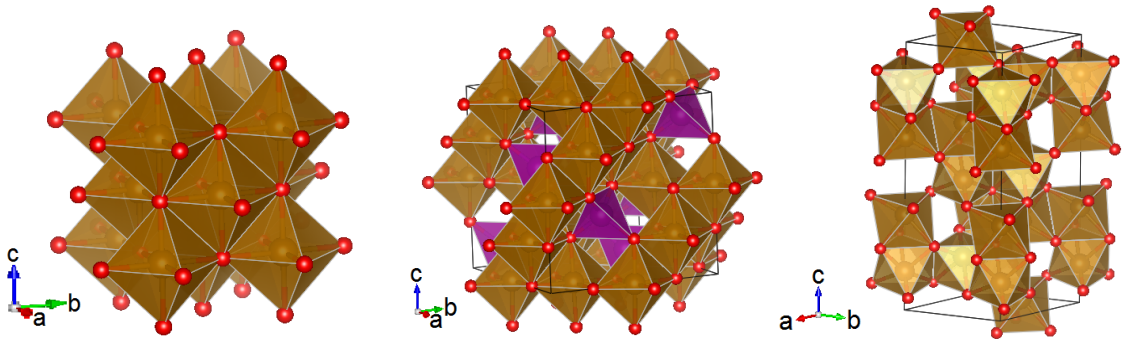

(a) wüstite (b) magnetite (c) hematite

Figure 79: Illustration of the crystal structures of (a) wüstite, (b) magnetite and (c) hematite. The brown and purple colours mark the octahedra and tetrahedra in the crystal structures, respectively. The red and brown spheres indicate the positions of oxygen and Fe atoms, respectively. The data used here are obtained from the Inorganic Crystal Structure Database (ICSD) and plotted using the software "Vesta" [114].

Magnetite Magnetite is known as natural magnet, which has the chemical formula Fe_3O_4. It is a black mineral containing both divalent and trivalent Fe. Magnetite has an inverse spinel structure with a lattice constant $a = 0.839$ nm as shown in Fig. 79(b) [109, 115]. On the tetrahedral sites, only trivalent irons can be found. However, an equal number of Fe^{2+} and Fe^{3+} occupy the octahedral sites.

Magnetite is a FiM below its Curie Temperature $T_C = 858$ K [112, 116, 117]. Fe^{2+} and Fe^{3+} on the octahedral sites interact ferromagnetically via double exchange. However, Fe^{3+} between tetrahedral and octahedral sites interact antiferromagnetically via superexchange. Even though magnetite possesses a large magnetization and coercivity, it is not suitable for recording devices due to its magnetic instability [118].

Due to the mixed valency and the double exchange mechanism, magnetite is a conductor at room temperature with a conductivity of 200 $(\Omega\,\mathrm{cm})^{-1}$ in its bulk form [119]. Other phases of iron oxide containing only divalent or trivalent iron are insulators. Moreover, the Verwey transition at $T_V = 120$ K has been observed for magnetite. Below 120 K, its conductivity drops two orders of magnitude [116, 117, 120]. Moreover, a slight crystallographic distortion below $T_V = 120$ K can be found [116, 117, 120].

Maghemite Maghemite (γ-Fe_2O_3) is a red-brown mineral with an inverse spinel crystal structure similar to magnetite. The lattice constant is a = 0.834 nm [109]. Different from magnetite, all or most iron ions in maghemite are in a trivalent state.

Maghemite is a FiM below $T_C \approx 948$ K [109,112,121]. Besides its low cost and chemical stability, maghemite possesses a large coercivity of $H_C = 20$ - 35 kA/m. Therefore, it is used as ideal magnetic pigment for electronic recording devices. When maghemite is doped or coated with cobalt, its coercivity can be increased to 40 - 75 kA/m and thus the stability is further improved. Besides cobalt, CrO_2 doped maghemite has often be used in audio tapes and floppy discs in the past due to its low cost. Moreover, an uniaxial magnetic anisotropy has also been observed in coated maghemite [118].

Hematite Hematite (α-Fe_2O_3) is an important pigment with a red colour. It has a hexagonal unit cell with a = 0.5034 nm and c = 1.375 nm as shown in Fig. 79(c) [122–125]. Due to the structural matching between the (111) plane of magnetite and the (001) plane of hematite, epitaxial growth of magnetite can possibly be observed in hematite and vice versa. α-Fe_2O_3 is extremely stable and is often found as the end product transformed from other iron oxides.

Hematite has two magnetic phase transitions. At $T_C = 948$ K, a PM-to-AF phase transition can be found [112]. However, weak FM behaviour below 948 K can be observed implying spin canting. Below the Morin temperature $T_M = 260$ K, hematite shows pure AF behaviour.

6.1.2 Iron Oxide Nanoparticles

Iron oxide NPs can potentially be used in biomedicine and spintronic devices [126, 127]. For example, carbon nanostraws filled with Fe_3O_4 NPs are potential candidates for drug transport as well as for medical diagnosis without surgical interference [16]. Using an external magnetic field, such "nanosubmarines" can pass through blood vessels and be guided to a specific position. Recent studies on iron oxide NPs usually show a SPM- or SSG-like behaviour in ZFC/FC magnetization curves [16,127,128]. The peak temperature decreases with decreasing NP size. Moreover, the peak temperature shows also a field dependence as expected for SPM or SSG systems [129]. With a prominent ratio of wüstite in the NPs, a steep increase near the Néel temperature of wüstite (198 K) can be observed [127]. Moreover, an EB field vanishing near $T_N \approx 198$ K can also be found. In case of magnetite NPs, the Verwey transition T_V can be observed. For smaller sizes of magnetite inside NPs, a reduced T_V has also been reported [127]. Fe_3O_4 NPs uniformly filled in carbon nanotubes display larger saturation magnetization as well as larger coercive field compared to single Fe_3O_4 NPs due to dipolar interactions [16]. AC-susceptibility results can be well fitted using the Vogel-Fulcher law indicating SG/SSG behaviour of both single Fe_3O_4 NPs and Fe_3O_4 filled carbon nanotubes [16].

Similar to its bulk form, wüstite is not chemically stable in NP form. It tends to decompose into α-Fe and Fe_3O_4 or oxidize to other iron oxide phases with a higher oxidation state of Fe. This makes the synthesis of wüstite difficult. As-prepared wüstite NPs are usually covered by an oxidized Fe_3O_4 shell [130, 131]. Such AF/FiM core/shell NPs are ideal to study the EB effect in NP systems. Horizontal and vertical shifts of the center of the hysteresis loops can often be found in Fe_xO/Fe_3O_4 core/shell NPs below the Néel temperature of wüstite (~ 198 K) after a FC procedure [127, 128, 130–132]. Under controlled

oxidation conditions, the thickness of the Fe_3O_4 shell can be varied [130]. After the NPs were oxidized in a dry air atmosphere at higher temperatures, an increase in the magnetization was observed. Moreover, the Verwey transition of Fe_3O_4 can also be observed in the ZFC/FC magnetization curves [130]. By controlling the oxidation temperature or time, the sizes of the core or shell can be tuned. As the oxidation temperature is increased, the Verwey transition of Fe_3O_4 becomes more prominent indicating an increased thickness of the Fe_3O_4 shell. Moreover, an asymmetry in the hysteresis loops has been reported [130].

Systematic studies on tuning the phases of iron oxide in NP systems have been reported in Ref. [2, 127]. By annealing the as-prepared wüstite NPs in an oxidizing atmosphere, they may transform into magnetite or maghemite nanocrystals [2,133,134]. When the NP dispersion is heated at 120°C for 90 min in a dry air atmosphere, Fe_xO NPs may be fully oxidized to Fe_3O_4 [2,130]. When wüstite NPs are annealed at 200°C for 30 min, γ-Fe_2O_3 can be achieved [2]. Moreover, almost single phase γ-Fe_2O_3 NPs have been reported after annealing Fe_xO NPs at 170°C for 20 min. The EB effect observed for these NPs indicated a small amount of wüstite, which could not be detected by XRD [127]. If the temperature is further increased, α-Fe_2O_3 can be produced after the Fe_xO NPs are oxidized at 500°C for 120 min in air or under an Ar atmosphere [2]. In addition, multi-phase Fe_xO/Fe_3O_4 or Fe_xO/γ-Fe_2O_3 has been reported when the as-prepared NPs were annealed at 230°C in vacuum for 20 min [127].

The EB effect has also been found in Fe_3O_4/γ-Fe_2O_3 core-shell NPs [135], Fe embedded in an iron oxide matrix [136], Fe/Fe_3O_4 core-shell and Fe_3O_4 hollow-shell NPs [137]. An increased squareness of the hysteresis loops after a FC procedure associated with the EB effect has been reported [31,127,138]. Due to the exchange coupling at the AF/FM(FiM) interface, an anisotropy axis is produced.

In several studies, a decrease in the magnetization has been observed in the FC curves below the peak temperature found in the ZFC curves . This might be due to the existence of AF wüstite or dipolar coupling between NPs [126, 127, 139]. With an increasing NP concentration, the peak temperature increases [129, 139]. Fe/FeO core/shell NPs are reported to show SSG behaviour due to inter-particle interactions [140]. AC-susceptibility of Fe_3O_4 NPs shows a frequency dependence. The peak temperature found in the χ' curves depending on frequency follows the Vogel-Fulcher law, which confirms the SSG model [129]. TRM/IRM curves of iron oxide NPs mainly show SPM or SSG behaviour with the influence of wüstite [127].

In order to obtain information about the phase and crystallographic structure of the NPs, XRD is often used [128,132]. However, both magnetite and maghemite have a similar spinel crystal structure. With the broadening of the reflections due to the small size of the NPs, it is difficult to distinguish magnetite and maghemite using XRD. Therefore, further methods such as absorption spectroscopy has been used to identify Fe_3O_4 or Fe_2O_3 [131]. Combining XRD and HR-TEM, a Fe_xO/Fe_3O_4 core-shell structure could be confirmed [132]. Using local electron energy loss spectra (EELS) the diameter/thickness of the Fe_xO core and Fe_3O_4 shell could be obtained [128]. The stoichiometry of Fe_xO can be characterized from the analysis of the iron oxidation state of the core. Neutron diffraction has been used to confirm the AF order in 45 nm iron oxide NPs [128]. However, no magnetic reflection indicating an AF order have been observed in 9 nm NP [128]. To obtain the size as well as the size distribution of the NPs, SEM, TEM and SAXS measurements have often been performed [52, 141–143]. The magnetization distribution inside NPs was studied in absolute units. A reduced magnetization as well as spin canting

was observed from SANS experiments [52, 141–143]. Furthermore, iron oxide NPs have also been studied using ferromagnetic resonance and Mössbauer spectroscopy [128].

6.2 Current State of Research on Self-Assembly

In analogy to atoms, NPs can be building blocks for NP supercrystals, which may possess novel electronic and magnetic properties. Self-organized NPs, especially magnetic NPs, have been intensely studied since decades. This is due to their potential applications in high density data storage, spintronic devices, functional materials and biomedicine.

The monodispersity of particles is an important prerequisite for the self-assembly over large areas. Colloidal particles such as silica and Au nanocrystals are readily prepared with very high degree of monodispersity in large quantities. Therefore, they are often used for self-assembly studies. Monodispersed magnetic NPs are usually stabilized by an oleic acid shell to avoid agglomeration and to be dispersed in solution. Various methods to achieve large areas of ordered particles have been summarized in Ref. 144 and 145.

Using a liquid-air interface method, colloidal spheres prefer to order two dimensionally. With modified surfactants, the spheres float on the surface of the liquid after they spread on the liquid-air interface. Due to attractive interactions, they spontaneously form a 2D hexagonal array. The ordered film is then transferred to a substrate. By varying parameters, such as the size of spheres, the concentration, the surface hydrophobicity, the charge density on the surface of the colloids, electrolytic properties of the underlying liquid, the morphology of the ordered structure can be tuned. With the control of the depth, which the colloidal spheres immersed in the liquid, 2D arrays with relatively large domain sizes can be achieved [146].

Another method for 2D self-organization is using capillary forces. When the particles are suspended in a thin liquid layer with a thickness smaller than or equal to the particle diameter, they tend to form hexagonal 2D arrays due to attractive capillary forces between them [147]. With a controlled evaporation rate, the speed of the convective particle transport can be controlled [147].

Spin-coating is often used to speed up the evaporation rate of the solution. By controlling the speed of rotation as well as the concentration of the particle dispersion, 2D order can be achieved [144, 148]. However, to obtain large areas of homogeneous self-assembly, the wetting throughout the entire substrate has to be controlled. This can be done by adding surfactants into the solution or precoating the substrate with a thin layer of the surfactant [144]. Moreover, patterned substrates were also used to improve the correlation length of the ordering [149].

There are further methods reported for 2D NP self-organisation such as electrophoretic deposition, where a dispersion of colloidal spheres is confined between two parallel solid electrodes [144]. When a sufficiently large electric field is applied, the spheres arrange in 2D hexagonal order. A “Doctor Blade” casting method has also been used for large area self-assembly of nanocrystals. Hereby, a droplet of NP dispersion is uniformly spread over the substrate using a blade moving at a constant height above the substrate with constant speed [150]. Using this method, NP thin films with fcc or hcp structures can be fabricated [150]. Moreover, drop-casting, or the Langmuir-Blodgett technique were also used to produce well-ordered self-organized particle thin films [150].

Self-organized films with a homogeneous thickness are not easy to be fabricated. Sometimes the self-organized monolayers are polycrystalline with domain boundaries, vacancies and other defects. At some places, a second layer may also be found. This can be due to different growth modes, i.e. Frank van der Merve, Volmer-Weber and Stranski-Krastanov modes. For monolayer self-assembly, the Frank van der Merve mode is desired. In this case, the particle-to-substrate interaction dominates. This mode prefers to grow a planar layer before starting the second one. With the control of the amount of particles settled onto the substrate, monolayers or multilayers can be produced [148].

However, when the particle-particle interaction dominates, Volmer-Weber growth is favoured. Particles prefer to attach to each other rather than to the substrate. Therefore, 3D islands are found. The Stranski-Krastanov growth mode is not of interest for self-assembly. With this mode, a mixture of 2D and 3D structures grows. By tuning the particle-particle and particle-to-substrate interactions, self-assembled particle films with various thickness can be formed [148]. Iron oxide NP dispersions spin-coated on a Si substrate usually form hexagonally ordered monolayers with defects. In this case, Frank van der Merve growth is preferred. However, when the Si substrate is coated e.g. with polymethyl methacrylate (PMMA), individual islands of closed-packed NPs with $\sim 1\mu$m size form after the NP solution is spin-coated on the substrate [148].

The methods introduced above have been successfully used for 2D assembly in previous studies. To achieve 3D structures, for example opal structures, other methods were used. The simplest method for 3D self-assembly is sedimentation in a gravitational field [144, 145]. As a result of gravitational settling, Brownian motion and electrostatic repulsion, the particles form a cubic-close-packed (ccp) or face-centered-cubic (fcc) lattice [144,145]. This method has been successfully used to produce 3D ordered silica particle superlattices. Apart from the density and size of the particles, the rate of sedimentation plays also an important role for the quality of the ordered 3D structures.

When the colloidal spheres are highly charged, they may spontaneously form a 3D structure in solution to minimize electrostatic repulsions [144]. Moreover, highly ordered 3D colloidal crystals with $\sim \mathrm{cm}^3$ can be achieved, when the particles are confined within a volume [144,145]. Template-directed self-assembly has been reported for 3D crystalline arrays. 3D structures composed of colloidal crystals can be produced with a size of $\sim 1\,\mathrm{cm}^3$ [151]. Using these highly ordered structures as a template, macroporous materials can be produced [144]. Moreover, flow-induced deposition such as horizontal deposition (for example, spin-coating) or vertical deposition can also be used for 3D particle lattices [145].

Co-assembly of two types of nanocrystals into binary superstructures may produce novel materials with programmable properties arising from interactions between different components [152]. Centimetre sized binary nanoparticle superlattices (BNSLs) have been successfully fabricated using the liquid-air-interface method [152]. By tuning the size and/or the concentration ratio of Fe_3O_4 and FePt NPs, BNSLs with various structures and stoichiometries can be produced. Fe_3O_4-FePt BNSLs are potential candidates for magnetoresistive devices. By varying the structure or stoichiometry of BNSLs, the magnetoresistance of the materials can be tuned [152].

The size, shape and size distribution of the particles can be obtained from TEM and SAXS measurements [52, 126, 127, 141–143, 148]. To characterize the structural order of self-organized particles, SEM, X-ray reflectivity (XRR) and GISAXS measurements have been used [52, 126, 141–143, 148, 150]. SEM images provide a direct view of the particle ordering within a small area in real space. XRR and GISAXS measurements

can provide information about the out-of-plane and in-plane ordering in reciprocal space. Magnetic correlations perpendicular and parallel to the film have been studied using polarized neutron reflectivity (PNR) and GISANS [52,126,141–143,148,150]. Using these methods, self-assembled mesocrystals composed of highly truncated cubic iron oxide NPs have been studied [52,141–143]. The magnetization distribution inside magnetic NPs can be obtained in absolute units. PNR results of iron oxide NPs show a strong correlation between self-assembled NPs [126]. The magnetic behaviours of the system was attributed to a quasi-2D dipolar SSG [126].

6.3 Sample Preparation

The iron oxide NPs used in this thesis are commercially available spherical NPs (Ocean NanoTech) with a diameter of 5, 15, and 20 nm, as well as 12 and 13 nm spherical NPs and 11 nm cubic NPs from a collaboration with Dr. Aladin Ullrich of the Institut für Physik at the University Augsburg. Here we focus on the NP 2D self-assembly as well as the magnetic properties of various phases of iron oxide NPs. In the following sections, self-assembly methods as well as annealing procedures to vary the iron oxide phases inside the NPs will be introduced.

6.3.1 Self-Assembly

In this thesis, large-areas of self-organized iron oxide NP monolayers are of interest. Various methods were used to produce 2D ordered NPs. They are illustrated in Fig. 80. Drop-casting is the simplest method. Here a certain volume of NP dispersion is dropped onto a Si(100) substrate. With the control of the evaporation rate and the amount of NPs on the substrate, self-organized NP films with different thicknesses and morphologies can be produced. Fig. 81 shows SEM images of NP films formed using 15 nm iron oxide NPs via drop-casting. As can be seen in Fig. 81(a), multilayers of hexagonally ordered iron oxide NPs can be observed when the NP dispersion has the original concentration from Ocean NanoTech (25 mg/ml).

In order to fabricate a monolayer, the original NP dispersion has to be diluted. After comparing the SEM images of self-organized films using various concentrations, we found that the original dispersion diluted with toluene to a ratio of 1:20 shows the best results for monolayer self-assembly. However, there are some areas which are not covered with NPs and some areas, where a second layer can be found (Fig. 81(b)). Interestingly, when the NPs have a broad size distribution, they tend to separate into different regions as shown in Fig. 81(c). NPs with similar sizes tend to stay together and form a hexagonal lattice. This result further proves the impact of NP monodispersity onto the self-assembly. Since the monolayers produced by the drop-casting method are usually polycrystalline and the morphology is not homogeneous over the entire sample, a “second chance” can be given to the NPs to improve their ordering by adding extra toluene to the already self-assembled films. Fig. 81(d) shows the SEM image of the NP monolayer fabricated with additional toluene added after drop-casting. During the second self-assembly procedure, the substrate is gently moved to help NPs being homogeneously distributed. As can be seen, the substrate is covered by a monolayer of well ordered NPs. However, the monolayer breaks into domains. Moreover, at the right bottom of the image, a second layer can be found. The reason is possibly that the movement during the second self-assembly

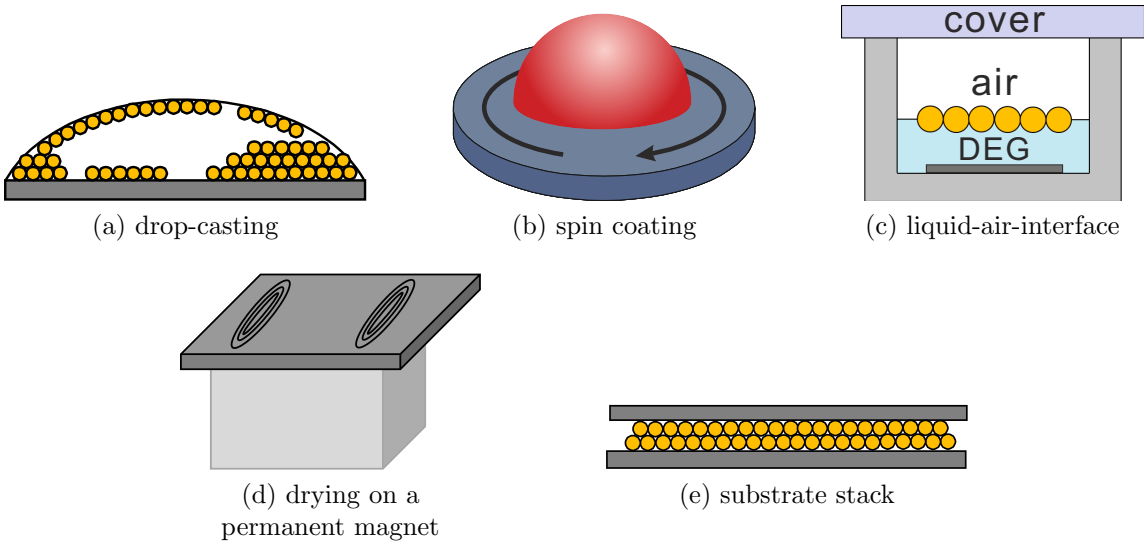

(a) drop-casting (b) spin coating (c) liquid-air-interface

(d) drying on a permanent magnet (e) substrate stack

Figure 80: Various methods for NP self-assembly used in this thesis: (a) drop-casting, (b) spin coating, (c) liquid-air-interface, (d) magnetic field guided self-assembly and (e) substrate stack.

process was too strong. Further experiments were performed without movement after extra toluene was added to the ordered NP film. The quality of the monolayers were slightly improved. The average size of the hexagonal ordered areas obtained from the SEM images is slightly increased.

Si(111) substrates were also used for NP self-assembly. After the oxide layer was removed using diluted hydrofluoric acid, the NP dispersion was drop-casted onto the substrates. During the second self-assembly iteration, the sample was kept unmoved. To reduce the evaporation rate and to prevent any inhomogeneous air flow at the surface of the dispersion, the sample container was covered by a foil. A SEM image of NP structures fabricated using this method is shown in Fig. 82. As can be seen, hexagonally ordered NPs with relatively large correlation lengths can be obtained. Even though a second layer or defects can be observed at some positions, the order over the entire sample is evidently improved compared to the 1-step drop-casting and the 2-step process with movement.

The same method was also performed on Si(100) substrates. Compared to Fig. 82, the morphology of NP ordering on Si(100) substrate is not as good as on Si(111) substrates. This might be due to possible steps on the Si(111) substrate because of a substrate miscut, which helps the NPs to order.

Due to surface tension, the NP dispersion dries faster at the edge of the substrate than in the middle using the drop-casting method. Thus the NP ordering is not homogeneous over the entire sample. This problem can be solved by using spin-coating (Fig. 80(b)). In this case, the substrate is fixed on a spin-coater, which can rotate around the substrate normal with a controllable speed. After the NP dispersion is dropped in the middle onto the substrate, it starts to rotate, so that the NPs can be homogeneously spread over the entire substrate. With the control of the concentration of dispersion as well as the rotation speed, NP films with various thickness may be produced. Using this method, the quality of the NP monolayers are similar to that fabricated using drop-casting.

A liquid-air-interface method has also been used for 2D self-assembly. As illustrated in

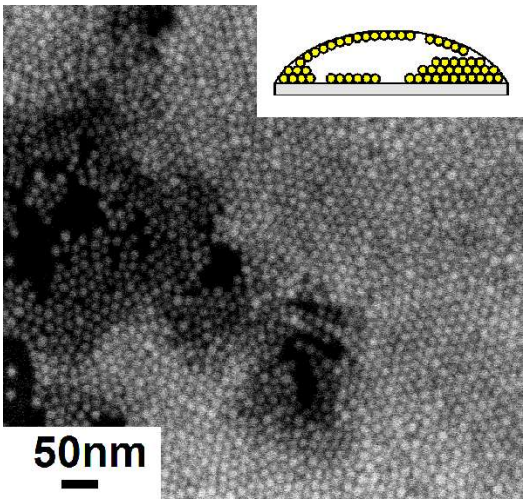

(a) drop-casting with original concentration

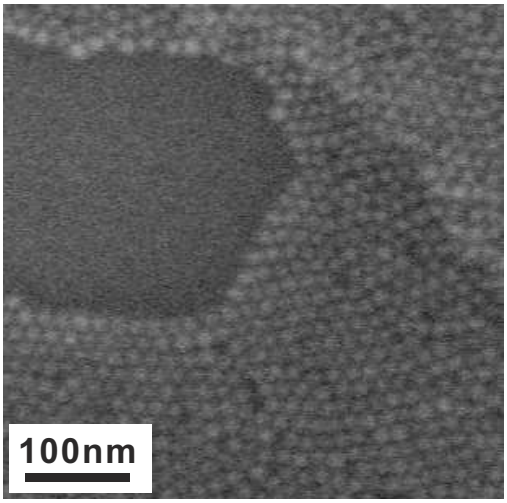

(b) drop-casting using diluted dispersion

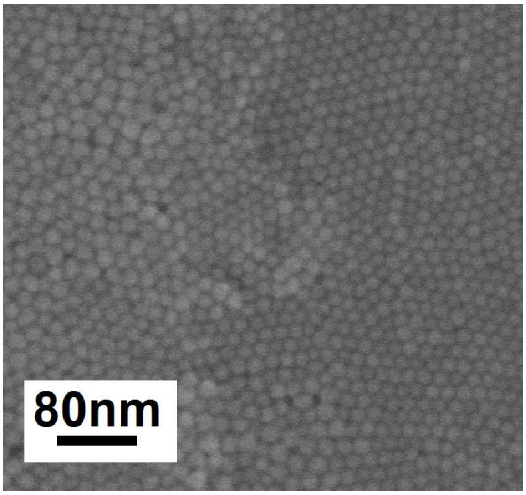

(c) NPs with a broad size distribution

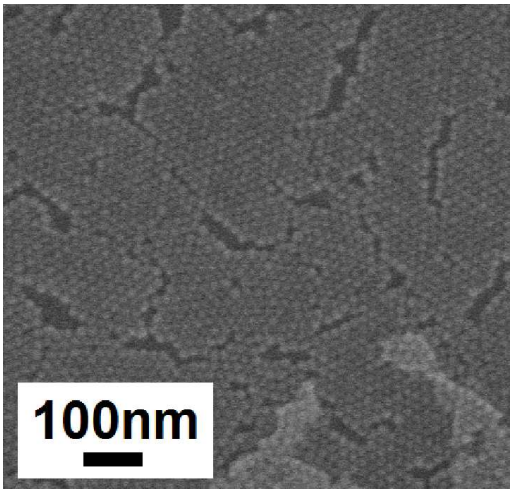

(d) adding toluene and moving after drop-casting on a Si(100) substrate

Figure 81: SEM images of self-assembled spherical iron oxide NPs with 15 nm diameter from Ocean NanoTech using various methods. (a) Drop casting of NPs with original concentration, (b) drop-casting of NPs diluted with toluene to a ratio of 1:20, (c) drop-casting of NPs with a broad size distribution and (d) adding toluene and moving the sample after drop-casting on a Si(100) substrate.

Fig. 80(c), 15 nm iron oxide NPs dispersed in toluene have been spread on the surface of diethylene glycol (DEG). With the control of the evaporation rate of toluene, a monolayer may form at the liquid-air interface. After the DEG is dried, the ordered NP film lands onto a Si substrate. As can be seen in Fig. 83, in this case NPs order hexagonally with an average correlation length of ~ 500 nm. However, this method is not successful for 20 nm NPs. This might be due to different thickness of oleic acid shells around 15 nm vs. 20 nm NPs, which influences the interaction between NPs. Moreover, to synthesize iron oxide NPs with different sizes, different parameters need to be used. This may lead to the growth of different iron oxide phases in 15 nm vs. 20 nm NPs, and thus lead to different

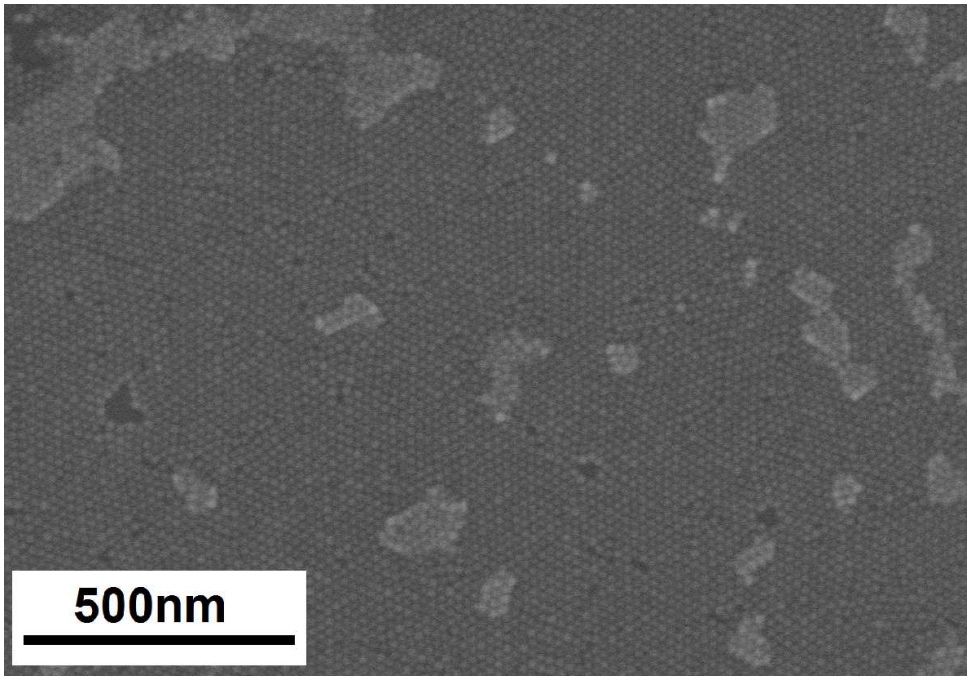

Figure 82: SEM image of self-assembled spherical iron oxide NPs with 15 nm diameter with extra toluene added after drop-casted on a Si(111) substrate.

densities of the NPs. Both the NP density and the surfactant influence how deep the NPs are immersed into DEG. If the interactions between NPs is not strong enough to attract them together, no order can be formed.

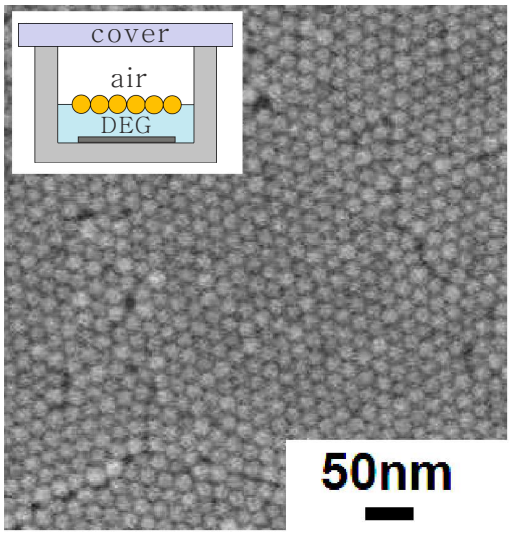

Figure 83: SEM image of self-assembled spherical iron oxide NPs with 15 nm diameter using the liquid-air-interface method.

The capillary force has been reported to play an important role in NP self-assembly. It can be used when filling NP dispersion between two polished substrates with a small distance. One way to achieve this is to stack two substrates. After that the NP dispersion is dropped near the gap between two substrates. Due to the capillary force, NPs can be

driven within the gap and a homogeneous film may form between the substrates. Another way is to drop a controlled amount of NP dispersion on one piece of Si substrate first, and then covering the droplet with another piece of Si substrate. Fig. 84 shows the SEM images of NP films produced with the help of capillary force. As can be seen in Fig. 84(a), large areas of almost perfectly ordered multilayers can be observed near the edge of the substrates. In the middle of the substrate, several μm^2 of area of hexagonally ordered monolayers with a few defects can be seen (Fig. 84(b)). If the NP concentration is reduced, monolayers of NP may be observed near the edges. However, only small NP clusters can form in the middle.

For magnetic NPs, their superspins may align along an external magnetic field and thus have an influence onto the self-assembly. Fig. 85 shows the SEM image of 20 nm NPs self-organized above a magnetic cube. Near the magnetic poles, stripes of NPs with different thickness can be seen (appendix H). This might be an indication of the magnetic field lines. A bit away from the magnetic poles, where the magnetic field is relatively homogeneous, monolayers of NPs with large correlation lengths can be observed (Fig. 85).

Summarizing the methods discussed above, the largest area of monolayers can be produced using substrate stacking or magnetic field guided self-assembly. However, such nice ordering is not homogeneous over the entire substrate. On the contrary, using drop-casting, spin-coating, or liquid-air-interface methods the morphology over the substrate is more homogeneous. Even though they cannot produce $\sim \mu m^2$ areas of perfectly ordered monolayers, samples prepared by drop-casting plus toluene on Si(111) have been focused on for scattering experiments, because in this case the average order of the entire sample area is of interest.

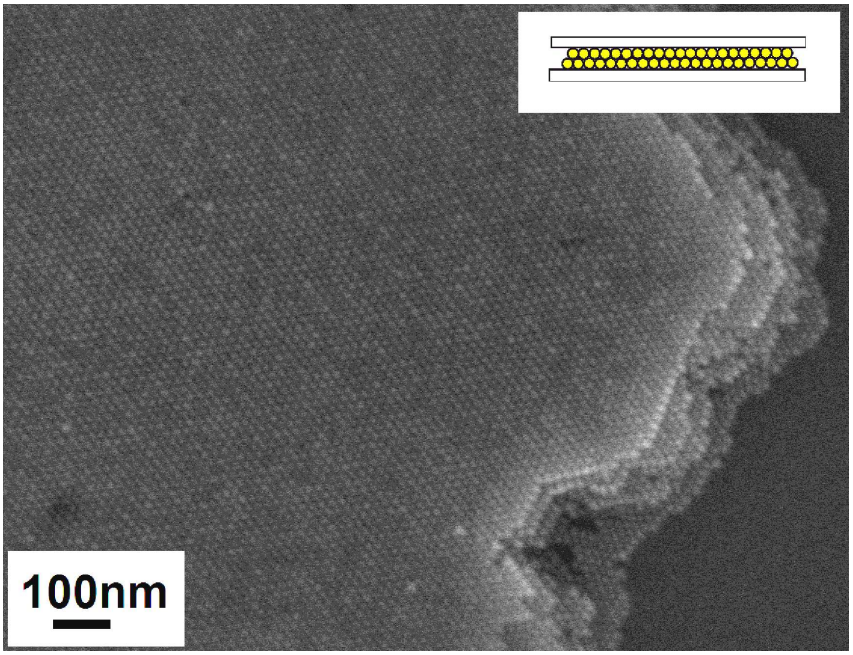

(a)

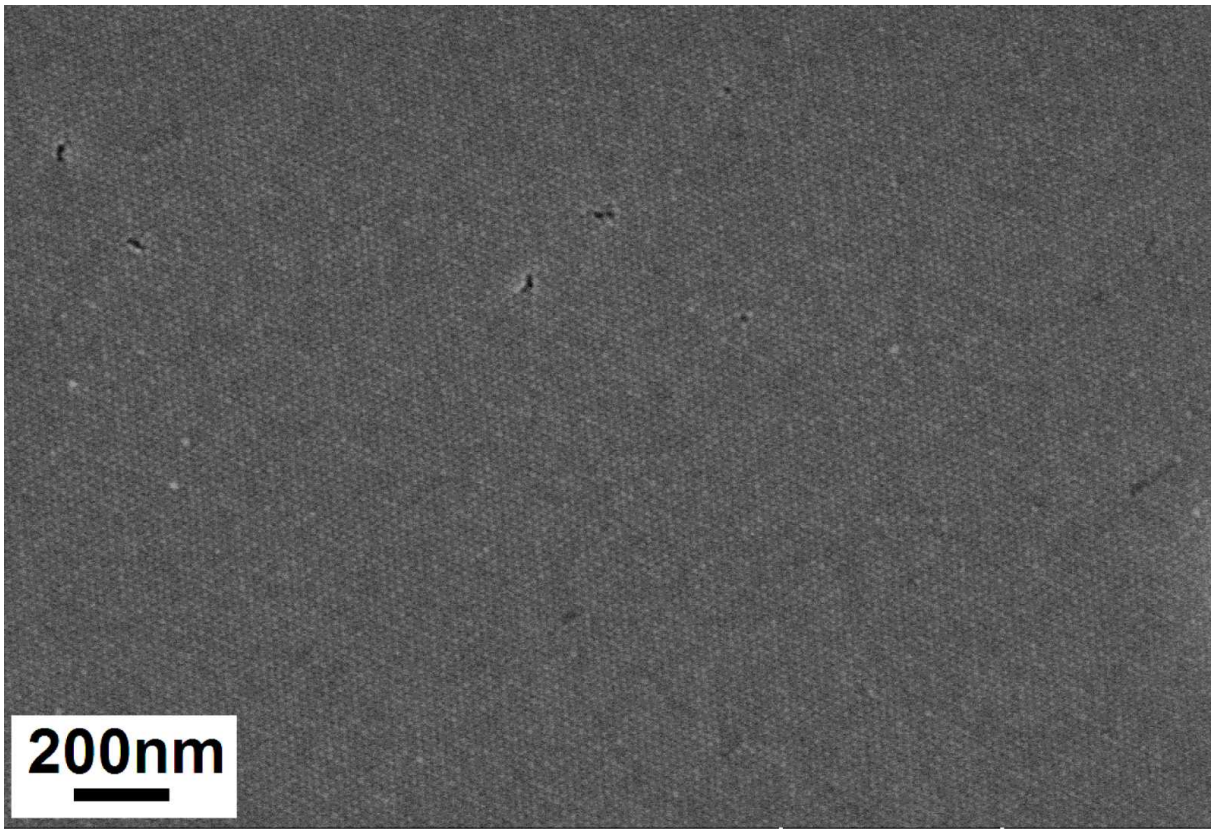

(b)

Figure 84: Self-assembled spherical iron oxide NPs with 15 nm diameter using the substrate stacking method at different regions of the sample: (a) near the edge and (b) in the middle of the substrate.

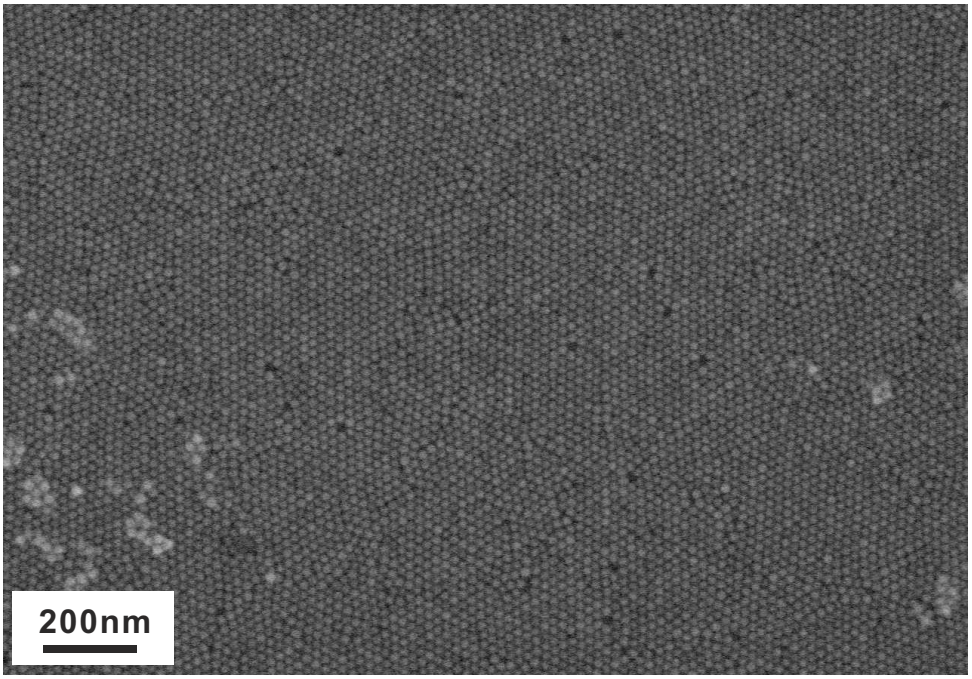

Figure 85: SEM image of self-assembled spherical iron oxide NPs with 20 nm diameter dried above a magnet cube.

6.3.2 Sample Annealing

As introduced in section 6.1.2, as-prepared iron oxide NPs are usually not single phase. In order to study magnetic properties of various phases of iron oxide NPs, self-assembled NP films produced using the drop-casting method were annealed in a vacuum chamber, which has already been introduced in section 5.2.3. In order to reduce the oxygen content, samples were heated in vacuum at 318°C for various durations. To achieve higher oxidation states of iron, the samples were heated in air at about 120°C for various durations.

All samples focused on in this thesis are listed in table 4. The dilution ratio indicates the ratio of the original dispersion to the added solvent. Samples without information about the annealing procedure are referred to as "as-prepared" NPs.

sample name	size [nm]	shape	dilution ratio	environment	T [°C]	t [h]
$ONT5_{ori}$	5	spherical	original	-	-	-
$ONT5_{dil}$	5	spherical	1:20	-	-	-
$ONT5_{ori}^{oxi}$	5	spherical	original	air	120	20
$ONT5_{ori}^{ann}$	5	spherical	original	vacuum	318	5.5
Aug11	11	cubic	original	-	-	-
Aug12	12	spherical	original	-	-	-
$Aug12^{oxi}$	12	spherical	1:5	air	120	16
$Aug12^{ann}$	12	spherical	1:1	vacuum	318	4.5
Aug13	13	spherical	original	-	-	-
$ONT15_{ori}^{a}$	15	spherical	original	-	-	-
$ONT15_{ori}^{b}$	15	spherical	original	-	-	-
$ONT15_{dil}^{a}$	15	spherical	1:30	-	-	-
$ONT15_{dil}^{b}$	15	spherical	1:30	-	-	-
$ONT15_{dil}^{ann}$	15	spherical	1:5	vacuum	318	4
$ONT15_{dil}^{oxi}$	15	spherical	1:15	air	122	15
$ONT20_{ori}$	20	spherical	original	-	-	-

Table 4: List of iron oxide NP samples focused on in this thesis. "ONT" and "Aug" in the sample names indicate that the samples are obtained from Ocean NanoTech and University Augsburg, respectively. The numbers in the sample names indicate the size of NPs. The "ori" and "dil" in the subscript mark the concentration of NP dispersions. The "oxi" and "ann" in the superscript mean that the samples have been treated in various procedures. T and t refer to the annealing temperature and duration, respectively. The superscripts a and b for sample ONT15 refer to samples with a size distribution of $\sim$20% and $\sim$10%, respectively.

6.4 Structural Characterizations

The mean size and the size distribution of the NPs have been characterized by TEM and small angle X-ray scattering (SAXS). Fig. 86 shows TEM images of the as-prepared iron oxide NPs from the collaboration with the University Augsburg. As can be seen, the 12 nm NPs exhibit a good monodispersity. Moreover, large areas of hexagonal ordering can be found (Fig. 86(a)). 13 nm spherical and 11 nm cubic NPs show a slightly worse monodispersity compared to the 12 nm sample. Short-range order can still be found in Fig. 86(b) and (c).

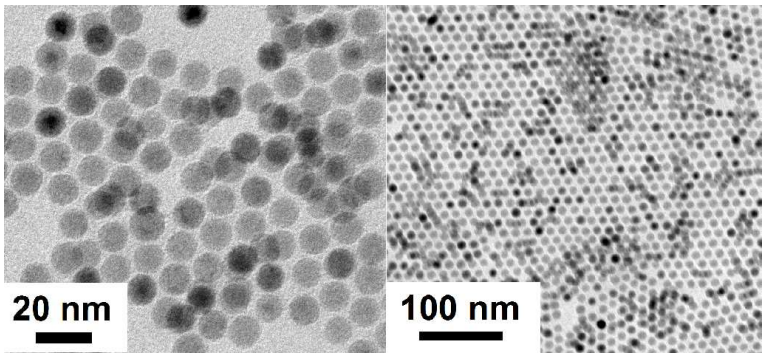

(a) spherical NPs with 12 nm size

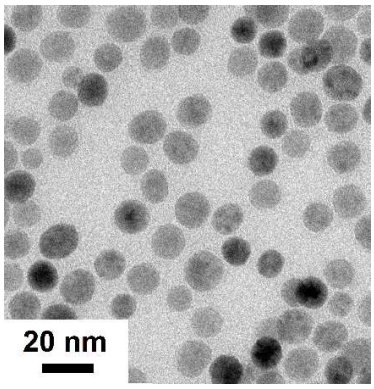

(b) spherical NPs with 13 nm size

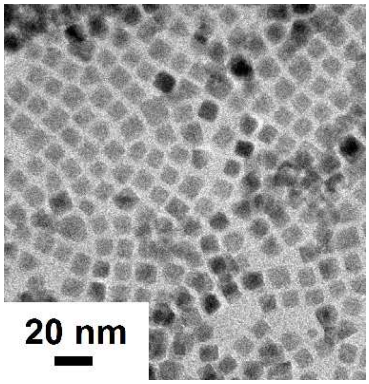

(c) cubic NPs with 11 nm size

Figure 86: TEM images of spherical iron oxide NPs with (a) 12 nm and (b) 13 nm size and (c) cubic NPs with 11 nm size from the collaboration with the University Augsburg.

Results obtained from the TEM images have been confirmed by SAXS measurements using the in-house instrument GALAXI. Table 5 lists the sizes and the size distributions obtained from SAXS measurements.

The crystal structure of the 15 nm iron oxide NPs has been measured using XRD (Fig. 87). Due to the nanometer size, the reflections in the XRD pattern are weak and broad compared to its bulk form. Moreover, the amount of particles used for XRD measurement is very small. Therefore, it is difficult to separate few weak reflections from background. In Fig. 87, the measured pattern is compared to the calculated intensity using the spinel structure of Fe_3O_4. The positions of the reflections expected for wüstite and magnetite bulk are marked with blue and red bars, respectively. As can be seen, the positions of most reflections measured for 15 nm NPs match very well with that of

sample name	size [nm]	size distribution
ONT5	5.8	23.6 %
ONT15	15.6	12.9 %
Aug11	10.6	29.2 %

Table 5: Sizes and the size distributions of the iron oxide NPs used in this thesis obtained from SAXS measurements.

magnetite bulk. However, the calculated intensity does not match the observed intensity. One has to note, that maghemite has also a spinel structure, which is similar to magnetite. Taking the broadening of the reflections into account, it is not easy to distinguish magnetite and maghemite in XRD patterns. Moreover, as discussed in the last chapter, a small ratio of impurities could not be separated from the background. Therefore, the existence of a small amount of wüstite inside the sample cannot be excluded.

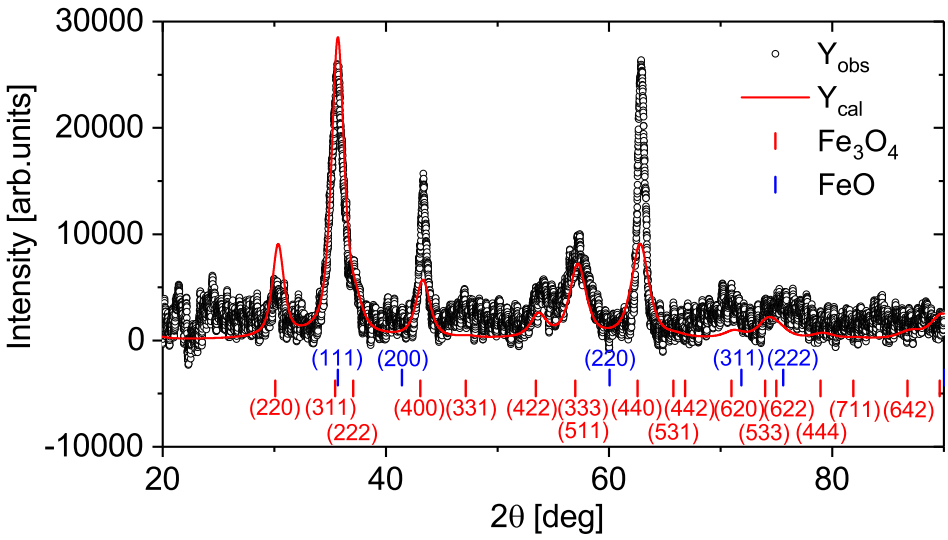

Figure 87: XRD pattern for iron oxide NPs with 15 nm diameter. Y_{obs} is the observed pattern, Y_{obs} is the calculated pattern using a single magnetite phase. Red and blue bars mark the positions of reflections expected for magnetite and wustite bulk, respectively.

The superstructure of self-organized NPs has been characterized using GISAXS. In Fig. 88(a), vertical lines can be observed in the GISAXS pattern. These lines mark the 2D order of NPs. Moreover, powder rings can also be found in Fig. 88(a), which are related to the form factor of the NPs. They are due to partially disordered particles and polycrystalline domains in the sample. Moreover, the GISAXS patterns have been simulated using the software "BornAgain" [67] and compared with experimental results. As can be seen in Fig. 88(b), the simulated patterns match the experimental data in (a). To obtain this simulated patterns, hexagonally ordered spheres with 13 nm size have been used. Such a NP size is smaller than the result of 15 nm obtained from TEM and SAXS measurements. This is possibly due to a slight deformation of the NPs, when they were

drop-casted on the substrate. Therefore, the form factor cannot be fully described by a spherical model. Another possibility is that the pixel-values in the measured data are not perfectly converted to the correct Q-value. The lattice parameter of the hexagonal lattice used for the simulated patterns is 18 nm. This value is a slightly larger than the distance between the center of two particles, when they are attached to each other. This might be due to the oleic acid shells covered around the NPs, which have a thickness of 1 - 2 nm. The powder rings in Fig. 88(b) arise from 1% disordered spheres to simulate polycrystalline domains in the real sample. However, the intensities in the simulated pattern do not quite match the experimental results. This is possibly because the well-ordered areas are much smaller in the real sample. The polycrystalline regions show more contributions to the disorder.

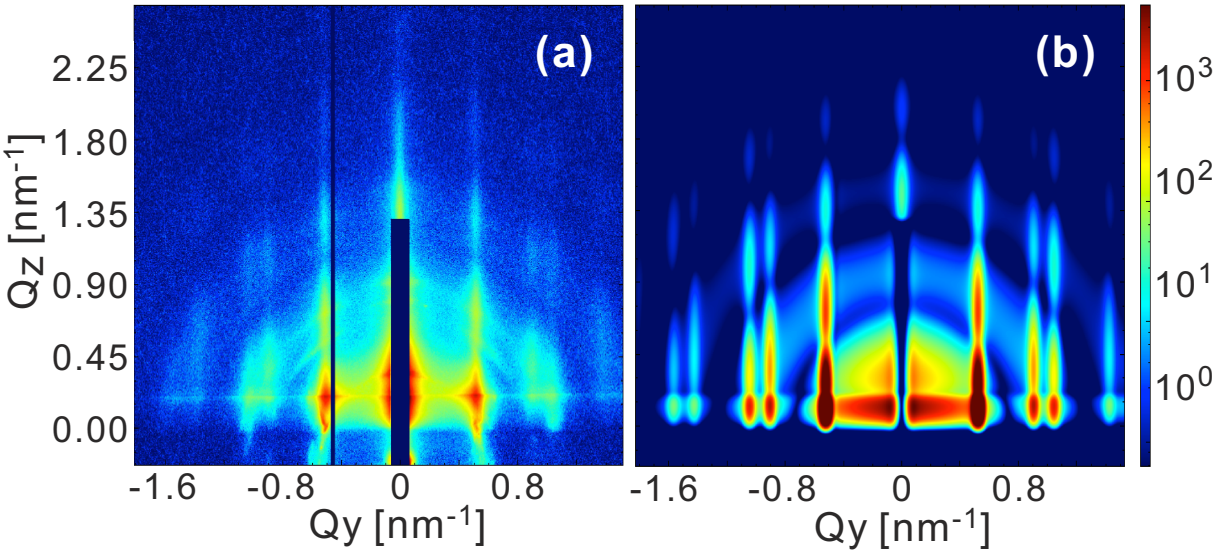

Figure 88: (a) GISAXS pattern from self-assembled iron oxide NPs with 15 nm diameter using the drop-casting plus toluene method. (b) GISAXS pattern simulated for hexagonally ordered spheres with 13 nm diameter. The lattice constant of the hexagonal lattice is 18 nm. The powder rings arise from 1 % disordered spheres.

6.5 Experimental Results

Apart from self-assembly, we have investigated the magnetic properties of iron oxide NPs as well as the influence of the dipole-dipole interaction. In this work, I focus on NPs with various sizes (5 - 20 nm). NP films produced using the drop-casting method have been measured using magnetometry. Moreover, we have also studied the magnetic properties of different phases of iron oxide after various annealing processes.

As-prepared NPs with 20 nm diameter (ONT20$_{ori}$)

Fig. 89(a) shows the ZFC/FC magnetization curves of 20 nm diameter iron oxide NPs measured at 2 mT. The ZFC curve start with a negative value. This is possibly due to a negative residual field in the superconducting solenoid during the cooling procedure. As can be seen in the ZFC curve, the magnetization increases rapidly above 200 K, which

matches the Néel temperature of wüstite, and reaches a maximum at about 300 K. Below the peak temperature (∼300 K), the ZFC and FC curves split. This is often observed in SPM and SSG systems. Below 200 K, the magnetic moments of magnetite and/or maghemite are exchange biased by AF wüstite. Above T_N of wüstite, the FiM moments are released and start to turn along the magnetic field. Therefore, the overall magnetic moment increases until thermal fluctuation destroys the order.

Above the peak temperature, the system is in an unblocked SPM or SSG state depending on the interaction strength between NPs. In the insets of Fig. 89(a), a peak near 100 K can be found. This might be an indication of the Verwey transition of magnetite, which is shifted to a lower temperature due to the finite size effect. As the feature at T_V is quite weak, the sample contains only a small amount of magnetite. Below the peak temperature (280 K), the overall magnetic moment of the sample decreases in the FC curve. Such decrease is often observed in AF systems. Moreover, this can also be due to dipolar interactions between NPs [41, 140]. Summarizing all information obtained from the ZFC/FC curves, this sample is likely composed of some wüstite, a small amount of magnetite, and mainly maghemite.

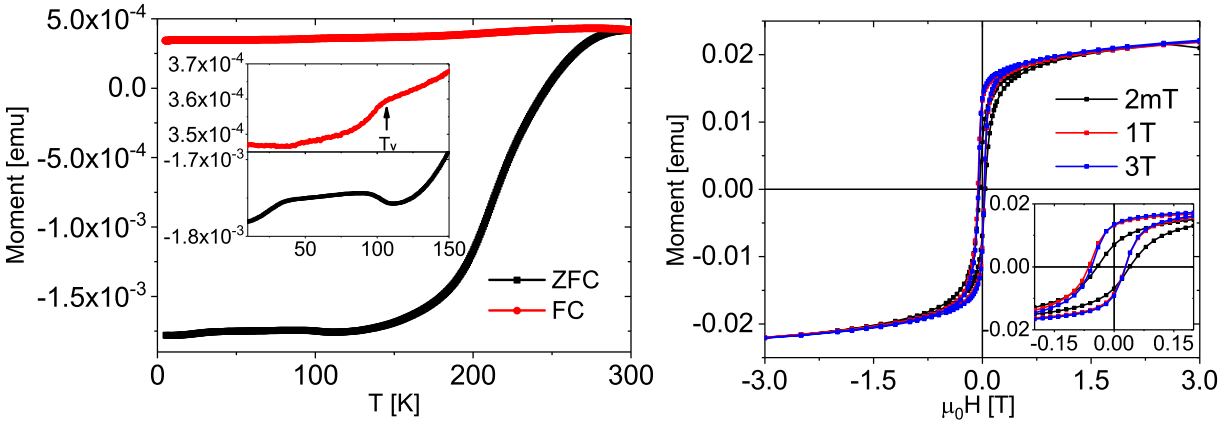

Figure 89: (a) ZFC/FC magnetization curves of 20 nm iron oxide NPs measured at 2 mT. Insets in (a) shows an enlarged view of the ZFC/FC curves at low temperatures. (b) Hysteresis loops of 20 nm iron oxide NPs measured at 5 K after cooling in various magnetic fields. Inset in (b) shows an enlarged view around the origin.

Field dependent magnetization curves of 20 nm NPs have been measured at 5 K after cooling in a magnetic field of 2 mT, 1 T and 3 T, respectively (Fig. 89(b)). As can be seen in the inset, an open loop can be observed. In this case, the NP superspins are in a blocked SPM or SSG state. The centre of the loops is slightly shifted towards the negative field direction. This indicates an EB effect, which can be expected at the interface between AF wüstite and FiM magnetite or maghemite. The EB field H_{ex} and the coercive field H_c depending on the cooling field H_{FC} is plotted in Fig. 91. This will be discussed later. Interestingly, the hysteresis loops become more square-like as the cooling field increases. This can be identified as a hardening effect, which has previously been observed in biased Fe nanodots [153] and ball-milled FM particles embedded in an AF matrix [154]. When the sample is cooled down in an external magnetic field, an additional anisotropy is induced due to the EB effect. The FM/FiM spins are locked in one direction by the biasing

AF spins. Therefore, the magnetization reduces slower compared to the case, when the FM/FiM moments are not or only weakly exchange biased. As the cooling field increases, the strength of the EB field increases. Thus it is harder to turn the FiM/FM spins away from the locked direction. Therefore, the hysteresis loop becomes more square-like.

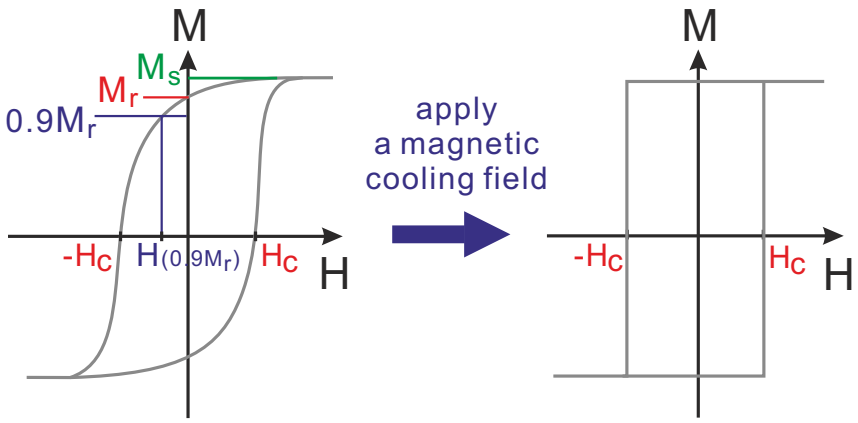

Figure 90: Schematic illustration of the hardening effect and definitions of several values.

A schematic illustration of the hardening effect is shown in Fig. 90. By comparing the hardness and squareness of the hysteresis loops, which are defined by:

$$Squareness = \frac{M_r}{M_s} \tag{71}$$

$$Hardness = \frac{H_{0.9M_r}}{H_c} \tag{72}$$

the hardening effect can be systematically studied. Fig. 91 shows the coercive field H_c, EB field H_{ex}, the squareness and the hardness of the hysteresis loops depending on the cooling field H_{FC}. As can be seen, all four values increase until 1 T and stay constant until 3 T. This indicates that the hardening effect is correlated with the EB effect. Moreover, above 1 T a weak decrease can be seen for H_c and H_{ex}. This can be understood, in the sense that the Zeeman energy overcomes the AF exchange interaction for large magnetic fields. As a result, the EB effect is reduced. For 20 nm iron oxide NPs, the squareness is doubled from 2 mT H_{FC} to 1 T. The hardness increases for about 60 %.

As-prepared NPs with 15 nm diameter (ONT15$_{ori}$)

In order to study the magnetic properties of iron oxide NPs for different sizes, also 15 nm NPs from the same company as the 20 nm particles have been studied. In Fig. 92(a), a peak at 200 K can be found in the ZFC curve. Compared to 20 nm NPs, the peak temperature T_p decreases from 300 K to 200 K. Even though the H_{FC} is slightly different for both samples (2 mT for 20 nm NPs and 5 mT for 15 nm NPs), the tendency of decreasing in the peak temperature can be obviously seen. The ZFC and FC curves split at a higher temperature than T_p. This is due to a broad distribution of peak temperatures for different sizes of NPs, which indicates a broad size distribution of the particles. Below 180 K, the magnetization in the FC curve decreases. This is possibly due to a small amount of wüstite in the NPs and/or the dipolar interactions between NPs. In the inset in (a), a weak feature in the FC curve at ~110 K can be found. This might be an indication of

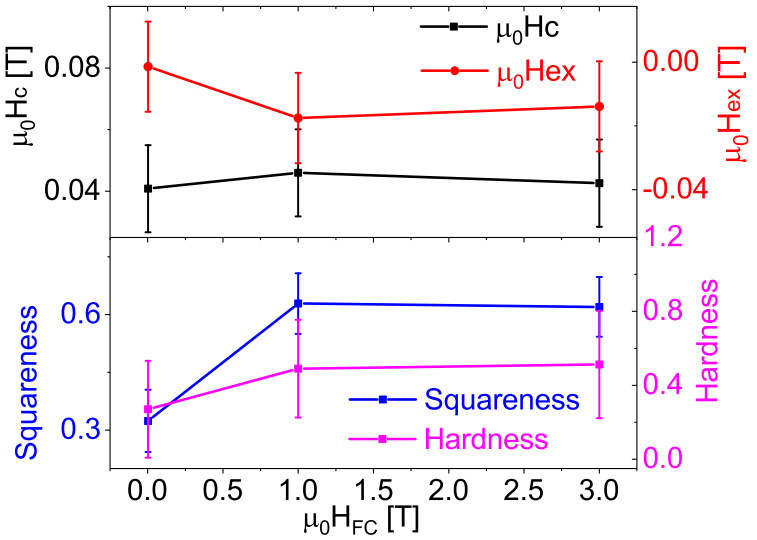

Figure 91: EB field (H_{ex}), coercive field (H_c), squareness and hardness of 20 nm iron oxide NPs obtained from hysteresis loops.

the Verwey transition of magnetite. This T_V is reduced possibly due to the finite-size effect. Since the feature is quite weak, the amount of magnetite is probably very small. Therefore one can conclude that this sample contains mainly maghemite with a small amount of wüstite and magnetite, being a similar composition as the 20 nm NPs.

As the magnetic field increases to 1 T, the peak temperature decreases from 200 K to 50 K (Fig. 92(b)). Such a strong field dependence of the peak temperature has often been observed in SPM and SSG systems. Moreover, the magnetization in the FC curve decreases faster above 200 K than below 200 K. This might be due to the existence of wüstite. When the AF domains of wüstite are aligned with the magnetic field, an anisotropy parallel to the field direction may be induced below T_N through exchange coupling between the AF and FiM moments inside the NPs.

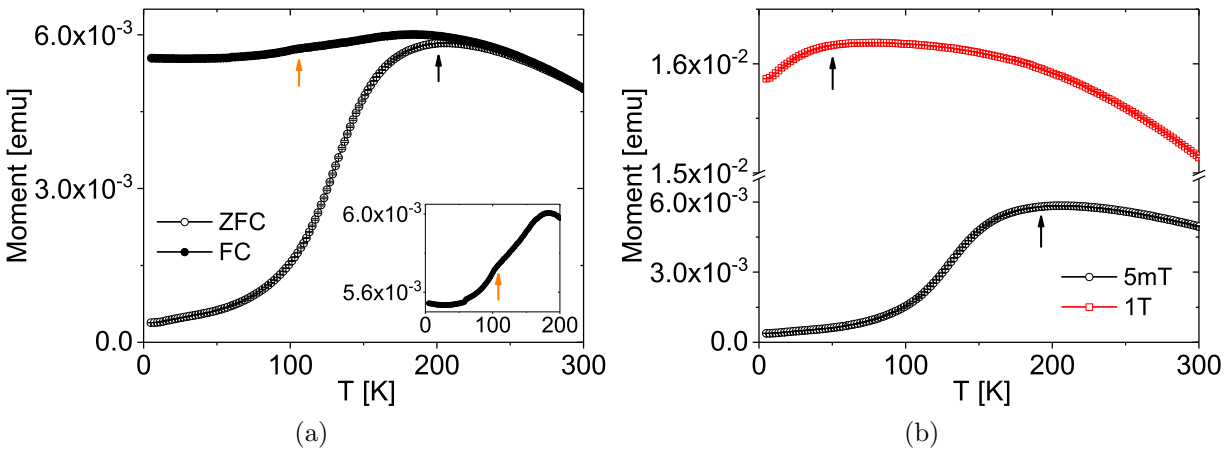

Figure 92: (a) ZFC/FC magnetization curves of 15 nm iron oxide NPs measured at 5 mT. (b) ZFC curves measured at two magnetic fields. The orange and black arrows mark the T_V of magnetite and the peak temperatures, respectively.

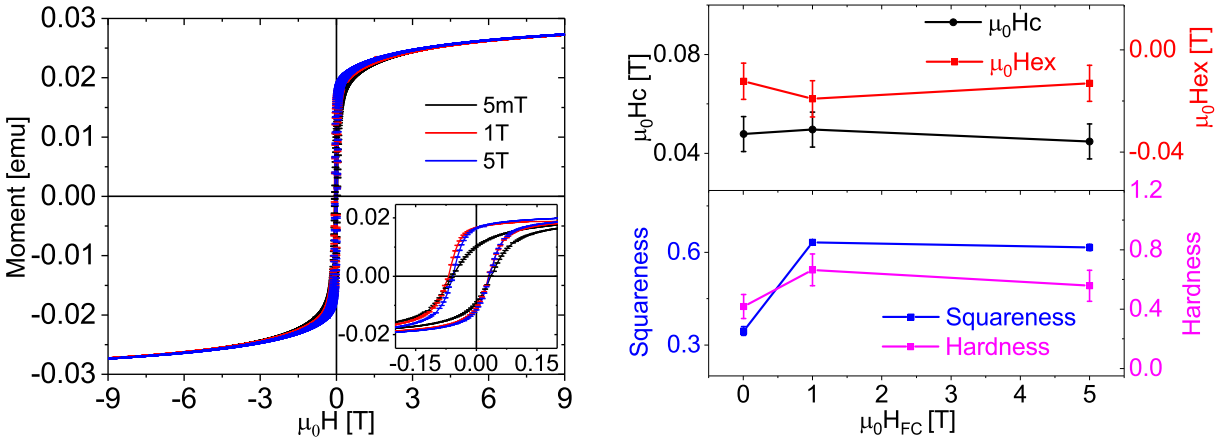

Figure 93: (a) Hysteresis loops of 15 nm iron oxide NPs measured at 5 K after cooling in various magnetic fields. Inset in (a) shows an enlarged view around the origin. (b) EB field (H_{ex}), coercive field (H_c), squareness and hardness of 15 nm iron oxide NPs obtained from (a).

The field dependent magnetization of 15 nm NPs shows similar results as found for 20 nm NPs. As can be seen in Fig. 93(a), the hysteresis loops measured at 5 K become more squared as the cooling field increases. An EB effect is also observed, which confirms the existence of wüstite inside the sample. In Fig. 93(b), H_c, H_{ex}, the squareness and hardness depending on H_{FC} are shown. Similar to the results on 20 nm NPs, all four values increase with an increasing H_{FC} until 1 T. This is due to an increasing strength of the EB field. Above H_{FC}=1 T, an obvious decrease in all curves can be observed. This might be due to a small amount or small sizes of wüstite existing in the sample, whose AF order is easier to be destroyed by a relatively high magnetic field compared to larger sizes of wüstite. Moreover, a training effect is measured for 15 nm NPs. As can be seen in Fig. 94, the EB field decreases, when the hysteresis loop is repeated for a second time. However, no further training effect is found after the second repetition.

Since the 15 nm NPs ONT15^a used for the measurements above have a broad size distribution of ∼20 %, another batch of relatively monodispersed 15 nm iron oxide NPs (ONT15^b) with a size distribution of ∼10 % has been measured to be compared with the results above. As can be seen in Fig. 95(a), the overall magnetic moment of the sample increases rapidly above ∼100 K and reach a local maximum at 200 K, below which the ZFC curve shows a similar behaviour as the polydispersed sample. However, above 200 K, the magnetization of this sample continue increasing until 280 K. This can be explained by the existence of wüstite, which locks the FiM spins on the maghemite/magnetite-wüstite interface below its T_N in a direction, which is not parallel to the magnetic field. As $T > T_N$, FiM spins are released and tend to turn towards the field direction. Thus the overall magnetic moment increases until thermal fluctuations overcome the Zeeman energy. In the FC curve, a kink at 200 K can also been observed. This is due to the same effect as the increase in the ZFC curve above 200 K. Due to an instrument problem, the FC curve was only measured until 110 K. Therefore, the existence of magnetite cannot be excluded. However, in the ZFC curves measured at various magnetic fields as well as

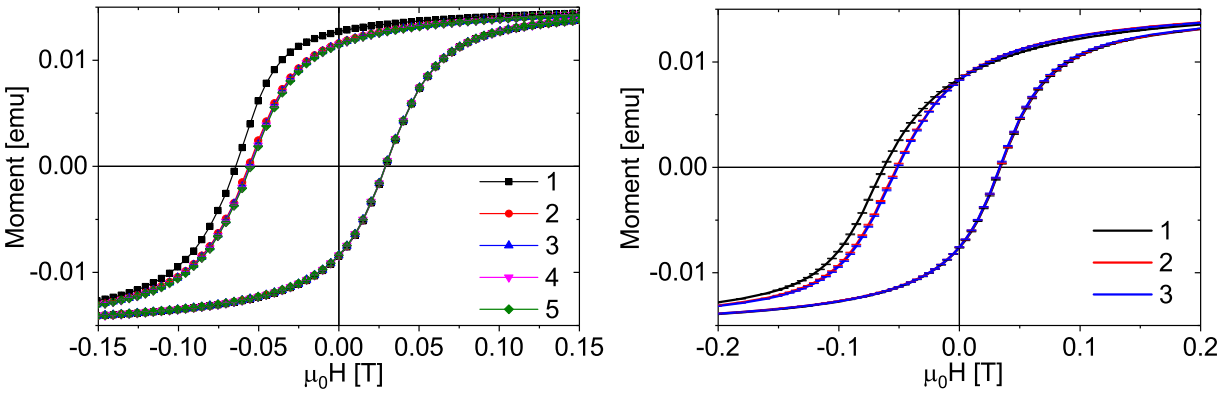

Figure 94: Hysteresis loops of 15 nm iron oxide NPs measured at 5 K after cooling in a magnetic field of (a) 1 T and (b) 5 mT repeated for various times.

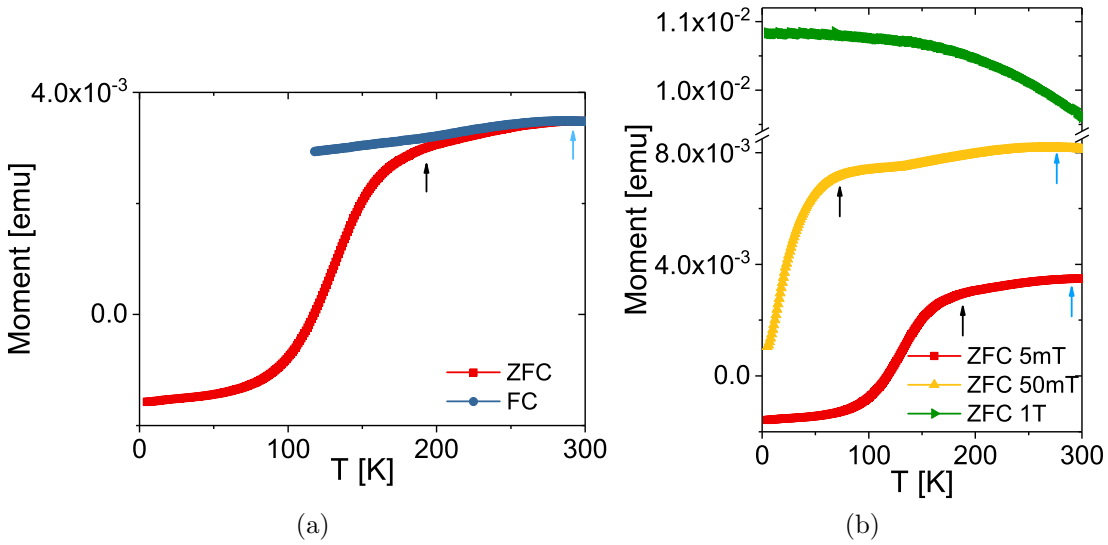

Figure 95: (a) ZFC/FC magnetization curves of relatively monodispersed spherical iron oxide NPs with 15 nm diameter measured at 5 mT. (b) ZFC curves measured at various magnetic fields. The black and blue arrows mark the peak temperatures resulting from the maghemite and the coupling between the AF wüstite and FiM maghemite/magnetite, respectively.

ZFC/FC curves measured for the same batch of NPs diluted with toluene to a ratio of 1:50 (Appendix I), no obvious feature indicating the Verwey transition of magnetite can be found. Below 280 K, the overall magnetic moment decreases in the FC curve possibly due to the existence of wüstite or dipolar interactions between NPs. The ZFC curves of this sample measured at various magnetic fields are shown in Fig. 95(b). Black and blue arrows mark the peaks resulting from nanosized maghemite and locked spins due to the EB coupling with AF wüstite, respectively. The peak temperature (black arrow) arising from the SPM/SSG-like magnetite part in the NPs shifts from 200 K to 75 K as the magnetic field increases from 5 mT to 50 mT, and disappears at 1 T. This phenomenon is

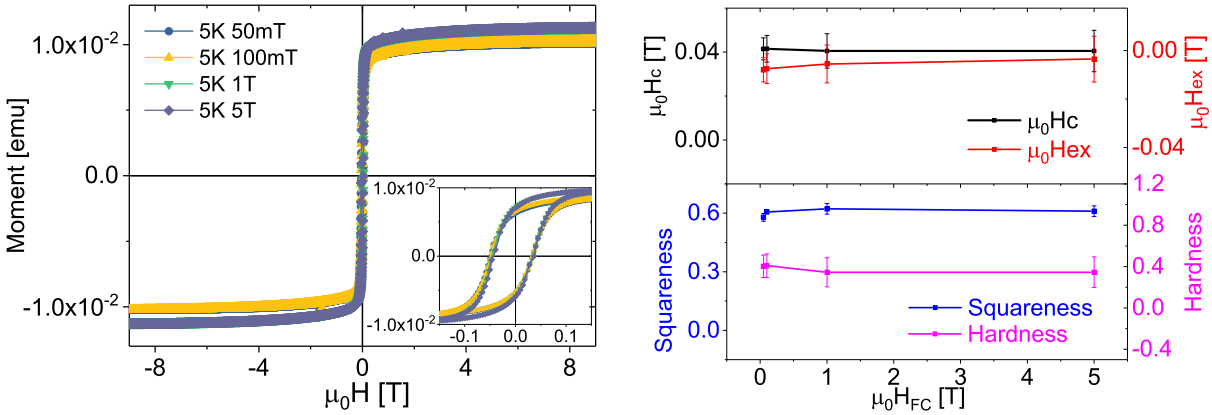

Figure 96: (a) Hysteresis loops of 15 nm NPs with a small size distribution measured at 5 K after cooling in various magnetic fields. Inset in (a) shows an enlarged view around the origin. (b) EB field (H_{ex}), coercive field (H_c), squareness and hardness obtained from (a).

expected for SPM/SSG systems.

The second peak (blue arrows) remains stable until 50 mT. At 1 T, this peak cannot be found. However, above ∼200 K, the overall magnetization decreases faster than below 200 K. This might be explained by the magnetization being saturated at low temperatures. As the temperature increases, the overall magnetic moment decreases due to thermal fluctuations. However, some of the FiM moments are locked by AF wüstite. Above T_N of wüstite, these spins also start to fluctuate, thus the magnetization drops rapidly. One should note that these two separated peaks were only observed at a magnetic field of 50 mT. At 5 mT and 1 T, no separated peaks were found. The ZFC/FC curves for the polydispersed NPs shown before were only measured at 5 mT and 1 T. Therefore, it is possible that the polydispersed NPs show also two peaks in the ZFC/FC curves at a magnetic field of 50 mT.

Hysteresis loops of 15 nm NPs with a narrow size distribution have been measured at 5 K after cooling in various magnetic fields (Fig. 96(a)). Compared to the relatively polydispersed sample, these hysteresis loops are more squared, and the saturation is reached at much lower fields. This might be due to a smaller amount or smaller sizes of wüstite. Moreover, a weak hardening effect can be found in the inset of Fig. 96(a). H_C, H_{ex}, squareness and hardness depending on H_{FC} obtained from the hysteresis loops are plotted in Fig. 96(b). As can be seen, no obvious increase in H_C and H_{ex} can be found. The squareness and hardness show a weak increase until 1 T. Compared to the sample with a broad size distribution, H_C, H_{ex}, squareness and hardness at 1 T of this sample is only slightly smaller. This can be explained by smaller sizes of wüstite in this sample, which can be saturated at lower magnetic fields.

In order to study the magnetic correlations between NPs, the memory effect has been measured. Due to the dipolar interactions between the superspins of the NPs, a glassy-like behaviour can be expected. As can be seen in Fig. 97, a peak near the stopping temperature at 155 K can be found in the difference between the ZFC curves measured with and without a stop. Both the ZFC and ZFC' curves have been measured after

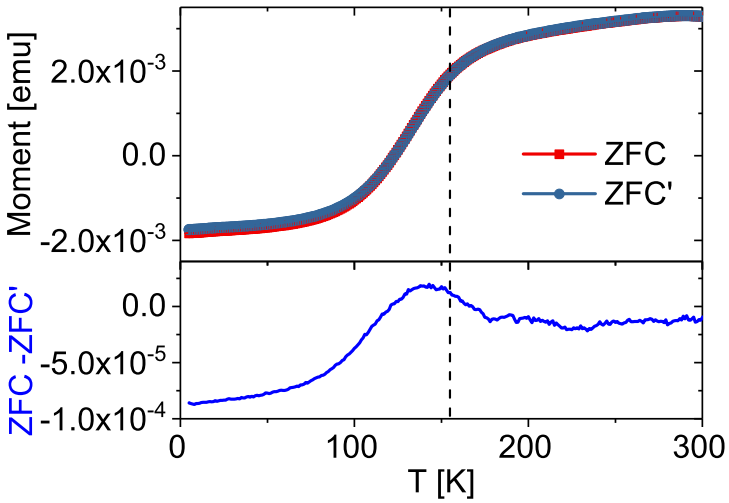

Figure 97: Memory effect of 15 nm monodispersed iron oxide NPs measured at 5 mT. The dashed line marks the stopping temperature at 155 K. ZFC' and ZFC curves indicate ZFC curves measured with and without a stop at 155 K, respectively.

the sample is cooled in the absence of a magnetic field with the same sweeping rate. This indicates a memory effect being present, which is usually observed only in SG/SSG systems [41, 155].

Diluted NPs with 15 nm diameter (ONT15$_{dil}$)

To have a better understanding of the influence of dipolar interactions between NPs onto the magnetic properties, NP dispersions of 15 nm iron oxide particles with a broad size distribution have been diluted. A SEM image of the sample produced with 15 nm NPs diluted with toluene to a ratio of 1:30 is shown in appendix H. As can be seen, the NPs form quasi-1D chain-like structures. However, 2D structures can also be found in some regions.

Fig. 98(a) shows the ZFC/FC curves of this sample measured at 5 mT. Both the ZFC and FC curves show a similar behaviour as that for the closely packed NPs (Fig. 92(a)). The peak temperature at 200 K is the same compared to the undiluted sample. This means, either the peak temperature indicates the blocking temperature of SPM NPs, which is not likely the case for densely packed NPs, or the NPs are not homogeneously diluted. In some regions, NPs may still stay close together, and thus the dipolar interaction is still strong enough so that the peak temperature does not show an obvious decrease.

ZFC curves measured at various magnetic fields are shown in Fig. 98(b). Two separated peaks can be found at magnetic fields between 50 mT and 500 mT. The black arrows mark the peak temperature resulting from nanosized maghemite. This peak temperature reduces from 200 K to ~60 K as the magnetic field increases from 5 mT to 500 mT. Such a strong field dependence of the peak temperature is expected for SPM or SSG systems. The field dependence of this peak temperature is plotted in Fig. 99. It can be fitted with an exponential function. The second peak, which is marked with blue arrows, remain stable with an increasing magnetic field. At small magnetic fields, AF domains in wüstite are randomly arranged below T_N. Thus the FiM moments coupled to AF wüstite are locked in different directions. Above $T_N \approx 200\,K$, the FiM moments are released. If

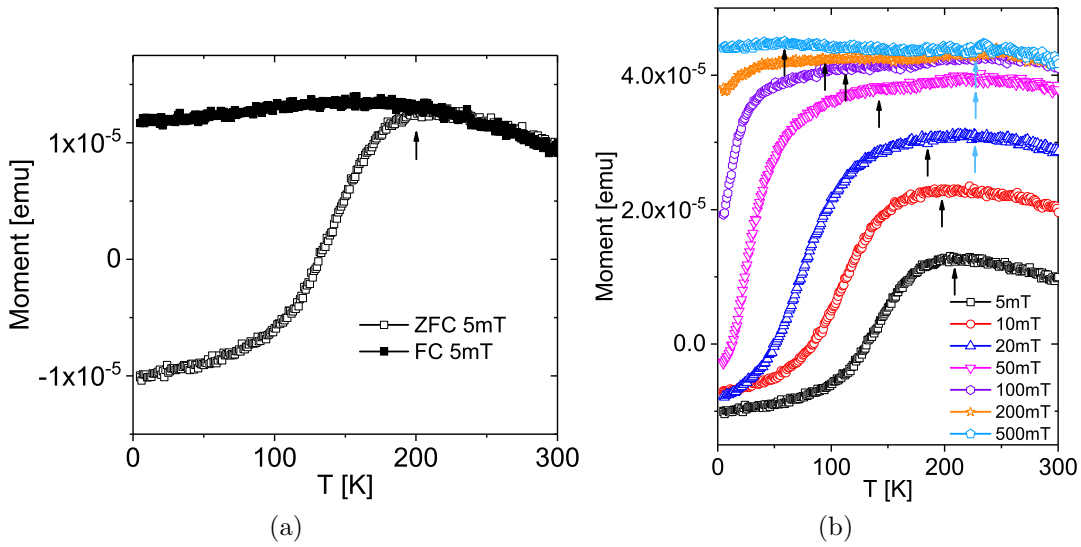

Figure 98: (a) ZFC/FC magnetization curves of spherical iron oxide NPs with 15 nm diameter diluted to a ratio of dispersion:toluene = 1:30 measured at 5 mT. (b) ZFC magnetization curves measured at various magnetic fields. The black and blue arrows mark the peak temperatures resulting from the maghemite and the coupling between the AF wüstite and FiM maghemite/magnetite, respectively.

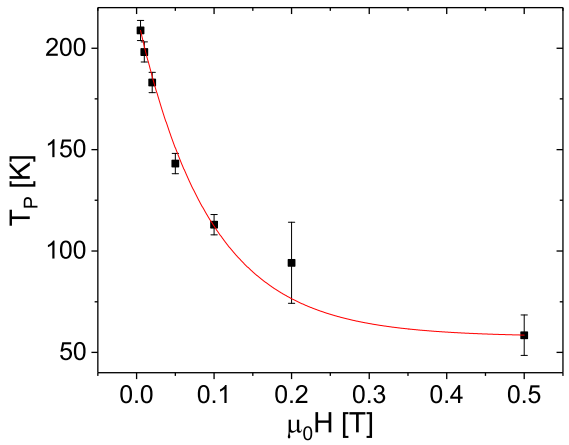

Figure 99: Peak temperature observed from ZFC magnetization curves measured at various magnetic fields. The red line shows a fit using an exponential function.

the external magnetic field is small, the Zeeman energy is not enough to overcome the thermal fluctuations. Therefore, the overall magnetic moment does not show an obvious increase above 200 K. As the magnetic field increases, the FiM moments can turn along the field direction. Therefore, an increase in the overall magnetic moment can be observed above T_N. In this case, a second peak may appear in the ZFC curves. As the magnetic field further increases, the AF domains start to align along the magnetic field. Then the coupled FiM moments may be locked along the magnetic field. After they are set free above T_N of wüstite, the magnetization does not increase any more. However, as the temperature increases, the magnetization decreases due to thermal fluctuations. As the

second peak is correlated with the AF Néel temperature of wüstite, it is expected that this peak temperature is stable with an increasing magnetic field.

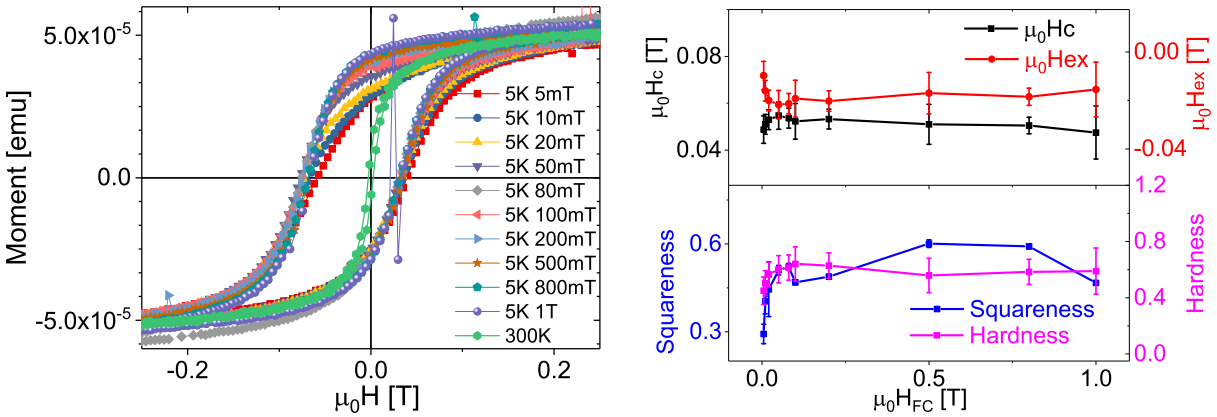

Figure 100: (a) Hysteresis loops of spherical iron oxide NPs with 15 nm diameter diluted to a ratio of dispersion:toluene = 1:30 measured at 5 K after cooling in various magnetic fields as well as at 300 K. (b) EB field (H_{ex}), coercive field (H_c), squareness and hardness obtained from (a).

Field dependent magnetization curves of diluted iron oxide NPs have been measured at 5 K after cooling in various magnetic fields as well as at 300 K. As can be seen in Fig. 100(a), an EB effect as well as a hardening effect can be observed. H_C, H_{ex}, squareness and hardness obtained from the hysteresis loops for various H_{FC} are plotted in Fig. 100(b). Compared to the undiluted sample, all four quantities show similar values at 5 mT and 1 T. Moreover, the hysteresis loops at additional cooling fields between 5 mT and 1 T have been measured for this sample. It shows that H_C, H_{ex}, squareness and hardness reach a maximum already at ∼200 mT.

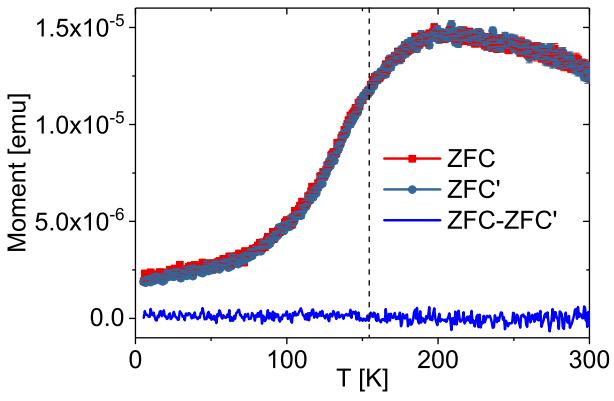

Figure 101: Absence of any memory effect of 15 nm iron oxide NPs diluted to a ratio of dispersion:toluene = 1:30 measured at 5 mT. ZFC' and ZFC curves indicate ZFC curves with and without a stop at 155 K (dashed line).

To compare the strength of interparticle interactions between NPs in the diluted NP sample with the undiluted one, the memory effect has been measured. After the sample is

cooled in the absence of a magnetic field with the same sweeping rate as for the undiluted sample with and without a stop at 155 K, ZFC' and ZFC curves were measured during warming up in a magnetic field of 5 mT. As can be seen in Fig. 101, no obvious feature can be seen in the difference between ZFC curves with and without a stop near the stopping temperature at 155 K. This means, that the dipolar interactions between NP superspins in this diluted sample are not strong enough to show a collective SSG behaviour. It is also possible that the collective behaviour is not strong enough to show a memory effect, which can be measured within the instrumental sensitivity.

As-prepared NPs with 13 nm diameter (Aug13)

To further study the size dependent magnetic properties of iron oxide NPs, 11 - 13 nm sized iron oxide NPs from the collaboration of University Augsburg have been studied. Fig. 102(a) shows the ZFC/FC magnetization curves of 13 nm spherical NPs. Compared to the 15 nm NPs, the peak temperature is further reduced from 200 K to ∼180 K. This is due to a reduced energy barrier as the NP size decreases. In the FC curve, the magnetization decreases at low temperatures. This is possibly due to the existence of AF wüstite or dipolar interactions between NPs. In both ZFC and FC curves, no feature indicating the T_V of magnetite is found. This sample is likely to be mainly maghemite with possibly a small amount of wüstite.

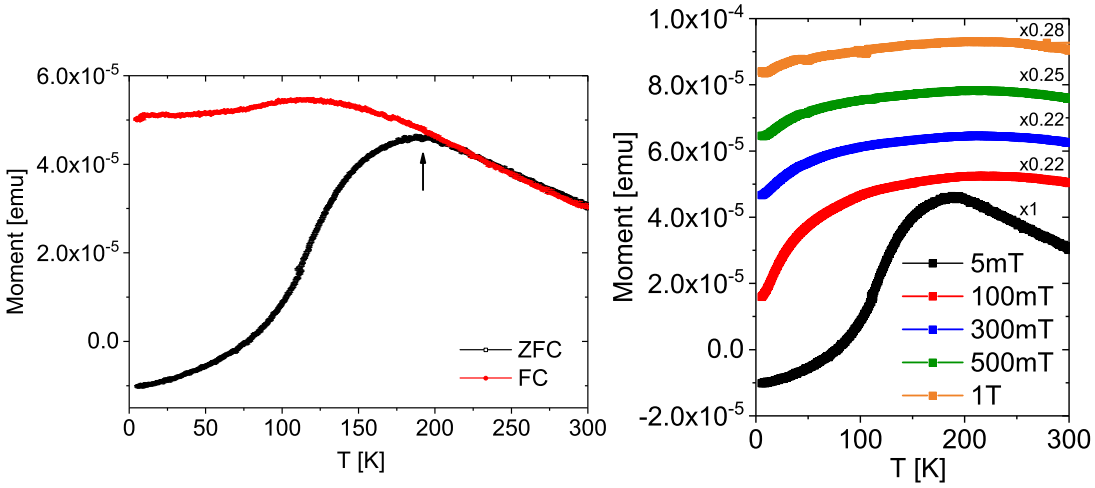

Figure 102: (a) ZFC/FC magnetization curves of spherical iron oxide NPs with 13 nm diameter measured at 5 mT. (b) ZFC magnetization curves measured at various magnetic fields.

ZFC curves of 13 nm NPs measured at various magnetic fields are shown in Fig. 102(b). At a magnetic field above 100 mT, only a weak decrease in the magnetization can be observed below 200 K until a steep decrease is found at about 50 K. Similar behaviour has also been found in Fig. 98 for 15 nm NPs, which is due to the overlap of two broad peaks. However, two separated peaks cannot be observed for this sample. It is likely that the two peaks are so broad that they cannot be separated any more. In this case, we assume a temperature slightly higher than the temperature, below which the magnetization

decreases steeply, as the peak temperature marking the SPM or SSG components. As can be seen, this peak temperature decreases rapidly as the magnetic field increases from 5 mT to 100 mT, and finally disappears at 1 T. Such a strong field dependence is usually observed for T_B or T_f of a SPM or a SSG system [5, 129, 156, 157]. In all ZFC curves measured at various magnetic fields, a second peak cannot be observed. Therefore, it is likely that there is no wüstite present in the NPs, or the amount of wüstite is negligibly small to induce a second peak.

Hysteresis loops of 13 nm NPs have been measured at 5 K after various cooling procedures as well as at 300 K (Fig. 103(a)). As can be seen in the inset, the center of the hysteresis loops at 5 K shifts towards the negative field direction, which indicates an EB effect. This might be due to the exchange coupling between the FiM maghemite and AF wüstite existing inside the NPs or surface spins. Moreover, a hardening effect can also be found in the hysteresis loops as H_{FC} increases. Fig. 103(b) shows the H_c, H_{ex}, squareness and hardness depending on H_{FC}. Compared to the 15 and 20 nm NPs, H_c and H_{ex} of 13 nm NPs is doubled. If the EB effect in this sample is caused by AF wüstite, this sample should contains much more wüstite compared to 15 and 20 nm NPs. However, the ZFC curves of 13 nm NPs do not show a second peak at ∼200 K. Therefore, the EB effect in this sample is possibly due to SG or FiM ordered surface spins. Above a cooling field of 1 T, H_c and H_{ex} show an obvious decrease. This is likely because the surface spins start to align along the magnetic field, and thus the coupling between the surface spins and FiM ordered core is suppressed. The squareness and hardness show a similar behaviour as that for 15 and 20 nm NPs.

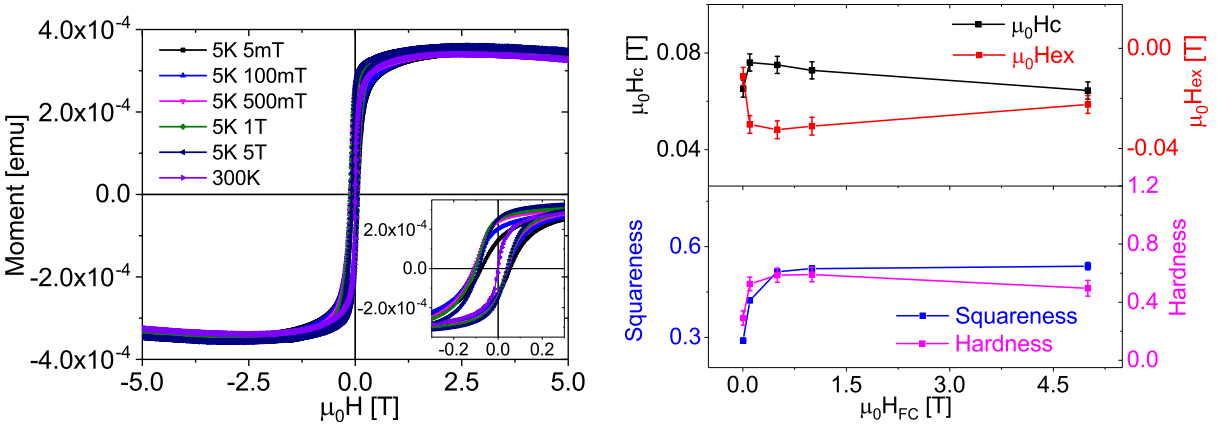

Figure 103: (a) Hysteresis loops of spherical iron oxide NPs with 13 nm diameter measured at 5 K after cooling in various magnetic fields as well as at 300 K. The inset in (a) shows an enlarged view around the origin. (b) EB field (H_{ex}), coercive field (H_c), squareness and hardness obtained from (a).

As-prepared NPs with 12 nm diameter (Aug12)

As the size of NPs further decreases to 12 nm, the peak temperature in the ZFC curve measured at 5 mT reduces to 120 K (Fig. 104(a)). Moreover, the magnetization in the FC curve shows also a decrease at low temperatures, which is possibly due to the existence

of wüstite or interparticle interactions. The peak temperature of this sample shows also a strong field dependence, which is expected for SPM and SSG systems (Fig. 104(b)). Moreover, no Verwey transition has been observed in the ZFC and FC curves of 12 nm NPs measured at various magnetic fields. No second peak has been observed in all ZFC curves. Therefore, this sample is mainly maghemite with possibly a negligibly small amount of wüstite.

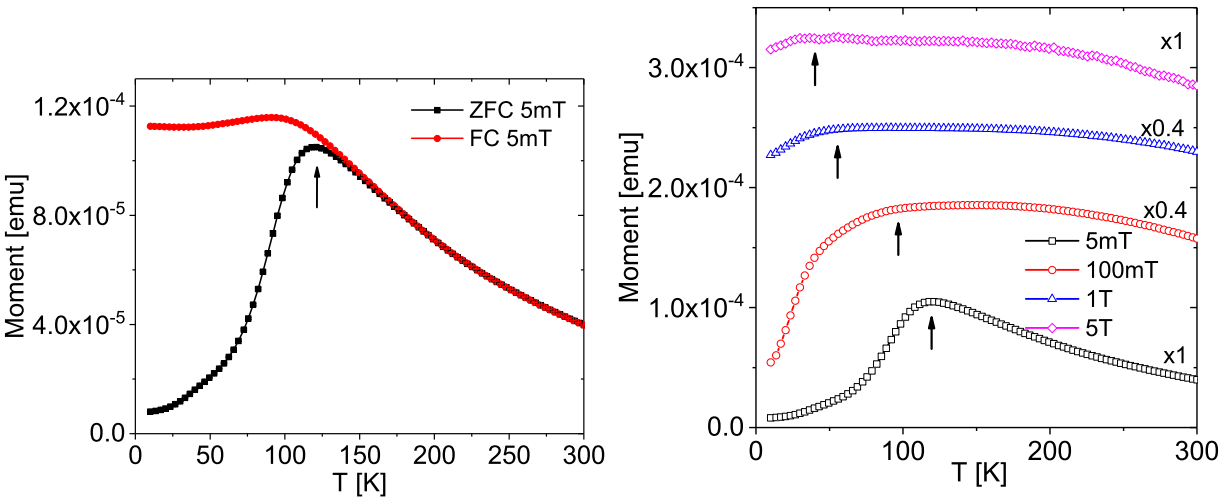

Figure 104: (a) ZFC/FC magnetization curves of spherical iron oxide NPs with 12 nm diameter measured at 5 mT. (b) ZFC magnetization curves measured at various magnetic fields.

Field dependent magnetization of curves of 12 nm spherical NPs measured at 300 K and 5 K after cooled at various magnetic fields are shown in Fig. 105(a). As can be seen in the inset, the magnetization curve measured at 300 K shows a SPM behaviour. However, at 5 K, open hysteresis loops can be found. This is often observed for blocked SPM. In the center of the hysteresis loops, an horizontal shift indicating an EB effect can be observed. Moreover, the hysteresis loops become more squared as the cooling field increases. H_c, H_{ex}, squareness and hardness obtained from the hysteresis loops are plotted in Fig. 105(b). For 12 nm NPs, the coercive field and EB field are further increased compared to the 13 nm NPs. This might be due to a larger ratio of surface spins for smaller particles, which has more influence onto the magnetic properties of NPs. The hardness and squareness increase until 1 T and stays at a constant value until 5 T.

As-prepared NPs with 11 nm diameter (Aug11)

The 11 nm iron oxide NPs from the University Augsburg have a cubic shape. ZFC/FC magnetization curves measured at various magnetic fields are shown in Fig. 106(a). At 5 mT, the peak temperature is ∼140 K, which is much higher than that of 12 nm spherical NPs. This might be because of much stronger dipolar interactions between the superspins with a cubic order. However, below the peak temperature, no obvious decrease in the FC curve can be seen. Moreover, no feature near T_V of magnetite is found. This sample is very likely purely maghemite.

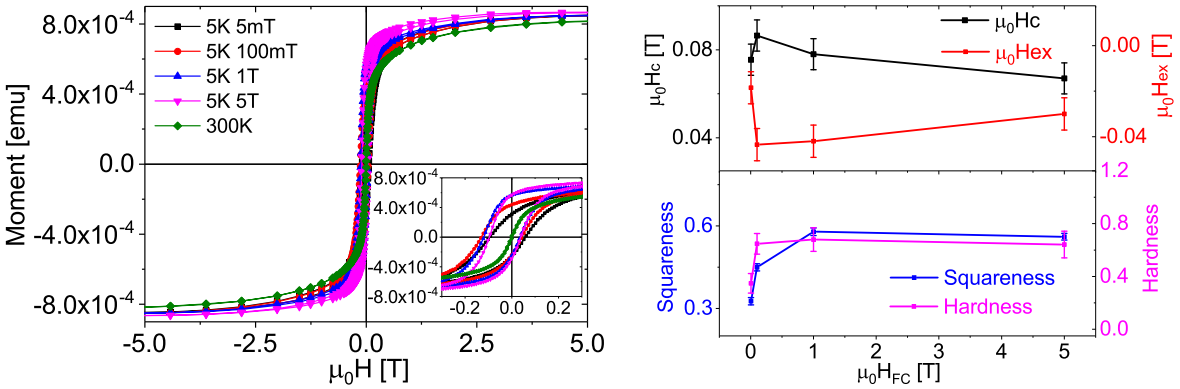

(a) (b)

Figure 105: (a) Hysteresis loops of spherical iron oxide NPs with 12 nm diameter measured at 5 K after cooling in various magnetic fields as well as at 300 K. Inset in (a) shows an enlarged view around the origin. (b) EB field (H_{ex}), coercive field (H_c), squareness and hardness of spherical iron oxide NPs with 12 nm diameter obtained from (a).

Field dependent magnetization curves measured with 11 nm iron oxide nanocubes are shown in Fig. 106(b). At 300 K, a SPM behaviour can be observed. After the NPs are cooled down to 5 K in a magnetic field, hysteresis loops can be measured. Near ±0.075 T, a steep increase in the magnetization can be observed. This behaviour is possibly due to the shape anisotropy of cubic particles. Values of H_c, H_{ex}, squareness and hardness are displayed in appendix I. A weak EB effect can be observed for these NPs. The H_c and squareness have similar values as that of the 15 and 20 nm NPs. Due to the extra shape anisotropy, the hardness of cubic NPs is much larger than that of spherical particles.

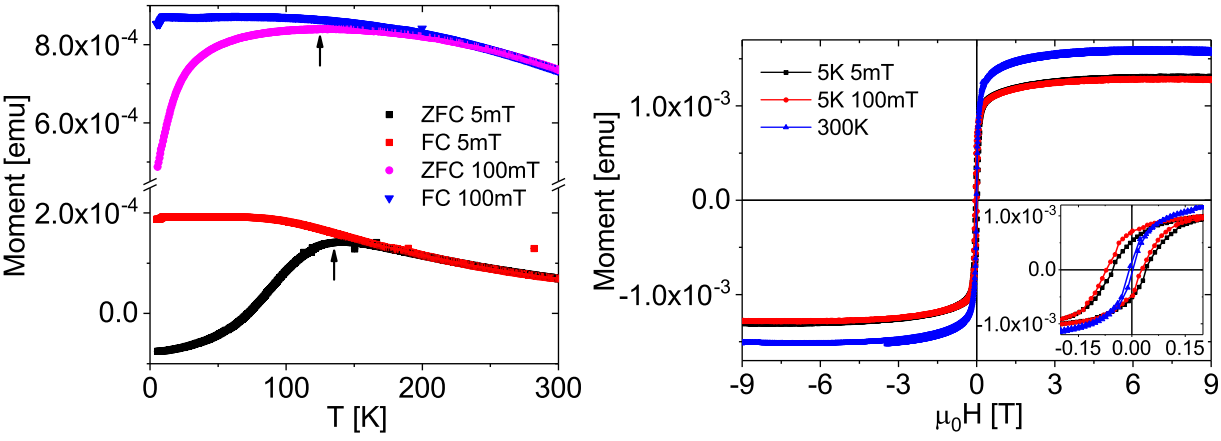

(a) (b)

Figure 106: (a) ZFC/FC magnetization curves of cubic iron oxide NPs with 11 nm diameter measured at various magnetic fields. (b) Hysteresis loops measured at 5 K after cooling in various magnetic fields as well as at 300 K. Inset in (b) shows an enlarged view around the origin.

As-prepared NPs with 5 nm diameter (ONT5)

The smallest iron oxide NPs studied in this thesis are 5 nm spherical NPs from Ocean NanoTech. Fig. 107(a) shows the ZFC/FC curves measured at 5 mT and 100 mT. Compared to larger particles, the peak temperature of 5 nm NPs measured at 5 mT is reduced to an even lower temperature (∼17 K). As the magnetic field increases, the peak temperature reduces. At 100 mT, the peak already disappears. The overall magnetic moment in the FC curve reduces below T_p. This might be an artefact of the instrument or due to the dipolar interactions between the NPs. With such a small size, these particles are very likely single phase. As maghemite is the most stable phase of iron oxide, these NPs are likely to be purely maghemite. Hysteresis loops of 5 nm particles measured at 300 K as well as 5 K after cooled in 5 mT and 100 mT are shown in Fig. 107(b). The hysteresis loops look much more square-like than that of the larger NPs. This is because the magnetization is already saturated at a much lower field. At 300 K, a SPM behaviour can be observed. At 5 K, the superspins are in a blocked state. Therefore, open hysteresis loops can be found. For this sample, no EB or hardening effect is observed in the hysteresis loops. In order to study the influence of the dipolar interactions onto the magnetic properties, the NPs were diluted and measured to be compared with the compacted NP samples. In appendix I, temperature and field dependent magnetization curves of 5 nm particles diluted with toluene to a ratio of 1:20 are shown. The T_p in the ZFC curve measured at 5 mT show no obvious increase compared to the undiluted sample. However, the magnetization continues to increase in the FC curve as the temperature decreases. This is an indication that the dipolar interaction in the diluted sample is weaker.

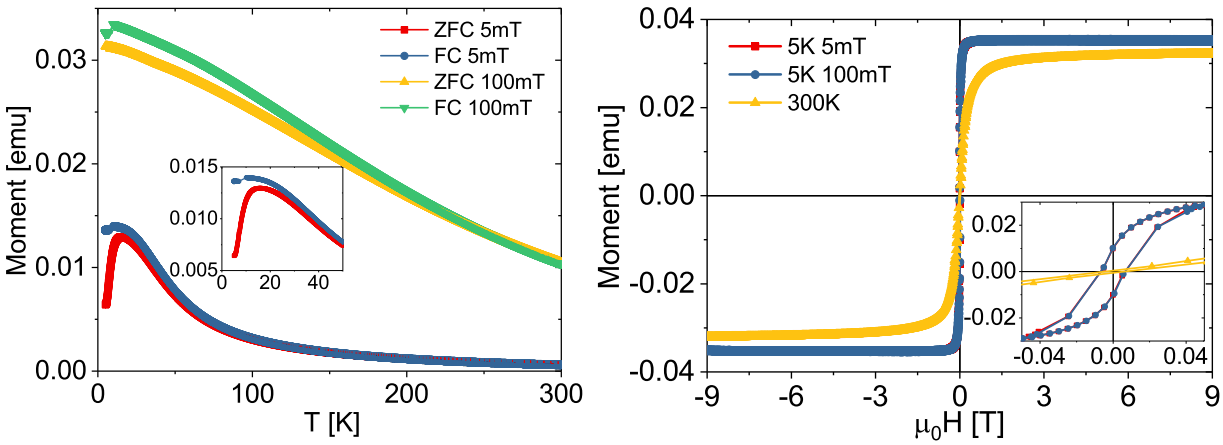

(a) (b)

Figure 107: (a) ZFC/FC magnetization curves of spherical iron oxide NPs with 5 nm diameter measured at various magnetic fields. Inset in (a) shows an enlarged view near the peak temperature. (b) Hysteresis loops measured at 5 K after cooling in various magnetic fields as well as at 300 K. Inset in (b) shows an enlarged view around the origin.

In order to study the magnetic properties of various phases of iron oxide NPs, several annealing procedures have been performed. As discussed above, the 15 and 20 nm iron oxide NPs are not single phase. They are composed of mainly maghemite with a small fraction of magnetite and wüstite. To obtain single phase iron oxide NPs, the oxygen content in the NPs has been varied. The magnetometry results of the annealed NPs are

compared with that before the annealing procedures. Since there is no obvious difference in the magnetization as found for the undiluted sample and the sample diluted with toluene to a ratio of 1:30, diluted NP dispersions up to a NP dispersion to toluene ratio of 1:30 used for annealing procedures are comparable to the results shown above.

Annealed NPs with 15 nm diameter ($ONT15^{ann}_{dil}$)

Fig. 108(a) shows the ZFC/FC magnetization curves of 15 nm NPs annealed in vacuum at 318 °C for 4 h. In this case, the oxygen content in the NPs is supposed to be reduced. As can be seen, an obvious feature at ∼110 K can be found indicating the T_V of magnetite. Compared to the as-prepared sample, the ratio of magnetite is evidently increased. Moreover, a peak at ∼250 K can be seen. This peak temperature is much higher than that observed for the as-prepared particles (200 K). This is possibly due to increased dipolar interactions between NPs because the oleic acid shell is burnt away and the NPs start to agglomerate. In the FC curve, a much stronger decrease can be seen below the peak temperature compared to the as-prepared NPs. This can be explained by an increasing amount of wüstite existing in the NPs or increased interparticle interactions.

The field dependence of the peak temperatures in the ZFC curves has also been studied. As can be seen in Fig. 108(b), the peak indicating the Verwey transition is stable with an increased magnetic field as expected. However, the peak at 250 K in the ZFC curve measured at 5 mT splits into two peaks. One at a much lower temperature (∼40 K), and one that stays near 240 K. This phenomenon is likely due to the coupling between the moments in AF wüstite and FiM maghemite/magnetite and has also been observed in the as-prepared NPs.

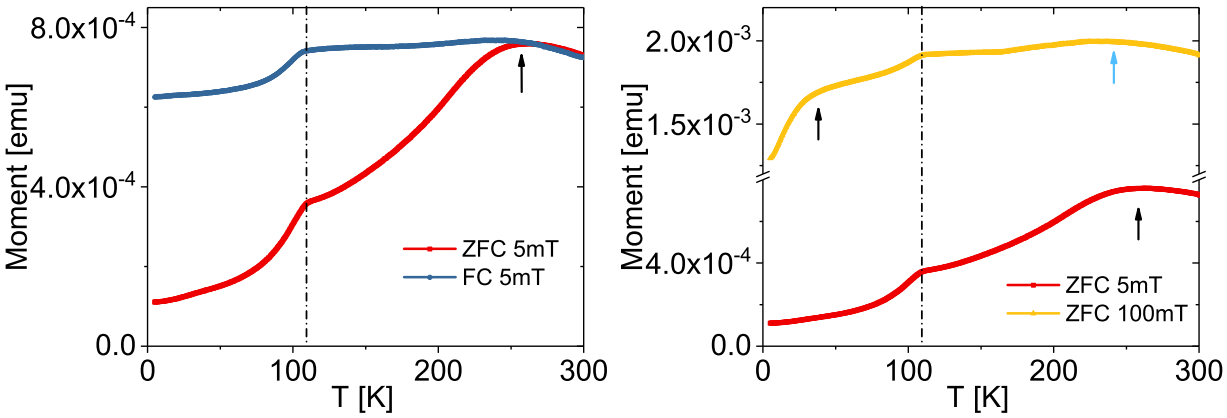

(a) (b)

Figure 108: (a) ZFC/FC magnetization curves of spherical iron oxide NPs with 15 nm diameter diluted to a ratio of dispersion:toluene = 1:5 annealed in vacuum at 318 °C for 4 h measured at 5 mT. (b) ZFC curves measured at two magnetic fields. The black and blue arrows mark the peak temperatures resulting from the maghemite and the coupling between the AF wüstite and FiM maghemite/magnetite, respectively.

From the temperature dependent curves, we can see that the maghemite content in the as-prepared NPs is partially transformed to magnetite and wüstite. To have a better understanding of the origin of the EB and hardening effects in iron oxide NPs, it is

interesting to compare H_c, H_{ex}, squareness and hardness of the hysteresis loops of NPs with various ratios of different iron oxide phases.

Fig. 109(a) shows the hysteresis loops of 15 nm NPs annealed in vacuum at 318 °C for 4 h. Similar to the as-prepared NPs, they are SPM at 300 K. At 5 K, hysteresis loops can be seen. Moreover, EB and hardening effects can also been observed. As can be seen in Fig. 109(b), H_c, H_{ex} and the hardness of the annealed NPs have similar values as that of the as-prepared sample. However, the squareness increases by 50 %. This is possibly due to a stronger anisotropy because of a larger fraction of magnetite and wüstite.

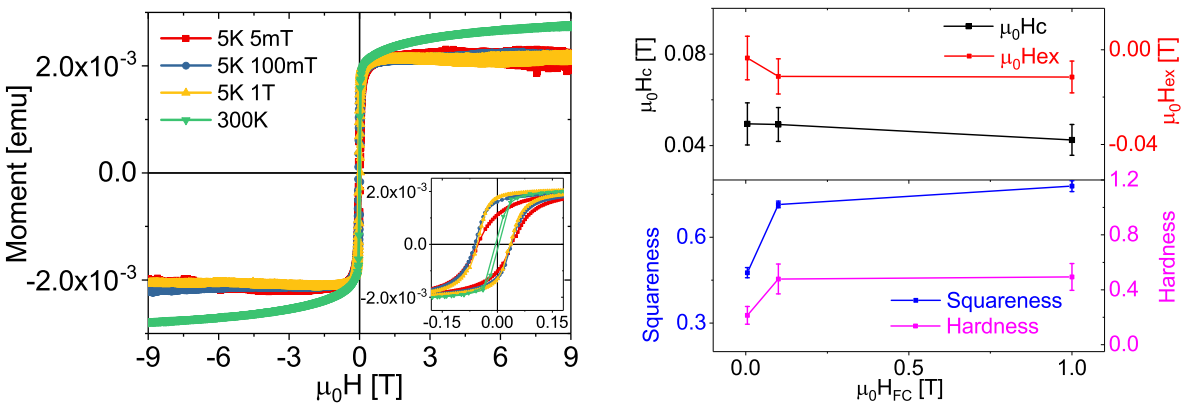

Figure 109: (a) Hysteresis loops of spherical iron oxide NPs with 15 nm diameter diluted to a ratio of NP dispersion:toluene = 1:5 annealed in vacuum at 318 °C for 4 h measured at 5 K after cooling in various magnetic fields as well as at 300 K. Inset in (a) shows an enlarged view around the origin. (b) EB field (H_{ex}), coercive field (H_c), squareness and hardness depending on the cooling field obtained from (a).

To further reduce the oxygen content in iron oxide NPs expecting single phase magnetite or wüstite, the annealing parameters such as temperature and heating duration have been varied. However, no single phase magnetite or wüstite has been successfully produced using 15 nm NPs.

Oxidized NPs with 15 nm diameter ($ONT15^{oxi}_{dil}$)

As reported in many articles, maghemite is a very stable phase of iron oxide. Hence by oxidizing iron oxide with previously lower oxidation states, maghemite can be produced. To obtain single phase maghemite NPs, 15 nm particles have been annealed in air at 120 °C for 12 h. As can be seen in Fig. 110(a), ZFC/FC curves show a similar behaviour as before annealing. However, the feature at ∼110 K indicating the Verwey transition of magnetite disappears after annealing. Below the peak temperature at 200 K, the magnetization in the FC curve decreases. This is likely due to the interactions between NPs. It is also possible that there is still a small amount of wüstite, which is not completely oxidized. ZFC curves of this oxidized sample have also been measured at various magnetic fields. As can be seen in Fig. 110(b), these curves show no obvious difference compared to that of the as-prepared sample. The peak temperature coming from the SPM/SSG maghemite reduces rapidly as the magnetic field increases. At 1 T, this peak disappears. Moreover,

a second peak at ∼220 K appears when a magnetic field above 100 mT is applied. This is also an indication that wüstite inside the NPs is not completely oxidized.

Hysteresis loops of the oxidized NPs have been measured to be compared with the results of the as-prepared NPs. As can be seen in Fig. 110(c), hysteresis loops at 5 K have been measured. A weak EB effect as well as a hardening effect can be observed in the inset of Fig. 110(c). Compared to the as-prepared NPs, hysteresis loops measured for the oxidized sample show a much smaller hardness (Fig. 110(d)). However, H_c, H_{ex}, and squareness have similar values as that before the oxidation.

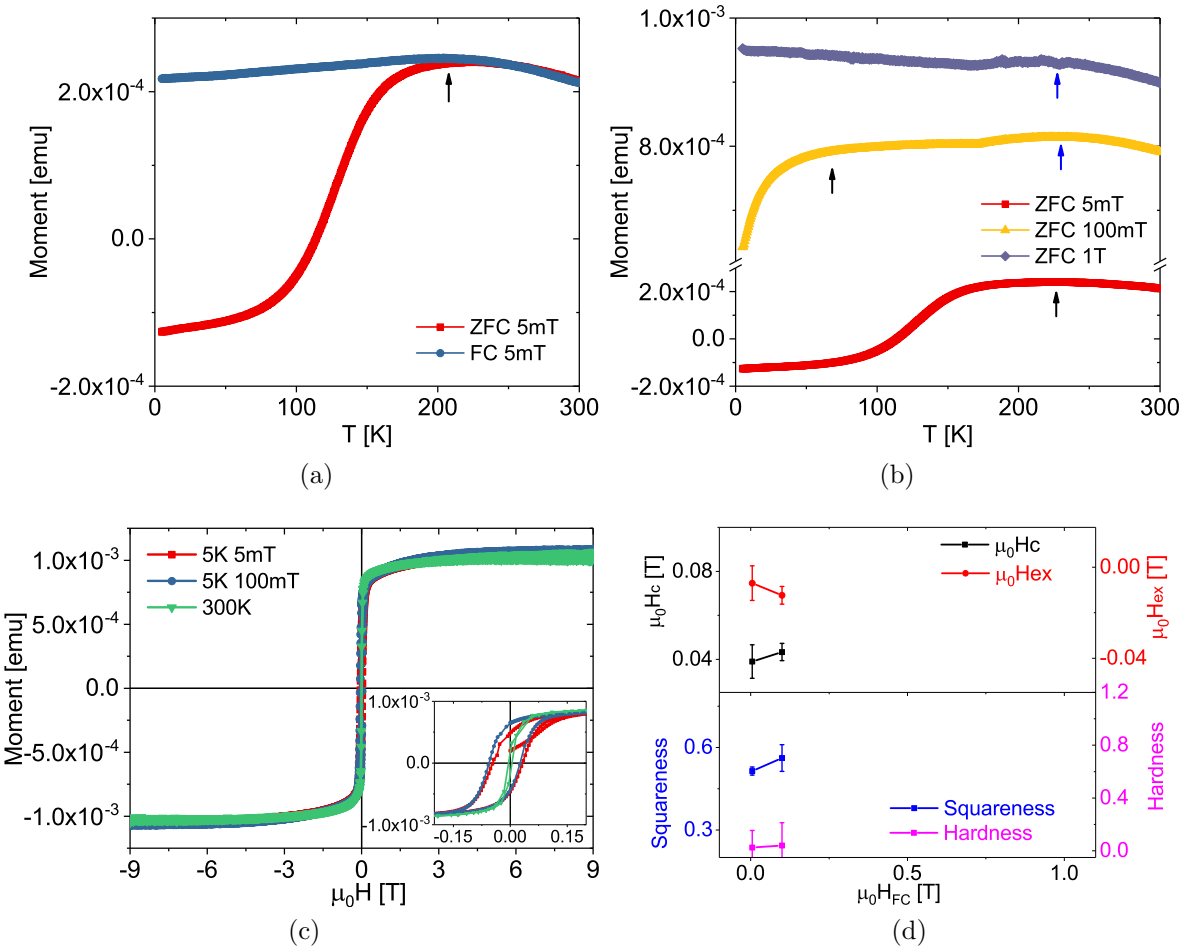

Figure 110: (a) ZFC/FC magnetization curves of spherical iron oxide NPs with 15 nm diameter diluted to a ratio of NP dispersion:toluene = 1:15 annealed in air at 120 °C for 12 h measured at 5 mT. (b) ZFC curves measured at various magnetic fields. The black and blue arrows mark the peak temperatures resulting from the maghemite and the coupling between the AF wüstite and FiM maghemite/magnetite, respectively. (c) Hysteresis loops measured at 5 K after cooling in various magnetic fields as well as at 300 K. Inset in (c) shows an enlarged view around the origin. (d) EB field (H_{ex}), coercive field (H_c), squareness and hardness obtained from (c).

As-prepared iron oxide NPs with 5 and 12 nm sizes are supposed to be single phase maghemite according to the results discussed above. Therefore, they are perfect candidates for a systematic study of the magnetic properties of NPs with various iron oxide

phases.

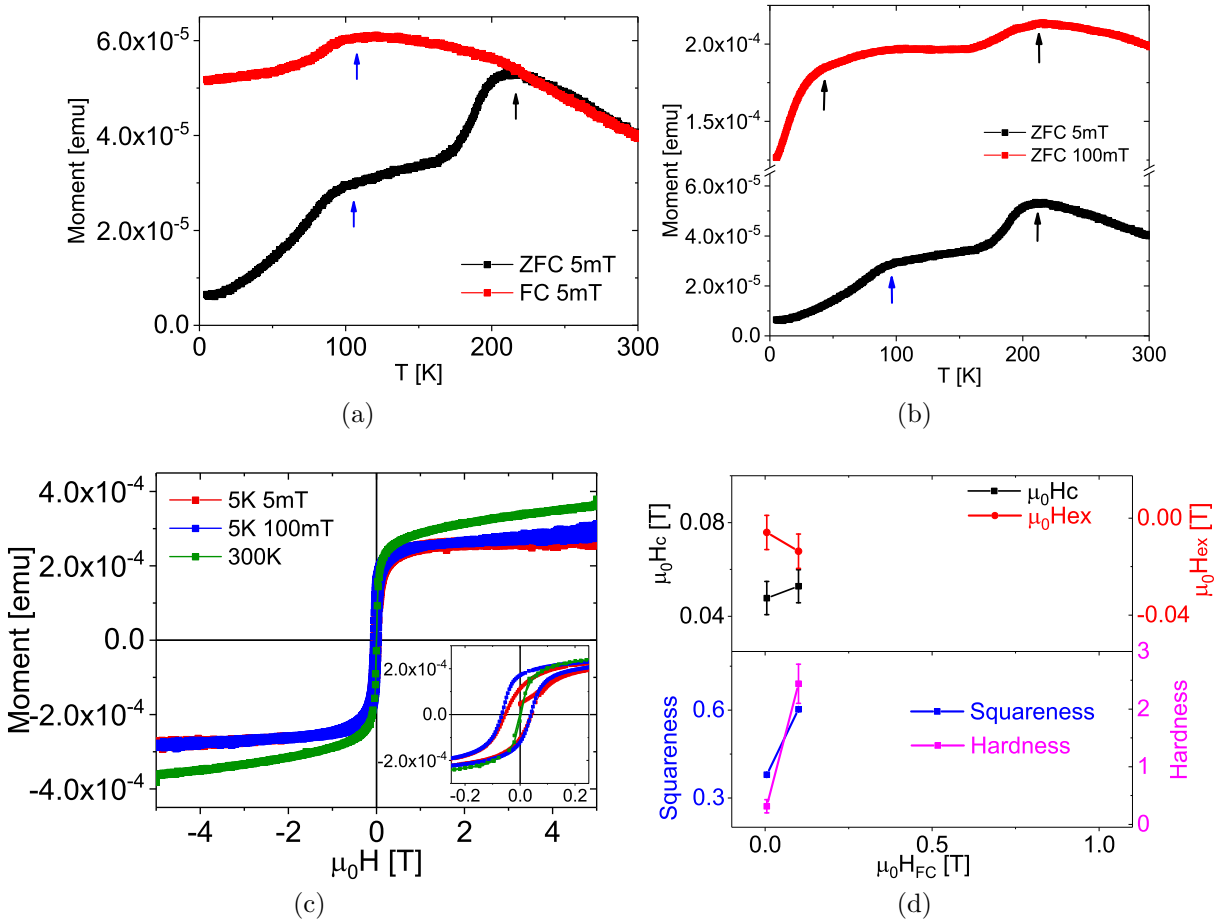

Figure 111: (a) ZFC/FC magnetization curves of spherical iron oxide NPs with 12 nm diameter annealed in vacuum at 318°C for 4.5 h measured at 5 mT. (b) ZFC magnetization curves measured at various magnetic fields. (c) Hysteresis loops of spherical iron oxide NPs with 12 nm diameter annealed in vacuum at 318°C for 4.5 h measured at 5 K after cooling in various magnetic fields as well as at 300 K. Inset in (c) shows an enlarged view around the origin. (d) EB field (H_{ex}), coercive field (H_c), squareness and hardness obtained from (c).

Annealed NPs with 12 nm diameter (Aug12^{ann})

Fig. 111 shows the magnetization results of 12 nm NPs after annealing in vacuum at 318°C for 4.5 h. As can be seen in Fig. 111(a), a feature at 110 K can be found in the ZFC/FC curves indicating the T_V of magnetite. Moreover, the overall magnetic moment decreases at low temperatures in the FC curve. This is due to the existence of wüstite inside the NPs. At ∼190 K, the magnetization in the ZFC curve shows a steep increase. This phenomenon is correlated to AF wüstite, which locks parts of the FiM moment below its T_N. As the temperature increases above T_N, the FiM moments are released and turn to align along the magnetic field. The field dependence of the peak temperature has been studied to have a better understanding of this sample. In Fig. 111(b), two peaks in the

ZFC curve at 100 mT can be found similar to the 15 nm NPs. The peak at ∼220 K is stable even at an increased magnetic field. This confirms our statement that the second peak often observed near 200 K in the ZFC curves of 15 nm NPs is due to the coupling between moments of FiM and AF components. The peak temperature from SPM/SSG maghemite or magnetite reduces as the magnetic field increases. Compared to the as-prepared NPs, a large amount of maghemite is obviously reduced to magnetite and wüstite.

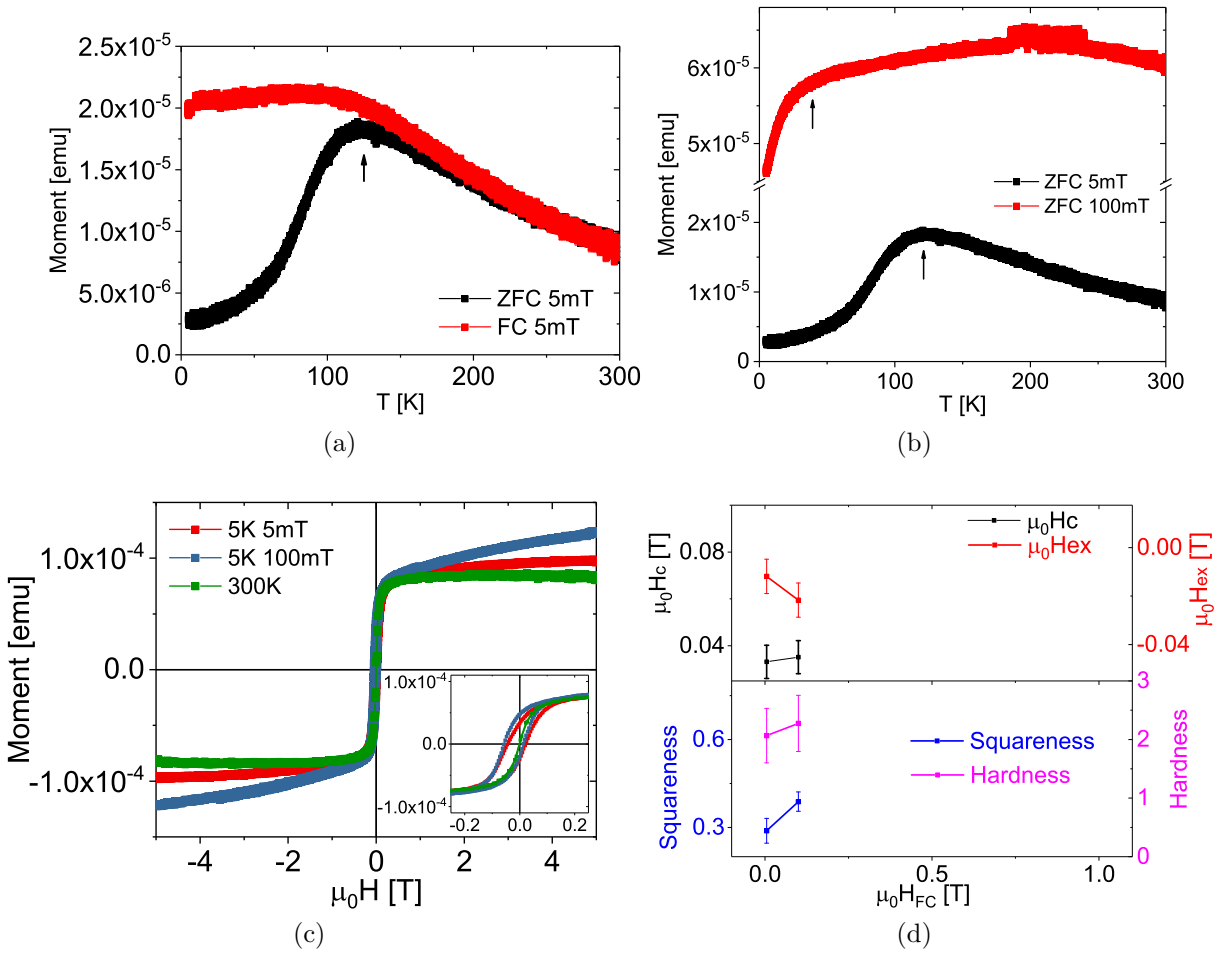

Figure 112: (a) ZFC/FC magnetization curves of spherical iron oxide NPs with 12 nm diameter annealed in air at 120°C for 16 h measured at various magnetic fields. (b) ZFC curves measured at various magnetic fields. (c) Hysteresis loops measured at 5 K after cooling in various magnetic fields as well as at 300 K. Inset in (c) shows an enlarged view around the origin. (d) EB field (H_{ex}), coercive field (H_c), squareness and hardness obtained from (c).

After the composition of these annealed NPs is known, the EB and hardening effect in the hysteresis loops are of interest. Fig. 111(c) shows the field dependent magnetization curves of the annealed NPs measured at 300 K and at 5 K after various cooling procedures. As can be seen in the inset, both an EB and a hardening effect can be observed. To better compare these effects of this sample with other iron oxide NPs, H_c, H_{ex}, squareness and hardness depending on the cooling field are shown in Fig. 111(d). Compared to the as-prepared particles, the annealed NPs have a much smaller coercive

and EB field. This might be because the reduced wüstite part is not as strongly coupled to magnetite/maghemite as surface spins with the maghemite core. The squareness shows no obvious difference compared to that of NPs before annealing. However, the hardness of this sample is largely enhanced.

Oxidized NPs with 12 nm diameter (Aug12^{oxi})

In order to confirm that the as-prepared NPs with 12 nm size are single phase maghemite, these NPs are further oxidized in air at 120°C for 16 h. It is reported that a temperature higher than 500°C is needed to transform iron oxide into hematite [2]. Therefore, our heating procedures at 120°C will only transform magnetite or wüstite into maghemite. As can be seen in the ZFC/FC curves measured at 5 mT, a peak at 120 K can be observed. This peak temperature as well as the shape of the ZFC/FC curves matches the results of the as-prepared sample. In addition, the ZFC magnetization curves measured at 100 mT show also the same behaviour before and after the oxidation process. The noise near 200 K is likely an artefact from the instrument. However, the hysteresis loops of the oxidized sample become more narrow (Fig. 112(c)). H_C and H_{ex} are reduced compared to that of the as-prepared NPs. It is possible that during the annealing procedure, iron oxide is recrystallized at the surface. Thus the SSG ordered surface spins are reduced, which lead to a reduction of the EB effect. The hardness is enhanced, which might also be due to an additional anisotropy induced by the recrystallized shell.

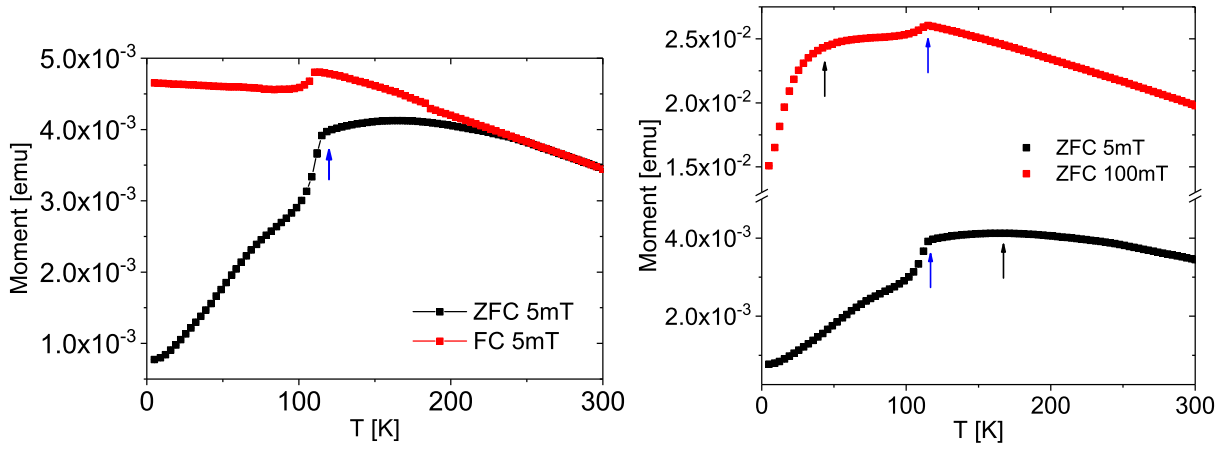

(a) (b)

Figure 113: (a) ZFC/FC magnetization curves of spherical iron oxide NPs with 5 nm diameter annealed in vacuum at 318°C for 5.5 h measured at 5 mT. (b) ZFC curves measured at various magnetic fields. The blue and black arrows mark the Verwey transition of magnetite and the peak temperature resulting from the maghemite, respectively.

Annealed NPs with 5 nm diameter (ONT5$^{ann}_{ori}$)

A complete reduction of maghemite has not been achieved for 12 nm iron oxide NPs. As the particle size decreases, they prefer to stay single domain. Moreover, it should be easier for smaller NPs to be fully reduced. Therefore, a similar procedure has been repeated for 5 nm NPs. Fig. 113(a) shows the ZFC/FC curves of 5 nm NPs annealed in

vacuum at 318 °C for 5.5 h. As can be seen, a clear peak at 120 K is found confirming the successfully reduction of maghemite to magnetite. At ∼160 K, a hump can be seen. This is possibly a peak indicating the crossover of the blocked to the unblocked SPM/SSG state of magnetite, since 5 nm NPs are very likely single domain. As the magnetic field increases, the hump at 160 K decreases to 50 K (Fig. 113(b)). Such field dependence of the peak temperature is expected for SPM/SSG systems.

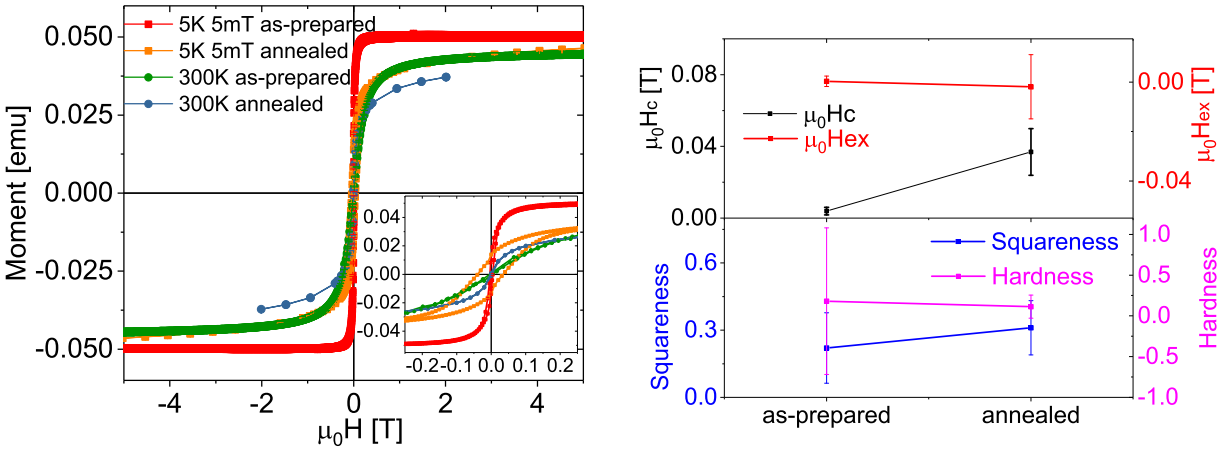

(a) (b)

Figure 114: Comparison of (a) hysteresis loops measured at 5 K after cooling in a magnetic field of 5 mT as well as at 300 K and (b) EB field (H_{ex}), coercive field (H_c), squareness and hardness of spherical iron oxide NPs with 5 nm diameter before and after annealing in vacuum at 318°C for 5.5 h. Inset in (a) shows an enlarged view around the origin.

Field dependent magnetization curves of the annealed NPs with 5 nm diameter have been measured and compared to that of the as-prepared sample. Fig. 114(a) shows the comparison of hysteresis loops of the same sample before and after the annealing procedure. As can be seen, hysteresis loops of the annealed sample become less squared. However, the coercive field become obviously larger. In Fig. 114(b), H_c, H_{ex}, squareness and hardness of the hysteresis loops are compared for NPs before and after annealing. Except a large enhancement of H_c, H_{ex} and the squareness as well as the hardness do not change.

Oxidized NPs with 5 nm diameter (ONT5$^{oxi}_{ori}$)

Temperature and field dependent magnetization curves of 5 nm iron oxide NPs after further oxidation process have been measured to be compared with the as-prepared sample. In Fig. 115, ZFC curve measured at 5 mT and hysteresis loops of 5 nm NPs annealed in air at 120 °C for 20 h are compared with the results before annealing. As can be seen in Fig. 115(a), both curves show a similar behaviour. The peak temperature agrees with each other. Hysteresis loops measured at 300 K does not show a difference before and after annealing. However, at 5 K the coercive field becomes smaller after annealing. H_C, H_{ex}, squareness and hardness of the hysteresis loops measured at 5 K before and after annealing have been compared. As can be seen in Fig. 116, no EB effect can be found in both samples. H_{ex}, squareness and hardness decrease. This can also be due to the recrystallization of the surface spins as for the oxidized 12 nm NPs.

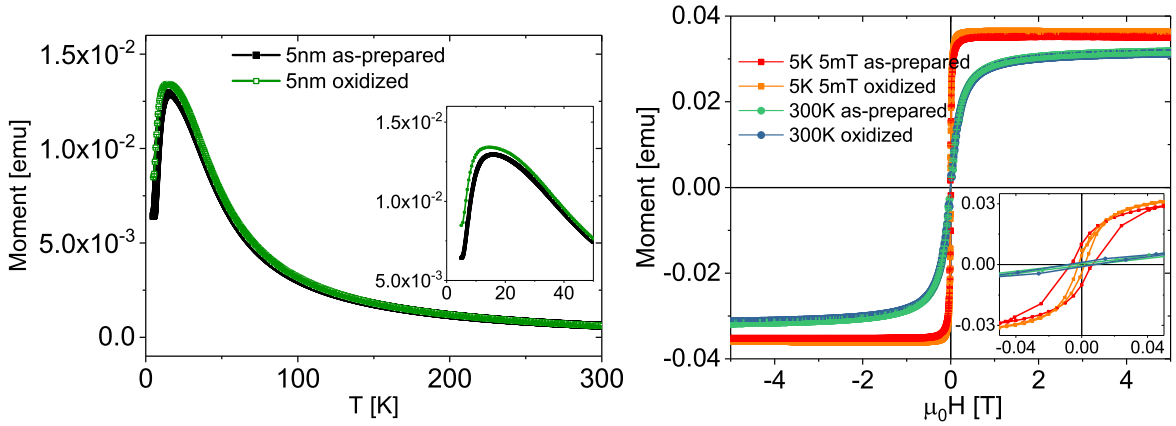

(a) (b)

Figure 115: Comparison of (a) ZFC/FC magnetization curves measured at 5 mT and (b) hysteresis loops measured at 5 K after cooling in a magnetic fields of 5 mT as well as at 300 K of spherical iron oxide NPs with 5 nm diameter before and after annealing in air at 120°C for 20 h. Inset in (a) shows an enlarged view near the peak temperature. Inset in (b) shows an enlarged view around the origin.

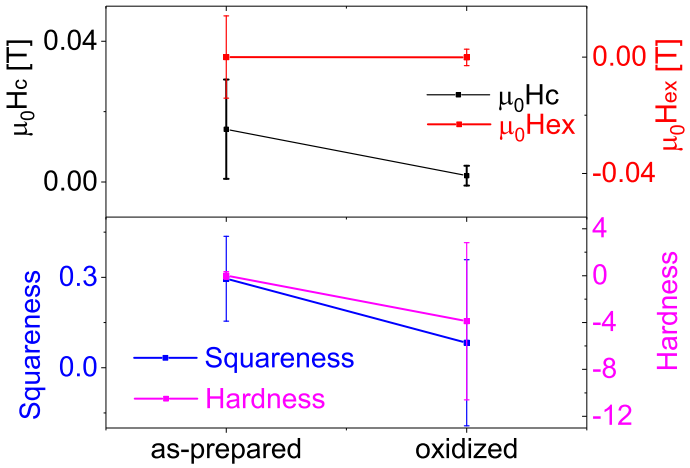

Figure 116: Comparison of EB field (H_{ex}), coercive field (H_c), squareness and hardness of spherical iron oxide NPs with 5 nm diameter before and after annealing in air at 120°C for 20 h.

In order to have a better understanding of the hardening effect observed in the hysteresis loops after cooling in various magnetic fields, torque magnetometry measurements have been performed for 20 nm NPs. The sample is cooled in a magnetic field of 0.5 mT to 5 K. Then the sample is rotated from 0° to 360° and back to 0°. During the rotation, the magnetic torque is measured at a magnetic field of 1 mT. As can be seen in Fig. 117, an 360° periodicity can be found. Reference measurements without sample have been performed at 300 K (appendix I). There, no 360° periodicity can be found. At 0° and 180°, the anisotropy axis induced by the cooling field is parallel and antiparallel to the magnetic field, respectively. Therefore, no torque is expected. The non-zero value measured at 0° is possibly due to the non-perfectly subtracted background. At 90° and 270°, a maximum

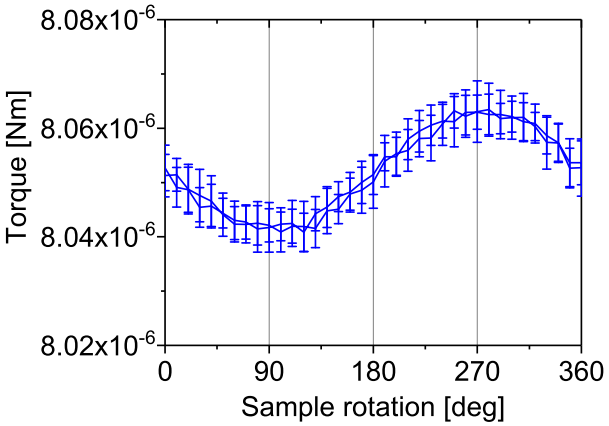

Figure 117: Torque magnetometry measurements of spherical iron oxide NPs with 20 nm diameter performed at 5 K after cooling in a magnetic field of 0.5 mT. The measurement is performed at 1 mT.

value of torque can be found in two opposite directions. These results confirm that a magnetic anisotropy axis is induced in iron oxide NPs during a field cooling procedure, which lead to an hardening effect in the hysteresis loops.

6.6 Summary

In this chapter, spherical and cubic iron oxide NPs with sizes between 5 and 20 nm have been investigated. Using TEM and SAXS, information about the size as well as the size dispersion of the NPs have been obtained. The crystal structure inside the NPs has been characterized using XRD. For nano-sized particles, it is difficult to verify the composition of NPs, because of the broadening of the reflections due to their small sizes as well as the low intensity due to the small sample amount. The reflections in the XRD patterns of 15 nm iron oxide NPs can be indexed using a spinel structure of magnetite. However, maghemite has a similar spinel structure. Taking the peak broadening into account, it is not possible to distinguish magnetite and maghemite from the XRD patterns alone. Moreover, no obvious evidence indicating the existence of wüstite has been found. However, a small amount of wüstite in the sample cannot be excluded.

The self-assembly of iron oxide NPs was also of interest in this thesis. To produce large areas of self-organized NP monolayers, various methods, such as drop-casting, liquid-air-interface and magnetic field guided self-assembly, have been used. Monolayers with the largest areas ($\sim \mu m^2$) were produced using capillary force or magnetic field guided self-assembly. However, the order is not homogeneous over the entire sample. Using spin-coating, drop-casting and liquid-air-interface methods, NPs order relatively homogeneous. However, the correlation length is much smaller. When a second iteration is given to the NPs by dropping additional toluene on the substrate after the NPs were drop-casted on the substrate, their order can be improved. Using this method, homogeneously ordered monolayers with $\sim 500\,nm^2$ domain sizes have been achieved.

Spherical NPs usually order in a hexagonal structure in self-assembled films. This was confirmed by both TEM and GISAXS. The measured reflections using GISAXS can be indexed with a hexagonal structure. Moreover, the measured patterns match well with simulated GISAXS patterns using a NP size of 13 nm and a hexagonal structure with a lattice constant of 18 nm.

The monodispersity plays an important role in the self-assembly. Monolayers composed of NPs with a broad size distribution have been compared with that formed by relatively monodispersed NPs. An interesting effect has been observed when the NPs are polydispersed. NPs with similar sizes tend to stay together and order hexagonally. Therefore, different areas of ordered NP with different sizes have been found in the SEM images.

Magnetic properties of iron oxide NPs have been studied using magnetometry. Temperature and field dependent magnetization curves of various sizes of iron oxide NPs from 5 - 20 nm have been compared. The peak temperature marking the crossover between the blocked and unblocked SPM or SSG states shows a linear increase with an increase in the particle size (Fig. 118). This is due to a larger energy barrier between two preferred spin alignments for larger particles.

According to the behaviour of ZFC/FC magnetization curves as well as the field dependence of the peak temperatures observed in the ZFC curves, conclusions about the composition of the NPs can be obtained. Magnetite usually shows a feature near its Verwey transition T_V =120 K as shown in Fig. 108, 111 and 114. When the amount of wüstite existing in the sample becomes larger, a steep increase in the ZFC magnetization curves can be found near its T_V at 198 K (Fig. 89 and 111). Moreover, an EB effect is usually observed in the hysteresis loops. If none of these feature can be observed in the temperature

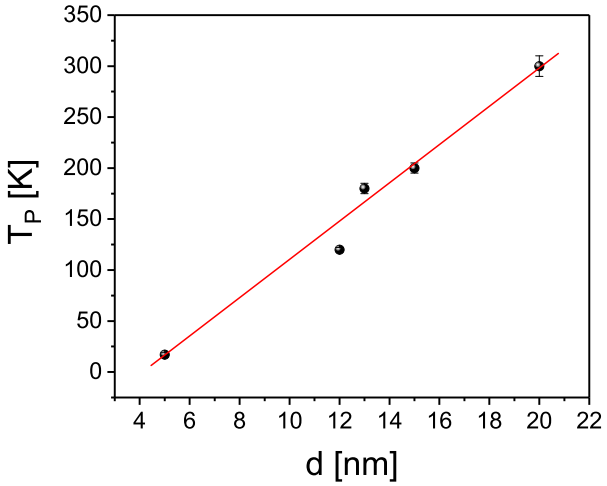

Figure 118: Peak temperature observed in the ZFC curves depending on the size of the iron oxide NPs.

dependent magnetization curves, the sample is likely composed of pure maghemite.

For 15 and 20 nm commercially available iron oxide NPs (Ocean NanoTech), a weak Verwey transition of magnetite is observed. Moreover, an increase in the ZFC curves above the T_N of wüstite (∼200 K) has been found in both 15 and 20 nm NPs. This can be due to some FiM spins, which are locked by AF wüstite below its T_N. As the temperature increases to above 200 K, theses spins are set free and start to turn along the field direction. Thus the overall magnetization increases. The magnetization in the FC curves decreases slightly at low temperatures possibly due to the existence of a small amount of wüstite or dipolar interactions between NPs. Therefore, both 15 and 20 nm iron oxide NPs are composed of mainly maghemite with a small ratio of magnetite and wüstite. In addition, a peak indicating the crossover between the blocked and unblocked SSG/SPM states of the NP superspins has been observed in the ZFC curves. This peak temperature shows a strong field dependence, which has often been observed for SPM and SSG systems. ZFC/FC magnetization curves of 11 - 13 nm iron oxide NPs from the collaboration of University Augsburg show the typical behaviour of SPM/SSG systems depending on the interaction strength between the particles. The peak temperature decreases rapidly with an increasing magnetic field and disappears at about 1 T. For all NPs from the University Augsburg, no Verwey transition is observed. Moreover, no increase in the magnetization near the T_N of wüstite is found. Hence these NPs are likely pure maghemite. Smaller NPs with a diameter of 5 nm from Ocean NanoTech were also studied. For these NPs, the peak temperature reduces to about 18 K at a magnetic field of 5 mT. At 100 mT, the peak already disappears. Such small particles are very likely to be single domain.

Field dependent magnetization curves of all iron oxide NP samples show a PM behaviour at 300 K. At 5 K, open hysteresis loops have been observed. An EB effect has been found in hysteresis loops of 11 - 20 nm NPs. For 15 and 20 nm samples, it can be due to exchange coupling between AF wüstite and FiM maghemite and magnetite. A training effect of the EB field has also been observed for 15 nm NPs. For pure maghemite NPs (11 - 13 nm sizes), the EB effect is possibly because of the coupling between SG-like surface spins and the FiM core. For 5 nm NPs, the FiM core is too small to induce an EB effect.

Moreover, a hardening effect has also been found in the hysteresis loops of 11 to 20 nm NPs. Due to the EB effect on the interface between AF and FiM components or between SG-like shell and FiM core, an additional anisotropy is induced when the samples are cooled in a magnetic field. With an increasing H_{FC}, the exchange coupling between the AF and FiM components or between the SG-like shell and the FiM core becomes stronger. Thus the anisotropy increases and the hysteresis loops become more square-like.

The coercive field, EB field, hardness and squareness obtained from the hysteresis loops measured at 5 K after various H_{FC} have been compared for different samples. An increase in H_{C}, H_{ex}, squareness and hardness can be found until H_{FC}= 1T. Above 1 T, they usually stay constant. This anisotropy axis induced by the EB field has also been measured using a torque magnetometer. A 360° periodicity is found in the angle dependent torque measurements at 5 K after cooling in a magnetic field of 0.5mT.

As the dipolar interaction between the superspins of iron oxide NPs increases, a SG-like behaviour may be found. This can be confirmed by a memory effect measurement. In the difference between ZFC curves measured with and without a stop, a peak near the stopping temperature is found for densely packed NPs. This indicates a memory effect, which results from the dipolar interactions between the superspins. However, this effect cannot be found for the diluted NP dispersion. This indicates no obvious or much weaker dipolar interactions in the diluted NP sample.

The oxygen content inside the NPs has been successfully varied by performing various annealing procedures. By heating the NPs in vacuum at 318 °C, the amount of magnetite and wüstite evidently increases. When the NPs are heated in air, magnetite tends to be fully oxidized to maghemite. However, for large particles it is difficult to remove wüstite completely.

7 Summary and Outlook

In this thesis, the focus is magnetism at the nanoscale. In particular two transition metal oxides, i.e. manganese oxide and iron oxide have been studied using various methods, such as SEM, XRD, (GI)SAXS, magnetometry and polarized neutron scattering. As other transition metals, manganese and iron may have various valences in different compounds. In the divalent state, both MnO and FeO have a cubic fcc crystal structure. In addition, they are both AFs with a similar spin structure below their Néel temperatures at 118 K and 198 K, respectively. The magnetic moments within the (111) planes align parallel. The magnetic moments in neighbouring layers align antiparallel. When Mn and Fe are partially oxidized to the trivalent state, Mn_3O_4 and Fe_3O_4 may occur. Both of them have a spinel crystal structure and a FiM magnetic structure. When all Mn or Fe ions are in the trivalent state, FiM Mn_2O_3 and Fe_2O_3 with a spinel crystal structure can form. In the NP form, it is difficult to synthesize single phase manganese oxide or iron oxide NPs. Therefore, it is interesting to tune the phases of manganese oxide and iron oxide by various annealing procedures. Then the magnetic properties of NPs in different phases can be compared.

For NPs it is difficult to refine their crystal structure using XRD patterns. Due to their small size as well as the small amount of sample, the reflections are very broad and weak. Therefore, it is not possible to distinguish two spinel crystal structures such as magnetite and maghemite using this method. In contrast, magnetometry is sensible to the magnetic properties, which is different for different phases of manganese and iron oxides. By comparing the temperature and field dependent magnetization curves with the results obtained using other methods, such as heat capacity, AC-susceptibility measurements and neutron scattering, the composition inside the NPs can be verified.

For MnO, we have studied the spin structure inside the NPs using magnetometry and polarized neutron scattering [18]. We propose a fluctuating AF-SPM MnO core with a FiM Mn_3O_4 shell model to explain the contradiction between the magnetometry and polarized neutron scattering results. The magnetization dynamics of the fluctuating MnO core have been further confirmed using AC-susceptibility measurements.

In order to have a better understanding of the spin structure inside MnO NPs, bulk MnO has been measured as a reference. The ZFC curves of both as-prepared MnO powder and single crystal show a low temperature peak beside the expected feature indicating the AF-to-PM phase transition of MnO. This is due to either some particles with nm size or partially oxidized Mn_3O_4, which is further confirmed by various measurements, such as polarized neutron scattering, SEM and heat capacity measurements.

Single phase MnO bulk has been successfully produced after the as-prepared powder was annealed in vacuum at 920 °C for 150 h. For this sample, only a peak at 118 K is found in the ZFC/FC curves as expected for pure MnO. No low temperature peak has been found.

The 2D self-assembly of magnetic NPs have been studied using spherical iron oxide NPs. The largest areas of hexagonally ordered NP monolayers with a few $\sim \mu m^2$ domain sizes have been achieved using magnetic field guided self-assembly and substrate stacking methods. However, the quality of order is very different in different regions of the sample. Using drop-casting, spin coating and liquid-air-interface methods, homogeneous ordered monolayers with a correlation length of 500 nm to 1 μm have been produced.

For iron oxide NPs, a hardening effect is found in the hysteresis loops. This is due to

an extra anisotropy, which is induced when the samples are cooled in a magnetic field. By varying the magnetic cooling field, the anisotropy can be tuned. This anisotropy has also been measured using a torque magnetometer. A 360° oscillation period has been found in the angle dependent torque data. This indicates a unidirectional anisotropy.

The phases of both manganese and iron oxide have been successfully varied by annealing the as-prepared NPs in a vacuum chamber. After the particles were annealed in vacuum at 310°C for several hours, the oxygen content is reduced. Both manganese and iron oxide NPs can be oxidized to higher oxidation states after heated in air at 100°C for various durations. The compositions of the NPs were checked using magnetometry.

Besides the results obtained from this work, there are still open questions about these systems. MnO is one of the materials firstly studied using neutron scattering. Despite numerous studies, the spin structure of bulk MnO is still under debate. To have a better understanding of the spin structure inside MnO, it is interesting to measure a piece of MnO single crystal using neutron scattering. The results can be compared with NPs to study the influence of the finite size effect. However, synthesis of single phase metal oxide NPs is difficult. At the surface of MnO NPs, an oxidized Mn_3O_4 shell is often found. The as-prepared iron oxide NPs are usually composed of various phases. Therefore, it is interesting to find the proper conditions for the annealing procedures to produce single phase manganese oxide and iron oxide NPs. A systematic study of the magnetic properties of manganese oxide and iron oxide NPs with a controllable phase needs to be done. By comparing the oxygen concentration before and after the annealing procedure inside the chamber, the exact amount of oxygen gain or loss in the sample is of interest. Single phase manganese oxide or iron oxide thin films are also interesting to be studied to be compared with the NP results. Moreover, the origin of the much larger coercive field found in the hysteresis loops of Mn_3O_4 NPs compared to that of their bulk form is still needed to be understood.

The quality of 2D ordered iron oxide monolayers can be improved by finding the proper parameters for the NP self-assembly, such as the evaporation rate, the NP concentration and the gas flow at the surface of the dispersion. Further methods, such as the doctor blade casting method and Langmuir-Blodgett technique can also be used for 2D self-assembly. Moreover, the magnetic correlations between the superspins in the 2D ordered NP monolayers can be studied using grazing incidence small angle neutron scattering (GISANS). However, one monolayer of iron oxide NPs is too little amount for a neutron scattering experiment. By stacking several NP monolayers on top of each other with a gap of $\sim$100 μm in between, the signal can be enhanced without introducing additional interactions between NPs in neighbouring layers.

Appendices

A Parameters used in MC simulations

Atomic spin of a Mn ion: $|S| = 5/2$
Bohr magneton: $\mu_B = 9.2740094980 \times 10^{-24}$ J/T
g-factor: $g_J = 2.0$
Exchange constants*:
for in-plane nearest-neighbours: $J_{1\mathrm{p}}$ = -1.371312×10^{-22} J (= 0.428 meV)
for nearest-neighbours in neighbouring planes: $J_{1\mathrm{m}}$ = -1.038096×10^{-22} J (= 0.324 meV)
an averaged exchange constant for nearest-neighbours (same for all nearest neighbours): $J_1 = \frac{1}{2} \cdot (J_{1\mathrm{m}} + J_{1\mathrm{m}})$ = -1.204704×10^{-22} J
for next nearest-neighbours: J_2 = -1.34568×10^{-22} J (= 0.420 meV)
Anisotropy constants*:
for an out-of-plane anisotropy: D_1 = -0.94518×10^{-23} J (= 0.059 meV)
for an in-plane anisotropy: D_2 = -0.6408×10^{-24} J (= 0.004 meV)

*: Exchange constants J_1, J_2 and the anisotropy constants D_1 and D_2 are taken from Ref. [75–77].

B Convergence test with various Monte Carlo steps

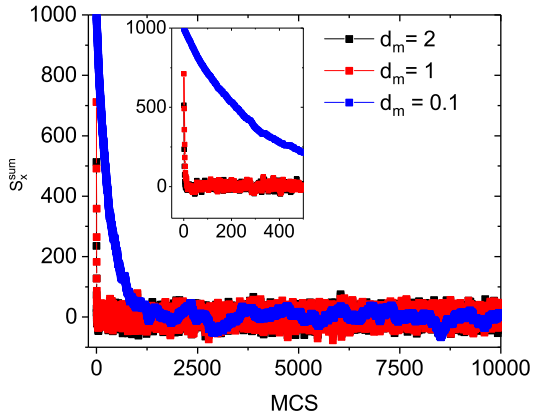

(a)

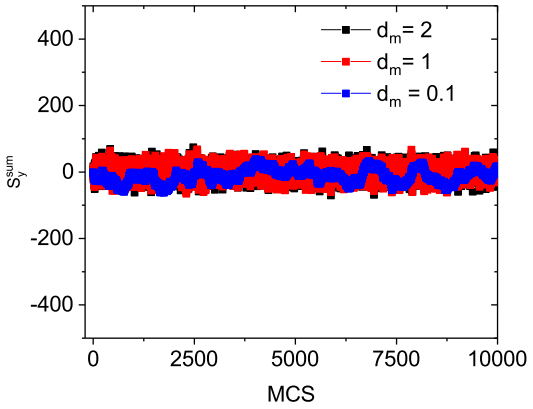

(b)

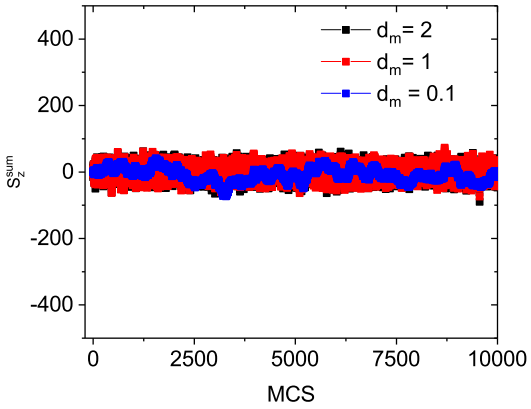

(c)

Figure 119: Sum of the x-, y- and z- components of 10×10×10 unit vectors depending on the Monte Carlo steps after a test rotation (d_m) with various lengths, respectively. All 1000 vectors have an initial state of $\vec{S}$=(100). After each test rotation, the vector is normalized to 1.

C XRD patterns of MnO powder after various treatments

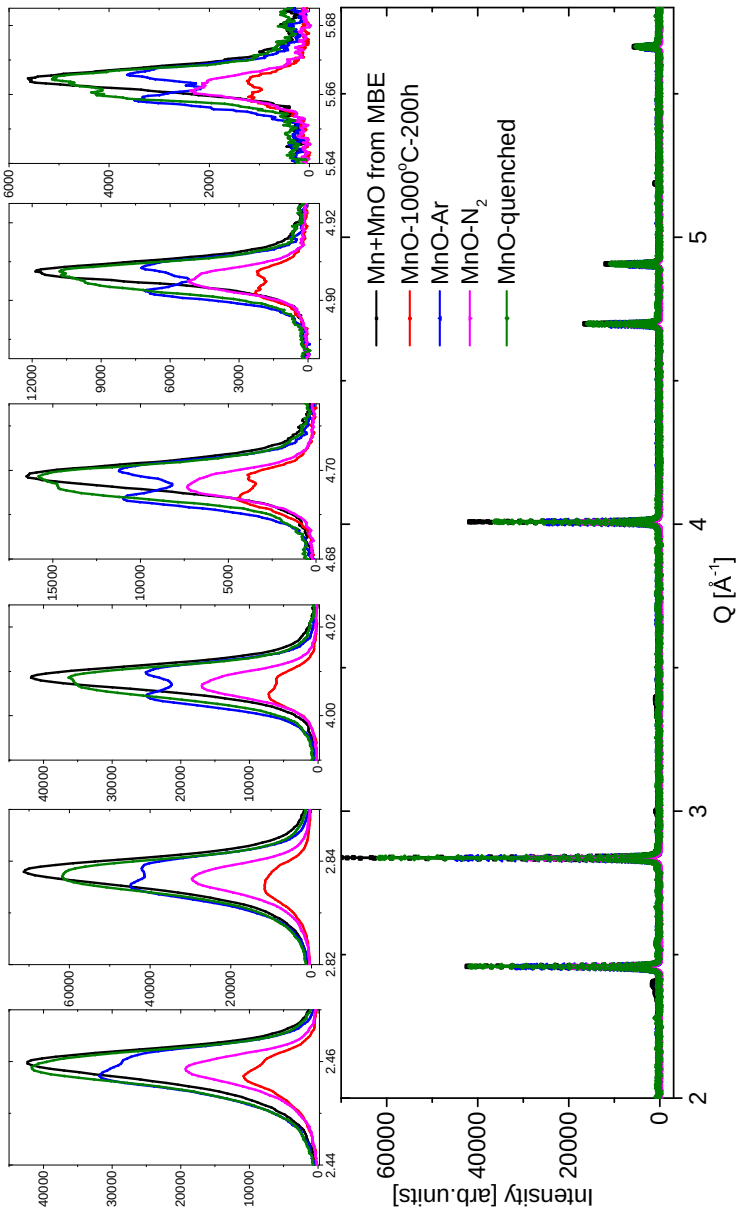

Figure 120: XRD pattern of MnO powder after various treatment: Mn target from MBE, which is a mixture of Mn and MnO (black); MnO powder from Alfa Aesar heated at 1000°C for 200h in vacuum (red); MnO powder from Alfa Aesar heated at 920°C for 100h and then at 1000°C for 12h in 20mbar Ar (blue) or N_2 (pink) atmosphere; MnO powder from Alfa Aesar quenched in water and partially oxidized to red colour (green).

D Magnetometry results of MnO

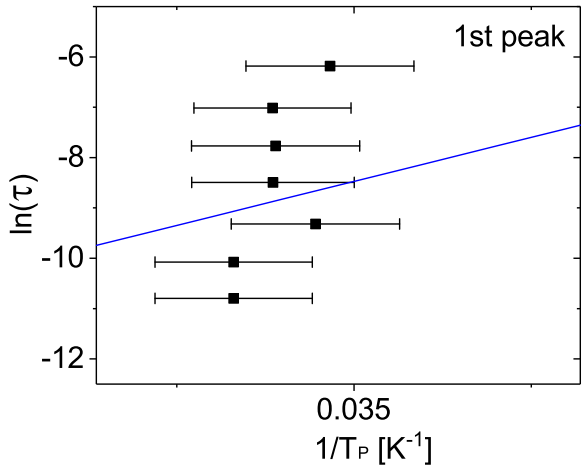

Figure 121: Relaxation time vs inverse peak temperature in a log-lin plot for the first peak at $\sim$ 28K in Fig. 33. The blue line indicates the Arrhenius equation with $\tau_0 = 10^{-10}$ s and $\frac{KV}{k_B} = 350$ K.

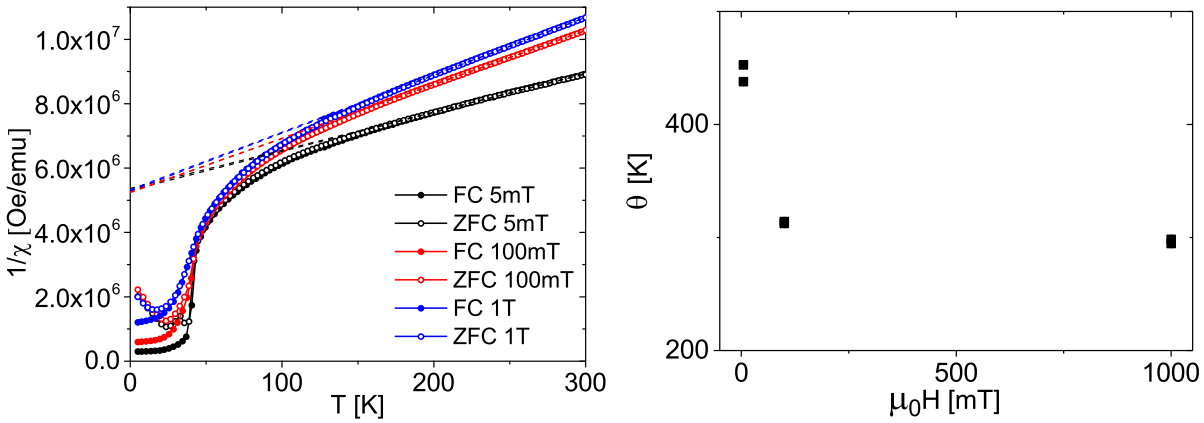

Figure 122: (a) Inverse dc-susceptibility as function of temperature for the as-prepared MnO NPs with 12 nm diameter. (b) Critical temperature extrapolated from various curves in (a) with error bars.

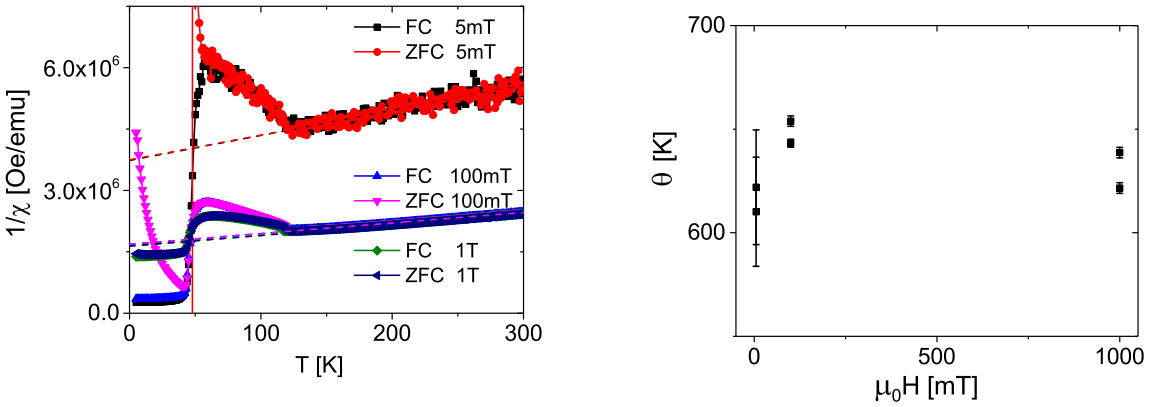

Figure 123: (a) Inverse dc-susceptibility as function of temperature for the as-prepared MnO single crystal. (b) Critical temperature extrapolated from various curves in (a).

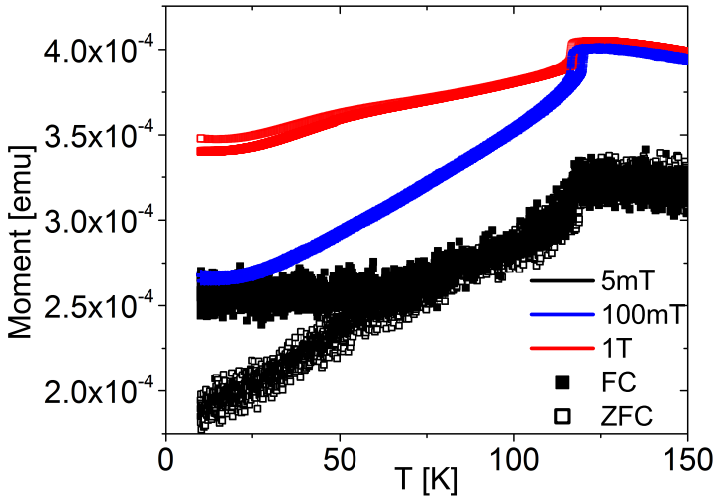

Figure 124: ZFC and FC curves for MnO powder annealed at 920°C for 150 h measured at various magnetic fields.

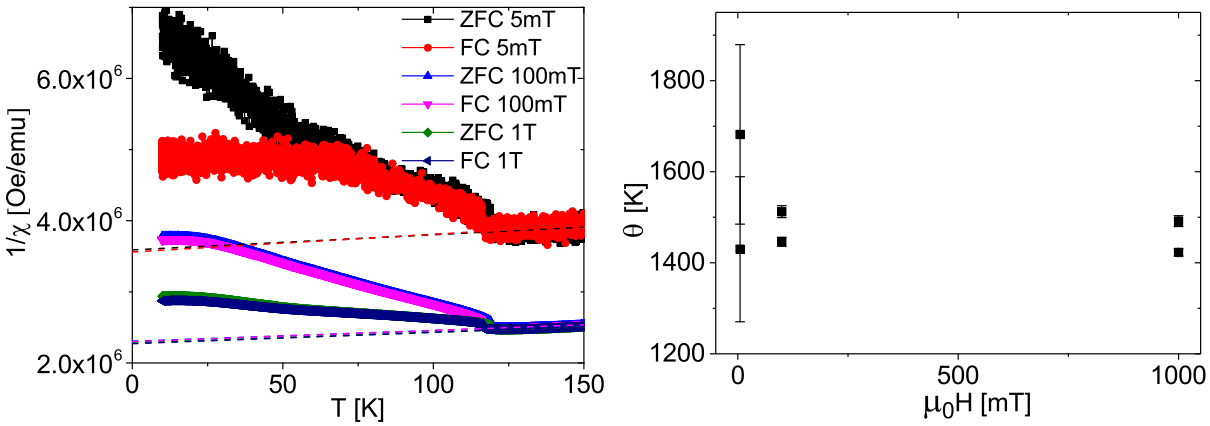

Figure 125: (a) Inverse dc-susceptibility as function of temperature for the annealed MnO powder at 920°C for 150 h. (b) Critical temperature extrapolated from various curves in (a).

E Polarized Neutron diffraction

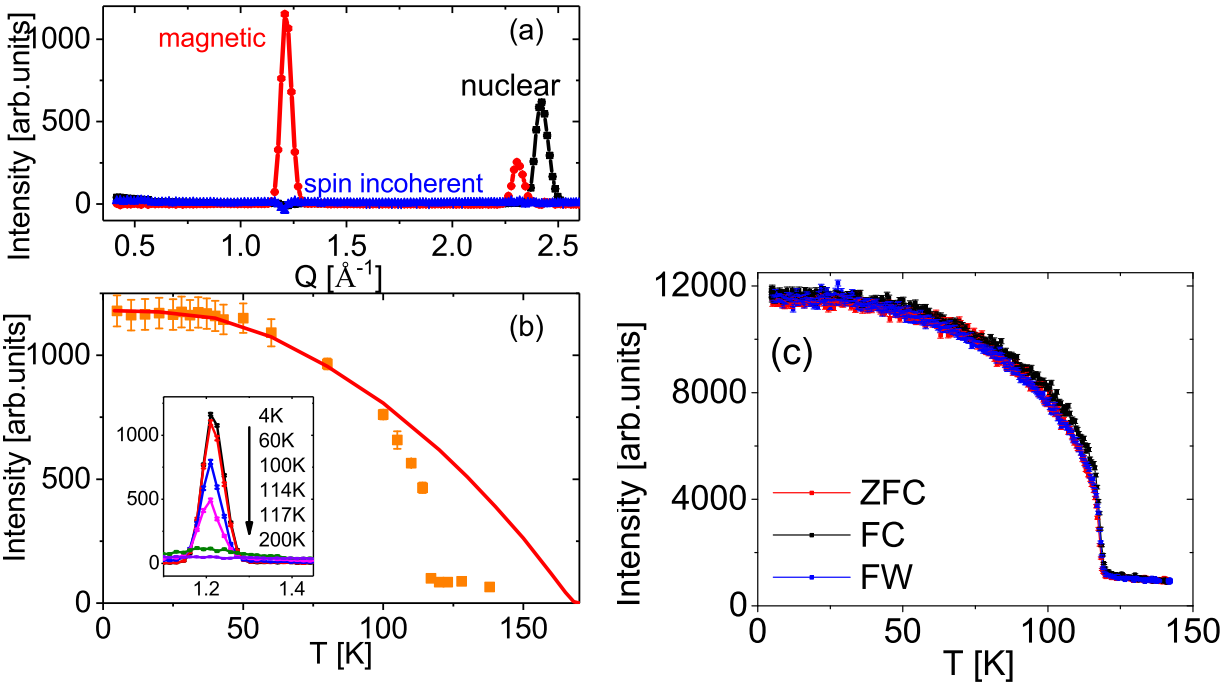

Figure 126: (a) Nuclear coherent (black), nuclear spin-incoherent (blue) and magnetic (red) components of the as-prepared MnO powder from polarized neutron scattering measured at 4 K. (b) Temperature dependence of the integrated intensity of the AF $\left(\frac{1}{2}\frac{1}{2}\frac{1}{2}\right)$ Bragg peak. The orange squares with error bars represent the integrated intensity of the AF $\left(\frac{1}{2}\frac{1}{2}\frac{1}{2}\right)$ Bragg peak and the red line is a fit using a mean field curve with $S = \frac{5}{2}$ assuming a "virtual" $T_N = 170$ K. The inset in (b) shows the magnetic $\left(\frac{1}{2}\frac{1}{2}\frac{1}{2}\right)$ Bragg peaks at different temperatures. (c) Temperature dependence of the intensity at the Q-value of the AF $\left(\frac{1}{2}\frac{1}{2}\frac{1}{2}\right)$ Bragg peak measured after a zero field cooling procedure, or during a FC / FW procedure at a magnetic field of 3 mT.

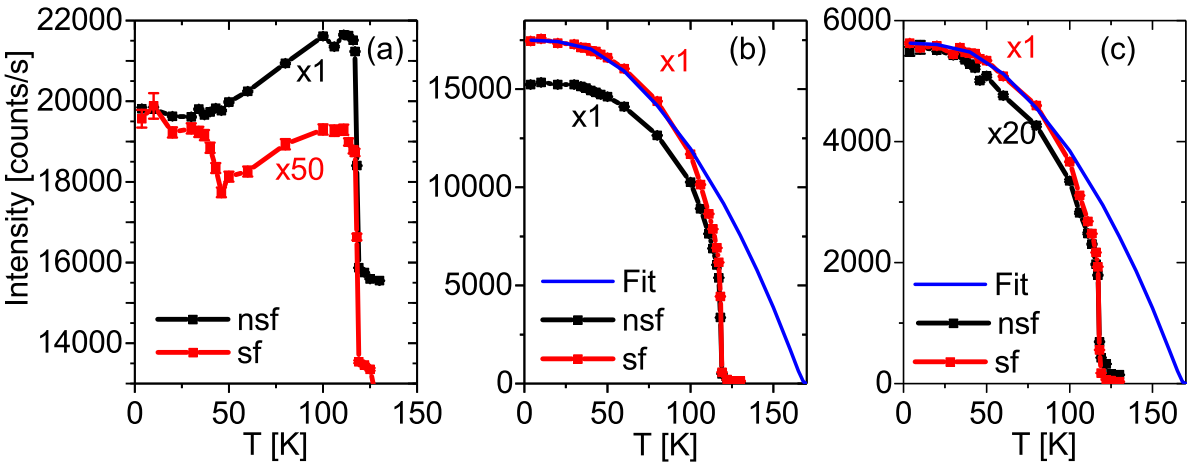

Figure 127: Temperature dependence of the intensities in the SF and NSF channel at the position of (a) $(\bar{1}\bar{1}\bar{1})$, (b) $\left(\frac{\bar{1}}{2}\frac{\bar{1}}{2}\frac{\bar{1}}{2}\right)$, and (c) $\left(\frac{\bar{1}}{2}\frac{\bar{1}}{2}\frac{\bar{3}}{2}\right)$ Bragg peaks of the as-prepared MnO single crystal.

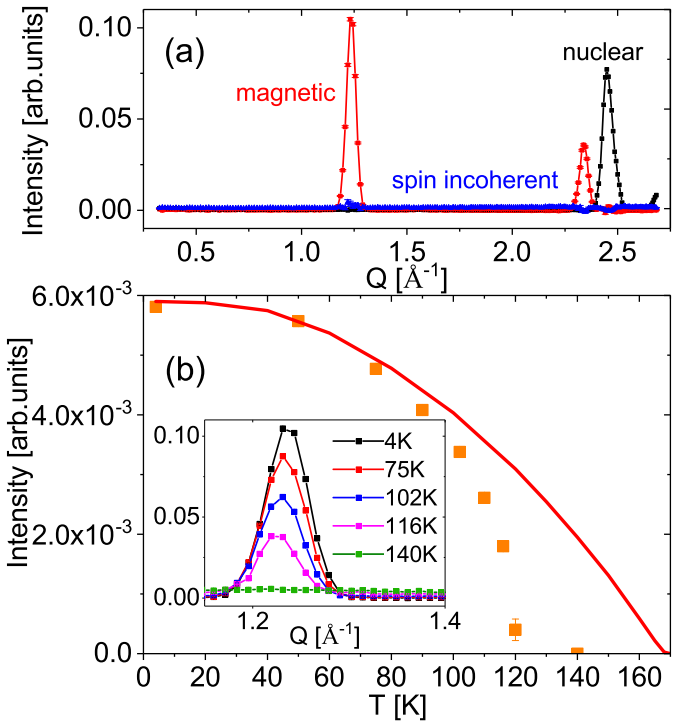

Figure 128: (a) Nuclear coherent (black), nuclear spin-incoherent (blue) and magnetic (red) components of the polarized neutron diffraction of MnO powder after annealing at 920°C for 150 h measured at 4 K. (b) Temperature dependence of the integrated intensity of the AF $\left(\frac{1}{2}\frac{1}{2}\frac{1}{2}\right)$ Bragg peak. The orange squares represent the intensity of the AF $\left(\frac{1}{2}\frac{1}{2}\frac{1}{2}\right)$ Bragg peak with error bars and the red line is a fit using a mean field curve with $S = \frac{5}{2}$. Inset in (b) shows the magnetic $\left(\frac{1}{2}\frac{1}{2}\frac{1}{2}\right)$ Bragg peak at different temperatures.

F Monte Carlo Simulations

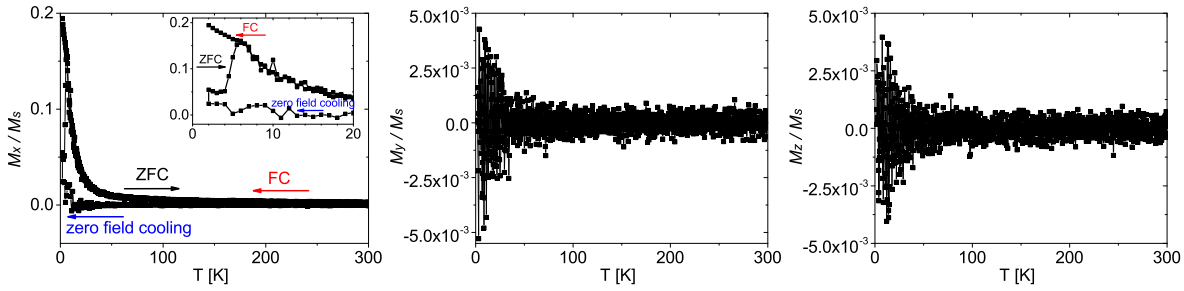

(a) (b) (c)

Figure 129: ZFC/FC magnetization curves of a 3x3x3 MnO NP simulated along (a) x-, (b) y-, and (c) z-directions at 1 T. Both the anisotropy axis and the magnetic field are parallel to the x-direction (crystallographic [111] direction of MnO).

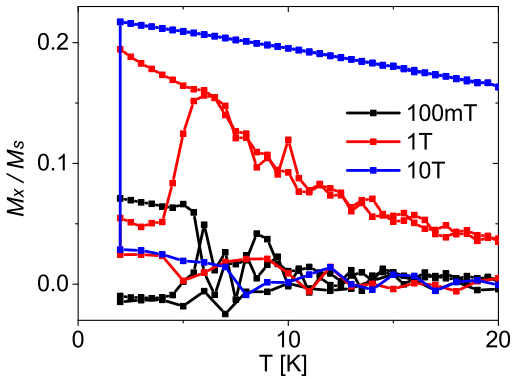

Figure 130: ZFC/FC curves of a 3x3x3 NP simulated at various magnetic fields.

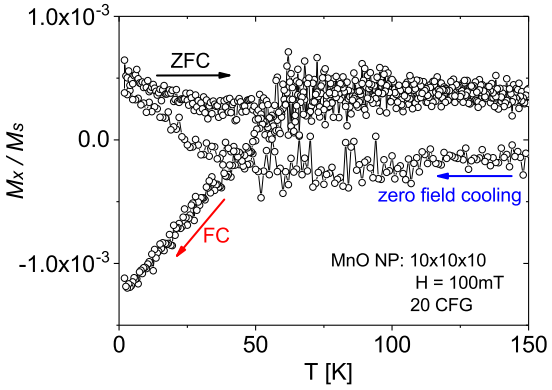

Figure 131: ZFC/FC curves simulated for a 10x10x10 NP at 100 mT. These curves were obtained after averaged over 20 configurations (CGS).

.

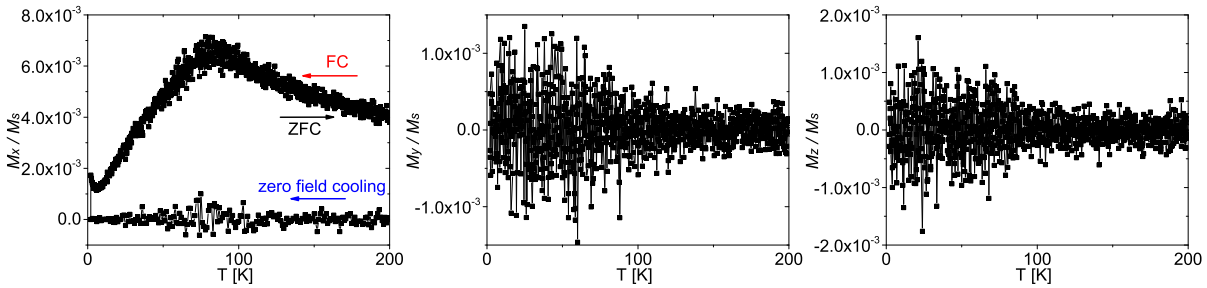

(a) (b) (c)

Figure 132: ZFC/FC magnetization curves of a 10x10x10 MnO NP simulated along (a) x-, (b) y-, and (c) z-directions at 1 T with 1000 MCS. Both the anisotropy axis and the magnetic field are parallel to the x-direction (crystallographic [111] direction of MnO).

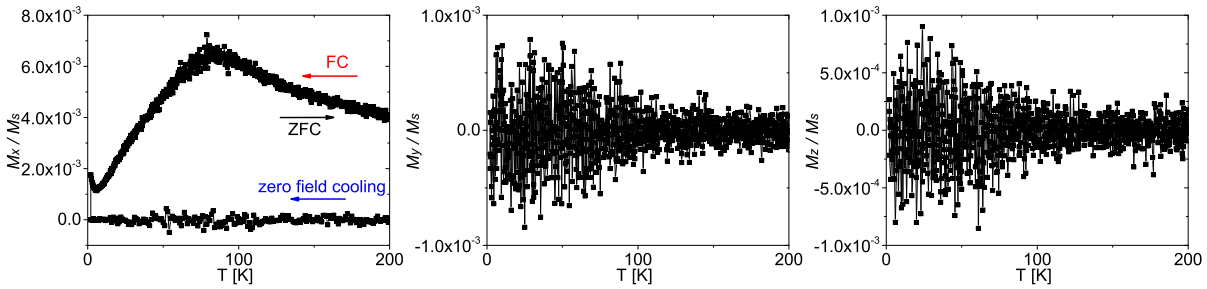

(a) (b) (c)

Figure 133: ZFC/FC magnetization curves of a 10x10x10 MnO NP simulated along (a) x-, (b) y-, and (c) z-directions at 1 T with 3000 MCS. Both the anisotropy axis and the magnetic field are parallel to the x-direction (crystallographic [111] direction of MnO).

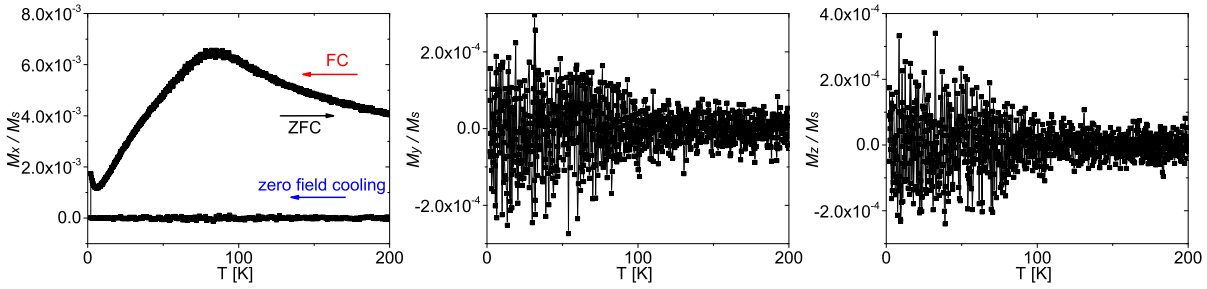

(a) (b) (c)

Figure 134: ZFC/FC magnetization curves of a 10x10x10 MnO NP simulated along (a) x-, (b) y-, and (c) z-directions at 1 T with 30000 MCS. Both the anisotropy axis and the magnetic field are parallel to the x-direction (crystallographic [111] direction of MnO).

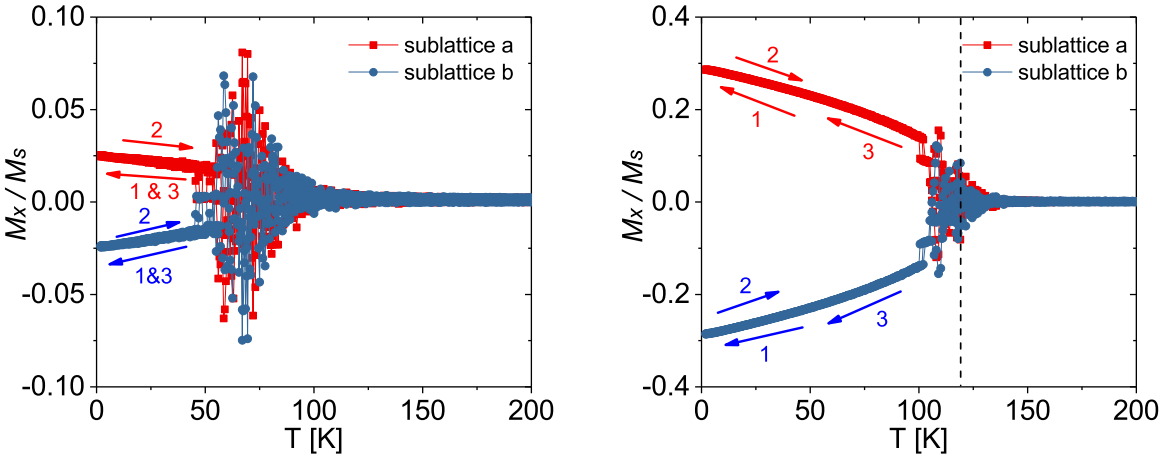

(a) (b)

Figure 135: X-components of the sublattices a and b magnetization curves of a 10x10x10 MnO NP simulated at 1 T. For (a) J_p=J_m=J and for (b) $J_p \neq J_m$. Both the anisotropy axis and the magnetic field are parallel to the x-direction (crystallographic [111] direction of MnO). 1, 2 and 3 in the figures indicate different simulation procedures. Procedure 1 is recorded during cooling the NP in the absence of a magnetic field. Procedure 2 is simulated during warming up within a magnetic field of 1 T. Procedure 3 is simulated during cooling within a magnetic field of 1 T.

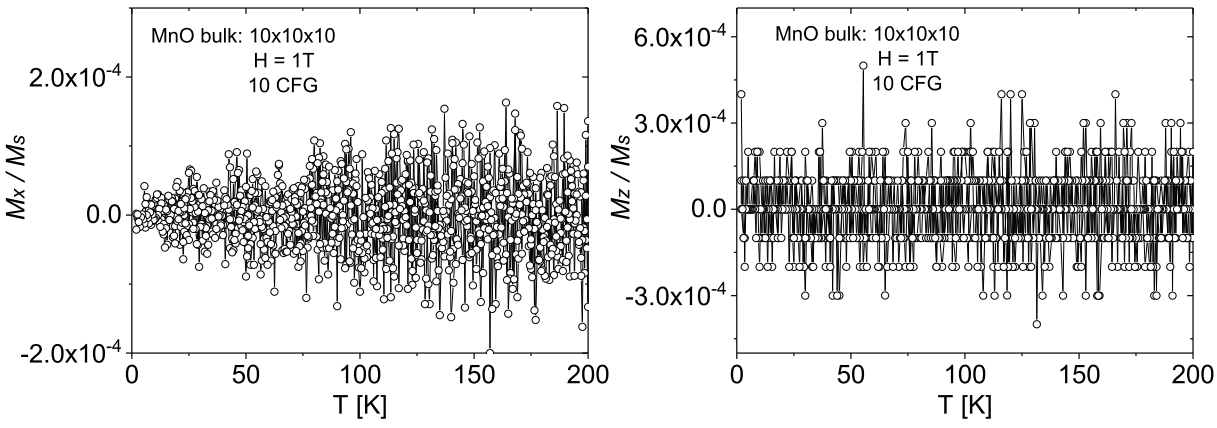

(a) (b)

Figure 136: ZFC/FC magnetization curves of MnO "bulk" simulated along (a) x-, (b) z-directions at 1 T. The anisotropy axis is along crystallographic [111] direction of MnO (parallel to x). The magnetic field is parallel to the y-direction (within the (111) plane).

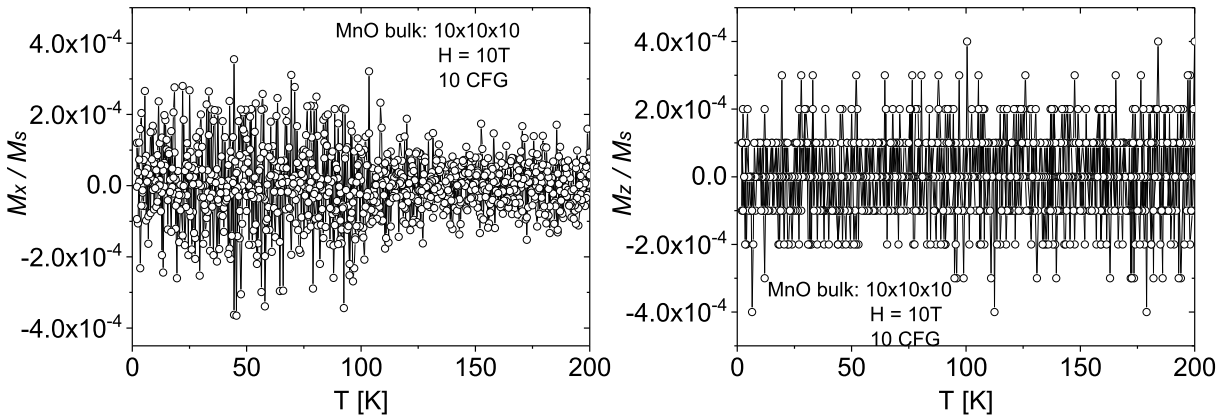

(a) (b)

Figure 137: ZFC/FC magnetization curves of MnO "bulk" simulated along (a) x-, (b) z-directions at 10 T. The anisotropy axis is along crystallographic [111] direction of MnO (parallel to x). The magnetic field is parallel to the y-direction (within the (111) plane).

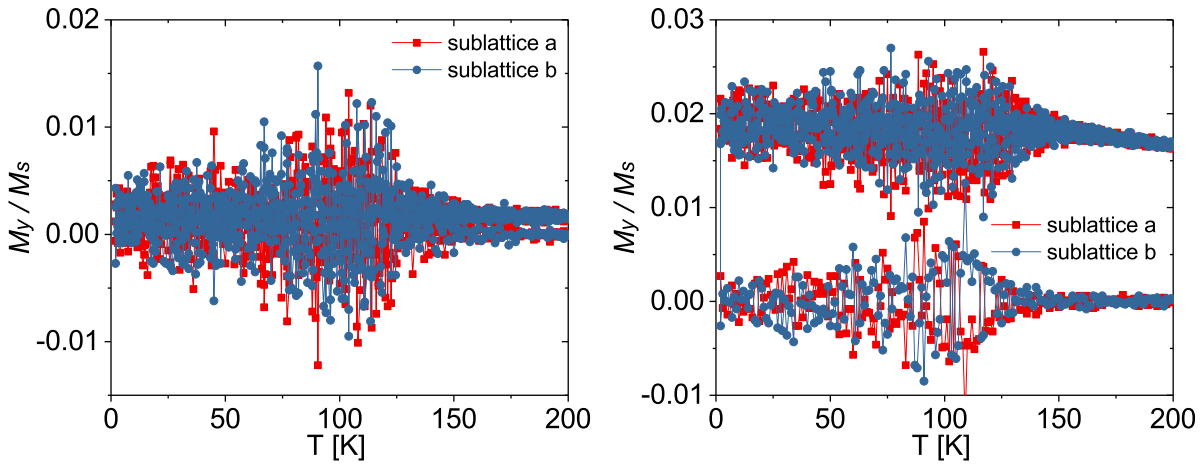

(a) (b)

Figure 138: Y-components of the sublattices a and b magnetization curves of MnO "bulk" simulated at (a) 1 T and (b) 10 T. The anisotropy axis is along crystallographic [111] direction of MnO (parallel to x). The magnetic field is parallel to the y-direction (within the (111) plane).

G Spin Visualizations

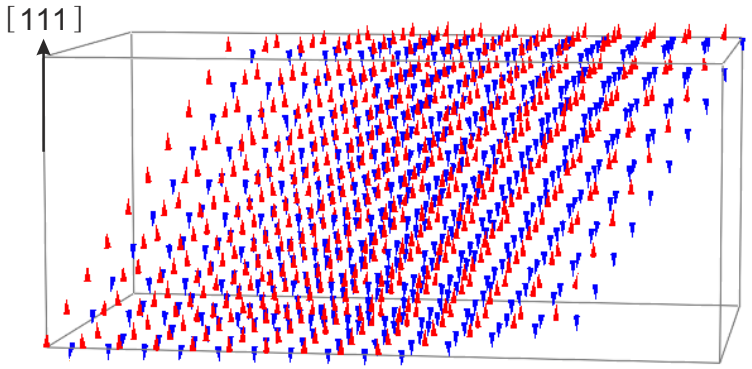

(a) 2 K at the beginning of a ZFC curve

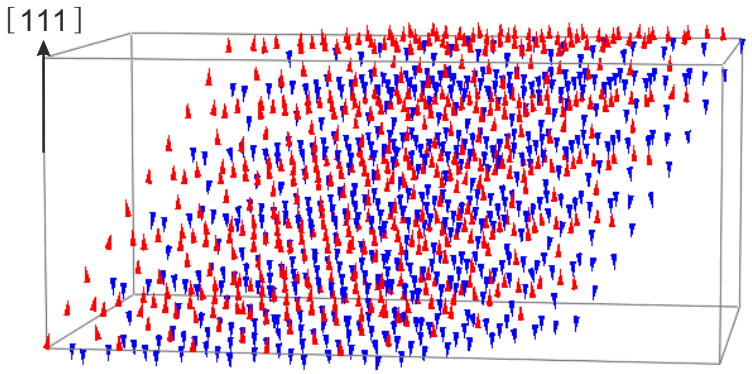

(b) 2 K after a FC procedure

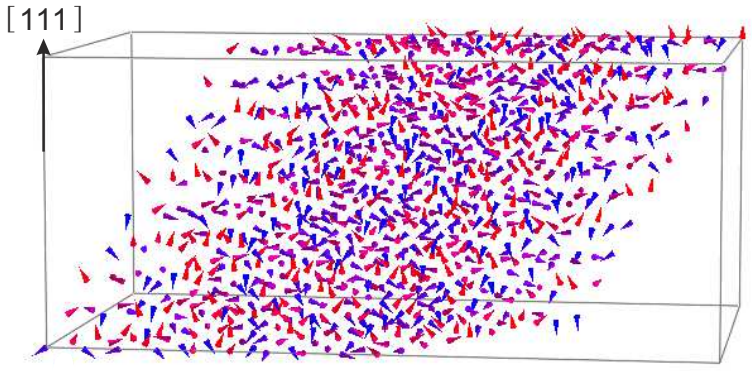

(c) 200 K

Figure 139: Illustration of the spin structure of "bulk" MnO simulated with a magnetic field of 1 T (a) at 2 K at the beginning of a ZFC curve, (b) at 2 K after a FC procedure, and (c) at 200 K resulting from the tenth configuration after 10000 average loops. Both the anisotropy axis and the magnetic field are parallel to the x-direction (crystallographic [111] direction of MnO).

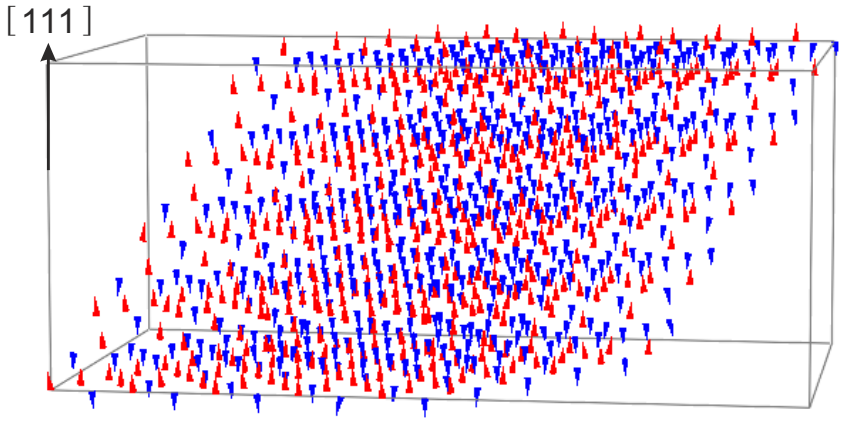

(a) 2 K at the beginning of a ZFC curve

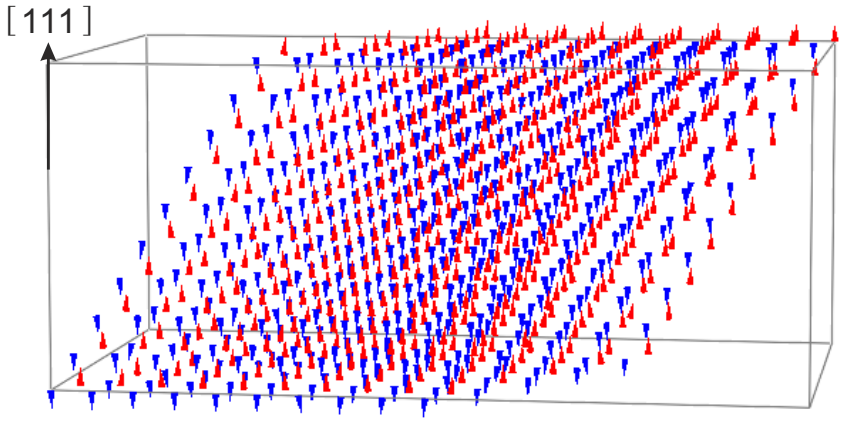

(b) 2 K after a FC procedure

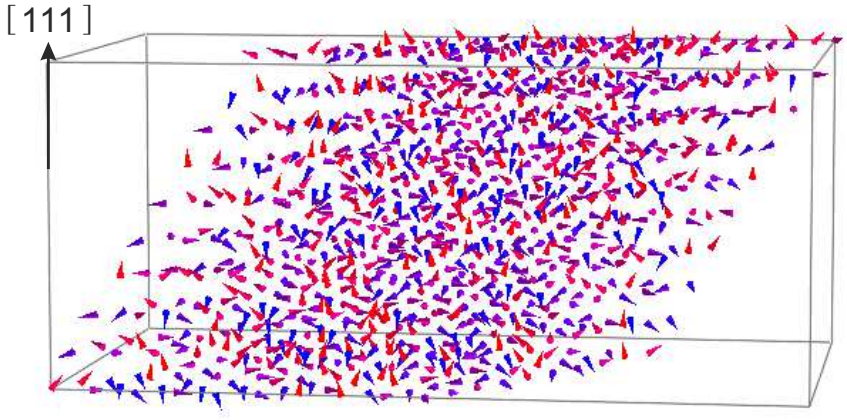

(c) 200 K

Figure 140: Illustration of the spin structure of "bulk" MnO simulated with a magnetic field of 1 T (a) at 2 K at the beginning of a ZFC curve, (b) at 2 K after a FC procedure, and (c) at 200 K resulting from the first configuration after 10000 relaxation loops. Both the anisotropy axis and the magnetic field are parallel to the x-direction (crystallographic [111] direction of MnO).

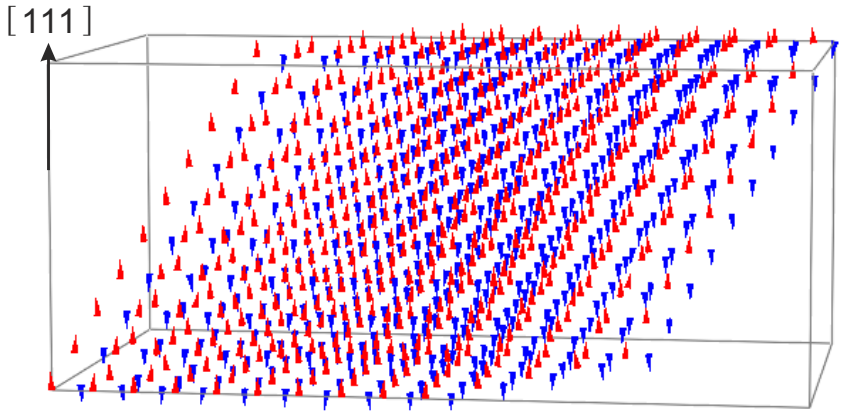

(a) 2 K at the beginning of a ZFC curve

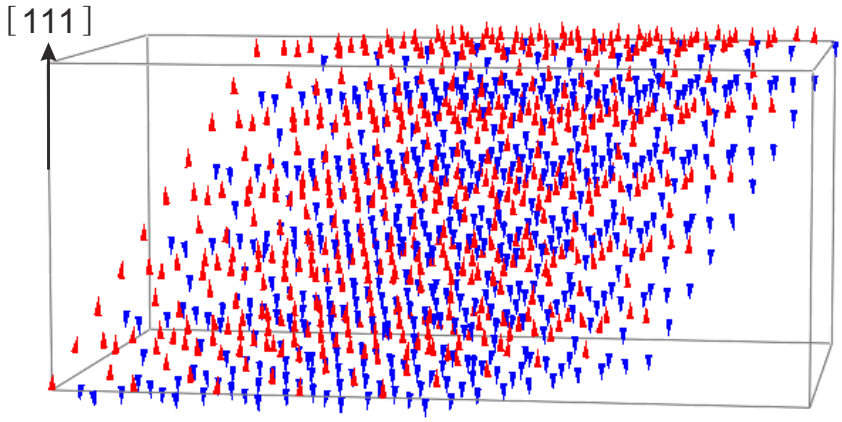

(b) 2 K after a FC procedure

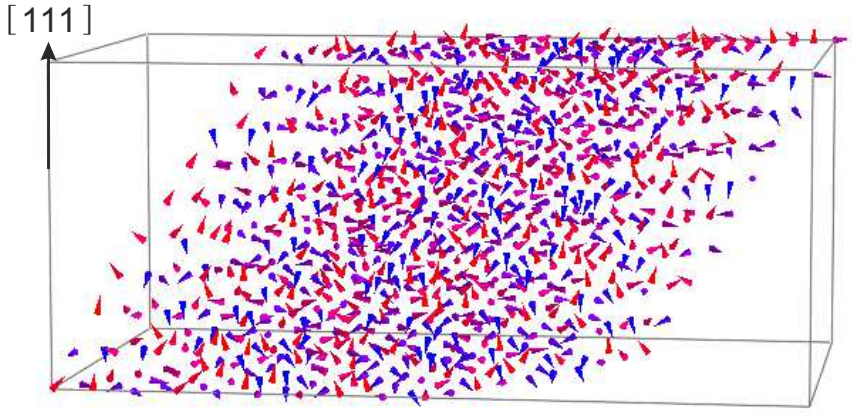

(c) 200 K

Figure 141: Illustration of the spin structure of "bulk" MnO simulated with a magnetic field of 1 T (a) at 2 K at the beginning of a ZFC curve, (b) at 2 K after a FC procedure, and (c) at 200 K resulting from the tenth configuration after 10000 relaxation loops. Both the anisotropy axis and the magnetic field are parallel to the x-direction (crystallographic [111] direction of MnO).

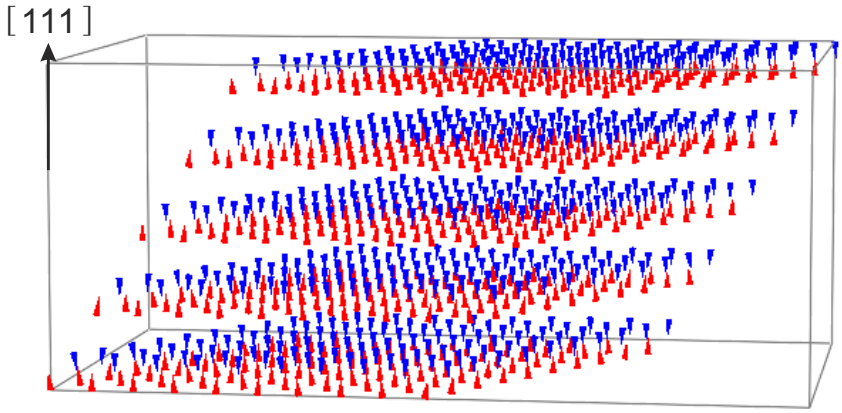

(a) 2 K at the beginning of a ZFC curve

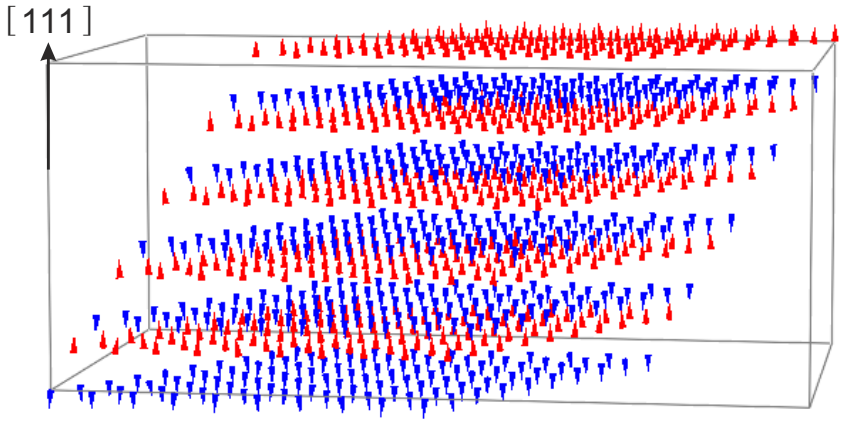

(b) 2 K after a FC procedure

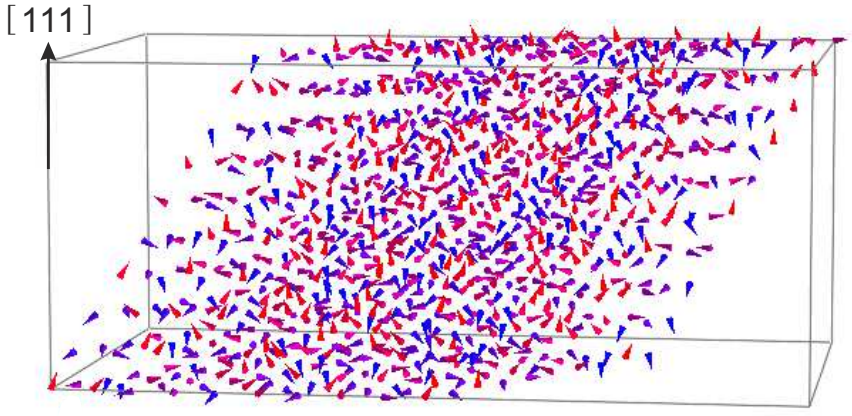

(c) 300 K

Figure 142: Illustration of the spin structure of "bulk" MnO simulated with a magnetic field of 1 T (a) at 2 K at the beginning of a ZFC curve, (b) at 2 K after a FC procedure, and (c) at 300 K resulting from the tenth configuration after 10000 average loops with $J_{1m} \neq J_{1p}$ for nearest neighbours in the same plane and in neighbouring planes. Both the anisotropy axis and the magnetic field are parallel to the x-direction (crystallographic [111] direction of MnO).

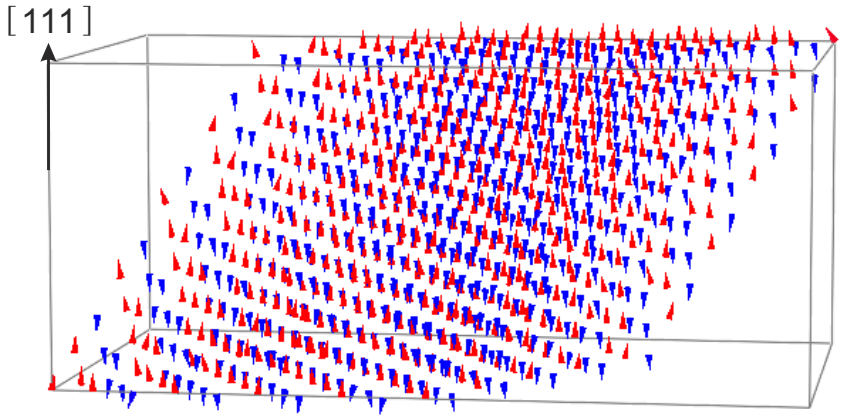

(a) 2 K at the beginning of a ZFC curve

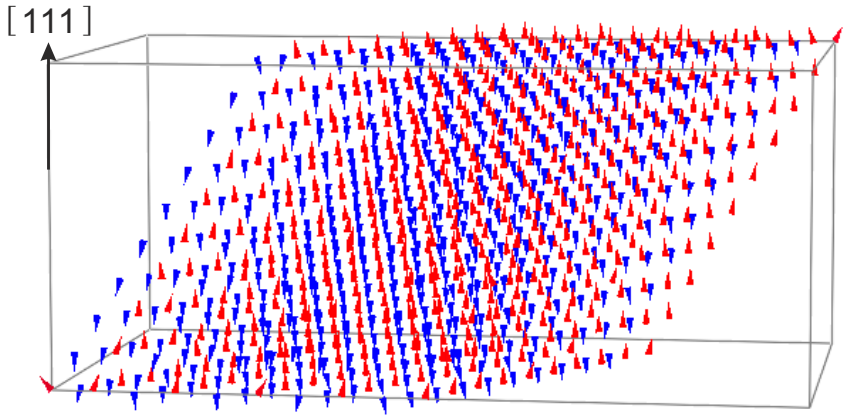

(b) 2 K after a FC procedure

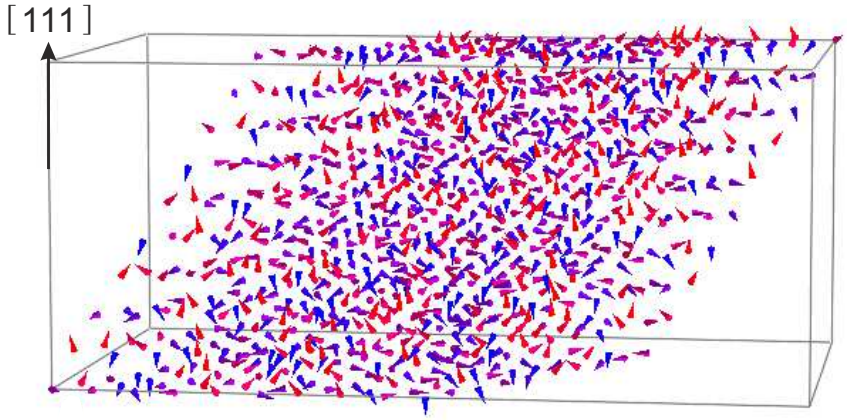

(c) 200 K

Figure 143: Illustration of the spin structure of a 10×10×10 MnO NP simulated with a magnetic field of 1 T (a) at 2 K at the beginning of a ZFC curve, (b) at 2 K after a FC procedure, and (c) at 200 K resulting from the tenth configuration after 10000 average loops. Both the anisotropy axis and the magnetic field are parallel to the x-direction (crystallographic [111] direction of MnO).

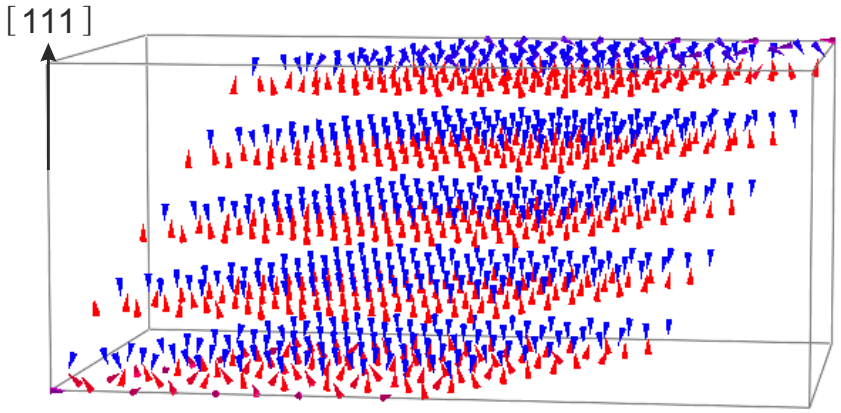

(a) 2 K at the beginning of a ZFC curve

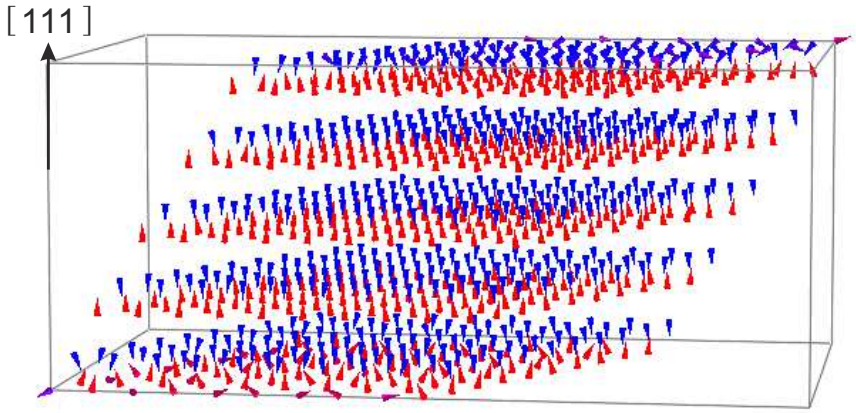

(b) 2 K after a FC procedure

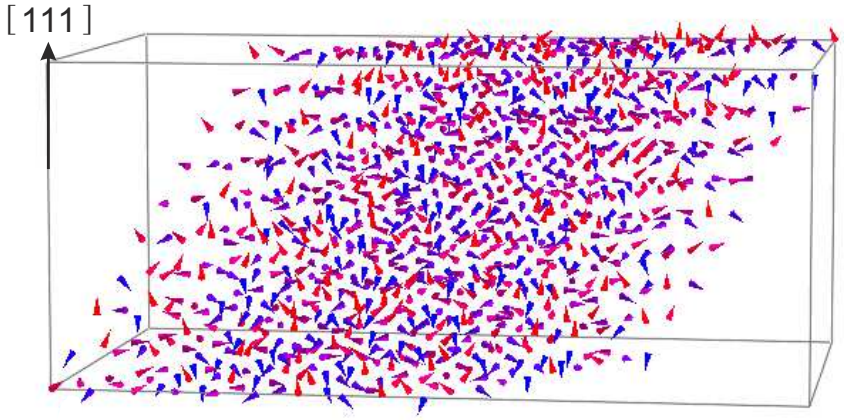

(c) 300 K

Figure 144: Illustration of the spin structure of a $10\times10\times10$ NP simulated with a magnetic field of 1 T (a) at 2 K at the beginning of a ZFC curve, (b) at 2 K after a FC procedure, and (c) at 300 K resulting from the tenth configuration after 10000 average loops with $J_{1m} \neq J_{1p}$ for nearest neighbours in the same plane and in neighbouring planes. Both the anisotropy axis and the magnetic field are parallel to the x-direction (crystallographic [111] direction of MnO).

H SEM Images of Iron Oxide NPs

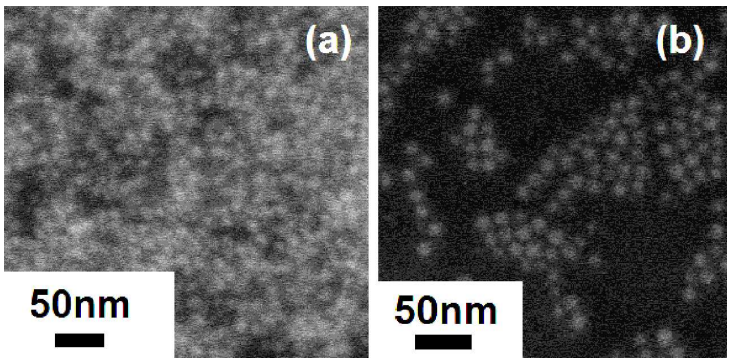

Figure 145: SEM images of spherical iron oxide NPs with 13 nm diameter from University Augsburg. (a) Hexane is added after drop-casting. (b) Toluene is added after drop-casting.

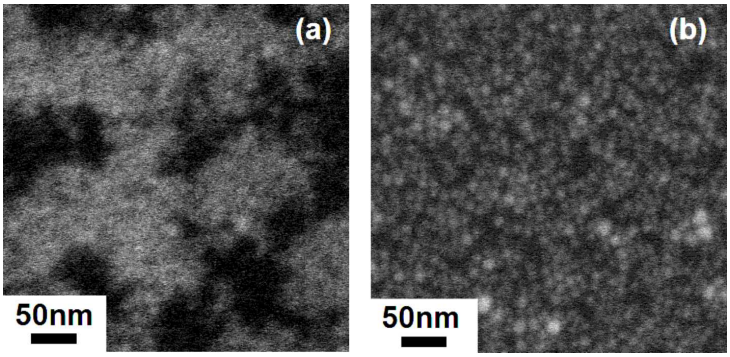

Figure 146: SEM images of cubic iron oxide NPs with 11 nm size from University Augsburg. (a) Hexane is added after drop-casting. (b) Toluene is added after drop-casting.

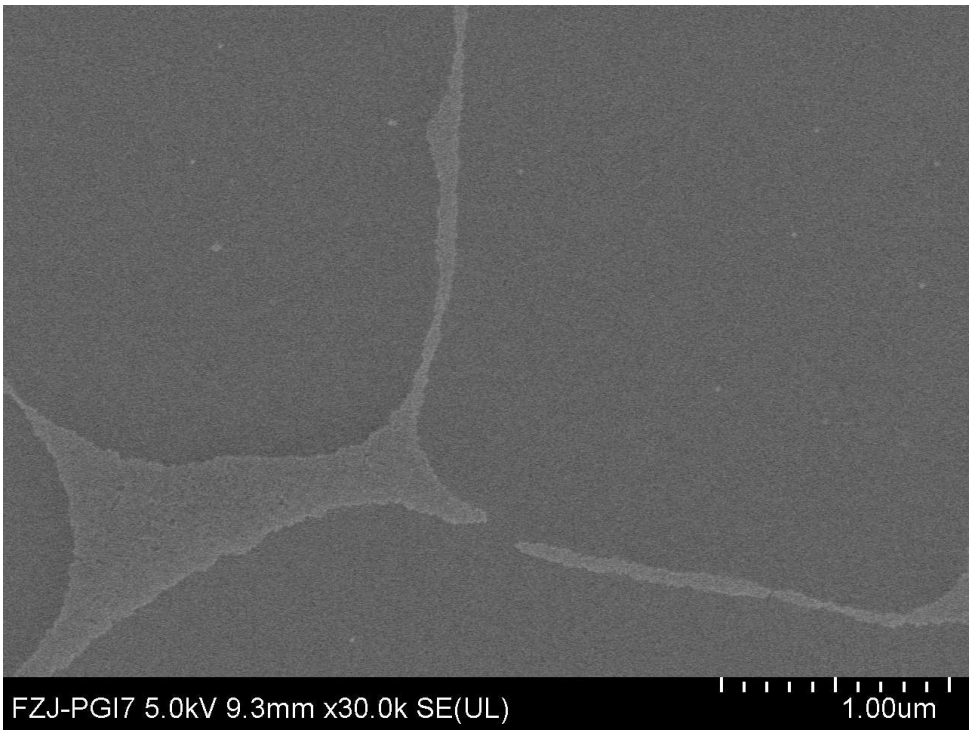

Figure 147: SEM image of self-assembled spherical iron oxide NPs with 15 nm diameter diluted to a ratio of solution:toluene = 1:30.

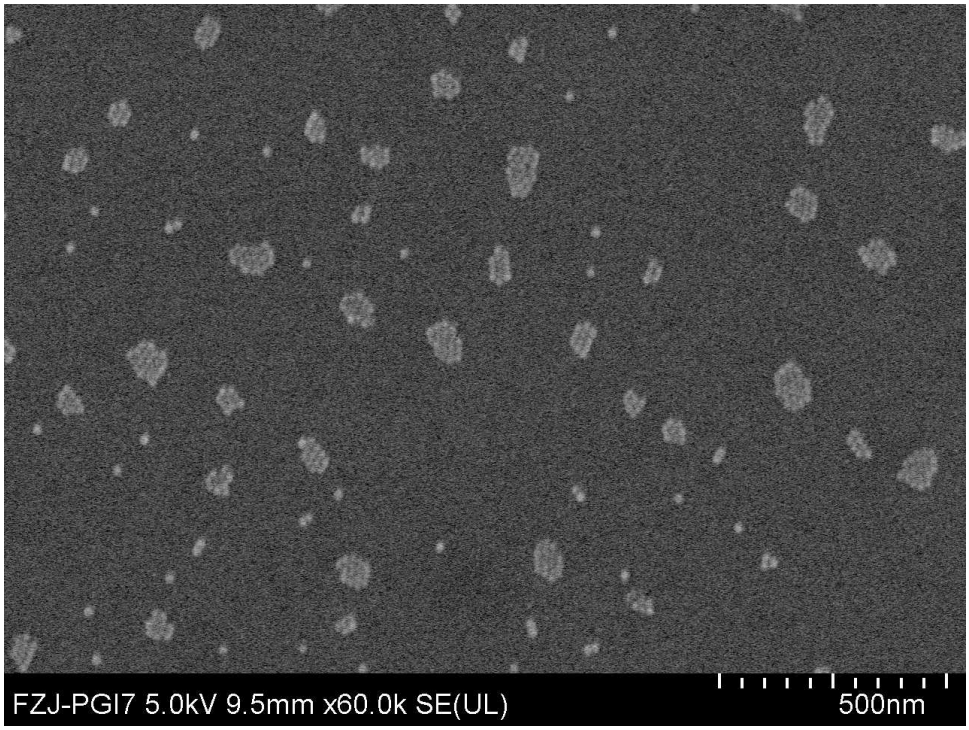

Figure 148: SEM image of self-assembled spherical iron oxide NPs with 15 nm diameter diluted to a ratio of solution:toluene = 1:50.

I Magnetization curves of Iron Oxide NPs

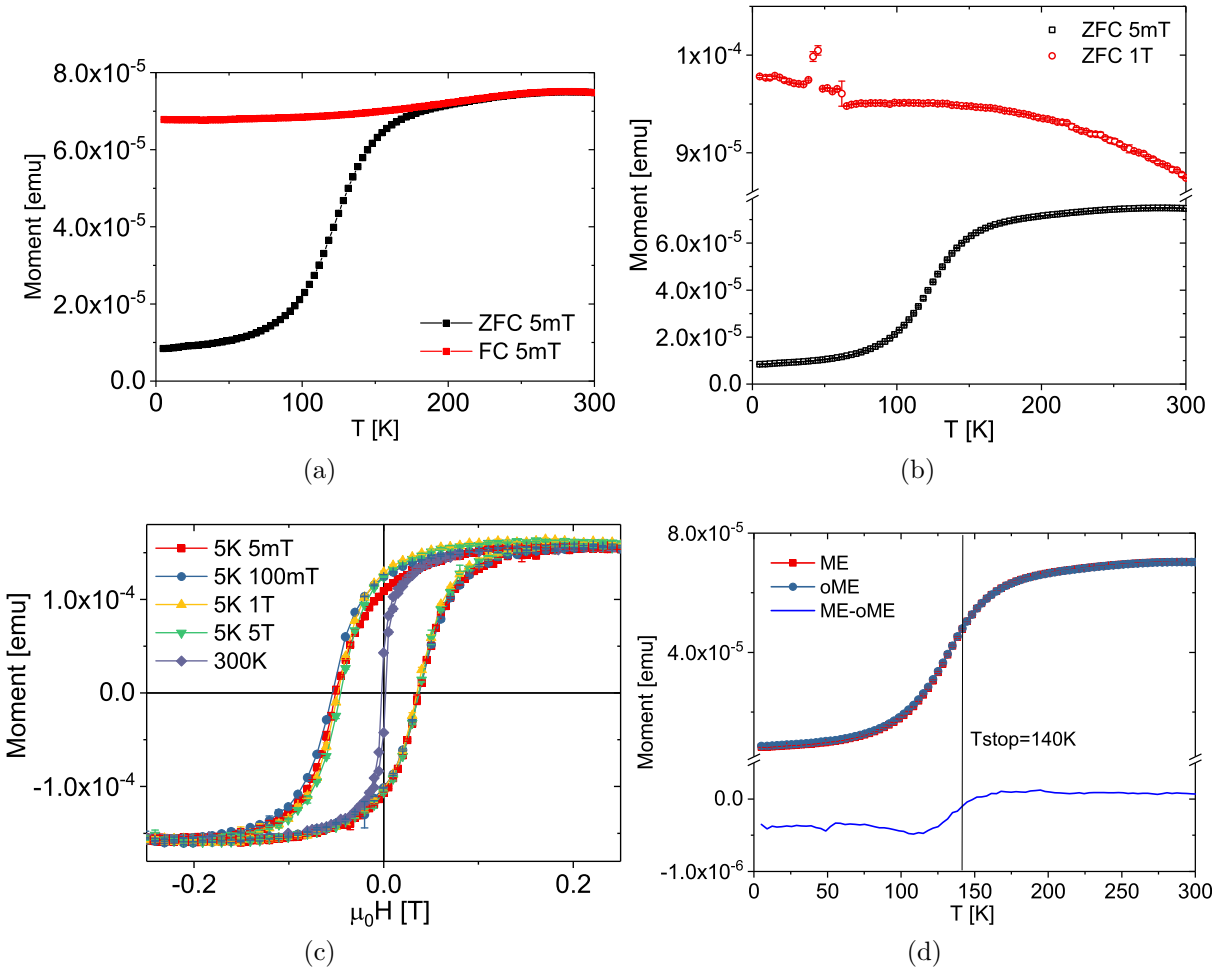

Figure 149: (a) ZFC/FC magnetization curves of spherical iron oxide NPs with 15 nm diameter diluted to a ratio of dispersion:toluene = 1:50 measured at 5 mT. (b) ZFC curves measured at various magnetic fields. (c) Hysteresis loops measured at 5 K after cooled at various magnetic fields and at 300 K. (d) Memory effect measured at 5 mT.

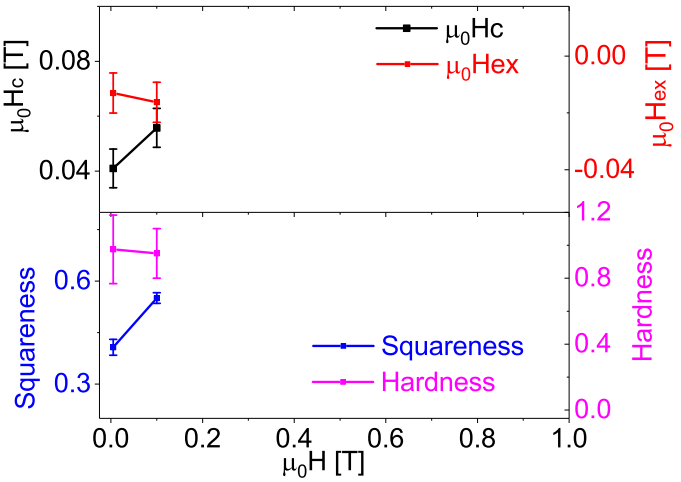

Figure 150: EB field (H_{ex}), coercive field (H_c), squareness and hardness of cubic iron oxide NPs with 11 nm size.

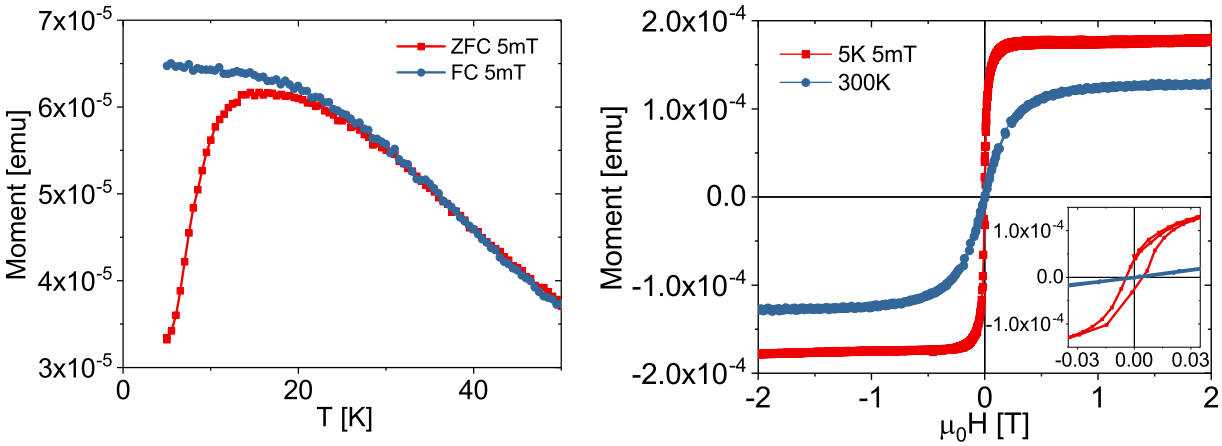

(a) (b)

Figure 151: (a) ZFC/FC magnetization curves of spherical iron oxide NPs with 5 nm diameter diluted to a ratio of dispersion:toluene = 1:20 measured at 5 mT. (b) Hysteresis loops measured at 5 K after cooled at 5 mT as well as at 300 K. Inset in (b) shows an enlarged view around the origin.

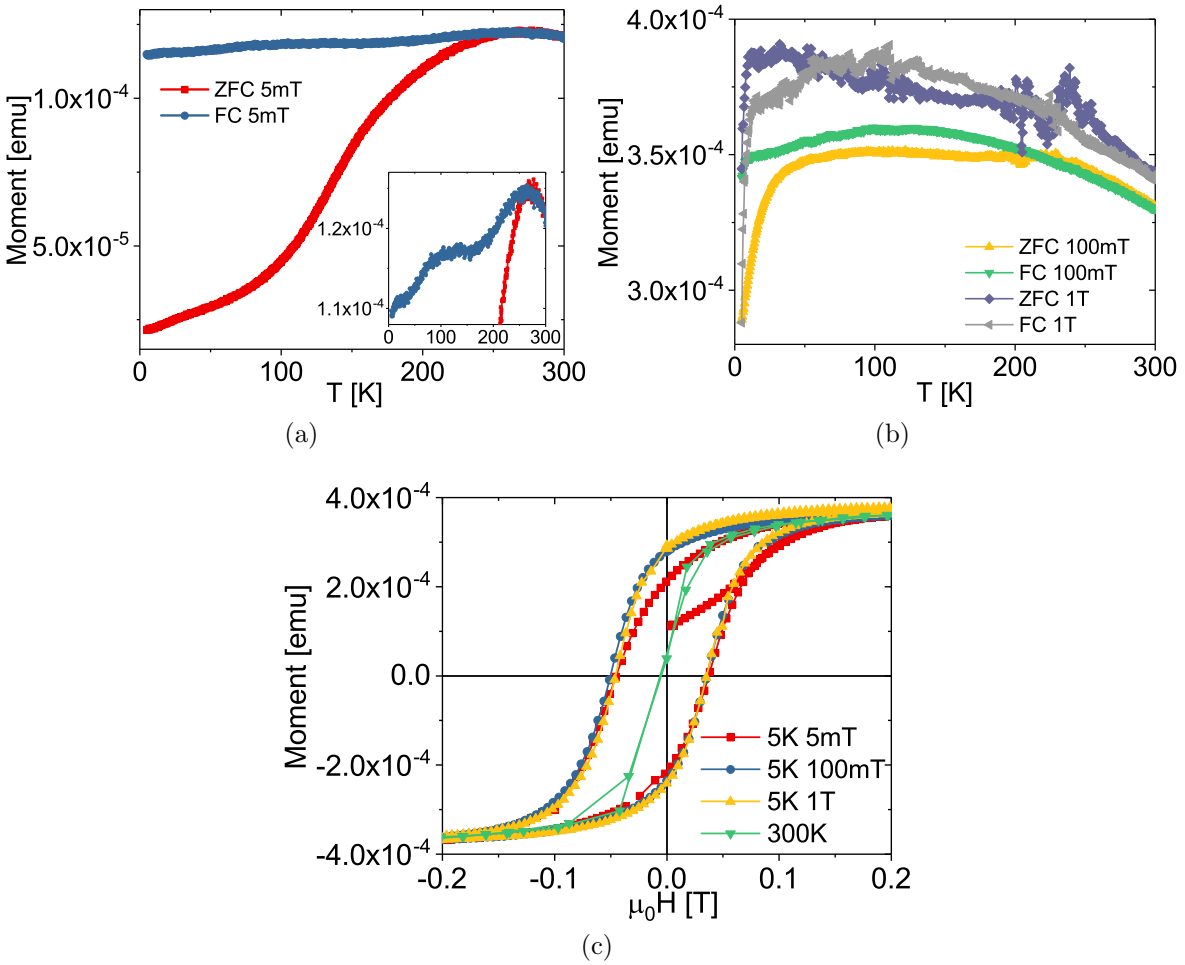

Figure 152: (a) ZFC/FC magnetization curves of spherical iron oxide NPs with 15 nm diameter diluted to a ratio of dispersion:toluene = 1:20 annealed in vacuum at 318 °C for 5 h measured at 5 mT. (b) ZFC/FC curves measured at a magnetic field of 100 mT and 1 T. (c) Hysteresis loops measured at 5 K after cooled within various magnetic fields as well as at 300 K. Inset in (c) shows an enlarged view around the origin.

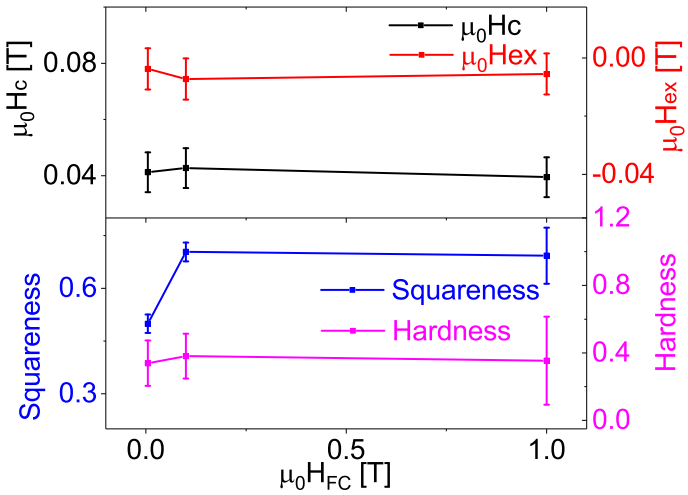

Figure 153: EB field (H_{ex}), coercive field (H_c), squareness and hardness of spherical iron oxide NPs with 15 nm diameter diluted to a ratio of NP dispersion:toluene = 1:20 annealed in vacuum at 318 °C for 5 h.

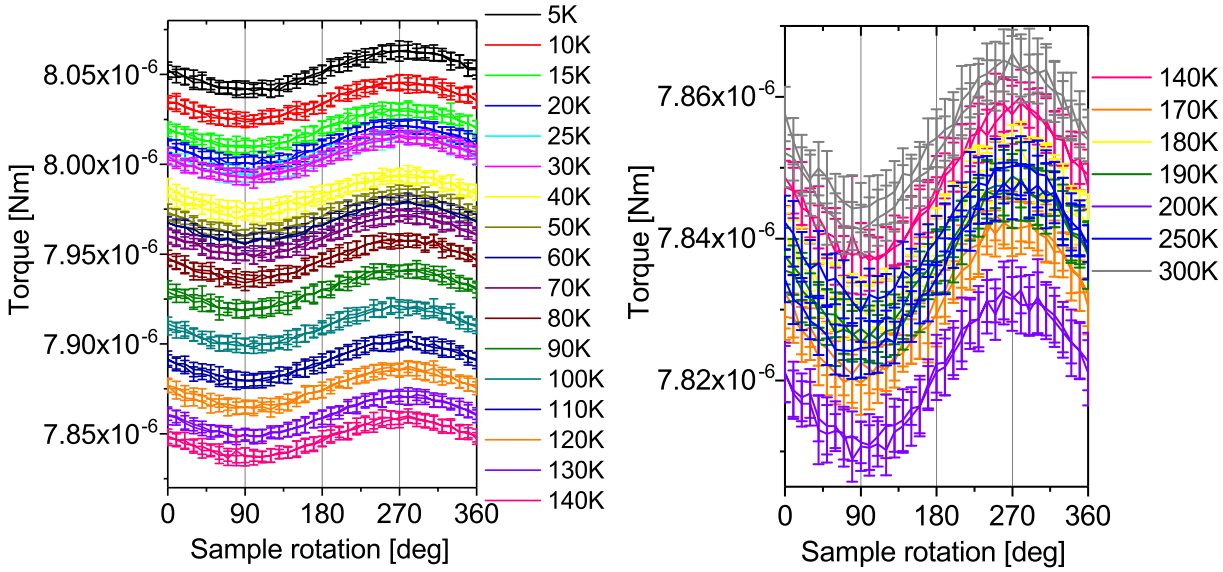

Figure 154: Torque magnetometry measurements of spherical iron oxide NPs with 20 nm diameter performed at various temperatures. The sample is cooled in a magnetic field of 0.5 mT before measured at 1 mT.

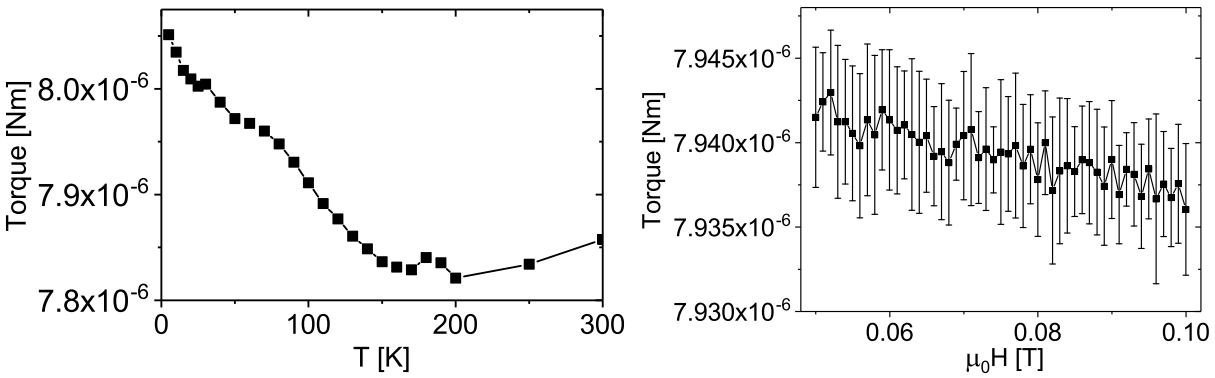

(a) (b)

Figure 155: Torque magnetometry measurements of spherical iron oxide NPs with 20 nm diameter performed at various temperatures. (a) Temperature dependence of the magnetic torque measured at 0°. (b) Field dependence of the torque performed at 300 K and 0° depending on the applied magnetic field. The sample is cooled in a magnetic field of 0.5 mT before measured at 1 mT.

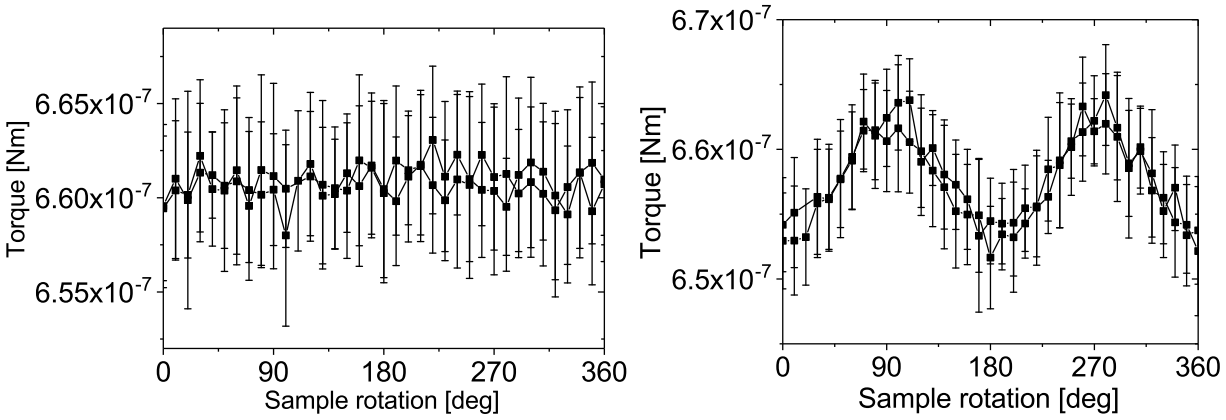

(a) (b)

Figure 156: Torque magnetometry measurements of an empty sample platform performed at 300 K in a magnetic field of (a) 0 T and (b) 9 T.

8 References

[1] D. Koziej, A. Lauria, and M. Niederberger. 25Th Anniversary Article: Metal Oxide Particles in Materials Science: Addressing All Length Scales. *Advanced materials*, 26(2):235–57, 2014.

[2] Y. Hou, Z. Xu, and S. Sun. Controlled synthesis and chemical conversions of FeO nanoparticles. *Angewandte Chemie - International Edition*, 46(33):6329–6332, 2007.

[3] M. J. Benitez, O. Petracic, H. Tüysüz, F. Schüth, and H. Zabel. Fingerprinting the magnetic behavior of antiferromagnetic nanostructures using remanent magnetization curves. *Physical Review B*, 83(13):134424, 2011.

[4] M. J. Benitez, O. Petracic, E. L. Salabas, F. Radu, H. Tüysüz, F. Schüth, and H. Zabel. Evidence for Core-Shell Magnetic Behavior in Antiferromagnetic Co3O4 Nanowires. *Physical Review Letters*, 101(9):097206, 2008.

[5] J. B. Yi, J. Ding, Y. P. Feng, G. W. Peng, G. M. Chow, Y. Kawazoe, B. H. Liu, J. H. Yin, and S. Thongmee. Size-dependent magnetism and spin-glass behavior of amorphous NiO bulk, clusters, and nanocrystals: Experiments and first-principles calculations. *Physical Review B*, 76(22):224402, 2007.

[6] S. A. Makhlouf, F. T. Parker, F. E. Spada, and A. E. Berkowitz. Magnetic anomalies in NiO nanoparticles. *Journal of Applied Physics*, 81(8):5561–5563, 1997.

[7] R. H. Kodama, S. A. Makhlouf, and A. E. Berkowitz. Finite Size Effects in Antiferromagnetic NiO Nanoparticles. *Physical Review Letters*, 79(7):1393–1396, 1997.

[8] L. He, C. Chen, N. Wang, W. Zhou, and L. Guo. Finite size effect on Néel temperature with Co3O4 nanoparticles. *Journal of Applied Physics*, 102(10):103911, 2007.

[9] M. J. Benitez, O. Petracic, H. Tüysüz, F. Schüth, and H. Zabel. Decoupling of magnetic core and shell contributions in antiferromagnetic Co3O4 nanostructures. *EPL (Europhysics Letters)*, 88(2):27004, 2009.

[10] M. Estrader, A. López-Ortega, S. Estradé, I. V. Golosovsky, G. Salazar-Alvarez, M. Vasilakaki, K. N. Trohidou, M. Varela, D. C. Stanley, M. Sinko, M. J. Pechan, D. J. Keavney, F. Peiró, S. Suriñach, M. D. Baró, and J. Nogués. Robust antiferromagnetic coupling in hard-soft bi-magnetic core/shell nanoparticles. *Nature Communications*, 4, 2013.

[11] M. Ghosh, K. Biswas, A. Sundaresan, and C. N. R. Rao. MnO and NiO nanoparticles: synthesis and magnetic properties. *Journal of Materials Chemistry*, 16(1):106, 2006.

[12] Th. D. Schladt, T. Graf, O. Köhler, H. Bauer, M. Dietzsch, J. Mertins, R. Branscheid, U. Kolb, and W. Tremel. Synthesis and Magnetic Properties of FePt@MnO Nano- heteroparticles. *Chemistry of Materials*, 24:525–535, 2012.

[13] A. Perro, S. Reculusa, S. Ravaine, E. Bourgeat-Lami, and E. Duguet. Design and synthesis of Janus micro- and nanoparticles. *Journal of Materials Chemistry*, 15(35-36):3745, 2005.

[14] Th. D. Schladt, K. Koll, S. Prüfer, H. Bauer, F. Natalio, O. Dumele, R. Raidoo, S. Weber, U. Wolfrum, L. M. Schreiber, M. P. Radsak, H. Schild, and W. Tremel. Multifunctional superparamagnetic MnO@SiO2 core/shell nanoparticles and their application for optical and magnetic resonance imaging. *Journal of Materials Chemistry*, 22(18):9253, 2012.

[15] Th. D. Schladt, K. Schneider, M. I. Shukoor, F. Natalio, H. Bauer, M. N. Tahir, S. Weber, L. M. Schreiber, H. C. Schröder, W. E. G. Müller, and W. Tremel. Highly soluble multifunctional MnO nanoparticles for simultaneous optical and MRI imaging and cancer treatment using photodynamic therapy. *Journal of Materials Chemistry*, 20(38):8297, 2010.

[16] S. Pal, S. Chandra, M.-H. Phan, P. Mukherjee, and H. Srikanth. Carbon nanostraws: nanotubes filled with superparamagnetic nanoparticles. *Nanotechnology*, 20(48):485604, 2009.

[17] J. M. Orozco-Henao, D. F. Coral, D. Muraca, O. Moscoso-Londoño, P. Mendoza Zélis, M. B. Fernandez Van Raap, S. K. Sharma, K. R. Pirota, and M. Knobel. Effects of Nanostructure and Dipolar Interactions on Magnetohyperthermia in Iron Oxide Nanoparticles. *Journal of Physical Chemistry C*, 120(23):12796–12809, 2016.

[18] X. Sun, A. Klapper, Y. Su, K. Nemkovski, A. Wildes, H. Bauer, O. Köhler, A. Schilmann, W. Tremel, O. Petracic, and Th. Brückel. Magnetism of monomer MnO and heterodimer FePt@MnO nanoparticles. *Physical Review B*, 95(13):134427, 2017.

[19] S. Bedanta, A. Barman, W. Kleemann, O. Petracic, and T. Seki. Magnetic Nanoparticles: A Subject for Both Fundamental Research and Applications. *Journal of Nanomaterials*, 2013(952540):1–22, 2013.

[20] B. D. Terris and T. Thomson. Nanofabricated and self-assembled magnetic structures as data storage media. *Journal of Physics D: Applied Physics*, 38(12):R199–R222, 2005.

[21] J. Yu, C. Geng, L. Zheng, Z. Ma, T. Tan, X. Wang, Q. Yan, and D. Shen. Preparation of High-Quality Colloidal Mask for Nanosphere Lithography by a Combination of Air/Water Interface Self-Assembly and Solvent Vapor Annealing. *Langmuir*, 28(34):12681–12689, 2012.

[22] M. Varón, M. Beleggia, T. Kasama, R. J. Harrison, R. E. Dunin-Borkowski, V. F. Puntes, and C. Frandsen. Dipolar magnetism in ordered and disordered low-dimensional nanoparticle assemblies. *Scientific reports*, 3:1234, 2013.

[23] A. Michels, S. Erokhin, D. Berkov, and N. Gorn. Micromagnetic simulation of magnetic small-angle neutron scattering from two-phase nanocomposites. *Journal of Magnetism and Magnetic Materials*, 350:55–68, 2014.

[24] K. Trohidou and M. Vasilakaki. Monte Carlo Studies of Magnetic Nanoparticles. In Shaul Mordechai, editor, *Applications of Monte Carlo Method in Science and Engineering*. InTech, 2011.

[25] W. S. Seo, H. H. Jo, K. Lee, B. Kim, S. J. Oh, and J. T. Park. Size-dependent magnetic properties of colloidal Mn3O4 and MnO nanoparticles. *Angewandte Chemie (International ed. in English)*, 43(9):1115–7, 2004.

[26] S. Blundell. *Magnetism in Condensed Matter*. Oxford University Press, Oxford, 2001.

[27] J. M. D. Coey. *Magnetism and Magnetic Materials*. Cambridge University Press, Cambridge, 2010.

[28] M. Angst. Lecture Notes: Condenced Matter physics, RWTH Aachen, 2015.

[29] P. Thakuria. *Magnetic structure in relation to the magnetic field induced ferroelectricity in Y-type hexaferrite Ba2-xSrxZn2Fe12O22*. PhD thesis, 2016.

[30] W. H. Meiklejohn and C. P. Bean. New Magnetic Anisotropy. *Physical review*, 102(5):1413–1414, 1956.

[31] J. Nogués and I. K. Schuller. Exchange bias. *Journal of Magnetism and Magnetic Materials*, 192(2):203–232, 1999.

[32] M. Kiwi. Exchange bias theory. *Journal of Magnetism and Magnetic Materials*, 234(3):584–595, 2001.

[33] J. Nogués, J. Sort, V. Langlais, V. Skumryev, S. Suriñach, J. S. Muñoz, and M. D. Baró. Exchange bias in nanostructures. *Physics Reports*, 422(3):65–117, 2005.

[34] V. Skumryev, S. Stoyanov, Y. Zhang, G. Hadjipanayis, D. Givord, and J. Nogués. Beating the superparamagnetic limit with exchange bias. *Nature*, 423:850–853, 2003.

[35] O. Petracic. Superparamagnetic nanoparticle ensembles. *Superlattices and Microstructures*, 47(5):569–578, 2010.

[36] J. A. Mydosh. *Spin Glasses: An Experimental Introduction*. London: Taylor and Francis, London, 1993.

[37] J. L. Dormann, D. Fiorani, and E. Tronc. Magnetic Relaxation in Fine-Particle Systems. *Advances in Chemical Physics*, 98:283, 1997.

[38] K. J. M. Bishop, C. E. Wilmer, S. Soh, and B. A. Grzybowski. Nanoscale forces and their uses in self-assembly. *Small*, 5(14):1600–30, 2009.

[39] O. Hellwig, L. J. Heyderman, O. Petracic, and H. Zabel. *Competing Interactions in Patterned and Self-Assembled Magnetic Nanostructures*, pages 189–234. Springer Berlin Heidelberg, Berlin, Heidelberg, 2013.

[40] S. Mørup, M. F. Hansen, and C. Frandsen. Magnetic interactions between nanoparticles. *Beilstein journal of nanotechnology*, 1:182–90, 2010.

[41] O. Petracic, X. Chen, S. Bedanta, W. Kleemann, S. Sahoo, S. Cardoso, and P. P. Freitas. Collective states of interacting ferromagnetic nanoparticles. *Journal of Magnetism and Magnetic Materials*, 300(1):192–197, 2006.

[42] O. Petracic, S. Sahoo, Ch. Binek, W. Kleemann, J.B. Sousa, S. Cardoso, and P.P. Freitas. Cole-Cole Analysis of the Superspin Glass System Co80Fe20/Al2O3. *Phase Transitions*, 76(4-5):367–375, 2003.

[43] J.-O. Andersson, C. Djurberg, T. Jonsson, P. Svedlindh, and P. Nordblad. Monte Carlo studies of the dynamics of an interacting monodispersive magnetic-particle system. *Physical Review B*, 56(21):13983–13988, 1997.

[44] A. K. Jonscher. *Dielectric Relaxation in Solids*. Chelsea Dielectrics Press, London, 1983.

[45] Th. Brückel, D. Richter, G. Roth, A. Wischnewski, and R. Zorn, editors. *Neutron scattering : lectures of the JCNS laboratory course held at Forschungszentrum Jülich and at the Heinz Maier-Leibnitz Zentrum Garching ; in cooperation with RWTH Aachen and University of Münster*. Forschungszentrum Jülich GmbH, Jülich, 2015.

[46] D.S. Sivia. *Elementary Scattering Theory, For X-ray and neutron users*. Oxford University Press, Oxford, 2011.

[47] G. L. Squires. *Introduction to the Theory of Thermal Neutron Scattering*. Dover Publications, New York, 1996.

[48] S. W. Lovesey. *Theory of Neutron Scattering from Condensed Matter Volume II: Polarization Effects and Magnetic Scattering*. Clarendon Press, Oxford, 1987.

[49] W. Schweika. XYZ-polarisation analysis of diffuse magnetic neutron scattering from single crystals. *Journal of Physics: Conference Series*, 211:012026, 2010.

[50] R. Schedler, U. Witte, M. Loewenhaupt, and J. Kulda. Coupling between crystal field transitions and phonons in the 4f-electron system CeCu2. *Physica B: Condensed Matter*, 335(1-4):41–43, 2003.

[51] J. R. Stewart, P. P. Deen, K. H. Andersen, H. Schober, J.-F. Barthélémy, J. M. Hillier, A. P. Murani, T. Hayes, and B. Lindenau. Disordered materials studied using neutron polarization analysis on the multi-detector D7. *Journal of Applied Crystallography*, 42:69–84, 2009.

[52] S. Disch. *The spin structure of magnetic nanoparticles and in magnetic nanostructures*. PhD thesis, Jülich, 2011.

[53] D. P. Landau and K. Binder. *A Guide to Monte Carlo Simulations in Statistical Physics*. Cambridge University Press, Cambridge, 2000.

[54] J. J. Binney, N. J. Dowrick, A. J. Fischer, and M. E.J. Newman. *The Theory of Critical Phenomena*. Oxford University Press, Oxford, 1992.

[55] F. J. Vesely. *Computational Physics*. Springer Science+Business Media New York, New York, 1994.

[56] H. Shaked, J. Faber, Jr., and R. L. Hitterman. Low-temperature magnetic structure of MnO: A high-resolution neutron-diffraction study. *Physical review. B*, 38(16):11901–11903, 1988.

[57] A. L. Goodwin, M. G. Tucker, M. T. Dove, and D. A. Keen. Magnetic Structure of MnO at 10 K from Total Neutron Scattering Data. *Physical Review Letters*, 96(4):047209, 2006.

[58] B. A. Frandsen and S. J. L. Billinge. Magnetic structure determination from the magnetic pair distribution function (mPDF): ground state of MnO. *Acta crystallographica. Section A, Foundations and advances*, 71(Pt 3):325–34, 2015.

[59] Quantum Design. Magnetic Property Measurement System MPMS XL Reference Manual. 2005.

[60] H. Weinstock, editor. *SQUID Sensors: Fundamentals, Fabrication and Applications*. Springer-Science+Business Media, B.V., Dordrecht, 1996.

[61] T. V. Duzer and C. W. Turner. *Principles of Superconductive Devices and Circuits, (Second Ed.)*. Prentice Hall PTR, Upper Saddle River, NJ, USA, 1998.

[62] Quantum Design. Physical Property Measurement System: Vibrating Sample Magnetometer (VSM) Option User's Manuel. 2004.

[63] Y. Su, K. Nemkovskiy, and S. Demirdis. DNS: Diffuse scattering neutron time-of-flight spectrometer. *Journal of Large-Scale Research Facilities*, A27:1–4, 2015.

[64] W. Schweika and P. Böni. The instrument DNS: polarization analysis for diffuse neutron scattering. *Physica B: Condensed Matter*, 297:155–159, 2001.

[65] X. Sun, E. Feng, Y. Su, K. Nemkovski, O. Petracic, and Th. Brückel. Magnetic properties and spin structure of MnO single crystal and powder. *Journal of Physics: Conference Series*, 862:012027, 2017.

[66] E. Kentzinger, M. Krutyeva, and U. Rücker. GALAXI : Gallium anode low-angle x-ray instrument. *Journal of Large-Scale Research Facilities*, 2(61):1–5, 2016.

[67] BornAgain. http://bornagainproject.org/, 2017.

[68] C. G. Shull, W. A. Strauser, and E. O. Wollan. Neutron Diffraction by Paramagnetic and Antiferromagnetic Substances. *Physical Review*, 83(2):333–345, 1951.

[69] T. R. McGuire and R. J. Happel. The magnetic susceptibility of an MnO single crystal. *J. Phys. Radium*, 20:424–426, 1959.

[70] M. S. Jagadeesh and M. S. Seehra. Principal magnetic susceptibilities of MnO and their temperature dependence. *Physical Review B*, 23(3):1185–1189, 1981.

[71] G. Srinivasan and M. S. Seehra. Magnetic properties of Mn3O4 and a solution of the canted-spin problem. *Physical Review B*, 28(1):1–7, 1983.

[72] R. Boire and M. F. Collins. The magnetic phase transition in MnO. *Canadian Journal of Physics*, 55(7-8):688–689, 1977.

[73] B. F. Woodfield, J. L. Shapiro, R. Stevens, J. Boerio-Goates, and M. L. Wilson. Critical phenomena at the antiferromagnetic transition in MnO. *Physical Review B*, 60(10):7335–7340, 1999.

[74] W. L. Roth. Magnetic structures of MnO, FeO, CoO, and NiO. *Physical Review*, 110(6):1333, 1958.

[75] M.E. Lines and E.D. Jones. Antiferromagnetism in the face-centered cubic lattice. II. Magnetic properties of MnO. *Physical Review*, 139(4A):1313–1327, 1965.

[76] G. Pepy. Spin waves in MnO; from 4K to temperatures close to TN. *Journal of Physics and Chemistry of Solids*, 35:433–444, 1974.

[77] M. Kohgi, Y. Ishikawa, and Y. Endoh. Inelastic neutron scattering study of spin waves in MnO. *Solid State Communications*, 11:391–394, 1972.

[78] J. J. Hauser and J. V. Waszczak. Spin-glass transition in MnO. *Physical Review B*, 30(9):5167–5171, 1984.

[79] Ms Jagadeesh and Ms Seehra. Study of some magnetic properties of a mixed phase (Mn3O4) in MnO crystals. *Physical Review B*, 21(7):2897–2904, 1980.

[80] G. B. Jensen and O. V. Nielsen. The magnetic structure of Mn3O4 (Hausmannite) between 4.7K and the Neel point, 41K. *Journal of Physics C: Solid State Physics*, 7(2):409–424, 1974.

[81] B. Boucher, R. Buhl, and M. Perrin. Magnetic structure of Mn3O4 by neutron diffraction. *Journal of Applied Physics*, 42(4):1615–1617, 1971.

[82] K. S. Nanjundaswamy and M. N. Sankarshanamurthy. Low-temperature stabilization of pure MnO. *Bulletin of Materials Science*, 7(5):459–463, 1985.

[83] E.R. Stobbe, B.A. de Boer, and J.W. Geus. The reduction and oxidation behaviour of manganese oxides. *Catalysis Today*, 47(1):161–167, 1999.

[84] T. E. Moore, M. Ellis, and P. W. Selwood. Solid Oxides and Hydroxides of Manganese. *Journal of the American Chemical Society*, 72(2):856–866, 1950.

[85] M. Regulski, R. Przeniosło, I. Sosnowska, D. Hohlwein, and R. Schneider. Neutron diffraction study of the magnetic structure of α-Mn2O3. *Journal of Alloys and Compounds*, 362(1-2):236–240, 2004.

[86] C. H. Wang, S. N. Baker, M. D. Lumsden, S. E. Nagler, W. T. Heller, G. A. Baker, P. D. Deen, L. M. D. Cranswick, Y. Su, and A. D. Christianson. Antiferromagnetic order in MnO spherical nanoparticles. *Physical Review B*, 83(21):214418, 2011.

[87] M. Feygenson, W. Schweika, A. Ioffe, S. B. Vakhrushev, and Th. Brückel. Magnetic phase transition in confined MnO nanoparticles studied by polarized neutron scattering. *Physical Review B*, 81(6):064423, 2010.

[88] T. Chatterji, Y. Su, G. N. Iles, Y.-C. Lee, A. P. Khandhar, and K. M. Krishnan. Antiferromagnetic spin correlations in MnO nanoparticles. *Journal of Magnetism and Magnetic Materials*, 322(21):3333–3336, 2010.

[89] I. V. Golosovsky, I. Mirebeau, G. André, D. A. Kurdyukov, Yu. A. Kumzerov, and S. B. Vakhrushev. Magnetic ordering and phase transition in MnO embedded in a porous glass. *Physical Review Letters*, 86(25):5783–5786, 2001.

[90] G. H. Lee, S. H. Huh, J. W. Jeong, B. J. Choi, S. H. Kim, and H.-C. Ri. Anomalous magnetic properties of MnO nanoclusters. *Journal of the American Chemical Society*, 124(41):12094–5, 2002.

[91] A. López-Ortega, D. Tobia, E. Winkler, I. V. Golosovsky, G. Salazar-Alvarez, S. Estradé, M. Estrader, J. Sort, M. A. González, S. Suriñach, J. Arbiol, F. Peiró, R. D. Zysler, M. D. Baró, and J. Nogués. Size-dependent passivation shell and magnetic properties in antiferromagnetic/ferrimagnetic core/shell MnO nanoparticles. *Journal of the American Chemical Society*, 132(27):9398–9407, 2010.

[92] X. Batlle and A. Labarta. Finite-size effects in fine particles: magnetic and transport properties. *Journal of Physics D: Applied Physics*, 35(6):R15–R42, 2002.

[93] A. Ebbing, O. Hellwig, L. Agudo, G. Eggeler, and O. Petracic. Tuning the magnetic properties of Co nanoparticles by Pt capping. *Physical Review B*, 84(1):012405, 2011.

[94] Y.-C. Lee, A. B. Pakhomov, and K. M. Krishnan. Size-driven magnetic transitions in monodisperse MnO nanocrystals. *Journal of applied physics*, 107(9):9E124, 2010.

[95] I. Golosovsky, I. Mirebeau, F. Fauth, D. Kurdyukov, and Yu. Kumzerov. Low-temperature phase transition in nanostructured MnO embedded within the channels of MCM-41-type matrices. *Physical Review B*, 74(5):054433, 2006.

[96] I. V. Golosovsky, G. Salazar-Alvarez, A. López-Ortega, M. A. González, J. Sort, M. Estrader, S. Suriñach, M. D. Baró, and J. Nogués. Magnetic Proximity Effect Features in Antiferromagnetic/Ferrimagnetic Core-Shell Nanoparticles. *Physical Review Letters*, 102(24):247201, 2009.

[97] A. E. Berkowitz, G. F. Rodriguez, J. I. Hong, K. An, T. Hyeon, N. Agarwal, D. J. Smith, and E. E. Fullerton. Antiferromagnetic MnO nanoparticles with ferrimagnetic Mn3O4 shells: Doubly inverted core-shell system. *Physical Review B*, 77(2):024403, 2008.

[98] N. J. O. Silva, M. Karmaoui, V. S. Amaral, I. Puente-Orench, J. Campo, I. da Silva, A. Ibarra, R. Bustamante, A. Millán, and F. Palacio. Shell pressure on the core of MnO/Mn3O4 core/shell nanoparticles. *Physical Review B*, 87(22):224429, 2013.

[99] P.Z. Si, D. Li, C.J. Choi, Y.B. Li, D.Y. Geng, and Z.D. Zhang. Large coercivity and small exchange bias in Mn3O4 / MnO nanoparticles. *Solid State Communications*, 142(12):723–726, 2007.

[100] E. Winkler, J. P. Sinnecker, M. A. Novak, and R. D. Zysler. Dynamic study of the internal magnetic order of Mn3O4 nanoparticles. *Journal of Nanoparticle Research*, 13(11):5653–5659, 2011.

[101] J. Du, Y. Gao, L. Chai, G. Zou, Y. Li, and Y. Qian. Hausmannite Mn3O4 nanorods: synthesis, characterization and magnetic properties. *Nanotechnology*, 17(19):4923–4928, 2006.

[102] S. H. Kim, B. J. Choi, G. H. Lee, S. J. Oh, B. Kim, H. C. Choi, J. Park, and Y. Chang. Ferrimagnetism in γ -Manganese Sesquioxide (γ-Mn2O3) Nanoparticles. *Journal of the Korean Physical Society*, 46(4):941–944, 2005.

[103] P. E. Jönsson. Superparamagnetism and Spin Glass Dynamics of Interacting Magnetic Nanoparticle Systems. page 62, 2003.

[104] Y.-Y. Li. Magnetic Moment Arrangements and Magnetocrystalline Deformations in Antiferromagnetic Compounds. *Physical Review*, 100:627–631, 1955.

[105] D. Peled, A. Silverman, and J. Adler. 3D visualization of atomistic simulations on every desktop. *IOP Conference Series*, 454:012076, 2013.

[106] U. Hofmann. Die chemischen Grundlagen der griechischen Vasenmalerei. *Angewandte Chemie*, 74(12):397–406, 1962.

[107] G. Lagaly. Eisenoxide-antike und moderne Pigmente. *Christiana Albertina*, 19:23–32, 1984.

[108] M. Bimson. Cosmetic Pigments from the "Royal Cemetery" at Ur. *British Museum IRAQ*, 42(1):75–77, 1980.

[109] R.M. Cornell and U. Schwertmann. *The iron oxides*. Wiley-VCH Verlag GmbH & Co. KGaA, 2003.

[110] B. Hentschel. Stoichiometric FeO as Metastable Intermediate of the Decomposition of Wustite at 225°C. *Zeitschrift für Naturforschung - Section A Journal of Physical Sciences*, 25(12):1996–1997, 1970.

[111] G.E. Kugel. Low-energy magnetic excitations in wüstite (Fe1-xO). *Physical Review B*, 18(3):1317–1321, 1978.

[112] Magnetic and Other Properties of Oxides and Related Compounds. In K.-H. Hellwege, editor, *The Landolt-Börnstein database*, volume 4, pages 8–16. Springer, Berlin, 1970.

[113] W. L. Roth. Defects in the crystal and magnetic structures of ferrous oxide. *Acta Crystallographica*, 13(2):140–149, 1960.

[114] K. Momma and F. Izumi. VESTA 3 for three-dimensional visualization of crystal, volumetric and morphology data. *Journal of Applied Crystallography*, 44(6):1272–1276, 2011.

[115] R. J. Hill, J.R. Craig, and G.V. Gibbs. Systematics of the spinel structure type. *Phys. Chem. Min.*, 4:317–339, 1979.

[116] F. Walz. The Verwey transition - a topical review. *Journal of Physics: Condensed Matter*, 14(12):R285–R340, 2002.

[117] J. García and G. Subías. The Verwey transition-a new perspective. *Journal of Physics: Condensed Matter*, 16(7):R145–R178, 2004.

[118] M. P. Sharrock and R. E. Bodnar. Magnetic materials for recording: An overview with special emphasis on particles. *Journal of Applied Physics*, 57(8):3919–3924, 1985.

[119] P. A. Cox. *Transition Metal Oxides*. Clarendon, Oxford, 1995.

[120] E. J. W. Verwey. Electronic Conduction of Magnetite (Fe3O4) and its Transition Point at Low Temperatures. *Nature*, 144(3642):327–328, 1939.

[121] E. Murad. Properties and Behavior of Iron Oxides as Determined by Mössbauer Spectroscopy. In J.W Stucki, B.A Goodman, and U Schwertmann, editors, *Iron in Soils and Clay Minerals*, pages 309–350. Springer Netherlands, Dordrecht, 1988.

[122] W. H. Bragg and W. L. Bragg. *X-rays and crystal structure*. G. Bell and Sons, London, 3 edition, 1918.

[123] L. Pauling and S. B. Hendricks. The crystal structures of hematite and corundum. *Journal of the American Chemical Society*, 47(3):781–790, 1925.

[124] R. L. Blake, R. E. Hessevic, T. Zoltai, and L. W. Finger. Refinement of the Hematite Structure. *American Mineralogist*, 51:123–129, 1966.

[125] Y. Sata and S. Akimoto. Hydrostatic compression of four corundum type compounds: alpha-Al2O3, V2O3, Cr2O3, and alpha-Fe2O3. *J. Appl. Phys.*, 50(8):5285–5291, 1979.

[126] D. Mishra, M. J. Benitez, O. Petracic, G. A. Badini Confalonieri, P. Szary, F. Brüssing, K. Theis-Bröhl, A. Devishvili, A. Vorobiev, O. Konovalov, M. Paulus, C. Sternemann, B. P. Toperverg, and H. Zabel. Self-assembled iron oxide nanoparticle multilayer: x-ray and polarized neutron reflectivity. *Nanotechnology*, 23(5):055707, 2012.

[127] M. J. Benitez, D. Mishra, P. Szary, G. A. Badini Confalonieri, M. Feyen, A. H. Lu, L. Agudo, G. Eggeler, O. Petracic, and H. Zabel. Structural and magnetic characterization of self-assembled iron oxide nanoparticle arrays. *Journal of Physics. Condensed Matter*, 23(12):126003, 2011.

[128] M. Estrader, A. López-Ortega, I. V. Golosovsky, S. Estradé, A. G. Roca, G. Salazar-Alvarez, L. López-Conesa, D. Tobia, E. Winkler, J. D. Ardisson, W. A. A. Macedo, A. Morphis, M. Vasilakaki, K.i N. Trohidou, A. Gukasov, I. Mirebeau, O. L. Makarova, R. D. Zysler, F. Peiró, M. D. Baró, L. Bergström, and J. Nogués. Origin of the large dispersion of magnetic properties in nanostructured oxides: FeO/Fe3O4 nanoparticles as a case study. *Nanoscale*, 7(7):3002–3015, 2015.

[129] V. B. Barbeta, R. F. Jardim, P. K. Kiyohara, F. B. Effenberger, and L. M. Rossi. Magnetic properties of Fe3O4 nanoparticles coated with oleic and dodecanoic acids. *Journal of Applied Physics*, 107(7):073913, 2010.

[130] X. Sun, N. F. Huls, A. Sigdel, and S. Sun. Tuning exchange bias in core/shell FeO/Fe3O4 nanoparticles. *Nano Lett.*, 12(1):246–51, 2012.

[131] D. W. Kavich, J. H. Dickerson, S. V. Mahajan, S. A. Hasan, and J.-H. Park. Exchange bias of singly inverted FeO/Fe3O4 core-shell nanocrystals. *Physical Review B*, 78(17):174414, 2008.

[132] S. K. Sharma, J. M. Vargas, K. R. Pirota, Shalendra Kumar, C. G. Lee, and M. Knobel. Synthesis and ageing effect in FeO nanoparticles: Transformation to core-shell FeO/Fe3O4 and their magnetic characterization. *Journal of Alloys and Compounds*, 509(22):6414–6417, 2011.

[133] J. Park, K. An, Y. Hwang, J.-G. Park, H.-J. Noh, J.-Y. Kim, J.-H. Park, N.-M. Hwang, and T. Hyeon. Ultra-large-scale syntheses of monodisperse nanocrystals. *Nature materials*, 3(12):891–5, 2004.

[134] F. X. Redl, C. T. Black, G. C. Papaefthymiou, R. L. Sandstrom, M. Yin, H. Zeng, C. B. Murray, and S. P. O'Brien. Magnetic, electronic, and structural characterization of nonstoichiometric iron oxides at the nanoscale. *Journal of the American Chemical Society*, 126(44):14583–14599, 2004.

[135] Y. Hwang, S. Angappane, J. Park, K. An, T. Hyeon, and J.-G. Park. Exchange bias behavior of monodisperse Fe3O4/γ-Fe2O3 core/shell nanoparticles. *Current Applied Physics*, 12(3):808–811, 2012.

[136] L. Del Bianco, D. Fiorani, A. Testa, E. Bonetti, and L. Signorini. Field-cooling dependence of exchange bias in a granular system of Fe nanoparticles embedded in an Fe oxide matrix. *Physical Review B*, 70(5):052401, 2004.

[137] Q. K. Ong, A. Wei, and X. M. Lin. Exchange bias in Fe/ Fe3O4 core-shell magnetic nanoparticles mediated by frozen interfacial spins. *Physical Review B*, 80(13):1–6, 2009.

[138] A. E. Berkowitz and K. Takano. Exchange anisotropy - a review. *Journal of Magnetism and Magnetic Materials*, 200(1-3):552–570, 1999.

[139] C. J. Bae, S. Angappane, J.-G. Park, Y. Lee, J. Lee, K. An, and T. Hyeon. Experimental studies of strong dipolar interparticle interaction in monodisperse Fe3O4 nanoparticles. *Applied Physics Letters*, 91(10):102502, 2007.

[140] P.A. Kumar, G. Singh, W. R. Glomm, D. Peddis, E. Wahlström, and R. Mathieu. Superspin glass state and exchange bias in amorphous Fe/Fe-O core/shell nanoparticles. *Materials Research Express*, 1(3):036103, 2014.

[141] S. Disch, E. Wetterskog, R. P. Hermann, A. Wiedenmann, U. Vainio, G. Salazar-Alvarez, L. Bergström, and Th. Brückel. Quantitative spatial magnetization distribution in iron oxide nanocubes and nanospheres by polarized small-angle neutron scattering. *New Journal of Physics*, 14(1):013025, 2012.

[142] S. Disch, E. Wetterskog, R. P. Hermann, D. Korolkov, P. Busch, P. Boesecke, O. Lyon, U. Vainio, G. Salazar-Alvarez, L. Bergström, and Th. Brückel. Structural diversity in iron oxide nanoparticle assemblies as directed by particle morphology and orientation. *Nanoscale*, 5(9):3969–75, 2013.

[143] E. Wetterskog, A. Klapper, S. Disch, E. Josten, R. P Hermann, U. Rücker, Th. Brückel, L. Bergström, and G. Salazar-Alvarez. Tuning the structure and habit of iron oxide mesocrystals. *Nanoscale*, 8(34):15571–80, 2016.

[144] Y. Xia, B. Gates, Y. Yin, and Y. Lu. Monodispersed Colloidal Spheres: Old Materials with New Applications. *Advanced Materials*, 12(10):693–713, 2000.

[145] F. Marlow, P. Sharifi, R. Brinkmann, and C. Mendive. Opals: status and prospects. *Angewandte Chemie (International ed. in English)*, 48(34):6212–33, 2009.

[146] M. Kondo, K. Shinozaki, L. Bergstrom, and N. Mizutani. Preparation of Colloidal Monolayers of Alkoxylated Silica Particles At the Air-Liquid Interface. *Langmuir*, 11(2):394–397, 1995.

[147] N. D. Denkov, O. D. Velev, P. A. Kralchevsky, I. B. Ivanov, H. Yoshimura, and K. Nagayama. Two-dimensional crystallization. *Nature*, 361(6407):26–26, 1993.

[148] D. Mishra, D. Greving, G. A. Badini Confalonieri, J. Perlich, B. P. Toperverg, H. Zabel, and O. Petracic. Growth modes of nanoparticle superlattice thin films. *Nanotechnology*, 25(20):205602, 2014.

[149] H. W. Deckman. Macromolecular self-organized assemblies. *Journal of Vacuum Science & Technology B*, 6(1):333, 1988.

[150] M. I. Bodnarchuk, M. V. Kovalenko, S. Pichler, G. Fritz-Popovski, G. Hesser, and W. Heiss. Large-area ordered superlattices from magnetic wüstite/cobalt ferrite core/shell nanocrystals by doctor blade casting. *ACS Nano*, 4(1):423–431, 2010.

[151] A. van Blaaderen, R. Ruel, and P. Wiltzius. Template-directed colloidal crystallization. *Nature*, 385(6614):321–324, 1997.

[152] A. Dong, J. Chen, P. M. Vora, J. M. Kikkawa, and C. B. Murray. Binary nanocrystal superlattice membranes self-assembled at the liquid-air interface. *Nature*, 466(7305):474–7, 2010.

[153] K. Liu, J. Nogués, C. Leighton, H. Masuda, K. Nishio, I. V. Roshchin, and I. K. Schuller. Fabrication and thermal stability of arrays of Fe nanodots. *Applied Physics Letters*, 81(23):4434–4436, 2002.

[154] J. Sort, J. Nogués, S. Suriñach, J. S. Muñoz, M. D. Baró, E. Chappel, F. Dupont, and G. Chouteau. Coercivity and squareness enhancement in ball-milled hard magnetic-antiferromagnetic composites. *Applied Physics Letters*, 79(8):1142, 2001.

[155] G. A. Badini Confalonieri, V. Vega, A. Ebbing, D. Mishra, P. Szary, V. M. Prida, O. Petracic, and H. Zabel. Template-assisted self-assembly of individual and clusters of magnetic nanoparticles. *Nanotechnology*, 22(28):285608, 2011.

[156] H. Kachkachi, W. T. Coffey, D. S. F. Crothers, A. Ezzir, E. C. Kennedy, M. Nogués, and E. Tronc. Field dependence of the temperature at the peak of the zero-field-cooled magnetization. *Journal of Physics. Condensed Matter*, 12:3077–3090, 2000.

[157] R. W. Chantrell, N. Walmsley, J. Gore, and M. Maylin. Calculations of the susceptibility of interacting superparamagnetic particles. *Physical Review B*, 63(2):024410, 2000.

Acknowledgements

It is my great pleasure to accomplish my PhD thesis in JCNS-2 at the Forschungszentrum Jülich. It was a great experience for me working in a comfortable atmosphere with all kind colleagues. I have learnt a lot from many experienced senior scientists in different fields during the last years. The large variety of instruments available in the institute allowed me to test and to verify my ideas in different ways. Here I would like to express my sincere gratitude in particular to the following people:

Prof. Dr. Thomas Brückel for providing me the opportunity to work on this interesting topic in this institute. I am grateful for his support and guidance during my work. I would like to especially thank him for providing me the opportunities to present my work at different national and international conferences.

Prof. Dr. Joachim Mayer for agreeing to be the second referee of my thesis. I would like to thank him for his excellent guidance and advices.

PD Dr. Oleg Petracic for being my supervisor. I sincerely acknowledge him for his encouragement, patience and support during my thesis. I sincerely appreciate his advices about the scientific career. I always enjoyed discussing with him.

Dr. Heiko Bauer and the colleagues of Universität Mainz as well as Dr. Aladin Ullrich from the University of Augsburg for providing me the beautiful nanoparticles.

Dr. Markus Waschk and Dr. Sonja Schröder for providing me various manganese oxide powder samples grown in the oxygen MBE.

Dr. Yixi Su, Dr. Kirill Nemkovski and Erxi Feng for their help and support during my neutron beamtime at DNS as well as for the data analyses.

Michael Smik, Dr. Emmanuel Kentzinger and Dr. Ulrich Rücker for their support during my (GI)SAXS measurements at GALAXI.

Dr. Karen Friese, Dr. Cheng Li, Jörg Perßon, Lei Cao and Paul Hering for their help during the characterizations, treatments as well as analysing the results of MnO powder and the single crystal.

Dr. Yinguo Xiao, Dr. Markus Waschk, Alice Hanke, Dr. Pankaj Thakuria, Dr. Liming Wang, Wenhai Ji, Hailey Williamson for the fruitful discussions.

Berthold Schmitz and Frank Gossen for their technical support during the measurements at MPMS, PPMS and Dynacool, and for building an oxygen chamber for the nanoparticle annealing.

Finally, I would like to thank my family, especially my parents, and my friends, who are always there for me. Without their support and encouragement, I could not have finished this thesis. They have made my life colourful.